Strengthening of arched masonry structures with composite materials

Reforço de estruturas de alvenaria em arco com materiais compósitos

Tese apresentada por

Ismael Basilio Sánchez

à Universidade do Minho para obtenção do grau de

Doutor em Engenharia Civil

Departamento de Engenharia Civil

Guimarães, Portugal

Julho, 2007

Supervisor:

Professor Paulo José Brandão Barbosa Lourenço, University of Minho

Co-supervisor:

Dr. Daniel Vitorino de Castro Oliveira, University of Minho

Dr. Amado Gustavo Ayala Milián, National Autonomous University of Mexico

Committee members:

President:

Professor António José Marques Guimarães Rodrigues, Rector of the University of Minho

Examining Committee:

Dr. Daniel Vitorino de Castro Oliveira, University of Minho

Professor Paulo José Brandão Barbosa Lourenço, University of Minho

Dr. Joaquim António Oliveira de Barros, University of Minho

Dr. Amado Gustavo Ayala Milián, National Autonomous University of Mexico

Dr. Eduardo Nuno Brito Santos Julio, University of Coimbra

Dr. Humberto Salazar Amorim Varum, University of Aveiro

Dra. Graça de Fátima Moreira de Vasconcelos, University of Minho

Copyright © 2007 I. Basilio Sánchez

All rights reserved. No part of this publication may be reproduced, stored in a retrieval system, or transmitted in any form or by means, electronic, mechanical, photocopying, recording or otherwise, without the prior written permission of the publisher:

University of Minho, Department of Civil Engineering, Azurém, 4800-058 Guimarães, Portugal

Printed in Portugal

Acknowledgments

The work reported in this thesis was possible thanks to the scholarship made available by the Mexican National Council of Science and Technology (CONACYT). This work was sponsored by the Portuguese Science and Technology Foundation (FCT), contract POCTI-ECM-38071-2001, "Strengthening of masonry arches with composite materials".

The work was developed at University of Minho (UM) in Guimarães, Portugal, under the supervision of Prof. Paulo B. Lourenço and meticulous guidance of Dr. Daniel V. Oliveira which is acknowledged for encouraging and fruitful discussion.

I would like to record my thanks to Dr. A. Gustavo Ayala from the Mexican Institute of Engineering, for making the first contacts leading my stay at UM possible to continue my studies since the time I was working for my Master's Degree.

My gratitude to the colleagues at UM for both academic and social interactions. There a few friends that I would like to name for his friendship: Dawid, Nuno, Miguel, Cátia, Cristina, and Senthivel. Some of the first analyses to calibrate the interface properties were possible due to Claudio Maruccio, which is also recognized. The assistance of the Structural Laboratory technicians during the construction of the specimens is appreciated.

The birth of our tender and unique "Abdula" during this period motivated my inspiration. Thanks to Milena for her love and understanding standing by my side. For them to whom I stole valuable time dedicate to write this work. An specially dedication to my parents Ismael and Raquel, who gave me life, encouraged me to embark on this trip and always have supported me. To my youngest brother Gilberto who always gives joy sparks to the family.

Finally to the memory of those relatives whose unreplaceable presence will remain in my mind, specially to my dearest grandmother Feliza Juárez Lomelí (RIP).

Resumo

Devido à importância histórica do património cultural para qualquer país, não só socialmente mas também do ponto de vista técnico, tem surgido um crescente interesse no estudo do seu comportamento. Como qualquer outra estrutura, ao longo da sua vida útil, as construções históricas estão sujeitas à deterioração devido a acções ambientais e acidentais como terramotos, assentamentos diferenciais e ruptura de elementos estruturais devido à falta de resistência mecânica. Pelas razões expostas, é importante perceber e interpretar o seu comportamento e a evolução do dano que eventualmente possa existir para se poder avaliar a necessidade duma intervenção estrutural.

Nesta tese descreve-se um estudo numérico e experimental sobre a alvenaria de tijolo antiga reforçada com materiais compósitos (FRP). Tendo em conta que os principais modos de colapso ocorrem na ligação da alvenaria com o material de reforço, como parte dos objectivos do programa experimental, estudou-se o comportamento da interface assim como o comportamento global de estruturas à escala reduzida com formas curvas, construídas com o propósito de reproduzir arcos e abóbadas.

Foram utilizados dois tipos de materiais de reforço, nomeadamente fibras de vidro e carbono. Na construção dos provetes experimentais, procurou-se reproduzir as características mais relevantes das construções antigas portuguesas, com a utilização de materiais representativos da região. Com o propósito de caracterizar a distribuição de esforços na interface FRP-alvenaria, adoptou-se um ensaio de corte simples, onde se aplicou uma carga monotónica crescente no material compósito até à ruptura do provete. Para determinar o comprimento de ancoragem para o qual o modo de colapso muda de escorregamento para a ruptura por tracção do FRP, foram testados diferentes comprimentos de ancoragem. Por intermédio da análise da distribuição de esforços de corte na interface FRP-alvenaria, determinou-se que

as fibras de vidro comportam-se melhor que as de carbono, devido à compatibilidade das suas propriedades mecânicas com a alvenaria. Os ensaios de corte directo foram modelados numericamente tendo em vista a calibração das propriedades da interface. Foi ainda desenvolvida uma simulação analítica dos ensaios de corte FRP-alvenaria, baseada em dados experimentais para a distribuição de esforços ao longo do comprimento de ancoragem.

Foram construídos e ensaiados arcos de alvenaria com a forma semicircular, à escala 1:2, e ensaiados sob carregamento monotónico. Para estudar os mecanismos de colapso de arcos de alvenaria, aplicou-se uma carga concentrada no quarto de vão. Os arcos de alvenaria e foram carregados até se alcançar o seu colapso. As diferentes alternativas de reforço aplicadas, confirmam que o reforço aplicado de forma contínua, quer no intradorso quer no extradorso, funcionam melhor que reforço descontinuo. Como reforço adicional, colocaram-se dispositivos de ancoragem do reforço, os quais atrasam o destacamento das fibras de FRP e aumentam a capacidade de carga dos arcos. Todos os resultados experimentais foram simulados mediante a utilização de modelos numéricos, admitindo-se que o comportamento não linear apenas poderia ocorrer nos elementos de interface.

No trabalho desenvolvido, verificou-se que os modelos numéricos adoptados conseguiram reproduzir os resultados experimentais duma forma satisfatória e que os resultados da simulação analítica estão de acordo com os resultados experimentais obtidos em laboratório.

Abstract

Given the historical importance of the cultural heritage for any country, not only social but also from the technical point of view it naturally emerges the interest to be studied. As any other structure during its period of life, historical constructions are exposed to deterioration due to environmental actions and hazard events caused by: earthquake, differential settlements and structural elements failures due to lack of strength. For these reasons, in order to evaluate the need for a retrofitting intervention, is important to understand and interpret his behaviour and damage evolution.

This thesis describes a numerical-experimental study of historical clay brick masonry, strengthened by Fibre Reinforced Polymers (FRP). Because the most critical results are found in the FRP-masonry substrate, the local interface study was included as a part of the experimental objectives. In addition, scaled masonry specimens with curved shapes were constructed with the purpose to observe the global behaviour of strengthened structures as well as reproduction of domes and vaults. Two types of FRP material were used namely glass and carbon fibres. The building technique of experimental specimens, considered the reproduction of the most relevant characteristic regarding old Portuguese constructions, using typical materials from the region. With the purpose to characterize the stress distribution along the interface, a far-end supported single shear test was modified and adapted. Monotonic load was applied to the FRP strip until failure was attained. To determine the anchor length where the failure mode changed from sliding to tensile failure in the FRP strip, different anchorage lengths were tested. After analysing the shear stress distribution in the masonry-FRP interface, it was concluded that glass FRP behaves better than carbon due to compatibility of its properties with masonry. The far-end supported single-shear tests were then numerically modelled aiming at calibrating the interface properties. An analytical

"bond-slip" simulation of the FRP strip was done, using the experimental results as data to plot the stresses distribution along the anchorage length.

Masonry arches with semicircular a shape at scale of 1:2 were constructed and tested under monotonic loading. In order to observe and study the collapse mechanism of masonry arches, a concentrated load was applied, at the quarter span. The masonry arches were loaded until the collapse was achieved. Different strengthening alternatives were adopted, confirming that the FRP strip applied continuously at the extrados or intrados, perform better that collocating it discontinuously. As an additional anchorage strengthening technique, saturated fibres soaked into resin and manually prepared, were use to delay the FRP detachment when reinforced at the intrados surface. An increase of the maximum load was also achieved. All experimental tests series were evaluated by means of numerical models where nonlinear behaviour was concentrated in interface elements.

Along the present research it was found that not only the numerical models adopted were able to reproduce the experimental results reasonable but also the corresponding results from the analytical simulation, support the experimental results obtained in the laboratory.

Resumen

Debido a la importancia histórica del patrimonio cultural para cualquier país, no solamente social pero también desde del punto de vista técnico, ha surgido un creciente interés creciente en el estudio de su comportamiento. Como cualquier otra estructura a lo largo de su vida útil, las construcciones históricas están expuestas al deterioro debido a acciones ambientales y accidentales como terremotos, desplazamientos diferenciales por hundimientos y falla de elementos estructurales debido a la falta de resistencia mecánica. Por las razones expuestas, es importante comprender e interpretar su comportamiento y evolución del daño que eventualmente pueda existir para poder evaluar la necesidad de una intervención estructural.

En esta tesis se describe un estudio numérico y experimental sobre mampostería de ladrillo antigua, reforzada con materiales compuestos (FRP). Teniendo en cuenta que los principales modos de colapso ocurren en la unión de la mampostería con el material de refuerzo, como parte de los objetivos del programa experimental, se estudió el comportamiento de la interfaz así como el comportamiento global de estructuras a escala reducida con formas curvas, construidas con el propósito de reproducir arcos y bóvedas.

Fueron utilizados dos tipos de materiales de refuerzo, específicamente fibras de vidrio y carbón. En la construcción de los especímenes experimentales, se buscó reproducir las características más relevantes de construcciones antiguas portuguesas, con la utilización de materiales representativos de la región. Con el propósito de caracterizar la distribución de esfuerzos en la interfaz FRP-mampostería, se adaptó un ensayo de corte simple, donde se aplicó carga monotónica creciente en el material compuesto hasta la falla del espécimen. Para determinar la longitud de anclaje para la cual el modo de colapso cambia de deslizamiento a ruptura por tensión del FRP se probaron diferentes longitudes de anclaje. Por medio del análisis de la distribución de esfuerzos cortantes en la interfaz FRP-mampostería,

se determinó que las fibras de vidrio se comportan mejor que las de carbón, debido a la compatibilidad de sus propiedades mecánicas con las de la mampostería. Los ensayos de corte directo fueron modelados numéricamente tomando en cuenta la calibración de las propiedades de la interfaz. Adicionalmente se desarrollo una simulación analítica de los ensayos de cortante FRP-mampostería, basada en datos experimentales para la distribución de esfuerzos a lo largo de la longitud de anclaje.

Fueron construidos y ensayados arcos de mampostería con forma semicircular, a escala 1:2 sometidos a carga monotónica. Para estudiar los mecanismos de colapso de arcos de mampostería, se aplicó una carga concentrada en el cuarto del claro. Los arcos de mampostería se fueron cargaron hasta alcanzar su colapso. Las diferentes alternativas de refuerzo aplicadas, confirman que el refuerzo aplicado de forma continua, sea en el intradós o extradós, funciona mejor que el discontinuo. Como refuerzo adicional, se colocaron dispositivos de anclaje de refuerzo los cuales retardaron el desprendimiento de las fibras de FRP y aumentaron la capacidad de carga de los arcos. Todos los resultados experimentales fueron simulados mediante la utilización de modelos numéricos, admitiendo que el comportamiento nolineal podría ocurrir en los elementos de interfaz.

En el trabajo desarrollado, se verificó que los modelos numéricos adoptados consiguieron reproducir los resultados experimentales de una forma satisfactoria y que los resultados de la simulación analítica empatan con los resultados experimentales obtenidos en el laboratorio.

Contents

Acknowledgments iii

Resumo v

Abstract vii

Resumen ix

Contents xi

Notation xvii

List of Figures xix

List of Tables xxvii

1 Introduction 1

2 State of the Art 7

2.1 Historical masonry constructions 7

2.1.1 Historical background 7

2.1.2 Evolution of structural shapes 8

2.2 Strengthening techniques 12

2.2.1 Traditional strengthening techniques 13

2.2.2 Modern solutions: FRP as a viable adoption 15

2.3 Composite materials as an alternative solution 16

2.3.1 Applications 17

2.3.2 General aspects on FRP materials 18

2.4 Bond behaviour assessment 20

2.4.1 Existing evaluation tests . . . 21
2.5 FRP durability . . . 22
2.5.1 Long-term material behaviour . . . 24
2.5.2 Effect of moisture/aqueous solutions . . . 25
2.5.3 Effect of alkaline environment . . . 25
2.5.4 Effect of loading cycles (fatigue) . . . 26
2.5.5 Effects of ultraviolet radiation . . . 26
2.5.6 Other aspects . . . 27
2.5.7 Standard tests . . . 28
2.6 Behaviour of arched structures . . . 28
2.6.1 Plain arches . . . 30
2.6.2 Arch behaviour modified by reinforcement . . . 32
2.7 Adopted numerical tools . . . 33
2.7.1 Advanced numerical simulation . . . 34
2.7.2 Interface elements . . . 35
2.7.3 Limit analysis . . . 36
2.8 Conclusions . . . 37

3 Experimental FRP-masonry bond behaviour 39
3.1 Introduction . . . 39
3.2 Clay brick (type 1) . . . 40
3.2.1 Compressive tests . . . 40
3.2.2 Specimen preparation . . . 41
3.2.3 Test setup and test procedure . . . 43
3.2.4 Test results . . . 44
3.3 Mortar . . . 46
3.3.1 Mortar composition . . . 48
3.3.2 Specimen preparation . . . 49
3.3.3 Test setup and test procedure . . . 49
3.3.4 Test results . . . 51
3.4 FRP composites . . . 53
3.4.1 Material selected . . . 53
3.4.2 Specimen preparation . . . 54
3.4.3 Test setup and test procedure . . . 56
3.4.4 Test results . . . 57

3.5 Composite components 59
3.5.1 Basic components 59
3.5.2 Preparation of specimens 60
3.5.3 Test setup and test procedure 63
3.5.4 Test results 63
3.6 Masonry type 1 67
3.6.1 General description 67
3.6.2 Specimen preparation 67
3.6.3 Test setup and test procedure 68
3.6.4 Test results 69
3.7 FRP Pull-off test 71
3.7.1 Introduction and objectives 71
3.7.2 Specimens preparation 72
3.7.3 Test setup and test procedure 73
3.7.4 Test results 73
3.8 FRP-Masonry bond behaviour characterization 75
3.8.1 Specimen preparation 76
3.8.2 Test setup and test procedure 80
3.8.3 Presentation and discussion of results 81
3.9 Summary and conclusions 93

4 Experimental behaviour of masonry arches 95
4.1 Introduction 95
4.2 Clay brick type 2 97
4.2.1 Brick description 97
4.2.2 Specimen preparation 98
4.2.3 Test setup and test procedure 99
4.2.4 Test results 100
4.3 Masonry type 2 102
4.3.1 Material introduction and objectives 102
4.3.2 Specimen preparation 102
4.3.3 Test setup and procedure 102
4.3.4 Test results 103
4.4 Initial parametric study 106
4.5 Semicircular scaled masonry arches 108

4.5.1 Arch preparation . . . 109
4.5.2 Test setup and test procedure . . . 111
4.5.3 Unstrengthened arches . . . 113
4.5.4 Strengthened arches . . . 115
4.5.5 Summary of experimental test results . . . 129
4.6 Conclusions . . . 131

5 Numerical modelling of bond tests 133
5.1 Structural model for the bond test . . . 135
5.2 Stress distribution along the FRP . . . 137
5.2.1 Normal stress at the FRP loaded-end . . . 137
5.2.2 Normal stress along the anchorage length . . . 142
5.3 Analytical approach . . . 146
5.3.1 Bond stress-slip formulation . . . 146
5.3.2 Strains distribution along the anchorage length . . . 148
5.3.3 Bond stress along the anchorage length . . . 153
5.3.4 Local bond stress-slip curve . . . 158
5.4 Conclusions . . . 161

6 Numerical modelling of masonry arches 163
6.1 Structural model for masonry arches . . . 164
6.2 First parametric study vs. experimental results . . . 166
6.3 Unstrengthened arches . . . 167
6.4 Locally strengthened arches . . . 171
6.5 Continuously strengthened arches at the extrados . . . 175
6.6 Continously strengthened arches at the intrados . . . 177
6.7 Second parametric study vs experimental results . . . 184
6.8 Summarized conclusions . . . 186

7 Concluding remarks and future work 189

References 195

A Appendix A 209

B Appendix B 211

C Appendix C **215**

D Appendix D **219**

E Appendix E **223**

Notation

E	young modulus	41
$LVDT$	Linear Varible Displacement Transducer	44
E_{sg}	young's modulus obtained with the strain gauge	44
E_{LVDT}	young's modulus obtained with the LVDT	44
ISO	International Standard Guideline	54
$ASTM$	American Society of Testing Material	43
σ	stress state at the material	49
ε	strain of the material	44
$C.V.$	coefficient of variation	44
FRP	Fiber Reinforced Polymer	96
$GFRP$	Glass FRP	96
$CFRP$	Carbon FRP	96
$G150RS$	GFRP with 150 mm of anchorage length	78
$G100RS$	GFRP with 100 mm of anchorage length	77
$G200RS$	GFRP with 200 mm of anchorage length	77
$G150RI$	GFRP with 150 mm of anchorage length, spike anchor	78
$G150RT$	GFRP with 150 mm of anchorage length, transverse bar	78
$G150ES$	GFRP with 150 mm of anchorage length, concave shape	78
$G150XS$	GFRP with 150 mm of anchorage length, convex shape	78
$C150RS$	CFRP with 150 mm of anchorage length	77
θ_i	internal diameter	109
US	unstrengthend arches	110
LS	locally strengthened arches	110
CSE	continuously strengthened arches at the extrados	110
CSI	continuously strengthened arches at the intrados	110

f_t	uniaxial tensile strength	53
ν	poisson ratio	136
k_n	interface tangential stiffness	138
k_s	interface shear stiffness	136
c	cohesion	153
$tan\phi$	tangent ϕ	136
$tan\psi$	tangent ψ	136
G_{fc}	compressive fracture energy	136
G_f^I	mode I fracture energy	136
G_f^{II}	mode II fracture energy	153
κ_p	plastic relative displacement to the peak stress	136
w_s	FRP strip width	147
t_s	FRP thickness	147
τ	shear stress along the FRP strip	147
dx	infinitesimal longitude	147
E_s	young's modulus of the FRP strip	147
$d\epsilon_s$	infinitesimal of the FRP strain	148
ds	infinitesimal of the slip	148
d^2s	second derivative of the slip	147
dx^2	second derivative of the infinitesimal longitude	147
s	slip for the bond stress formulation	134
k	stiffness of the structure	168
$k_{0,exp}$	initial experimental stiffness of the structure	169
$k_{0,num}$	initial numerical stiffness of the structure	168
F	sustained load on masonry arches	182
F_{max}	maximum sustained load on masonry arches	166
1_{st}	first hinge detected	180
2_{nd}	second hinge detected	115
3_{rd}	third hinge detected	176
4_{th}	fourth hinge detected	169
q	self weight of the arch	164

List of Figures

2.1 masonry conceptions in Greece 9
2.2 True arch construction 10
2.3 Examples of combined barrels 11
2.4 Advanced curved structres built 12
2.5 Walls and cracks injection. 14
2.6 Example of FRP strips use in masonry vaults strengthening. 16
2.7 Composite formation 18
2.8 Composite shipment in various industries 19
2.9 Classification of bond tests (Chen et al. 2001). 22
2.10 durability concepts and damage tolerance 23
2.11 Fatigue life and remaining strength 27
2.12 Basic of the line of thrust 30
2.13 Hinging failure mode 31
2.14 Three-hinges for a semi-circular masonry arch 33
2.15 The Newton Rapson Method 35

3.1 Clay brick type 1 42
3.2 Test setup clay brick type 1 43
3.3 Brick type 1 compressive strength tests 45
3.4 Typical failure mode for the clay brick type 1. 46
3.5 setup for mortar compressive and Young's modulus 50
3.6 Mortar compression results 52
3.7 Mortar failure modes after monotonic compressive tests. 52
3.8 Degussa rolled sheets selected 53
3.9 Specimen specifications from the ISO guideline 55
3.10 (a) Vertical band saw to cut FRP strips; (b) cutting procedure. . . 55

3.11 General setup for the sheet strip strain gauge position. 56
3.12 Stress-strain diagrams of glass and carbon 58
3.13 FRP failures modes 59
3.14 Putty components and dimension for the tensile strength test . . . 61
3.15 Preparation of the putty specimen 61
3.16 Primer and Resin, kit components and dimensions of specimen . . . 62
3.17 Stress-strain diagrams for the composite 66
3.18 Failures modes of the composites 66
3.19 Dimensions adopted for the masonry type 1 prism 68
3.20 (a) Test setup; (b) lvdts arrangement around the steel plate. 68
3.21 Masonry compressive stress strain diagrams 70
3.22 Cracking sequence to the masonry type 1 70
3.23 stress-strain diagrams obtained from masonry components 71
3.24 Pull-off test specimens. 72
3.25 Sequential stages of the pull-off 73
3.26 failures modes of pull-off test using glass and carbon 75
3.27 Strengthened masonry elements and applied layers 77
3.28 Branch tree relations derived from a reference arrangement. 79
3.29 Adapted Test setup for the bond test specimens 80
3.30 stress along the anchorage length for the G150RS and G100RS . . . 86
3.31 stress along the anchorage length for G100RS and G200RS 86
3.32 stress along the anchorage length for G150RI and G150RT 87
3.33 Stress along the anchorage length for G150ES and G150XS 87
3.34 Peak stress for each series (average and standard deviation values). 88
3.35 Normal stress along the anchorage for different length and material 89
3.36 Envelope of displacement vs. normal stress for G150RS & G100RS . 90
3.37 Envelope of displacement vs. normal stress for G200RS & C150RS . 90
3.38 Envelope of displacement vs. normal stress for G150RI & G150RT . 91
3.39 Envelope of displacement vs. normal stress for G150ES & G150XS. 91
3.40 Representative failures modes for each series 92

4.1 Clay brick type 2 98
4.2 Test setup for the clay brick type 2 99
4.3 Brick type 2 compressive test results 101
4.4 Typical failure modes of the clay brick type 2 units. 101

4.5 Dimensions of masonry type 2 test specimen. 102
4.6 Masonry type 2 setup 103
4.7 Masonry type 2 compressive test results 105
4.8 Crack pattern recorded for the masonry type 2 105
4.9 Masonry type 2 and its components on a single stress strain plot. . 106
4.10 Influence of the FRP width strip on the load of arches 107
4.11 Arch geometry, dimensions in (mm). 109
4.12 Phases involved in the construction of masonry arches 110
4.13 Arch test setup 112
4.14 Instrumentation for the test specimen. 113
4.15 Plain arches diagrams of US-1 and US-2 114
4.16 Deformed shape and localization of hinges for US 115
4.17 Strengthened masonry strategies 117
4.18 Strengthening procedure 118
4.19 Load-displacement diagram for LS-1 and LS-2 119
4.20 Load-displacement diagram for US-1 and LS-1 120
4.21 Load-displacement diagram US-2 and LS-2 120
4.22 Mechanism of failure of the locally strengthened arches 121
4.23 Final stage of strengthened masonry arches at the extrados 122
4.24 Load-displacement diagrams for the CSE w/ 100 mm strip width . 123
4.25 Load-displacement diagrams for the CSE w/ 160 mm strip width . 123
4.26 Failure mechanisms of continuous external strengthened arches. . . 124
4.27 Preparation of the non-conventional anchorage devices 125
4.28 Load-displacement diagrams for CSI w/ 100 mm strip width 126
4.29 Load-displacement diagrams for CSI w/ 100 mm strips width along with spikes 127
4.30 Deformed shape and failure mechanism mode for the CSI series . . 128
4.31 Influence of the FRP width on the load of the LS 130

5.1 Adopted shapes for the numerical bond tests 135
5.2 Experimental envelope and numerical results for G150RS 138
5.3 Comparison of experimental envelopes and numerical results concerning G100RS; G200RS and for the three anchorage lengths. . . . 139
5.4 Experimental envelope and numerical response for carbon, comparison with the G150RS 140

5.5 Experimental envelopes and numerical results concerning bond test specimens w/ curved shapes and comparison w/ the G150RS 141
5.6 Numerical results and experimental envelopes of the FRP normal stress for the G150RS-*n*, 25% and 75% 143
5.7 Numerical results and experimental envelopes of the FRP normal stress for the G100RS-*n*, 25% and 75% 143
5.8 Numerical results and experimental envelopes of the FRP normal stress for the G200RS-*n*, 25% and 75% 144
5.9 Numerical results and experimental envelopes of the FRP normal stress for the C150RS-*n*, 25% and 75% 145
5.10 Numerical results and experimental envelopes of the FRP normal stress for the G150ES-*n*, 25% and 75% 145
5.11 Numerical results and experimental envelopes of the FRP normal stress for the G150XS-*n*, 25% and 75% 146
5.12 Free body diagram of the bond test specimen. 148
5.13 Numerical results and experimental envelopes of the FRP strains for the G150RS-*n*, 25% and 75% 149
5.14 Numerical results and experimental envelopes of the FRP strains for the G100RS-*n*, 25% and 75% 150
5.15 Numerical results and experimental envelopes of the FRP strains for the G200RS-*n*, 25% and 75% 151
5.16 Numerical results and experimental envelopes of the FRP strains for the C150RS-*n*, 25% and 75% 151
5.17 Numerical results and experimental envelopes of the FRP strains for the G150ES-*n*, 25% and 75% 152
5.18 Numerical results and experimental envelopes of the FRP strains for the G150XS-*n*, 25% and 75% 152
5.19 Numerical results and experimental envelopes of the FRP bond stress for the G150RS-*n*, 25% and 75% 154
5.20 Numerical results and experimental envelopes of the FRP bond stress for the G100RS-*n*, 25% and 75% 154
5.21 Numerical results and experimental envelopes of the FRP bond stress for the G200RS-*n*, 25% and 75% 155

5.22 Numerical results and experimental envelopes of the FRP bond stress for the C150RS-n, 25% and 75% 155
5.23 Numerical results and experimental envelopes of the FRP bond stress for the G150ES-n, 25% and 75% 157
5.24 Numerical results and experimental envelopes of the FRP bond stress for the G150XS-n, 25% and 75% 157
5.25 Analytical local bond stress-slip for G150XS specimen 159
5.26 Envelope of the analytical bond stress vs. displacement along the anchorage length for the G150RS-n and G100RS-n 160
5.27 Envelope of the analytical bond stress vs. displacement along the anchorage length for the G200RS-n and C150RS-n 160
5.28 Envelope of the analytical bond stress vs. displacement along the anchorage length for the G150ES-n and G150XS-n 161

6.1 Modelling of semicircular arches 165
6.2 Preliminary parametric study versus experimental results 167
6.3 Experimental US-1 and US-2 compared with numerical response . . 168
6.4 Numerical sequence of hinges formation for the US 170
6.5 Numerical US arch 171
6.6 Experimental LS-1 and LS-2 compared with numerical response . . 172
6.7 Numerical sequence of hinge formation for the LS 173
6.8 Numerical LS arch 174
6.9 Experimental CSE-1 and CSE-2 compared w/ numerical response . 175
6.10 Hinge development sequence for the numerical CSE arch with 100 mm strip width 176
6.11 Numerical CSE arches with 100 mm FRP width 177
6.12 Experimental CSE-3 and CSE-4 compared w/ numerical response . 178
6.13 Hinge development sequence for the numerical CSE arch w/ 160 mm strip width 178
6.14 Numerical CSE arches with 160 mm 179
6.15 Experimental CSI-1 and CSI-2 compared w/ numerical response . . 179
6.16 Hinge development sequence for the numerical CSI model without anchor devices 180
6.17 Numerical CSI arches without anchor devices 181
6.18 Experimental CSI-3 & CSI-4 compared w/ its numerical response . 182

6.19 Hinges developed for the numerical CSI model w/ spikes 183
6.20 Numerical CSI arches with spikes anchor devices 184
6.21 Second parametric study 185

A.1 Typical normal stress-relative displacement at the loaded end 209

B.1 Numerical results and experimental envelopes in terms of the FRP normal stress for the G150RS, 50 & 100% of the maximum 211
B.2 Numerical results and experimental envelopes in terms of the FRP normal stress for the G100RS, 50 & 100% of the maximum 212
B.3 Numerical results and experimental envelopes in terms of the FRP normal stress for the G200RS, 50 & 100% of the maximum 212
B.4 Numerical results and experimental envelopes in terms of the FRP normal stress for the C150RS, 50 & 100% of the maximum 213
B.5 Numerical results and experimental envelopes in terms of the FRP normal stress for the G150ES, 50 & 100% of the maximum 213
B.6 Numerical results and experimental envelopes in terms of the FRP normal stress for the G150XS, 50 & 100% of the maximum 214

C.1 Numerical results and experimental envelopes in terms of the FRP strains for the G150RS, 50 & 100% of the maximum 215
C.2 Numerical results and experimental envelopes in terms of the FRP strains for the G100RS, 50 & 100% of the maximum 216
C.3 Numerical results and experimental envelopes in terms of the FRP strains for the G200RS, 50 & 100% of the maximum 216
C.4 Numerical results and experimental envelopes in terms of the FRP strains for the C150RS, 50 & 100% of the maximum 217
C.5 Numerical results and experimental envelopes in terms of the FRP strains for the G150ES, 50 & 100% of the maximum 217
C.6 Numerical results and experimental envelopes in terms of the FRP strains for the G150XS, 50 & 100% of the maximum 218

D.1 Numerical results and experimental envelopes in terms of the FRP bond stress for the G150RS, 50 & 100% of the maximum 219
D.2 Numerical results and experimental envelopes in terms of the FRP bond stress for the G100RS, 50 & 100% of the maximum 220

D.3 Numerical results and experimental envelopes in terms of the FRP bond stress for the G200RS, 50 & 100% of the maximum 220
D.4 Numerical results and experimental envelopes in terms of the FRP bond stress for the C150RS, 50 & 100% of the maximum 221
D.5 Numerical results and experimental envelopes in terms of the FRP bond stress for the G150ES, 50 & 100% of the maximum 221
D.6 Numerical results and experimental envelopes in terms of the FRP bond stress for the G150XS, 50 & 100% of the maximum 222

E.1 Analytical local bond stress-slip for the G150RS specimen 224
E.2 Analytical local bond stress-slip for the G100RS specimen 225
E.3 Analytical local bond stress-slip for the G200RS specimen 226
E.4 Analytical local bond stress-slip for the C150RS specimen 227
E.5 Analytical local bond stress-slip for the G150ES specimen 228

List of Tables

3.1 Compressive characterization of clay brick type 1. 45
3.2 Technical information from the manufacturer for Mapei-Antique MC. 49
3.3 Mechanical characterization of the mortar (15 days). 51
3.4 Manufacturer data for the FRP composite material. 53
3.5 Tensile strength and Young's modulus for GFRP specimens. 57
3.6 Tensile strength and Young's modulus for CFRP specimens. 58
3.7 Manufacturer data for the composite components. 62
3.8 Tensile strength and Young's modulus of putty specimens. 63
3.9 Tensile strength and Young's modulus of primer specimens. 64
3.10 Tensile strength and Young's modulus of resin specimens. 64
3.11 Mechanical characterization of masonry prism type 1. 69
3.12 Pull-off specimens using masonry prism type 1. 74
3.13 Pull-off specimens using masonry prism type 2. 74
3.14 Peak stresses for reference specimens. 81
3.15 Peak stresses for G100RS-n specimens. 82
3.16 Peak stresses for G200RS-n specimens. 82
3.17 Peak stresses for the C150RS-n specimens. 83
3.18 Peak stresses for G150RI-n specimens. 83
3.19 Peak stresses for G150RT-n specimens. 84
3.20 Peak stresses for the G150ES-n specimens. 84
3.21 Peak stresses for G150XS-n specimens. 85

4.1 Compressive mechnical characterization of clay brick type 2. 100
4.2 Mechanical characterization of masonry type 2. 104
4.4 Summary of masonry arches results. 129

5.1 Elastic properties for the masonry, FRP and interface. 137

5.2 Inelastic properties for the interface, see Diana (1999) for details. . 137
5.3 Experimental and numerical comparison of bond test specimens . . 140

6.1 Elastic properties for the bricks, FRP and interfaces. 165
6.2 Inelastic properties adopted for the masonry and composite interfaces. 166
6.3 Masonry arches stiffness. 169
6.4 Hinges formation sequence. 170
6.5 Maximum load sustained by arches. 174

Chapter 1

Introduction

Most of the physical phenomena that surround us have a simplified interpretation and can usually be reproduced by, for example, theoretical models implemented into computers programs.

Conservation and restoration of the built heritage is an issue that has deserved much interest for many years and in many countries. Large funds are being spent to preserve either key buildings, such as the Tower of Pisa in Italy, the Jerónimos Monastery in Lisbon and the Mexico City Cathedral, or historical city centres. Although empirical rules were enough to build these odd constructions, the application of modern concepts of mechanics and the development of tools for the structural analysis of ancient masonry constructions have been the topic of very active research mainly in the past decades. Heritage conservation is a challenging objective for engineers and constitutes a topic of the highest relevance for the society, which, as a consequence, has been adopted as part of research activities around the globe. The engineer participation in conservation or restoration projects is twofold. First, it is necessary to assess the structural safety of the construction and then, if necessary, to design strengthening solutions. In both cases, the engineer needs adequate structural analysis tools.

For structural assessment purposes, technicians need to elaborate models of the mechanical behaviour of materials. These models can vary widely from very accurate to very simplified. Accurate models allow to predict closely the behaviour of the analysed structures when the loads and model parameters are known with good accuracy. This type of models is likely to be the best choice for the monuments assessment, although it requires a great deal of data that is not always available.

On the other end, very simplified models produce limited and approximated information about the structural behaviour. Even though, this information may be enough in quantity and accuracy for engineering assessment purposes when the available data about material properties, boundary conditions and loads is only roughly approximated. Together with the material model, the engineer needs to elaborate a structural model. To simplify this task, the structure is generally divided into several elements. The behaviour of each element is modelled separately and, finally, the single elements are assembled to form the whole structural model. There is also a variety of model types for structures, from very elaborated to very simplified. With the former is possible to model a wide variety of structures, *e.g.*, continuum finite elements.

Several combinations of material and structural models are possible. Advanced finite element method models (FEM) have been developed in the past decades combining accurate material and structural models. They include both discrete (micro) models, *e.g.*, Lourenço et al. (1998) and Lofti and Shing (1994), and continuous anisotropic models, *e.g.*, Lourenço and Rots (1997). A drawback in the use of these sophisticated models in the practical assessment of structures is the large amount of time needed for the structural model elaboration, for performing the nonlinear analyses and for reaching proper understanding of the results significance. These models are much likely to be used for structural analysis of special cases, such as complex, important or large structures like historical monuments.

Furthermore, the mechanical characterization of ancient masonries is a difficult task because these structures were built with poor quality control standards and, in many cases, have been already subjected to extensive modifications. These materials usually are very heterogeneous, making it difficult to assign mean values to the model parameters.

Linear elastic FEM analysis combines an elaborated structural model with a very simplified material model. It can be assumed as a more practical tool, even if the time requirements to construct the model are the same as for nonlinear analysis. However, due to the low tensile strength of masonry, this material presents nonlinear behaviour since very low load levels. Therefore, it is necessary to perform localized changes to the model, such as Young's modulus modifications or element discontinuities by node duplication, to approximate cracking behaviour.

This process implies a series of analyses, model changes and possible in objective results that render it unattractive for practical applications.

In summary, nonlinear FEM or other sophisticated models are an alternative for the assessment of important monuments, while simplified approaches like limit analysis are more appropriate for small buildings. Also, if the assessment indicates insufficient load carrying capacity, strengthening solutions must be designed. Nonlinear displacement methods are excessively time consuming and can only be used for validation. Even in the case of large and important monuments, once identified the main failure modes through sophisticated models, simplified models are better for strengthening design.

The main objective of this work is to investigate the performance of arched masonry structures strengthened using composite materials through experimentation and numerical simulation. In the second part, masonry arches unreinforced and strengthened with FRP materials were compared to characterize their behaviour and collapse mechanism, primordially. The main focus is the assessment of ancient masonry constructions. Detailed goals are:

- to perform the experimental characterization of FRP and masonry components and the FRP-masonry bond behaviour characterization, namely in terms of ultimate load capacity and stress distribution along the anchorage length and the bon-slip relationship at the loaded end;

- to investigate key parameters relative to the FRP-masonry interface response, particularly anchorage length and FRP materials. The anchoring scheme adopted and the curvature of masonry surface are considered and studied in detail;

- to obtain normal stress and sliding of the FRP strip along the anchor length are computed from the strain gauges data acquired in the tests;

- to carry out a parametric study where the FRP strip width influence on the peak load and failure mechanism served as an indication before initiating the masonry arches experimental tests;

- to get a reliable database of experimental results on masonry arches, together with adapted numerical models and analytical formulation;

- numerical and analytical tools were useful on the assessment of the bond test specimens as well as masonry arches behaviour.

To obtain a deeper understanding and interpretation of the major challenges regarding historical constructions, motivated by the above reasons, an experimental campaign interacting with the application of numerical and analytical tools was followed. The project undertaken at University of Minho was sponsored by the Portuguese Foundation for Science and Technology (FCT). The content of the thesis is covered in seven chapters including this introduction.

Chapter 2 is a review of historical background concepts and previous work regarding historical masonry constructions including assessment and strengthening techniques, emphasizing the use of FRP materials. Then, main topics about FRP durability and applications are outlined, together with aspects related to arched structures. This chapter also presents the numerical tools used in research to assess and predict structural behaviour.

Chapter 3 presents the first part of the experimental campaign, concerning a comprehensive mechanical characterization of materials utilized in the bond test specimens and results on the stress transmission at the interface between masonry and FRP reinforcement over the anchorage length.

In Chapter 4, results on scaled masonry arched structures are presented. As a complementary part of the experimental work, semicircular arches monotonically loaded at a quarter span were tested until failure. Since different materials were used, their mechanical characterization was also carried out. Diagrams of load versus displacement under the load application point are displayed showing the damage along the test, with development of hinges. Continuous and localized strengthening was adopted for the studied cases. The first parametric study carried out before initiating the tests is also presented.

Chapter 5 presents a numerical model constructed within a commercial program, where the Finite Element Method is implemented, to reproduce the bond test specimens. By means of the analysis carried out it was possible to reproduce the normal stresses at the FRP loaded strip and along the anchorage length. All results were compared with experimental envelops superimposing the numerical response obtained from the model. At the end of the chapter an analytical bond

slip simulation was develop to estimate bond stresses and strains. The analytical formulation was based on discrete points measured during testing. Analytical envelops results were compared with the numerical model output as well.

Chapter 6 presents the numerical model to simulate the experimental masonry arches. Such model was capable of reproducing detailed information regarding the displacements and damage stages through the loading process. Plain and strengthened arches are compared with the experimental results presented in chapter four.

Finally, Chapter 7 summarizes the main aspects of the work and the key conclusions obtained, as well as required future works to be developed within the field of research.

Chapter 2

State of the Art

2.1 Historical masonry constructions

2.1.1 Historical background

Historical evidence shows that mortars existed and have been used for millions of years to satisfy different purposes. Historical sources refer to mortars as isolating lining materials in cisterns, wells, aqueducts, shafts and duct drains, as supporting materials for pavements and mosaics, as plasters on external and internal walls, as supporting materials for frescoes, and as joint mortars of masonry structures. In the southeastern Mediterranean, especially in the island of Rhodes, the craftsmanship of mortars flourished from the second millennium BC (Efstathiadis 2000), showing examples of architectural and structural applications stemming from the various historical periods through the Hellenistic, Byzantine, Knights and Ottoman periods until nowadays.

Mud as the cheapest material utilised since the Egyptian and Greeks, was used on the brick construction. Bricks became the first prefabricated building elements. However the earliest known concrete produced intentionally by human beings was discovered in the floor of a crude shelter built about 5600 BC on the banks of the Danube river in Yugoslavia.

For some reason, it appears that the technique for using lime based mortars was lost for at least 2500 years, until indications of use by the ancient Assyrians and Babylonians civilizations around 3000 BC.

The used mud bricks mixed with straw to bind dried bricks by Egyptians

delayed the discover of lime and gypsum mortar as a binding agent for building the pyramids. At that time, ancient Chinese used lime materials to hold bamboo together in theirs boats and in the Great Wall. By 500 BC the art of making concrete had spread to the Mediterranean island of Crete, and from there to the ancient Etruscan and Greeks.

Yet, it was the Romans who brought the manufacture and use of lime-based concrete to an art form. Roman's concrete was employed not only in foundations, as, for instance, in the raft of the Coliseum, but also for the construction of walls and vaults. 300 BC saw the Romans widely employing slaked lime and volcanic ash called pozzolan, named after the town of Pozzuoli near Mount Vesuvius (Singer et al. 1965). This was an hydraulic binder that can harden when mixed with water in air as well as under water. Moreover, natural additions such as animal fats, milk and blood were also used throughout this era (Kirca 2005). After the Roman Empire, knowledge of concrete was almost lost till the 18^{th} century.

Limestone containing a proportion of clay is often seen as an advantage in building as they produce hydraulic limes. In fact, traditional limes do not posses hydraulicity, since they need carbon dioxide for their hardening reaction (Erdoğan 2002).

Traditional lime plasters were often mixed with animal hair to improve cohesion and adhesion. Today, the addition of gypsum, portland cement or pozzolans to increase durability and give faster setting times are more common.

The addition of aggregates is important to increase the mass density, to reduce the amount of lime that must be burnt and slaked, and to reduce shrinkage.

Bearing structures and in particular walls, piers and arches, were made from dry stone, worked so that a prefect matching surface was obtained or else from natural or roughly worked stones or bricks assembled using thin layers of mortar.

2.1.2 Evolution of structural shapes

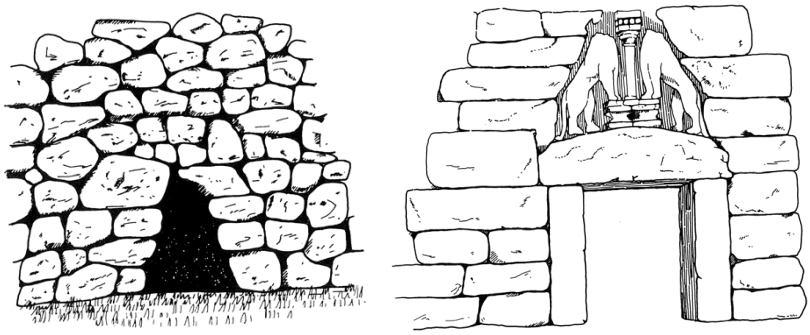
Horizontal space is most easily spanned when placing a beam across an opening. This occurs naturally when a tree trunk falls across a creek or small river. Primitive men used the same technique by balancing a stone across two other stones. In this post and lintel form of construction the long or the balanced stone bends to produce compressive stresses at the top and tensile stresses at the bottom. Because the tensile strength of rock is low and it is prone to crack, the stone beam or lintel

had a relatively large cross section and span over only a short distance. Post and lintel construction is a fundamental form of masonry construction used all over the world. Stone lintels were also used to support the masonry above openings walls.

In addition to the simple corbelled arch, in the 13^{th} century BC the Lion's Gate at Mycenae (Greece) was constructed with a lintel spanning just over 3 m above a triangular slab placed, enabling to see the beginnings of the arched behaviour that would dominate the following millennia, Figure 2.1. Arches do not exist in nature: it is an invention, which appeared in Babylon perhaps 6.000 years ago (Aztecs and Incas built in masonry for centuries without knowing the arch).

The technique of arching with blocks placed as corbels one on top of the other has been applied to build both false domes and arches, much older than the true arches and domes systematically constructed in the Roman period.

With this brief background, it is clearly seen how the change from linear to curved structures, *e.g.* arches and vaults, represented a significant structural advance, which allowed to replace stone and timber lintels in walls, with stone or brick masonry spanning wider openings. Indeed, in curved elements, it is usual to find only compressive stresses in a given section and consequently no tensile on resistant materials are required, Figure 2.1b.

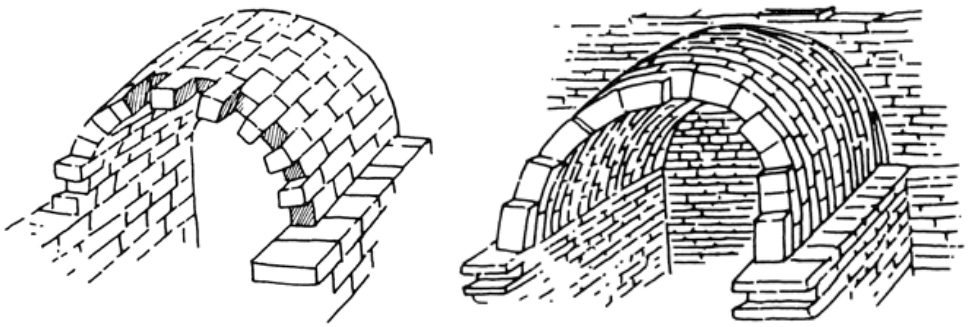


(a) (b)

Figure 2.1: Two samples of the first masonry conceptions in Greece: (a) Corbelled arch in wall Tiryns (c.600 B.C); (b) The Lion Gate (c.1250 B.C.).

Figure 2.2b, shows an alternative design of a circular vault, which can be built from tiles without the use of centring; this method was developed in Egypt and Assyria, and can be found in some Byzantine work. The tiles laid back at an angle

(starting from a vertical end wall), and each course acts as permanent formwork for the next course to be laid.



(a) (b)

Figure 2.2: True arch construction, construction of vaults (a) requiring temporary support; (b) using end walls and previous construction for stability during construction.

Although in others cultures such as the Islamic architecture, the shape of arches and domes was often dictated by architecture intentions than by structural efficiency. The arch was the structural element that best exploited the characteristic of masonry and for two thousand years it was also the dominant feature of bridges.

Vaults and domes

Vault represents the three dimensional extension of the arch in space, although their initial beginnings, its techniques of construction and materials are different. Potentially the vault has a big advantage in relation to the arch: its two dimensional behaviour, which may be considered as an individual series or arches (meridians) and parallels in domes with bending moments.

Another structural element that encloses space is the dome. This can be thought of as the shape formed by the rotation of an arch about its vertical axis. Once again the earliest domes were formed by the corbelling technique which leads to a fairly pointed dome. In this case, each course of masonry forms a horizontal ring in which, to some extent, each masonry units is prevented from unbalancing by adjacent unit forming a compression ring.

Great ingenuity was often shown in combining barrels vaults to create pleasing buildings. The culmination of this development was the cross vault, or groin vault,

so named after the lines created by its intersecting surfaces. Examples of vaults are shown in Figure 2.3.

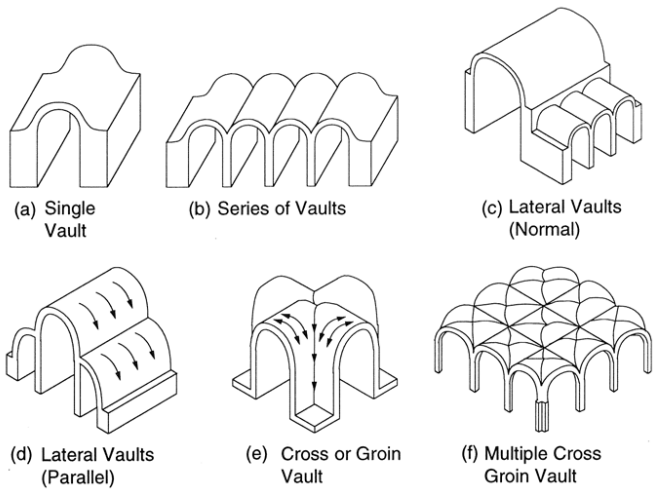
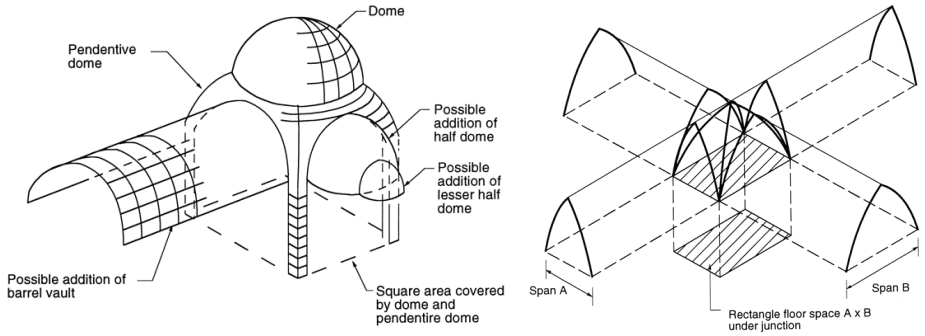


Figure 2.3: Examples of combined barrels: (a) single vault; (b) series of vaults; (c) lateral vaults (normal); (d) lateral vaults parallel; (e) cross or groin vault and (f) multiple cross groin vault.

Hemispherical domes were set upon cylindrical walls or more interestingly over polygonal or even square supporting walls. In latter cases, the supporting walls were made thick enough to contain the base of the dome or thinner walls used with lintels or arches spanning across the corners to support the dome. There is another elegant solution, to support a dome over a square plan area, using portions of another hemispherical surface called a pendentive dome. In this solution the top dome had a diameter equal to the side of the square area below. The pendentive dome was a hemisphere encompassing the square below, but truncated at the base of the top dome and the vertical side of the square as indicated in Figure 2.4a.

In domes where stresses in the parallel directions exceed the weak tensile strength, cracks along the meridians occur, and as the cracks increase, the behaviour approaches that of independent arches, defined by the arches along the meridians, the bending moments may then become significant and unstable situations may occur (Croci 1998).

Interesting and efficient roof structures can be generated on a rectangular grid by using variations of this junction illustrate in Figure 2.4b.



(a) (b)

Figure 2.4: (a) combinations of domes and vaults; (b) intersections of a pointed vaults.

2.2 Strengthening techniques

Structures during its life expectancy are prone to ageing effects, movements in the abutments or other accidental factors (like ground motion) causing structural damage on elements belonging to arches, thus affecting global stability. To appraise maximum resistant loads, deformation patterns and collapse mechanisms of masonry arches, a good understanding of their structural behaviour is required. Because structural remedial measures might be needed after a structural evaluation, a significant concern in actual research is the need for efficient strengthening techniques to re-establish the performance of these structures, preventing its brittle collapse when subjected to ultimate limit state.

Since the beginning of structural restoration, architects and engineers have envisaged and actually applied a wide variety of repair or strengthening interventions to improve the structural response of ancient masonry structures. In practice, the possible solutions must be carefully considered and their actual applicability to each specific problem must be assessed in detail.

Many historic constructions are structurally inadequate for current use. Additional material deterioration due to environmental factors and lack of maintenance have caused significant weakening of historically important structures (Drysdale et al. 1993).

In recent years an increasing interest in masonry construction has been observed. A variety of innovative techniques have been developed to restore deteriorating structures by using advanced composite materials (Tan and Patoary

2004). Among several strengthening types available on the market (glass, carbon, or aramid fibres) the selection of the FRP based system shall take into account the physical and chemical properties of the masonry to choose the most suitable solution (CNR-DT 200/2004 2004).

When selecting possible repair or strengthening solutions, it is also essential to keep in mind the principles of conservation and the modern criteria for the analysis and restoration of historical structures.

2.2.1 Traditional strengthening techniques

Any decision concerning conservation and restoration should be taken after a careful diagnosis and evaluation of the safety of the structure in its current state. The extent and the nature of the actions must then be balanced to achieve the required safety levels. A few decades ago, strengthening of structures was accomplished by the materials available at that time.

The criteria for choosing a particular solution must take into account not only its structural effectiveness and cost, but also the compatibility with the techniques and materials used in the construction of the monument regarding its original conception and historical value.

The problem is thus a complex one and calls for careful consideration of all the matters affecting safety, primarily a clear understanding of the structural behaviour, and for scrupulousness in decision making. The availability of recommendations drawn up specifically for heritage architecture is a positive contribution (CNR-DT 200/2004 2004; EU-India ALA/95/23/2003/077-122 2006). Suggestions and recommendations are already contained but some improvements and acceptability still remains in process.

The art of restoration thus must be tempered with caution and backed by a broad background of scientific knowledge. If properly used, however, modern technologies can offer interesting solutions and effectively help to preserve heritage.

Different techniques for retrofitting historical constructions have been adopted, *e.g.*, prestressing cables, injected mortar Figure 2.5, inserted steel bars, wooden planks, iron cramps and synthetic polypropylene fibres. Special stainless steel, vitreo /resin bars, synthetic resin bars, carbon fibres, polymeric fibres or other synthetic ropes are all alternative materials to steel, wood or iron rings. As a particular

case, quite often the problems of the vaults cannot be resolved without considering the structure as a whole and in particular the interaction between columns vaults and roofs. For a complete detailed description and objective of different strengthening techniques, readers are referred to EU-India ALA/95/23/2003/077-122 (2006).

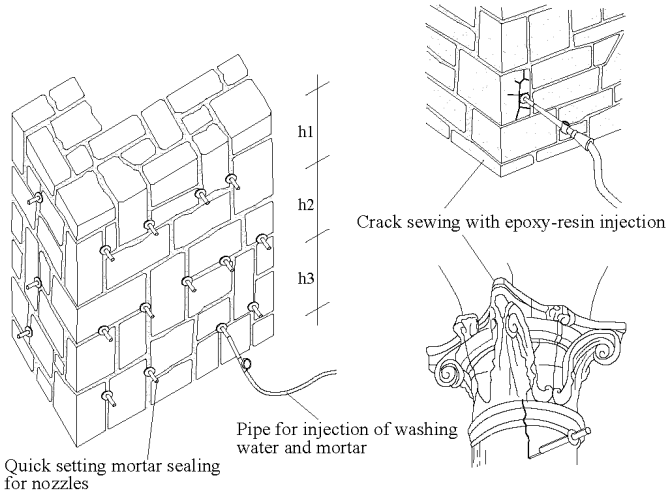


Figure 2.5: Walls and cracks injection.

It is important to note that some of the oldest techniques are still in use, such as dismantling and remounting with possible improved material substitution. In the process masonry element or structures contain parts that have to be removed, substituted or repaired, if a local intervention is not feasible. The main objective is to recover the functionality of a structure maintaining its historical and cultural value, modifying an erroneous design.

A variety of concrete repair methods have been developed many of which rely on adhesion between a repair material and the concrete substrate (Mays and Hutchinson 1992). If increased structural capacity is needed then the external plate bonding as an alternative.

Application of strengthening to arched structures in the last 20-25 years allowed to develop several methods. Such methods include the installation of stainless steel reinforcing bars in the near surface zones of the masonry (Sumon 1997). As an example the use of nearsurface mounted reinforcement (NSM) in masonry arch bridges can enhance the load carrying capacity, delaying the formation of cracks

and hinges and, at the same time, minimize any disruption to the bridge users (Garrity 1995).

The fact that NSM have actually been used does not automatically mean that the system is adequate or effective solutions have been sanctioned by a proven positive performance. It neither means the solutions comply with the restoration principles and criteria.

A rough distinction can be made between the traditional and the modern strengthening techniques. Traditional techniques employ the materials and building processes used originally for the construction of ancient structures. Modern techniques aim at more specific or efficient solutions using non-traditional materials and technologies.

2.2.2 Modern solutions: FRP as a viable adoption

The ability to perform satisfactory stress analysis in structures and to design appropriate reinforcements has been an important problem for engineers. The stress analyses should provide information about the safety of the structure, even if the presence of cracks in historic masonry structures is normal and not necessarily indicates a need for strengthening.

Simplified stress analyses and strengthening procedures are suggested in specialized literature. Modern approaches are based on the idea that the strengthening should be light and removable and, if possible, it should not change the structural scheme or the construction. Recently, advance composites have been successfully adopted to restore masonry structures. This fact emphasizes the increasing interest in the use of FRP for the strengthening of existing masonry, and the need to develop satisfactory structural analysis techniques. It can be pointed out that appropriate models and computational procedures capable to predict the response of strengthened masonry are insufficient (Marfia and Sacco 2000). Furthermore it should be noted that, when the masonry is in compression and delamination is present, the FRP could lose any loading capability because of the instability effects of the reinforcement.

During the 1970's and up to the end of the 1990's steel plate bonding was not unusual, however, in the last decade, the use of advance composites for external strengthening has become quite common (Täljsten 2004; Teng et al. 2003) and a

great number of models for debonding have been presented (Täljsten 1994; Täljsten 1997b; Chen et al. 2001).

Among the innovating techniques to rehabilitate deteriorated structures, there has been an increasing interest in composite fibre materials, commonly known as fibre reinforced polymers (FRP). These materials present several advantages, as low specific weight, corrosion immunity and high tensile strength. Their flexibility and somewhat easy application allow a wide range of intervention scenarios.

The use of FRP in special applications in construction is highly attractive and cost-effective due to durability improvement, reduced life-cycle maintenance costs and also savings from easier transportation and enhancement on site-productivity, (Triantafillou and Fardis 1997). However precautions using this material must be taken, due to its brittle behaviour.

Among the current methods of rehabilitation, the use of FRP bars as near surface mounted (NSM) reinforcement is now prevailing as a promising technology for increasing flexural and shear strength of deficient RC members (De Lorenzis 2000). Although the use of FRP rods for this application is very recent, NSM steel rods have been used in Europe for strengthening of RC structures since the early 1950s. However, the use of steel bars in NSM method has resulted in several disadvantages including difficult handling on site and possibility of corrosion.

The FRP materials have the advantage that they easily adapt to the surface to be strengthened, on the external face of the element locally (*e.g.* strips) or to the whole surface of the structure (*e.g.* grid reinforcement). The connection with the masonry parameter is normally obtained with the use of epoxy resins or mortar. An effective use of this technique requires certain regularity in the masonry surface. Examples of applications in arches and vaults are shown in Figure 2.6.

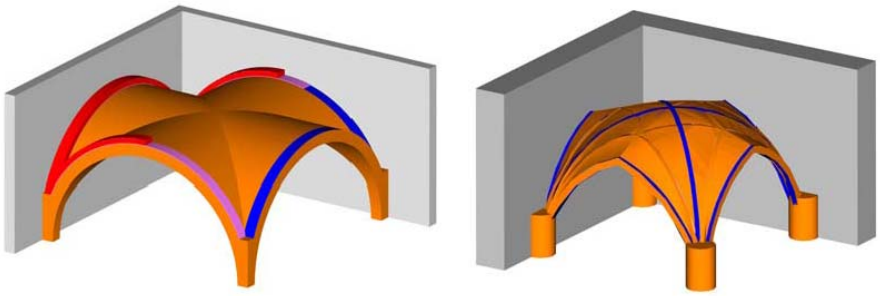


Figure 2.6: Example of FRP strips use in masonry vaults strengthening.

2.3 Composite materials as an alternative solution

Early large-scale commercial applications of composite materials started during World War II (late 1940s and early 1950s) with marine applications for the military; but today, composite products are manufactured by a diverse range of industries, including aerospace, automotive, marine, boating, sporting goods, consumer, infrastructure, and more.

Over the past few years, there has been extensive research into their potential applications in the construction industry. Recent special issues of journals have been devoted exclusively to the use of FRP's in construction. The American Society of Civil Engineers has since 1997 a journal dedicated to the subject, namely, the Journal of Composites for Construction.

There is significant potential for the application of FRP's in the masonry industry, both in new construction and for rehabilitation. For new and existing masonry, the ranges of conditions under which the currently observed modes of failure occur need to be clarified together with simple analytic methods.

Numerical modelling of FRP strengthened arches Lourenço and Martins (2001) showed the possibility of improving our understanding of the relation between the properties, amount and location of the FRP with the properties and dimensions of the masonry. Finite element analysis provides significant insight given the large number of variables, as long as the materials and the bond between them can be modelled appropriately.

When a "strengthened" member is loaded, stresses are transferred from the substrate to the FRP through shear across the epoxy interface. Epoxies can creep under shear, so the concern arises that strengthening with FRP's against dead loads should allow for this additional time-dependent feature. Finally there are serviceability issues which have received little attention to date but should be investigated. Therefore further work is needed to explore the many possibilities of improving the performance of masonry, with FRP reinforcement.

2.3.1 Applications

A wide range scenario applications might be found for FRP materials, including:

- Reinforcing bars for concrete structures, typically with E-glass fibres embedded in a vinylester or epoxy matrix. Aramid, carbon, vinylon, as well as hybrid rebars can also be obtained;
- prestressing strands;
- fibre glass sheets to retrofit columns;
- carbon sheets to retrofit columns, beams and slabs;
- gratings and railings, structural shapes;
- cables.

2.3.2 General aspects on FRP materials

The growth in composite usage also started because of increased awareness regarding product performance and increased competition in the global market for lightweight components. Among all materials, composite materials have the potential to replace steel and aluminium with better performance. Besides replacing steel components with composite components can save up to 60% to 80% in component weight, and 20% to 50% weight by replacing aluminium parts. Nowadays, it appears that composites are the materials gaining more acceptance in terms of choice in many engineering applications.

A composite material is made by combining two or more materials to give a unique combination of properties. The above definition is more general and can include metals alloys, plastic copolymers, minerals, and wood. Fibre reinforced composite materials differ from the above materials because the constituent materials are different at the molecular level and are mechanically separable. In bulk form, the constituent materials work together but remain in their original forms. The final properties of composite materials are better than constituent material properties. The main concept of a composite is that it contains matrix materials.

Typically, composite material is formed by reinforcing fibres in a matrix resin as shown in Figure 2.7. The reinforcements can be fibres, particulate, or whiskers, and the matrix materials can be metals, plastics, or ceramics.

The important thing fact about composites is that the fibre carries the load and its strength is greatest along the axis of the fibre. Long continuous fibres in

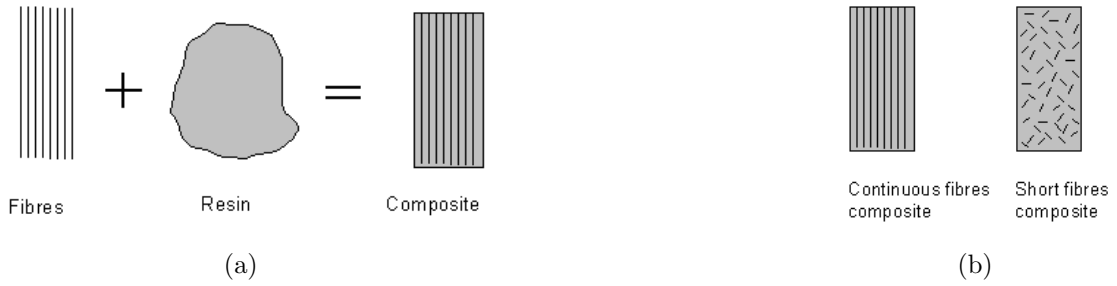


Figure 2.7: (a) Formation of composite material using fibres and resins; (b) continuous and short fibres composite.

the direction of the load result in a composite with properties far exceeding those of the matrix resin itself. The main function of the fibres in a composite is: to carry the load. In a structural composite, 70% to 90% of the load is carried by fibres. The important functions of the matrix material include the following:

- The matrix material binds the fibres together and transfers the load to the fibres;
- The matrix isolates the fibres so that individual fibres can act separately. This stops or slows the propagation of a crack;
- The matrix provides protection to reinforcing fibres against chemical attack and mechanical damage (wear);
- The failure mode is strongly affected by the type of matrix material used in the composite as well as its compatibility with the fibre.

Steel and aluminium alloys exhibit good fatigue strength up to about 50% of their static strength. On the other hand unidirectional carbon/epoxy composites have good fatigue strength up to almost 90% of their static strength. All the above characteristics allowed the construction industry to reach the second place in terms of utilization for FRP materials in the United States of America Figure 2.8.

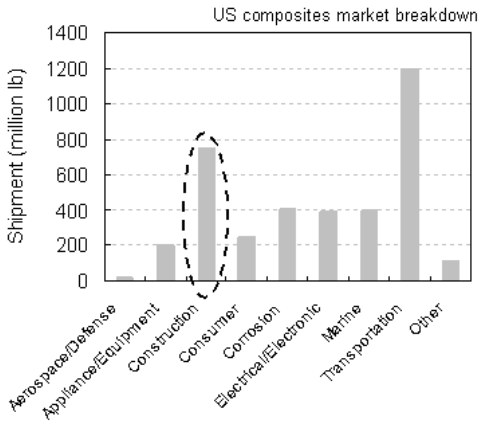


Figure 2.8: Composite shipment in various industries (source: Data adapted from the Composites Fabricators of 16 Associations).

2.4 Bond behaviour assessment

External bonding of fibre reinforced polymer (FRP) plates or sheets (referred to as plates hereafter for simplicity) has emerged as a popular method for the strengthening or retrofitting of reinforced concrete (RC) structures (Teng et al. 2002; Teng et al. 2002). In this strengthening method, the performance of the FRP-to-concrete interface in providing an effective stress transfer is of crucial importance.

In RC beams bonded with a tension face plate, debonding is also likely at the plate ends where debonding is due to a combination of high shear stresses and high normal stresses (Smith and Teng 2003). It should be noted that while the authors focused on FRP-to-concrete joints, the analytical solution is equally applicable to similar joints between thin plates of other materials (*e.g.* steel and aluminium) and concrete. Indeed, debonding failures of RC beams bonded with steel plates have also been studied extensively in the literature (Oehlers 2005).

Concerning the representation of the shear bond interface there are several publications addressing the subject, however just a few contain information regarding the strengthened masonry interface using composite materials. Most of the available literature is focused on RC members which indicates the need of masonry bond behaviour characterization.

Yao et al. (2005) present a comparison of experimental bond tests based on an analytical model previously reported (Chen et al. 2001). The authors give a general overview of studies carried out on the same research area and include a

recent review see also Yuan et al. (1994), showing that many different experimental setups have been used for determining the FRP-to-concrete bond strength, but no consensus on a standard test procedure has been reached.

The application of transverse FRP strips does not provide an improvement in terms of bond strength and strain values. However, an improvement of the strain distribution along the sheet was observed (Aiello and Sciolti 2006).

The ultimate bond load (*e.g.* the maximum transferable load) depends strongly on concrete strength. A very important aspect of the behaviour of these bonded joints is that there exists an effective bond length beyond which an extension of the bond length cannot increase the ultimate load (Chen et al. 2001). Yuan et al. (1994) presented an analytical solution for the prediction of the entire debonding propagation process, which provides not only a rigorous and complete theoretical basis for understanding the full-range load-displacement behaviour of FRP-to-concrete bonded joints, but also a method for identification of interfacial properties using experimental load displacement responses.

A lot of modelling has been done regarding the bond behaviour subject. Täljsten (1996) analytically obtained the expression for the ultimate load using a linear ascending bond-slip model. Brosens and Germet (1998) derived expressions for the maximum transferable load at both the serviceability and the ultimate limit state. Yuan et al. (1994) and Wu et al. (2002) developed equations for the ultimate load, the interfacial shear stress distribution and the effective bond length for various interfacial bond-slip models. Yuan et al. (1994) provided a rigorous and complete theoretical basis on understanding the full range load displacement behaviour of FRP to concrete bonded joints, and provided a method for identification of interfacial properties using experimental load displacement response. Both issues are important for the correct modelling of the FRP-to-concrete interface which is the key for the accurate prediction of the serviceability and ultimate behaviour of FRP-strengthened members.

A complementary work by Teng et al. (2005) presents an analytical solution for the debonding process in a FRP-to-concrete bonded joint model where the FRP plate is subjected to tension at both ends. However no analytical solution has been presented which is capable of considering shear stress distribution through the thickness of the adhesive. Tasi et al. (1998) proposed an improved analytical

solution, in which the assumptions of a linear shear stress distribution through the thickness of the adhesive and a linear local bond-slip law were adopted.

Probably one of the few combined investigations of masonry and concrete is reported by (Saadatmanesh 1997), which reports failure initiated by compression crushing of the bricks near the top of the test beam, followed by sudden diagonal cracking of the beam in the shear span, inconvenient attribute to the low tensile mortar brick joints. Examination of the specimens during and after the tests indicated that none of them exhibited any visible sign of slip or bond failure at the epoxy/fabric interface whatsoever.

2.4.1 Existing evaluation tests

Several different setups have been used to study the strain (stress) distribution in FRP along the bonded length, bond and force transfer mechanism, the effective stress transfer length and the bond strength (Horiguchi and Saeki 1997; Bizindavyi and Neale 1999; Wendel 2001), but very few experimental researches have been concerned with the local bond stress-slip behaviour (Cao et al. 2004).

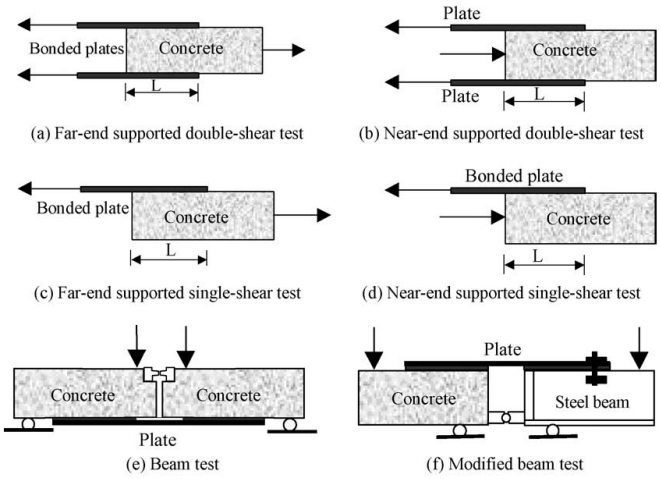


Figure 2.9: Classification of bond tests (Chen et al. 2001).

Assuming the average bond stress-slip curves of the specimens with the shortest bonded length and modelled analytically, quantities of interest from a design perspective, such as the bond failure load as a function of the bonded length, the

load at onset of free-end slip corresponding to the ascending portion of the bond-slip curve, and the corresponding minimum bonded length have been determined (De Lorenzis and Nanni 2002).

In Figure 2.9 an adopted classification of different bond tests is shown. A large number of studies have been carried out on simple pull test (near-end supported, single shear tests) on bonded joints (Teng et al. 2002). Closed form analytical studies of the simple pull test model are given in Täljsten (1996), Yuan et al. (1994) and Teng et al. (2005).

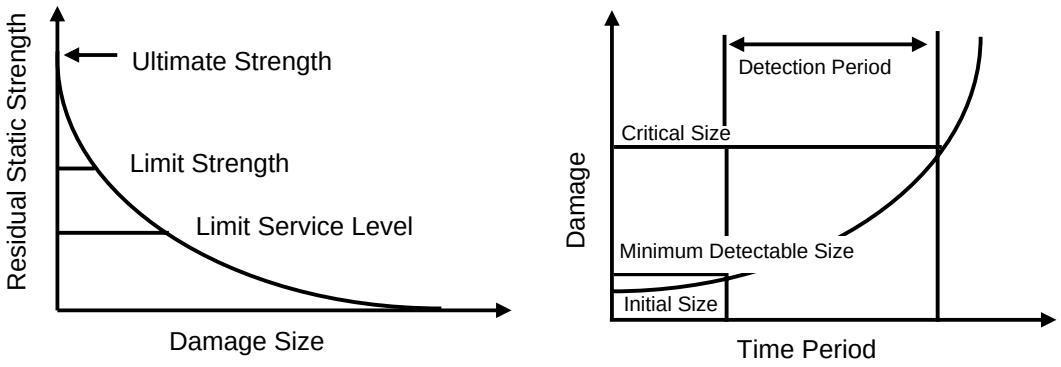
2.5 FRP durability

One of the major challenges for the civil engineering community is the structural damage caused by natural degradation and hazards. The new composites material generation have been tested to different cycles temperatures, simulated degradable actions, sustained stresses, fatigue and outdoor conditions mainly.

A variety of different constituent materials are commercially available and the appropriate combination of these constituents allows the development of a FRP composite system that provides the performance attributes for its intended use.

The durability of a material or structure can be defined as its ability to resist cracking, oxidation, chemical degradation, delamination, wear, and/or the effects of foreign object damage for a specified period of time, under certain load conditions and specified environmental conditions. This concept is considered in design through the application of sound principles and limited damage, whereby levels of performance are guaranteed through relationships between performance levels and damage/degradation accrued over specified periods of time. The overall concept is shown schematically in Figure 2.10.

Acceptance of Fibre-Reinforced Polymer (FRP) on the construction industry is highly influence by its performance considered from the structural intervention until completing its expected life period. Although a number of durability studies on FRP bars have been reported by various researchers, no general conclusions are possible as researchers used different testing procedures and conditions. In some cases, even conflicting results have been reported (Karbhari et al. 2003). The fibre-matrix interface is a heterogeneous area between the matrix and the fibres and is a few micrometers thick. This interface plays a critical role in the transfer of load



(a) (b)

Figure 2.10: Diagram showing the application of (a) durability concepts; (b) damage tolerance.

between fibres and matrix (Thomason 2002). For that reason, special attention is necessary for a such delicate issue where the most representative results regarding debonding are concentrated in that fragile zone.

In the case of historic structures, durability is a much relevant issue due to the low mechanical properties of traditional materials and the long expected life for the building.

Several experimental and analytical studies were reported in the literature for the residual performance of the samples exposed to various environmental conditions without loading (Benmokrane et al. 2002). The combination of moisture and elevated temperature has been found to be even more deleterious to composite material properties than either condition individually (Department of Defense 1997).

As a part of the primary concern in the FRP durability, the most important temperature at which changes take place is known as the glass transition temperature, denoted by T_g. In simple terms, the glass transition temperature is the temperature at which the polymer transitions from a rigid to a rubbery state and vice-versa. It marks a point beyond which significant changes in the properties of the matrix occur and considerable reduction of the mechanical properties takes place. The durability tests conducted by different authors on the latest generation of GFRP bars subjected to stresses higher than the design limits, combined with aggressive mediums at high temperatures, had concluded that the strength reduction factors adopted by current codes and guidelines are conservative (Nkurunziza

et al. 2005).

Excellent mechanical and corrosion resistant characteristics have promoted the use of fibre reinforced plastics (FRP's) in many structural applications. Glass fibres are chemically vulnerable to many acids and bases and will deteriorate if in direct contact with concrete. In composites, it is generally expected that the matrix will provide the chemical protection needed for the fibres.

2.5.1 Long-term material behaviour

Research reported on long term tests is most valuable but also time consuming on the feedback of response results. Slattery (2000) reports that long-term tests on glass/epoxy composites showed failure of about one half of the samples tested at a sustained stress of only 50% of the ultimate strength, after about 7 years. PARAFIL ropes using the high modulus Aramid fibres limit the long-term (100 year) tensile strength to 50% of the short-term strength. This matches tests on Kevlar/Epoxy composites which show a sustained strength of 60% after about 7 years. Test data on carbon fibres shows very few failures after several years and a sustained stress of 80% of the short-term ultimate (Slattery 2000).

There are also results which describe the results of long-term ageing studies on glass/polyester, glass/epoxy, and bare glass strands under load in distilled water. It is demonstrated that if the impregnated bundles are assumed to be monolithic, average time to failure under load can be reasonably predicted on the basis of short-term crack growth experiments. The authors speculate that failure is initiated by cracking from an exposed fibre under the combined influence of environment and stress (Aveston et al. 1982).

There are other effects that must be investigated regarding long-term behaviour as creep and stress relaxation. In fact, since polymers are viscoelastic materials, they exhibit creep and stress relaxation to a great extent (Dillard 1991). As a result, FRP are more susceptible to creep than traditional construction materials, especially under the influence of moisture and temperature (Franke and Meyer 1992).

2.5.2 Effect of moisture/aqueous solutions

To understand outdoor conditions sustained by the composite materials, reproduction of aggressive environmental effects have been studied. Schutte (1994) provides a comprehensive review of effects of various environments, including moisture and aqueous solutions, on glass fibres and glass fibre-reinforced polymer composites. Effects are described at the levels of the fibre, the resin, the fibre-matrix interphase, and at the FRP composite level. Influences of various aqueous solutions are described at each level, and the paper provides an extensive review of the literature (217 references).

The effects of moisture as well as alkaline and acid solutions were recognized as the most critical parameters (Vijay and Gangarao 2001). Another study addresses the environmental durability of the GFRP under the combined effect of moisture, temperature, and sustained stress for a short duration (Helbling and Karbhari 2002). The study shows that the durability of the composites is affected by water immersion and the increase in water temperature, and to a lesser extent by an increase in the applied stress.

2.5.3 Effect of alkaline environment

Studies carried out on FRP exposed to an alkaline environment in the presence of loading at various temperatures are limited (Phillips 1983). The stress levels used in these tests exceeded the levels expected at service conditions to bring the samples to failure relatively quickly.

The alkaline solution produces, when it can penetrate the composite, an embrittlement of the glass fibres and a damage at the fibre resin interface level by chemical attack and growth of hydration products. These effects lead to a loss in tensile strength and interlaminar transverse properties (Phillips 1983).

Previous researches showed how temperature influences the absorption and diffusive properties of alkaline solutions in glass fibre reinforced concrete, comparing natural ageing and accelerated test results (Litherland et al. 1981).

Replacement of steel bars by GFRP bars is becoming a tangible solution most references are related to the composite bars. Another line of research focus on accelerated ageing which present a significant effect on ultimate tensile strength and maximum strain capacity of GFRP concrete reinforcement and prestressing when

subjected to high alkalinity. However, this testing was felt to be conservative, with most of the specimens directly exposed to a high pH environment. The authors concluded that accelerated studies cannot replace a real time ageing investigation. All of the specimens on one bar type failed while under the stress and still in the solution. All of the GFRP bars showed significant losses. The CFRP composites investigated in this study did not appear to be affected by the long-term exposure to the highly alkaline environment (Porter et al. 1997).

2.5.4 Effect of loading cycles (fatigue)

Fatigue life is usually measured as the number of cycles to failure for a given applied level, as shown in Figure 2.11a. A fundamental feature of fatigue is remaining strength. This is illustrated in Figure 2.11b (the ordinate is the same as the Figure 2.11a, but normalized by initial static strength). If the material or component does not fail on the first application of load, then the level of applied load must be lower than the initial static strength.

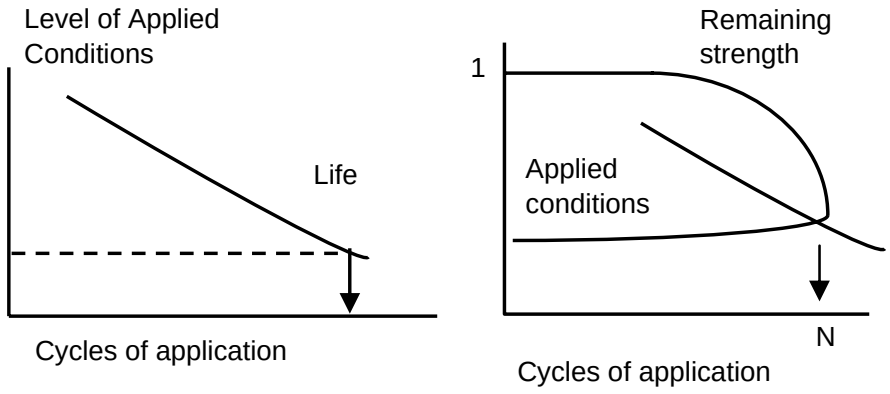


Figure 2.11: (a) Fatigue life representation; (b) remaining strength as a representation of life.

2.5.5 Effects of ultraviolet radiation

The wide FRP applications scenarios create difficulties do define standardized test processes, particularly when several types of climatic zones needs to be covered. Since not always the applied FRP remains at unexposed (hidden) substrates, sun

rays are a natural degradation agent. It has been confirmed that ultraviolet (UV) exposure leads to surface oxidation due to different chemical mechanisms related to the resin type (Chin et al. 1997). On the other hand, physical and chemical transformations occur in the epoxy binder during outdoor exposure. The resulting laminate properties are determined by the superposition of post-curing phenomena and matrix degradation. Matrix degradation is the dominant process beyond five years of exposure. UV exposure could actually improve short-term properties due to postcuring phenomenon, but eventually matrix degradation occurs and leads to decrease in mechanical properties (Startsev et al. 1999).

2.5.6 Other aspects

Some of the most common attempts to reproduce natural conditions concerning FRP durability have been outlined. It is not possible to give major importance or neglect either of them, specially because under real demand conditions, a combinations of two or more are always present.

For example the effect of water for unidirectional carbon composites has been found to reduce compressive and shear strengths, while a small effect on the tensile strength has been reported (Sen et al. 1996). Graphite composites used as bonded external reinforcement in beams and subjected to 100 freeze-thaw and wet-dry cycles showed little effect on the composite itself, but some loss of the composite-to-concrete adhesion (Karbhari and Engineer 1996).

Effects in another material such as aramid fibres *e.g.*, Kevlar, absorb and are affected by water, mostly at higher temperatures (Dolan 1993). Saturated aramid composites have been reported to lose 35% of their flexural strength at room temperature, and up to 55% if stressed and under wet/dry and thermal cycles (Sen et al. 1996).

It is worth noticing that manufacturer recommendations for the FRP application, usually include a final matrix protection (for the resins and fibres). This cover, gives additional endurance to the whole reinforced material, slight stiffer properties as well as an aesthetic aspect, conditions that make the reinforcement more robust. In the experimental work carried out in this thesis a simple matrix without any other complement was applied. The main reason to test just the indispensable components (putty, primer, resin and fibres) relies on the assumption

that further complements might not give representative results and complicate the interpretation.

2.5.7 Standard tests

Despite of the adversities encountered to standardize environmental tests, some procedures are already available as norms. While the International Conference of Building Officials (1997) specifies selected physical and mechanical properties to be measured and reported for composite materials used for repair and retrofit of concrete structures, existing design guides for FRP composites such as the American Concrete Institute document ACI 440.1R-01 "Guide to the Design and Construction of Concrete Reinforced with FRP Bars" use mechanical property data for FRP to determine design allowable stresses.

One of the most widely accepted tests are the freeze thaw cycles, raising the temperature of specimens from 4.4 to 17.8 °C and lowering it from 17.8 to 4.4 °C in not less than 2 h nor more than 5 h (ASTM C666/C666M-03 1997). Also there is the humidity exposure test according to ASTM D2247 (1995). Standard ultraviolet (UV) resistance test ASTM G53 (1995) is being used to determine the effects of alternating ultraviolet light and condensating humidity exposures.

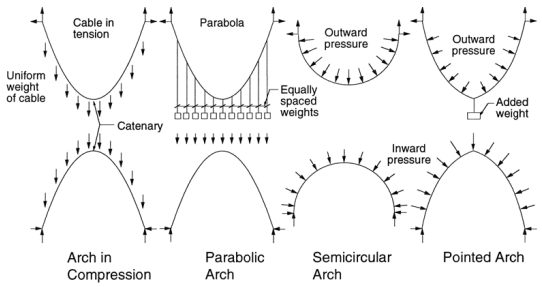
2.6 Behaviour of arched structures

To analyse arched structures there are some concepts that must be outlined. Curved geometries under its own weight are usually subjected to compressive stresses delineating a virtual line inside its thickness known as thrust line. When the line of thrust moves outside the central core given by middle third of a cross-section, the formation and consequent opening of a crack takes place. Safety is maintained as long as the line of thrust is kept inside the thickness of the arch. The shape of the thrust line depend upon the applied loads to the arch and can be determined mathematically. However, the arching action is readily visualised by simple analogy.

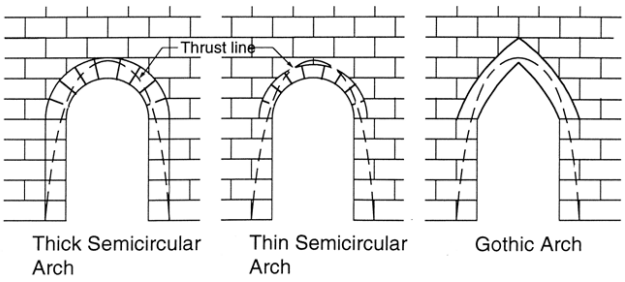
A cable when suspended between two points takes up a catenary shape under its own weight and is in pure tension. If the cable is then imagined to be rigidly inverted, and supported at the same two points, its weight would act in the reverse

direction and the cable would be in pure compression rather than in tension. An inverted catenary is, therefore the best shape for an arch that must resist only its own weight.

If the arch resists other applied loads, then the required shape can be obtained by applying equivalent weights to the cable model. The shape taken by the cable will depend upon the positions of the added weights and the relative magnitudes of these weights compared with the magnitude of the cable. In many practical cases, the weight of the arch (cable) is predominant. It is instructive to note that if very large additional forces are applied the weight of the arch (cable) becomes insignificant and three common geometric shapes can be obtained. The first is a parabola, obtained by applying equal weights at closely spaced horizontal intervals across the cable span. The second is a circular arc obtained by applying closely and evenly spaced radial loads to the cable. And finally, a Gothic arch shape is obtained if in addition to evenly spaced radial loads a concentrated load is applied to the midspan of the cable. The cables theory mentioned and utilized for the compressive stress analogies is presented in Figure 2.12a.



(a)



(b)

Figure 2.12: Basic of the line of thrust: (a) cable arch analogy; (b) thrust lines in typical arched structures.

Although the geometries of the catenary and parabola are similar as the loadings required to produce them, the semicircular shape and its associated radial loading are quite different. The Gothic shape is closer to the catenary and parabola is to the semicircle. The superposition of the line of thrust to some typical arched structures is respectively presented in Figure 2.12b.

A practical loading on arches in buildings is vertical uniform loading and hence the thrust line is often parabolic. The semicircular is therefore, not the best shape to use in a building. However, semicircular arches were commonly used up to and throughout the Roman period (300 BC to AD 365), probably due to the easiness of setting out the shape rather than any notion of the thrust line configuration. The semicircular arches that survived evidently did so, because they were thick enough for the roughly parabolic thrust line to be contained within the arch.

2.6.1 Plain arches

When a masonry arch is well designed, it must be perfectly comfortable under the action of its own weight and at certain intensity of the superimposed load P. The stresses are low and the deflections negligible, and both will remain so as the value of P is increased. However, at a certain value of P a sudden change puts an end to this stability. A point is reached at which the structural forces can no longer be contained within the arch, stress remain low but an unstable mechanism of collapse is formed as seen in Figure 2.13a.

The semicircular arch of Figure 2.13a will carry a given load P provided that the arch ring has a certain minimum thickness; the design of the arch consists in the process of assigning this thickness for a given span and a given load.

The physical arch in Figure 2.13a demonstrates the necessity of sufficient depth to accommodate a range of thrust lines arising from the self-weight of the material of the arch. If this weight is distributed uniformly in the arch, then the shape of the thrust line is that of the mathematical catenary (as sketched in Figure 2.13b), and a minimum thickness of semicircular arch must contain a catenary. Such an arch (of thickness just over 10 percent of the radius) is sketched in the top of Figure 2.13b. Any line of thrust within the arch is a possible equilibrium solution. But this solution is not unique. It is evident that, in an arch of sufficient thickness, there are infinite possible inverted catenaries or lines of thrust. The arch is a statically indeterminate (hyperstatic) structure. The equations of equilibrium are

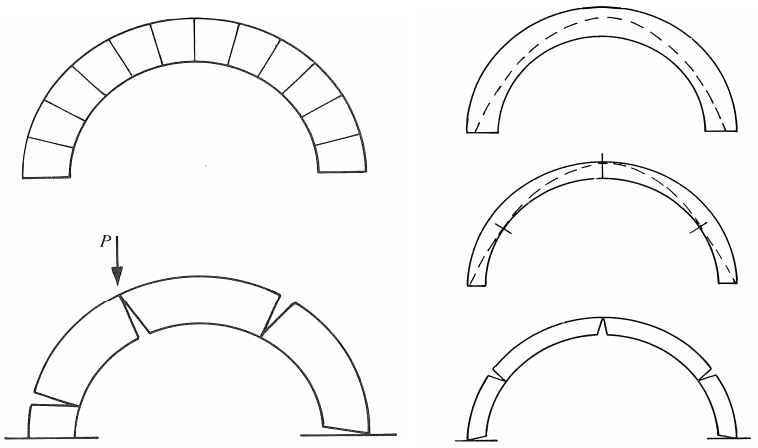


Figure 2.13: Hinging failure mode; (a) collapse mechanism of masonry arch; (b) the semicircular arch stable and minimum thickness.

not sufficient to obtain the inner forces. Once the arch thickness is reduced to the absolute minimum to contain the line of thrust, a failure mechanism is with four hinges formed (see middle and bottom of Figure 2.13b).

Poncelet (1952) was conscious of the problem and his historical review of arch theory suggested to apply the elastic theory to masonry arches to obtain a unique solution, since the theory for circular arches had been developed by Bresse (1848). Already in the 1860's some elastic analysis of masonry arches were made, for example by the Spanish engineer and architect Saavedra (1860). Castigliano (1879) applied his theory of elastic systems also to masonry bridges. But it was Winkler (1880) who made the first in depth discussion of the elastic approach to masonry arch analysis. After a revision of all the contemporary theories, it was concluded that elastic analysis was the best option.

Engineers of the end of the XIXth were looking for the actual, true solution and elastic analysis appeared to be best option. Nevertheless, masonry arches cracked visibly during construction and/or after decentering. Although the material was irregular, anisotropic and discontinuous, elastic analysis was wrongly considered the best theory. In fact, it was named "the modern theory of arches" in contrast to the "old theory" (Huerta 2001).

2.6.2 Arch behaviour modified by reinforcement

The principles to interpret and understand structures with arched geometries have been briefly presented. Since strengthening of masonry structures is one of the main targets of this work, the present section describes how the external applied reinforcement in arched structures modifies the basic theoretical understanding of plain arches.

The presence of a bonded FRP strengthening to the arches substrate changes the structural behaviour of the structure. The fibres, which possess a high tensile strength, prevent the aforementioned mortar-brick interface openings (hinges) and may change significantly the failure mechanism. Since the use of FRP sheet strips provides bending moment resistance, the line of thrust may now safely move outside the thickness of the arch.

For the arch illustrated in Figure 2.14 and considering the reinforcement located either at the extrados or at the intrados of the arch, the formation of a fourth hinge mechanism is prevented. Hence, only three hinges are able to rise, transforming the arch into an isostatic structure, resulting on a new failure mechanism different from the one afore-mentioned. Due to the FRP tensile strength resistance, the compressive stress in masonry will increase their values so failure of the arch caused by masonry crushing has to be taken into account.

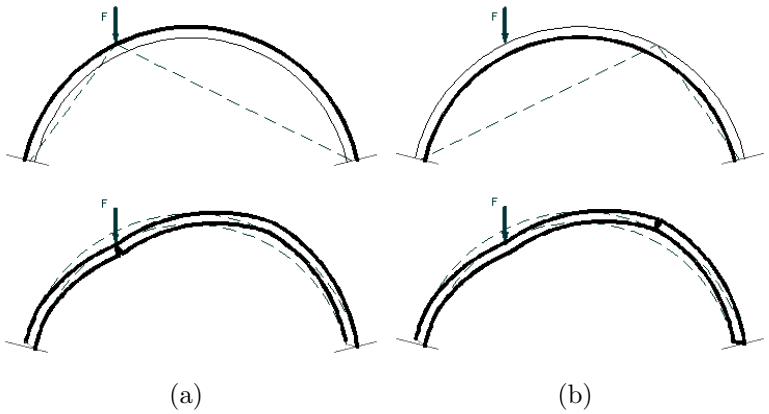


Figure 2.14: Three-hinges for a semi-circular masonry arch submitted to an asymmetrical loading. Continuously strengthened at: (a) the extrados; (b) the intrados.

The presence of the reinforcement also allows the development of higher shear

stresses in masonry and, therefore, shear failure due to sliding along a mortar joint may occur. Moreover, in addition to the usual stresses parallel to the fibres, the curved shape of arches originates stresses with a component normal to the fibres, which may lead to the detachment of reinforcement from masonry, namely in arches strengthened at the intrados. For those reasons, the following failure mechanisms are usually added to the unstrengthened case:

- Failure due to masonry crushing,
- Failure due to detachment of the fibers and,
- Failure due to sliding along a masonry joint.

Sliding between the fibres and its support is usually neglected since shear stresses at the FRP-masonry interface are of minor magnitude (Valluzzi et al. 2001). Also FRP tensile failure is not likely to occur due to its high tensile strength. It is known that, for a given arch shape, the type of failure to be obtained depends both on the mechanical properties of the materials (brick, mortar and FRP) and on the quantity and location of the reinforcement.

2.7 Adopted numerical tools

Most practical problems arising in engineering have to be solved approximately by a numerical method. This is true not only for structural analysis but physical and engineering models in general. It has been shown that modern investigations involve careful direct observation, supported as necessary by appropriate surveys, historical research of events which influenced the structural behaviour, and appropriate use of mathematical models. This methodology can provide a correct diagnosis and a reliable evaluation of the structure safety and finally the most suitable strategy for strengthening and restoration.

2.7.1 Advanced numerical simulation

Representation of physical phenomena still remains as a technical challenge for scientists and engineers. Despite the current powerful tools that facilitate the simulation process, specific expertise to interpret such results will always be needed.

The most used techniques of advanced numerical simulation is the finite element method. The adoption of non-linear constitutive laws requires an incremental iterative process to apply external loading. The usual approach to deal with the resulting set of nonlinear equations is the Newton Raphson method. Each iteration involves three computationally expensive operations:

1) Evaluation of the internal forces,
2) Evaluation of the global tangent stiffness matrix and,
3) Solutions of a system of linear equations.

For large scale models steps 2 and specifically 3 may be excessively time-consuming. The computational cost can be reduced if the stiffness matrix is not updated in every iteration. The modified Newton- Raphson method evaluates the stiffness matrix only at the beginning of the incremental step and does not alter it in the subsequent iterations. It is important to distinguish between the criterion that fixes the size of each incremental step, and the iterative procedure that solves the equilibrium equations.

Examples of step-size control techniques include the load control, direct or indirect displacement control, or various versions of the arc-length control (Zienkiewicz and Taylor 2005). Examples of iterative methods include the standard or modified Newton Raphson iteration, initial stiffness method, or quasi-Newton methods, look at Figure 2.15 for complete illustration of the Newton Rapson Method and its modification. Additional components of an incremental iterative solution strategy are the convergence criteria and, optionally, convergence accelerators such as line-search techniques (Crisfield 1984) and/or step-size adjustment rule.

It might be worth mentioning that computational modelling frameworks applied for masonry historic buildings range from highly simplified methods to complex nonlinear finite element or discrete elements. In the majority of cases the macro level nonlinear finite element models (Crisfield 1984) and homogenisation techniques are adopted. Attention has also been given to assessment methodologies (discrete element method, rigid block spring method, lattice modelling, discontinuous deformation analysis, combined discrete/finite elements), which deal more directly with the discontinuous nature of structural masonry.

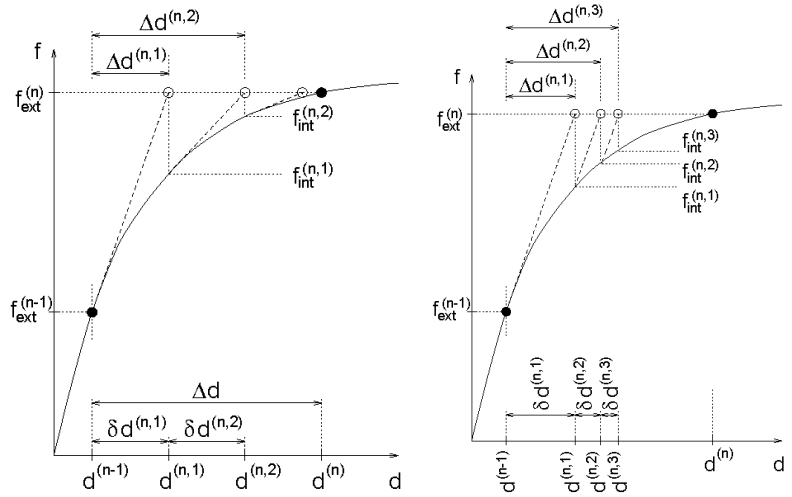


Figure 2.15: The Newton Rapson Method: (a) the standard iteration; (b) modified version.

2.7.2 Interface elements

Interface constitutive models are usually expressed in terms of contact tractions and conjugate relative displacements. The interfaces can simulate the inelastic phenomena which develop at mortar joints and are mostly responsible for the overall non-linear behaviour of the masonry assembly. These assumptions are mostly suitable in the case of old masonry with mortar joints often deteriorated by aggressive environmental agents and mechanically weak if compared to blocks.

To understand the kinematical phenomena at joints and investigate their effects on the mechanical behaviour assembly several experimental programs have been carried out with laboratory tests on single joints, performed in pure tension (Van der Plujim 2000) or compression and direct shear (Atkinson et al. 1989), exploring also the peculiar contributions and mutual interaction of masonry constituents, namely, units and mortar in such assembly. The study of the post-peak regime allowed to focus on the quasi-brittle properties of mortar (loss of cohesion and crack growth, material dilatancy and related stability effect) the residual strength (affected by geometrical dilatancy due to crack roughness) and the adhesion units-mortar.

Most of the studies in micro-modelling concentrate on the formulation of the interface law and a numbers of models are reported in the literature. The first

attempt was due to Page (1978), who assumed elastic behaviour of the bricks and a nonlinear response for the joints. The joints behave elastically until a failure criterion is violated. In the presence of combined compression and shear, the joint failure occurs by a shear stiffness degradation until a residual frictional strength value is attained depending on the value of the applied normal stress. The joints failure in tension only occurs in brittle mode with no load-carrying capacity over the tensile bond strength.

Lofti and Shing (1995) and Lourenço and Rots (1997) have proposed other interface models, formulated in a rigorous manner, which incorporate some concepts develop in the theory of plasticity for non-standard materials and in fracture mechanics. All these models adopt failure criteria for the Mhor-Coulomb type and use internal variables to describe a post-peak softening behaviour. Lourenço and Rots (1997) adopted a cap model capable to take into account masonry failure due to high compressive stresses.

A simple interface model was proposed by Giambanco and Di Gati (1997). It possesses general features similar to the previous models, but with a particular attention addressed to the cohesive-frictional joint transition, taking into account the geometrical dilatancy which appears in the pure frictional stage, related to the roughness of fracture-slip surface.

2.7.3 Limit analysis

Non-linear analysis is a powerful method of analysis, capable to trace the complete structural response of a masonry structure from the elastic range, through cracking and crushing, up to failure. Limit analysis can be regarded as a practical computational tool, since it only requires a reduced number of material parameters and it can be provide a good insight into the failure pattern and limit load.

Heyman (1969) was one of the first to consider (vaulted) masonry block structures in the context of the plastic limit analysis theorems which emerged during the last century. Whilst in practice some dilatancy are likely to occur when two rough blocks pass over each other, experimental evidence indicates that real joint behaviour is quite complex, with the amount of dilatancy being dependent on the micro-scale geometrical and mechanical features of the masonry joint (Van Zijl 2004).

For the limit analysis there are some simplification that must be considered, namely:

- *Masonry has no tensile strength.* Masonry pieces have indeed tensile strength, but the joints between them may be dry or made with weak mortar;
- *Masonry has an infinite compressive strength.* In ancient masonry structures the compressive stresses are usually small compared with the corresponding strength, so, crushing is often not applicable;
- *Sliding failure cannot occur.* This is a simplification accepted by Heyman (1966) for his hand calculations, although he recognised that sliding failures occur sometimes;
- *Failure occur under small displacements.* This is a structural assumption independent of the material and necessary for limit analysis to be applicable.

The above hypotheses were used by Coulomb several years ago (Heyman 1966) for the analysis of masonry arches, and for the same purpose but already within the limit analysis theory by (Kooharian 1952). That these hypotheses render masonry perfectly plastic in tension and perfectly rigid in compression and shear, so limit analysis is clearly applicable.

2.8 Conclusions

The present chapter outlines, an overview throughout masonry history, an introduction of the recent appearance of FRP materials to strengthen damage structures, the main changes on natural patterns of arched structures and available tools to interpret and study masonry structures.

One of the current issues on acceptance of composites materials, relies on the durability at the substrate interface where the most critical and fragile results are encountered. Hence, FRP composites acceptability on the masonry community depends also on indicative durability results. However, much effort is needed before reaching standardized tests.

There are few experimental results concerning the bond test specimens on masonry materials. On the other hand studies on reinforced concrete are helpful

when setup schemes for other materials are needed. Considering the low tensile strength of masonry, an adapted setup of the near end supported single-shear test originally designed for concrete was adopted.

The natural behaviour of arched structures, designed for compressive strength mainly, changes when externally strengthened by materials with high tensile strength. In this case the line of thrust moves outside the structure, and additional failure mechanisms need to be taken into account.

With the fast evolution of computer technology, nowadays it is possible to construct sophisticated models allowing a deep insight into structural behaviour, passing through different damages states until collapse. After inducing cracking patterns to structures, it is possible to study post-damage, when retrofitting strategies are applied to reestablish stability and assure serviceability conditions.

Chapter 3

Experimental FRP-masonry bond behaviour: material and structural characterization

3.1 Introduction

To accomplish a comprehensive mechanical behaviour characterization of any material type or structure, it is essential to perform experimental tests. In this way, it is possible to follow the behaviour of the material perceiving its evolution from the undamaged state through the softening state. Therefore, only a complete material description allows a full understanding and knowledge of the material performance. The experimental material characterization has also an important role on the calibration and use of advanced numerical models. In fact, numerical modelling can confer realistic results when adequate experimental data are available.

Masonry as itself, is designed to work in compression mainly due to the low tensile strength of its bonded joints, when mortars exists. A possible solution to improve the masonry mechanical behaviour and take advantage of its compressive strength property, may be accomplish by reinforcing masonry, combining tensile and compressive strength. Among all the strengthening techniques, a relative new emerging solution has recently gained acceptance into the construction industry, such material is known as Fibre Reinforced Polymer (FRP). However the strengthening of masonry structures with FRP materials, necessarily, requires a clear understanding of its structural behaviour.

Before testing masonry with composite materials, in direct shear loading, special attention must be given to the mechanical characterization of its individual components. Moreover, masonry joints represent the weakest element of masonry and notably affect the overall structural response. The strengthened FRP masonry interface behaviour, represents a fragile zone which must be fully characterized. Once the substrate strength is fully exhausted. The interface becomes a fragile zone where the most relevant results concerning the failure mode occur at the interface, including sliding or detachment of reinforcement.

To typify the raw materials utilized in the current research, sets of standards tests of the material components used were carried following existing standard guidelines when applicable. The main objectives of the experimental research described in this chapter are related to the experimental characterization of FRP and masonry components and the FRP-masonry bond behaviour characterization, namely in terms of ultimate load capacity and stress distribution along the anchorage length and shear-relative displacement relationship at the loaded end. For this purpose, key parameters relative to the FRP-masonry interface response, particularly anchorage length, FRP materials; anchor scheme adopted and shape of masonry surface were considered and studied in detail. Additionally, normal stress and sliding of the FRP strip along the anchorage length were computed using the strain gauges data acquired during the tests.

3.2 Clay brick (type 1)

3.2.1 Compressive tests

To reach a good understanding of masonry behaviour it is necessary to test their components separately, mortar and bricks, under the same action demand during service conditions. The brick compressive strength (f_b) is a fundamental property, when individual masonry components need to be studied and when numerical models are to be used.

With the objective of reproducing old Portuguese masonry constructions, clay bricks were chosen specifically from Galveias, a village localized in the central part of Portugal, where handmade bricks can still be found. Some physical properties from Galveias bricks such as porosity and permeability were already previously

characterized, by Fernandes and Lourenço (2005). In this thesis two different types of clay bricks were used. The bricks from Galveias are here designated as brick type 1. In the next chapter another clay brick was used designated as brick type 2.

Monotonic force or displacement test control of specimens under compressive loading depend on the different material properties namely porosity and chemical composition that affects stiffness and subsequently Young's modulus (E) (Binda et al. 1996a). The control technique used during testing depends essentially on the postpeak behaviour of the specimen. A height/diameter relation ratio aspect bigger than one is an advisable solution overcoming problems as: low strength, stiffness material and friction with the steel platens to overcome (Binda et al. 1996a). The use of teflon sheets between the surface of the specimen and the platens was not used due to lack of possibility to assess such deformability of the material.

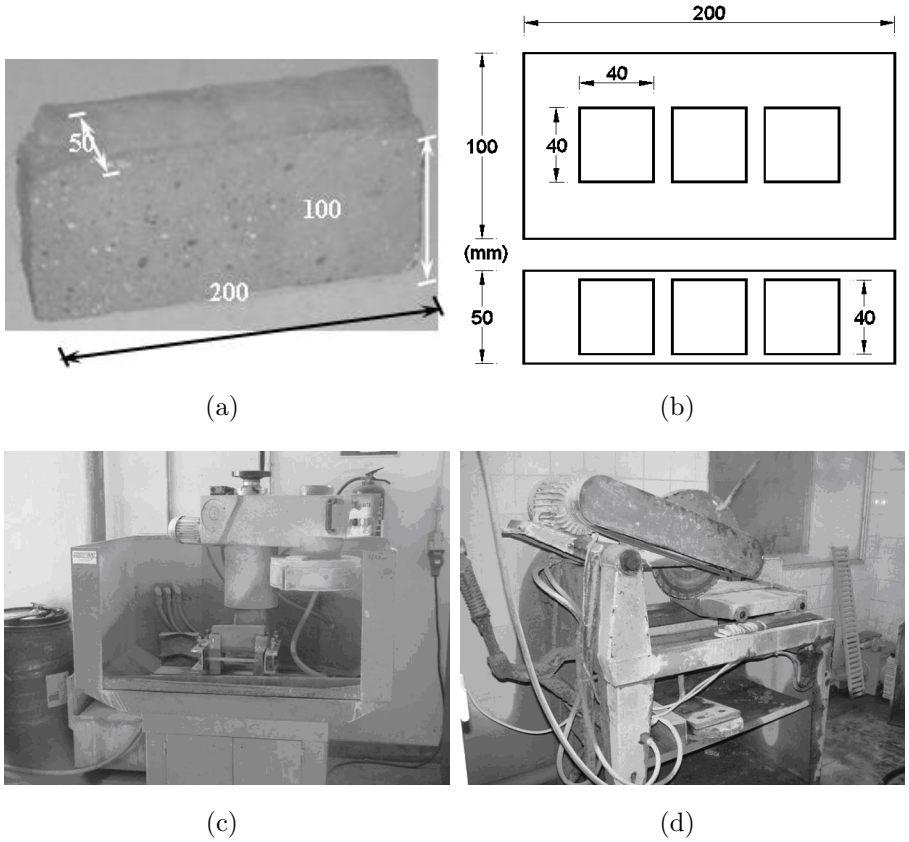
In this work ten compressive tests divided in two sets of five specimens each were performed. The first set, carried out without strain gauges (CGB-n), had the purpose of defining the average compressive strength and the second set with a strain gauge per specimen, was focused on assessment of the Young's modulus (YGB-n) of the clay brick type 1. As a complementary mechanical property, compressive strength was also measured in the second set.

3.2.2 Specimen preparation

Brick units had average dimensions of 200×100×50 mm^3, Figure 3.1a. Burning edges were commonly found in the bricks due to handmade firing process. Therefore extraction of the cubic pieces were taken out from the internal brick volume perpendicular to the flatwise direction, as shown in Figure 3.1b. By means of a mechanical machine with a ball bearing grinding, showed in Figure 3.1c, the top and bottom brick surfaces were smoothly regularized until a flat surface was attained. Operating a masonry saw, cubic specimens of 40 mm side were cut from the original unit, Figure 3.1d.

For the first set, the day before testing, cubic units were immersed in water for 24 hours to saturate them. Prior to the compressive strength tests, the units were removed from water. Three cubic pieces were stacked and aligned to carry out the test without any external bond agent among them. In this way, a final

height/diameter ratio aspect of 3/1 was obtained, looking for a uniform stress distribution at least in the centre of the specimen (Neville 1966).



(a) (b)

(c) (d)

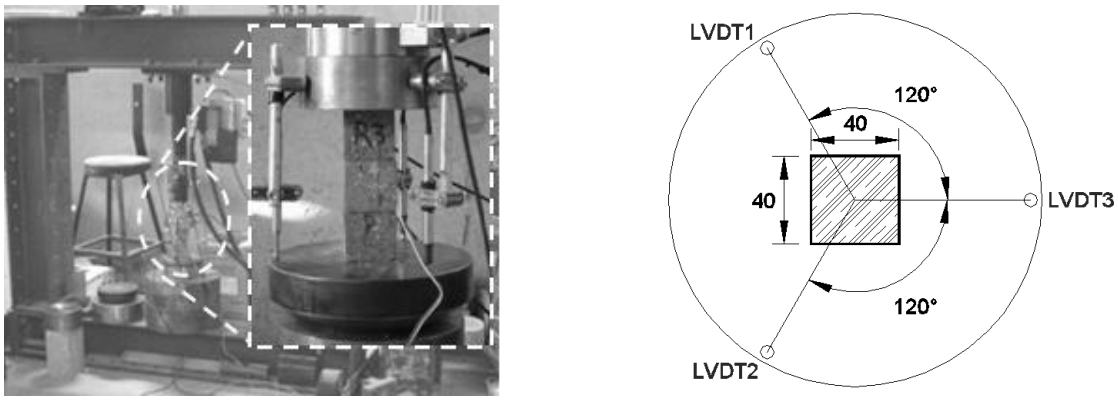
Figure 3.1: Clay brick type 1: (a) average specimen dimensions in (mm); (b) cutting scheme; (c) ball bearing grinding machine and (d) sawing equipment.

For the second set, a strain gauge was glued on the central prismatic cube where an uniaxial compressive stress state is theoretically present.

3.2.3 Test setup and test procedure

The test setup consisted of a steel frame which supported a servo-controlled actuator, with a 25kN load cell capacity, Figure 3.2a. To accomplish the brick mechanical characterization, three linear variable displacement transducers (lvdt's) were placed over the circular steel plate, as schematically represented in Figure 3.2b. The whole test was controlled by axial displacement.

All tests were performed under monotonic displacement control at a rate of 5μm/s.



(a) (b)

Figure 3.2: (a) General overview of the test setup for brick compressive testing; (b) plan view detail, showing the specimen and its instrumentation (dimensions in mm).

The lack of specific guidelines on the Young's modulus evaluation for ancient clay bricks did not allow following any general recommendations. The upper limit stipulated in some guidelines (RILEM CPC8 1975; ASTM C67-98a 1998) specifies 30% of the maximum stress to evaluate the Young's modulus; this limit represents a very low value and a better assessment was found by adopting a higher percentage. The stress range considered to evaluate the Young's modulus was comprehended between 30% and 60% of the maximum stress, as done by other researches (Binda et al. 1996a; Oliveira 2003).

3.2.4 Test results

The results of the mechanical characterization under compression are presented in Table 3.1, where the compressive strength and Young's modulus assessment for each specimen are included. The Young's modulus was evaluated using two sources of data, namely strain gauges and lvdt's, and the comparison of their values may be found in the same table.

The average compressive strength of the clay brick type 1 found in this study may be considered as relative low, according to the comprehensive studied carried

out on Portuguese bricks by Fernandes and Lourenço (2005) where the values presented variations between the limits of 6.7 and 21.8 MPa of average compressive strength. The coefficients of variations (C.V.) indicates a moderate scattering on the samples. Two values of Young's modulus with similar results computed but using different approaches are provided in Table 3.1. It may be seen that the Young's modulus assessed by the average of the three lvdt measurements (E_{lvdt}) has a lower coefficient of variation and the estimation based on strain gauges measurements (E_{sg}) provides a local assessment, commonly considered as a more reliable value. The differences between both values appeared as a result of several issues related with: porosity, excessive void inherent in the brick moulding, influence of the resin used to glue the strain gauge which changes locally the original brick stiffness. In fact the pores are filled with the glue used to fix the strain gauges, which significantly increased the local stiffness and makes the strain gauge measurements unreliable.

Table 3.1: Compressive characterization of clay brick type 1.

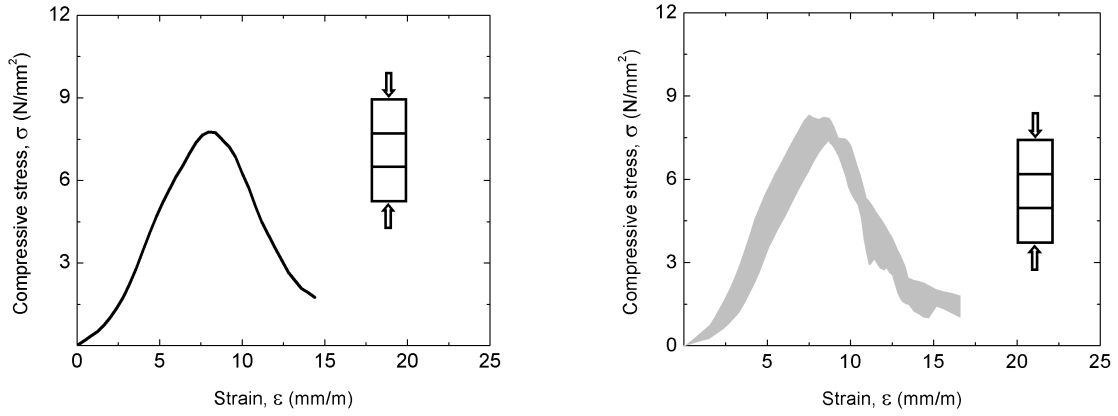
Specimen	Compressive stress, (MPa)	Young's modulus (GPa)	
		E_{sg}	E_{lvdt}
CGB-1	7.1	-	-
CGB-2	7.3	-	-
CGB-3	7.1	-	-
CGB-4	5.8	-	-
CGB-5	5.3	-	-
YGB-1	6.8	3.9	1.13
YGB-2	7.5	3.86	1.17
YGB-3	8.3	3.12	1.31
YGB-4	7.6	2.95	1.31
YGB-5	8.4	2.59	1.25
Average	7.1	3.28	1.23
C.V. (%)	13.7	17.6	6.6

E_{sg} : Young's modulus obtained from the strain gauge measurements
E_{lvdt} : Young's modulus obtained with the lvdt measurements

Similar differences and values regarding Young's modulus measurements have

been also reported by other researchers (Binda et al. 1996a).

A typical stress-strain ($\sigma - \epsilon$) curve resulting of a compressive test is illustrated in Figure 3.3a. The "range of variation" (hereinafter designated as "envelope") of all curves, depicted in Figure 3.3b, obtained by simple superimposition of the ten stress-strain curves, shows that all specimens presented a similar stress-strain behaviour, although some differences are noticeable with respect to the pre-peak stiffness.



(a) (b)

Figure 3.3: Brick compressive strength tests: (a) typical stress-strain curve; (b) envelope for all curves.



Figure 3.4: Typical failure mode for the clay brick type 1.

The typical failure mode is illustrated in Figure 3.4, where vertical cracks can be observed in the central cubic brick unit. After being submitted to compressive

testing, specimens (without any external bonding agent) behave as a whole unit. Uniaxial compressive strength was accomplished in the central brick, as expected, due to the low confinement effect and platen influence.

3.3 Mortar

Mortar consisting of lime and sand has been used as an integral part of masonry structures for thousands of years. Some examples of ancient binding materials are: mud, gypsum, lime and lime-pozzolan mixture.

The use of bonding materials is very old. The first evidence of its existence dates back to 1200 BC in Israel. An example of an ancient binder is the natural occurrence of the bitumen by the Babylonians and Assyrians in their bricks and gypsum plaster construction. The Egyptians improved the technology of lime and gypsum mortar building the pyramids using such mortars. The Greeks made further improvements and finally the Romans developed the cement that produced structures of remarkable durability and that can set and harden even under water.

Historic mortars are composite, comprised of hydraulic or aerial binding material, or a mixture of binding materials, aggregates - not always in crystalline form. Additives, passive or active, react with the binding material and are modified during their setting, hardening and ageing, according to processes as yet not well known (Chiari et al. 1992).

Many of the desired characteristic of a masonry as a construction system are the result of how mortars and grouts are placed in combination and interact with masonry. While straight sand-lime mortars had been used before the 1930's the use of mixtures of Portland cement, lime, sand and water had become the norm (Efstathiadis 2000).

The modern cement, *e.g.* Portland cement was invented by Joseph Aspdin in England in 1824. After that time, modern Portland cement and concrete technology has proceeded till today by invention of new chemical and mineral admixtures and additions.

The use of lime mortars, partly due to its slower application and mainly due to changes in construction technology, fell into disuse and the traditional "crafts" experience was lost. The field of preservation was polarized: those strongly in favour of using only traditional lime, or hydraulic lime, mortars and those favouring

mixed cement-lime or even plain cement mortars (Erdoğan 2002). Cement-lime mortars were developed to replace the natural hydraulic limes, which were also used traditionally where available (Ashurst 1984).

However, in many cases these hybrid mortars may also have the disadvantages of both materials. In brief, lime cement mortars, when compared with pure cement mortars, have better workability, larger deformability, higher porosity, greater resistance to cracking and less retraction.

As a result, it can be said that the whole process of modern binding materials, mortars and concrete should be re-examined beginning from the raw components, production process of binding materials up to mixing, placing, compaction, finishing and curing process of mortars and concrete (Kirca 2005).

Although mortar represents a smaller volume compared to brick in masonry construction, the masonry compressive strength is highly conditioned by the mortar thickness and strength. There is a close relationship between consistence and compressive strength. The concept of consistence is related to workability or water content of the mix. In fact, a water quantity exceeding the necessary amount to hydrate mortar causes porosity thus reducing the masonry strength, Binda (1996a, 1996b). Mortar, as a masonry component, represents an important and delicate issue to work with, particularly when adequate results are sought and computational modelling is on the target. Therefore, a careful consideration of the mechanical behaviour of mortar under compressive loading is needed.

Mechanical tests serve to give information regarding the structural resistance (as reflected by the compressive strength) and the deformation behaviour (as reflected by the elasticity modulus).

As discussed elsewhere (Henriques 1996), not only there is a wide variety of tests methods suggested by the various national standards, but even the preparation of the samples for laboratory testing varies significantly. It is therefore important that during the development of new standards the following two points must be taken into account: the preparation of the mortar samples to be tested, and the tests to be performed.

Lime mortars and plasters have been used since prehistoric times. As with any material, its selection, preparation and/or formulation was first carried out by trial and error and the empirical knowledge gained was transmitted from craftsman to

craftsman over generations. No performance standards were objectively established, Vitruvius being one of the first to give written guidelines for the selection and preparation of lime mortars (Vitruvius 1960).

Given the importance of the above mentioned reasons, compressive strength and Young's modulus are necessary parameters to obtain. The tests were divided in two sets, carried out similarly to the procedure adopted for the bricks; the first set was used to assess the average compressive stress (CMM-n); and the second set to evaluate the Young's modulus within 30% and 60% of the peak stress (YMM-n) measured in each specimen. The compressive strength was also measured in the second set and four tests were performed for each set.

3.3.1 Mortar composition

It is well know that old masonry constructions usually present low mechanical properties as a result of both ageing processes and weak binders. With the main purpose of finding a representative commercial product, a general survey of lime-based mortars available in the market was carried out. Among the existing commercial mortars, a mortar produced by a world leader in products for the building industry (MAPEI) and developed for the repair of historic masonry constructions was selected. Mape-Antique MC is a premixed light-coloured cement-free powder mortar based on special hydraulic binders with pozzolanic action, natural sand, special additives and synthetic fibres. This mortar can be defined as a mortar based on a hydraulic lime binder.

Table 3.2: Technical information from the manufacturer for Mapei-Antique MC.

Mechanical properties	Cure period of testing (days)	
	7	28
Compressive strength, σ(MPa)	2-4	4-6
Young's modulus, E (GPa)	3-4	4-6

A summary of technical data given by the manufacturer is given in Table 3.2, where the mechanical parameters were chosen to compare them with experimental values.

3.3.2 Specimen preparation

During the preparation of the mortar all recommendations from the manufacturer were followed, namely pouring in a steady flow and using a minimum amount of water of approximately 3.5 litres per each 25 kg of product.

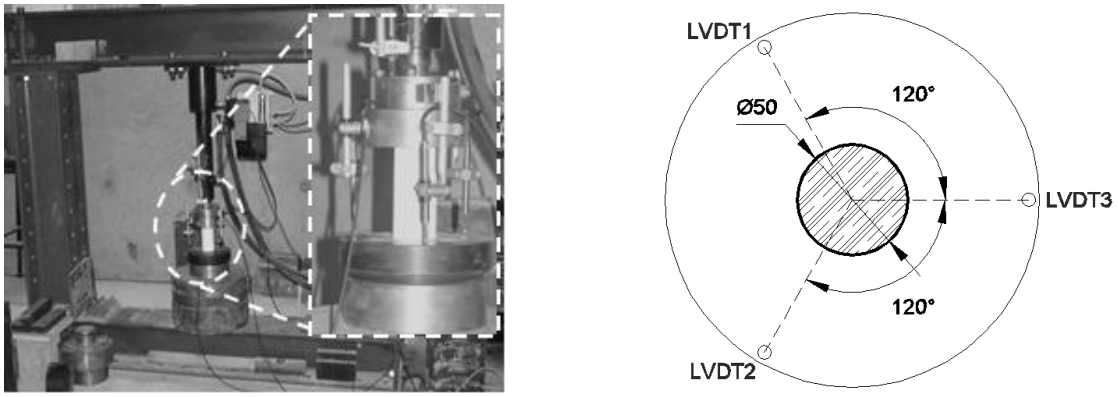
Considering that the European Norm EN 1015-11 (2004) recommends specimen sizes of $40\times40\text{mm}^2$, which theoretically present confinement effects under compressive testing, different sizes and shapes were adopted for the specimens within this study.

Because the strength measured by the load cell varies as a function of the ratio height/diameter (h/d) of the specimen dimension, an appropriate value of the ratio is needed, (Neville 1966). Cylinders having a ratio of 2/1 were selected to accomplish the mechanical characterization of the mortar, focusing on the compressive strength as well as in the Young's modulus assessment. After grinding the top and bottom surfaces, average dimensions of 50 mm diameter and approximately 110 mm height were used for all the specimens. All mortar specimens were tested under monotonic compressive loading at an age of two weeks, to replicate subsequent tests.

3.3.3 Test setup and test procedure

To achieve the mechanical mortar characterization, an arrangement similar to that used for brick specimens was assembled, using the same servo-controlled actuator and a load cell of 25 kN. The specimen deformability was recorded using three lvdt's, around a circular plate, equally separated by an angle of 120°. A picture illustrating the mortar specimen and the lvdt arrangement to carry out the test is presented in Figure 3.5.

All tests were performed under monotonic allow increasing displacement at a control rate of $3\text{m}\mu/\text{s}$.



(a) (b)

Figure 3.5: (a) General overview of the setup for mortar compressive and Young's modulus evaluation; (b) plan view detail showing the specimen and lvdt's arrangement.

3.3.4 Test results

The results corresponding to the testing of the two sets are shown in Table 3.3. Although the value of 7.3 MPa for the compressive strength could be considered as high for mortar, the Young's modulus of 1.8 GPa is very similar to the experiments reported in the literature (Binda et al. 1996b). Wide scattering represented by a higher variation coefficient was obtained for the Young's modulus.

The average compressive strength of the mortar obtained experimentally in Table 3.3, was higher than the manufacturer value given in Table 3.2. This depends mainly on the poured water quantity and the humidity conditions during the curing process.

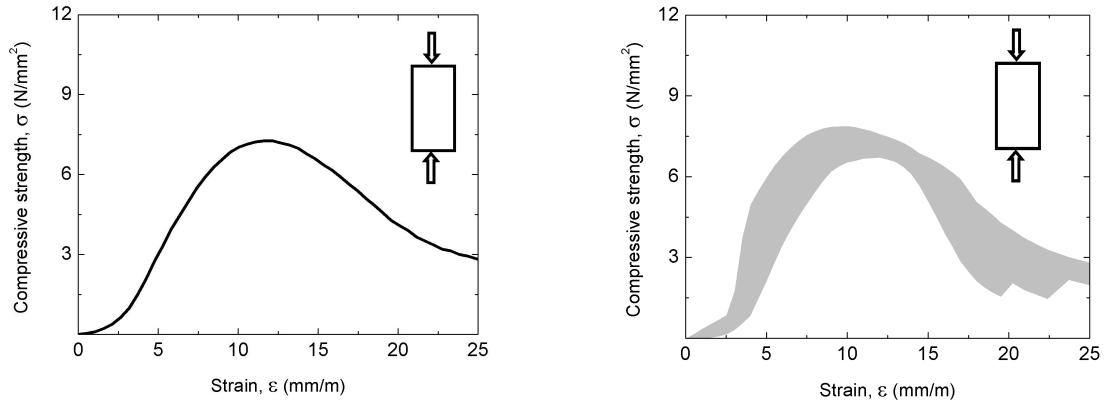
An alternative set of compressive strength tests of prismatic size specimens, with geometries of $40\times40\text{mm}^2$ recommended by the European Norm EN 1015-11 (2004) indicated that, the confinement effect due to the height/width ratio for the mortar utilized here was quite low. As the new average compressive strength was $\sigma_m = 7.1$ MPa.

In Figure 3.6a a typical compressive strength strain-stress curve is shown. Considering all compressive curves, it was possible to obtain a stress-strain envelope curve as illustrated in Figure 3.6b. The stress-strain curves presented a linear behaviour up to 70% of the peak load. During the initial loading phase the envelope curve shows the seating effect, which should be avoided on the computed

Table 3.3: Mechanical characterization of the mortar (15 days).

Specimen	Compressive Stress, σ (MPa)	Young's modulus, E (GPa)
CMM-1	6.4	-
CMM-2	7.3	-
CMM-3	7.1	-
CMM-4	6.7	-
YMM-1	7.7	1.37
YMM-2	7.6	1.67
YMM-3	8.0	2.79
YMM-4	7.9	1.37
Average	7.3	1.80
C.V. (%)	7.8	37.5

results treatment (ASCE 5-95TMS 402-95 1989). Figure 3.6 shows that post-peak behaviour was characterized by a smooth decrease in strength, easily captured in the test.



(a) (b)

Figure 3.6: Mortar compressive tests: (a) single curve; (b) envelope from a all tests.

The most representative failure modes are shown in Figure 3.7. A swelling effect on the cylinder is noticeable especially on the bottom part since the load applied by the servo-controlled machine was from the upper side; as expected,

vertical cracks are visible in the specimens. Vertical cracks at the mid height specimen indicate pure compression stress state in the centre of the specimen.

The test results seems to indicate that the mortar selected could fit better the purpose of a close resemblance with historical mortars in terms of mechanical properties. For practical reasons, this mortar was used in the subsequent tests.

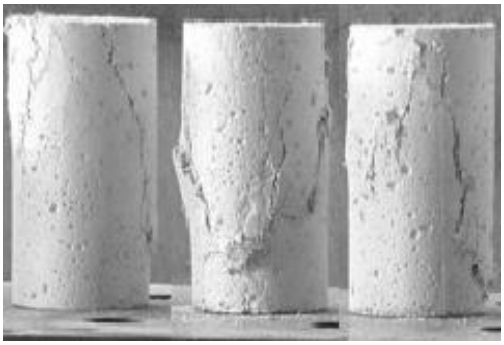


Figure 3.7: Mortar failure modes after monotonic compressive tests.

3.4 FRP composites

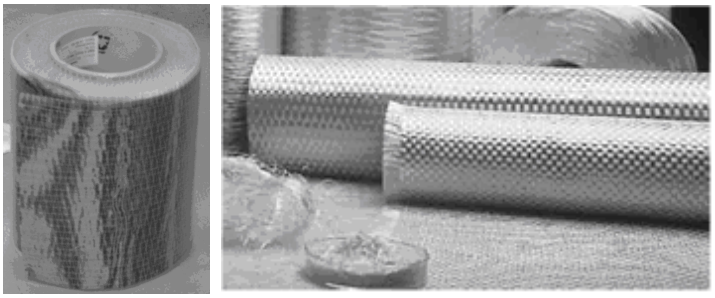
3.4.1 Material selected

The acceptance of composite materials in the last few years is mainly due to the excellent performance when used in the strengthening and retrofitting of structures, namely with respect to historical constructions (Triantafillou and Fardis 1997).

To accomplish the objectives of this thesis, two kinds of composites were selected from the wide variety of available materials in the market: carbon and glass FRP sheets as shown in Figure 3.8.

Table 3.4: Manufacturer data for the FRP composite material.

Material	Ultimate tensile stress, f_t (MPa)	strain, ϵ (%)	Young's modulus E (GPa)	Width, w (mm)	Weight, g/m^2	Density, g/cm^3
GFRP	3000	4.3	65	0.149	440	2.68
CFRP	3800	1.55	240	0.117	200	1.7



(a) (b)

Figure 3.8: Technical reference of Degussa, rolled sheets selected: (a) CFRP sheet CF-120 (S&P240); (b) GFRP sheet G-AR 90/10.

To fully appreciate the role of composite materials in a structure, a deep understanding of the component materials and the ways in which they can be processed is required. Considering that the mechanical properties of the FRP composites, tensile strength (f_t) and Young's modulus (E) are central parameters to be taken into account in any experimental characterization, five specimens from each material were considered representative enough as to obtain this information. The mechanical parameters provided by the manufacturer are included on Table 3.4. It must pointed out that those values are calculated per unit length and may differ from the tensile strength obtained experimentally.

3.4.2 Specimen preparation

Besides following the manufacturer indications, specimen preparation was complemented with applicable standards, namely ISO 527-1 (1993) and ISO 527-5 (1997) . Considering other norms (ASTM D638-97 1988; ASTM D3039/ D3039-93 1993) were useful to describe the rupture failure and to compute results. There are two different possibilities to prepare tensile specimens, as suggested by the ISO 527-5 (1997). Even though specimen type A was recommended for the longitudinal direction, specimen type B was chosen due to the lower data dispersion observed in preliminary results, when compared with type A.

The rectangular strips of 250×25 mm^2 of average final dimensions were obtained, Figure 3.9, following the recommendations given by the manufacturer, where three days of curing are suggested as a minimum time before cutting the specimens.

Square sheets having an average side dimension of 250 mm, were encapsulated completely with a tiny layer of resin, and uniformly brushed on both sides to provide the FRP sheet with a uniform finishing. The FRP sheet specimens had to be reinforced at its ends, with the purpose of avoiding sliding from the testing steel grips as well as relieving them from stress concentrations, to assure the failure at the gauge length. For that reason, four rectangular sheet strips of 50 mm width (w) by 250 mm length were cut parallel to the fibres direction and impregnated with resin too. The FRP rectangular pieces were glued at the FRP square ends (two per each side) acting as a grip mechanism and leaving a free gauge length of 150 mm. The overlapping of the rectangular over the square FRP sheet created a mesh with fibres aligned in two perpendicular directions, as shown in Figure 3.10.

Final strip specimens, including the double grip scheme, were cut with the vertical band saw shown in Figure 3.10a.

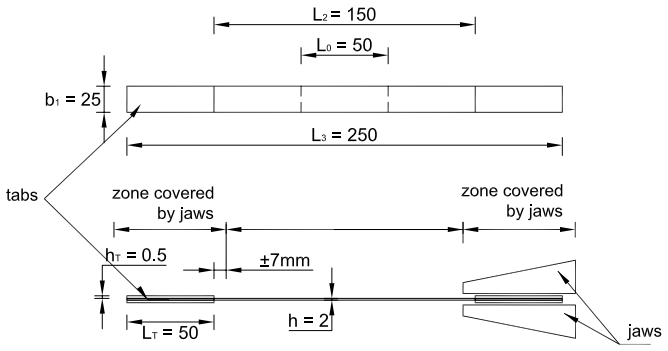
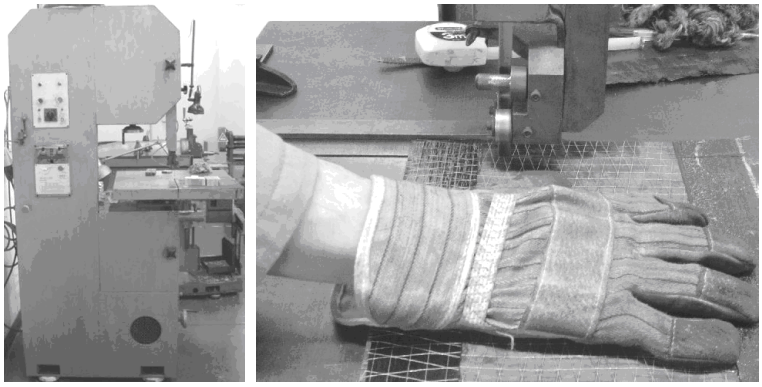


Figure 3.9: Specimen specifications from the ISO guideline (dimensions in mm).

To obtain an accurate measurement of FRP deformation, a strain gauge per specimen was glued at its mid-height and aligned with its longitudinal axis. Strain gauges were not embedded simultaneously in the handmade preparation process due to the risk of misalignment along the fibres and doubtfulness of weave area captured (Yang et al. 2002).

All gauges were installed with an adhesive type BFLA-5-3 give brand/manufacturer. For proper bonding of strain gauges, the surface was chemically clean and free of contaminants before applying the adhesive. There is a strong component of hand-work involved in making consistently successful strain gauge installations, which causes a wide scattering in results.

The quality of the solder joints is a critical issue in the performance of any strain gauge installation, especially due to requirements associated with strain gauge circuit. All wires and cables used were field-tested and found to give excellent sensor performance when properly used in normal environmental conditions.



(a) (b)

Figure 3.10: (a) Vertical band saw to cut FRP strips; (b) cutting procedure.

While it is often practical, in laboratory applications, to operate gauges without additional protection, open-faced gauges were covered with a suitable coating after installation, avoiding any possible damage.

3.4.3 Test setup and test procedure

The FRP composites were characterized at the Mechanical Properties Laboratory of the Polymers Department at the University of Minho.

The FRP rectangular strips were mounted and tested in an Instron Machine 4505, which its steel grips allow for a mechanical adjustment of specimens, as shown in Figure 3.11. At the beginning of the test, cell calibration and displacement trigger is pseudo controlled by means of a console. After setting these parameters, the Instron machine software carried out the monotonic displacement test at a displacement rate of 1 μm/min. On average, each test took about 45 minutes; the same guideline followed to prepare specimens was here used as a reference to carry out the tests (ISO 527-5 1997).

Strain gauges data acquisition was performed by means of a MGC+ external device controlled by a CATMAN software capable of registering lvdt's and strain gauges electronic measurements. The same data acquisition frequency for the

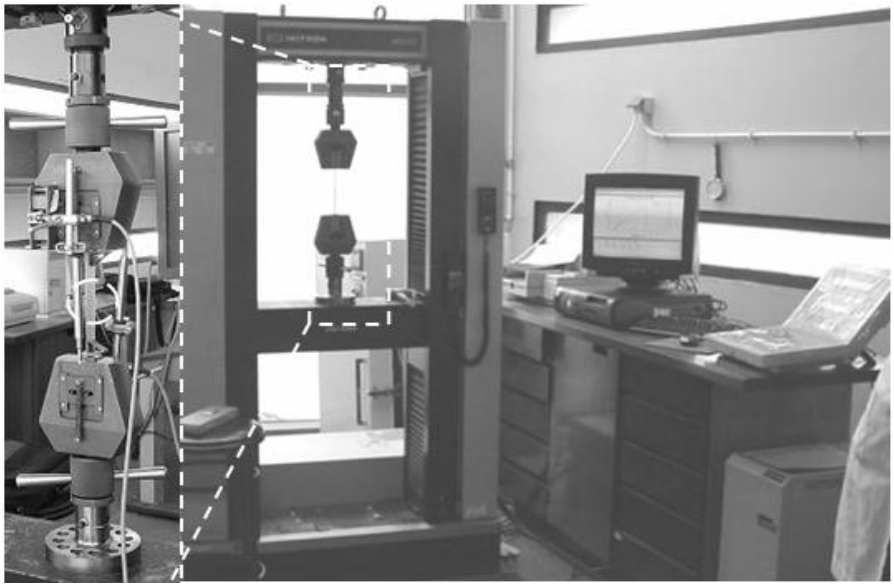


Figure 3.11: General setup for the sheet strip strain gauge position.

MGC+ equipment and Instron machine was used. Therefore, tests results from both devices could be synchronized and correlated on post-processing procedures.

3.4.4 Test results

The tensile strength of FRP specimens, as well as its corresponding Young's modulus, is presented in Table 3.5 and 3.6, for glass and carbon fibres respectively. The Young's modulus was assessed using two different starting deformations, specified according to ISO 527-1 (1993) and ASTM D638-97 (1988) norm. While the segment range to calculate the tangent modulus for the ISO norm is fixed, the ASTM norm suggests ignoring any seating effect as well as a possible initial toe in the stress-strain curve. Minor differences are found in the results.

The experimental values of tensile strength and Young's modulus are in good agreement with the values obtained in Barros and Ferreira (2005) previous investigations where similar materials were tested.

Figure 3.12 illustrates the typical stress-strain curves recorded. The tensile behaviour is characterized by an almost linear stress-strain pre-peak relationship. Even though both materials failed to present a post-peak behaviour, the tougher material CFRP had an sudden failure when compared with the smoother misaligned thread of GFRP at collapse.

Table 3.5: Tensile strength and Young's modulus for GFRP specimens.

Specimen	Ultimate tensile stress, f_t (MPa)	strain, ϵ (‰)	Young's modulus, E (GPa) ISO	ASTM
GFRP-1	1191.6	29.86	82.09	79.94
GFRP-2	1622.0	40.97	75.47	74.20
GFRP-3	1478.9	34.31	85.37	82.02
GFRP-4	1330.0	39.02	76.21	82.45
GFRP-5	1743.0	38.72	80.10	81.78
Average	1473.1	36.58	79.85	80.16
C.V. (%)	15.0	12.2	5.2	4.4

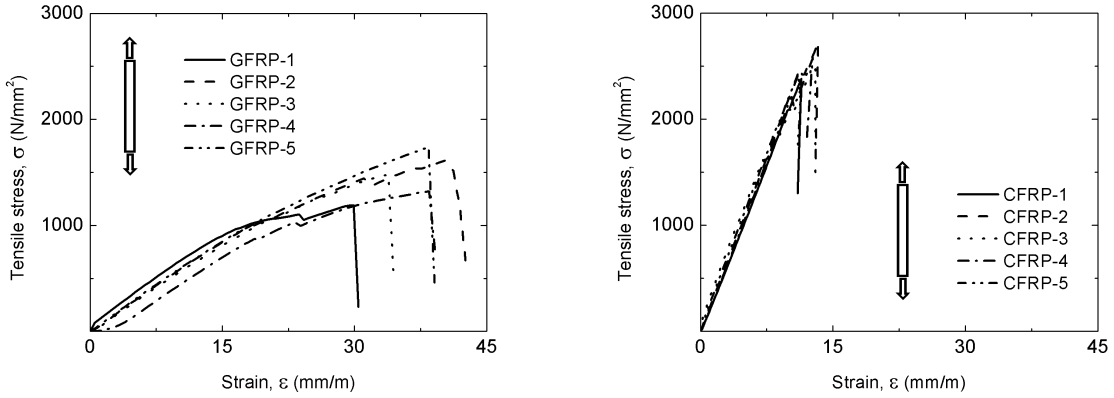
Experimental GFRP strains, tensile strength and Young's modulus measured presented a 20% increment when compared with the technical documents of the manufacturer, Table 3.4 and 3.5. On the other hand, the CFRP experimental Young's modulus and tensile stress are 10% and 30% lower than the technical documentation of the manufacturer, Table 3.6.

Table 3.6: Tensile strength and Young's modulus for CFRP specimens.

Specimen	Ultimate tensile stress, f_t (MPa)	strain, ϵ (‰)	Young's modulus, E (GPa) ISO	ASTM
CFRP-1	2396.3	11.40	205.89	209.88
CFRP-2	2714.4	13.34	213.92	216.66
CFRP-3	2511.2	13.01	229.27	216.55
CFRP-4	2590.2	12.72	208.30	215.44
CFRP-5	2433.9	11.44	223.86	219.54
Average	2534.6	12.38	216.25	215.62
C.V. (%)	5.4	7.3	4.6	1.6

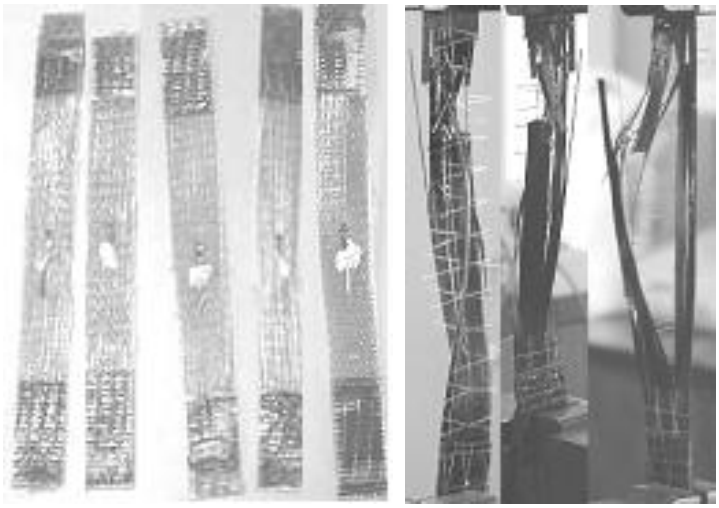
The GFRP, as a less stiff material when compared with CFRP, seems more adequate to strengthen masonry structures, which usually present very low stiffness. CFRP seems a suitable option for a stiffer material with lower deformability, as concrete for example.

In Figure 3.13 the failure modes for the GFRP (Figure 3.13a) and CFRP (Fig-



(a) (b)

Figure 3.12: Stress-strain diagrams for: (a) glass; (b) carbon fibres under monotonic loading.



(a) (b)

Figure 3.13: FRP failures modes observed for: (a) glass; (b) carbon.

ure 3.13b) specimens are illustrated. All failure of specimens occur always at the gauge length meaning that the clapping system adopted worked correctly. The external device to record data remained after failure only on the GFRP specimen while the CFRP had an explosive final stage. Edge delaminating gauge at the middle tensile failure patterns for the GFRP was observed under ASTM D3039/ D3039-93 (1993) specifications nomenclature (DGM). For the CFRP explosive gauge at the middle gauge length was observed (XGM).

3.5 Composite components

3.5.1 Basic components

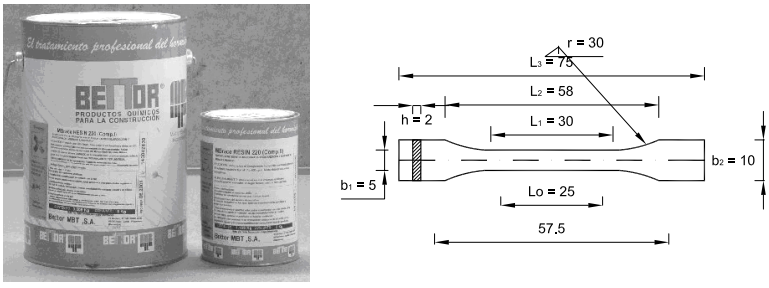
When the masonry-FRP interface is to be studied, reference values from their components are needed. Once the structures strengthened with FRP surpass service load conditions the most critical stress distribution occurs at the interface, turning into a fragile zone to study. Therefore the mechanical characterization of its components becomes of importance to interpret experimental results. To form a composite, the application requires a set of three sequential components (putty, primer and resin, in that order), combined at different stages and working together when finished, known as a composite. Regularization, filling up voids for preparing the surface and bond agent are the corresponding tasks of each component. Independently from the FRP material selected, *e.g.* glass, carbon or aramid, its preparation follows the same steps.

Putty is recommended by manufacturers to level small surface defects and to provide a smooth surface. Primer is the second component of the matrix that is applied to masonry substrates. It is used to provide proper adhesion of the composite to the substrate. Finally, resin is a 100% solid, low viscosity epoxy material used to encapsulate fibre fabrics. When structures are retrofitted applying fibre fabrics, the resin curing provides a high performance of the FRP sheet, resulting in additional strength to masonry.

3.5.2 Preparation of specimens

Putty

Putty is obtained by the mixtures of 2 components usually termed as parts A and B. Part A and part B were mechanically premixed separately for 3 minutes, Figure 3.14a. After premixing, part A and part B were blended with a mechanical mixer until a homogeneous mixture was achieved (additional mixing time took 3 minutes approximately). Putty should be applied within a temperature range between 10˚and 50°C.

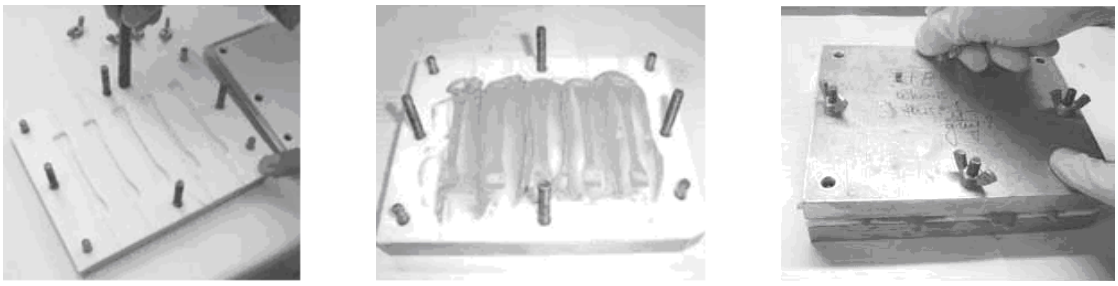


(a) (b)

Figure 3.14: Putty: (a) kit components; (b) dimension for the tensile strength test in mm.

Due to the component consistence there were two different types of dog bone shape specimens to obtain the tensile strength and Young's modulus.

In terms of consistence, there are two main basic kinds noticeably recognizable among the matrix components: liquid and doughy. The latter consistence, innate putty consistence, requires more delicate conditions than the liquid when moulding specimens. To overcome this inconvenience, a teflon sheet was used to mould putty specimens. A couple of rectangular steel plates, protected by a thick teflon plate, made a sandwich effect on the negative teflon sheet, pressured by four bolts, located on the corners fixing the film cast. Manual pressure was used to remove voids from the paste, Figure 3.15. According to ISO 527-2 (1993), final rectangular average dimensions of $75 \times 10 \times 2$ mm^3 were obtained.



(a) (b) (c)

Figure 3.15: Preparation of the putty specimen: (a) specimen mould; (b) casting; and (c) pressure applied.

Primer and resin

The liquid consistence for the composite components, primer and resin, make its moulding relatively easy. To accomplish such task, a square teflon plate was used as a base and four rectangular teflon strips fixed with bolts were used to mould rectangular plates. From the initial square plate, made of primer and resin mixed together, smaller rectangular strips were cut. The gauge length was mechanically prepared obtaining average final dimensions of 150×20×4 mm^3, Figure 3.16b. For a more manageable and advisable size specimen, a type A specimen from ISO 527-2 (1993) was selected.

Each composite component was obtained similarly to the putty, by joining two components A and B. Primer and resin components had the same mixing time, curing time and general recommendations were followed. Figure 3.16a shows the kit components A and B for the primer and resin respectively. Equal specimens dimension than the primer were adopted for the resin, Figure 3.16b. As soon as the specimens were finished, strain gauges were glued at the middle of the gauge length and aligned with the specimen longest symmetrical axis.

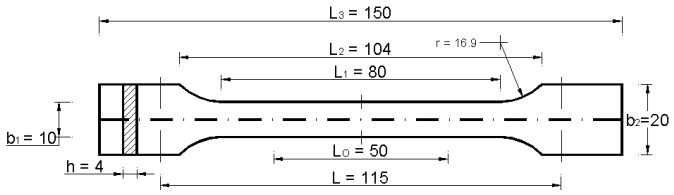
Table 3.7 was obtained from the American manufacturer of the same brand and the values contained should be considered only as indicative since no details specified by the European manufacturer were found.

3.5.3 Test setup and test procedure

All the tensile tests on the three composite components were carried out by means of a Universal ZWICK machine with a load cell of 5 kN mounted according to



(a)



(b)

Figure 3.16: Primer and Resin: (a) kit components; (b) dimensions of the specimen in mm.

Table 3.7: Manufacturer data for the composite components.

Material	Ultimate tensile stress, f_t (MPa)	strain, ε (%)	Young's modulus, E (GPa)	Density, ϱ (kg/m^3)
Putty	15.2	1.5	1.80	1258
Primer	14.5	40	0.72	1102
Resin	54	25	3.03	983

an expected maximum capacity. Tests were carried in accordance with (ISO 527-1 1993; ISO 527-2 1993; ASTM D638-97 1988). Tensile strength and Young's modulus parameters were calculated from strain gauges glued externally and load applied by the Universal testing machine. The same mounting process and alignment of the specimen was adopted for the three matrix components. Monotonic tensile tests were carried out under displacement control at a rate of 1 μm/min and using a sampling frequency of 0.5 Hz.

3.5.4 Test results

In this section, the results for the three tested matrix components are presented in Table 3.8 to 3.10. The results exhibit low coefficients of variation for the matrix components, which seems to confirm satisfactory moulding and testing procedure. Similar experimental data range values of tensile strength and Young's modulus for the putty component have been reported elsewhere, Bonaldo et al. (2005). For the other components, primer and resin, similar experimental values were presented by Casareto et al. (2002). Lack of further details in the technical files provided by the European manufacturer did not allow the comparison of results.

Table 3.8: Tensile strength and Young's modulus of putty specimens.

Specimen	Ultimate tensile stress, f_t (MPa)	strain, ϵ (‰)	Young's modulus, E (GPa)	
			ISO	ASTM
PU-1	32.8	4.3	7.47	7.06
PU-2	33.5	4.3	7.65	7.12
PU-3	30.7	4.1	7.50	6.72
PU-4	32.4	4.9	7.19	6.10
PU-5	31.6	4.2	7.35	6.77
Average	32.2	4.4	7.44	6.75
C.V. (%)	3.4	7.2	2.4	6.0

As shown before for the FRP sheets, the results computed using the ASTM norm gave smaller coefficient of variation than the ISO norm for the matrix com-

Table 3.9: Tensile strength and Young's modulus of primer specimens.

Specimen	Ultimate tensile stress, f_t (MPa)	strain, ϵ (‰)	Young's modulus, E (GPa)	
			ISO	ASTM
PR-1	6.1	51.46	0.28	0.20
PR-2	5.9	47.6	0.32	0.23
PR-3	5.8	41.0	0.37	0.25
PR-4	5.7	55.0	0.31	0.22
PR-5	6.1	43.0	0.31	0.26
Average	5.9	47.62	0.32	0.23
C.V. (%)	3.0	12.2	10.3	10.3

Table 3.10: Tensile strength and Young's modulus of resin specimens.

Specimen	Ultimate tensile stress, f_t (MPa)	strain, ϵ (‰)	Young's modulus, E (GPa)	
			ISO	ASTM
RE-1	51.4	21.39	3.79	3.23
RE-2	50.5	20.93	3.54	3.25
RE-3	49.7	18.64	4.14	3.21
RE-4	40.8	14.1	3.43	3.25
RE-5	50.4	20.29	3.44	3.21
Average	48.6	19.07	3.67	3.23
C.V. (%)	9.0	15.6	8.3	0.6

ponents characterization. Much care is needed in putty specimens moulding due to its natural fragility.

Figure 3.17 illustrates typical tensile stress-strains curves for the three matrix components. No post-peak was possible to capture, due to the brittle behaviour of the components. Some interpretation remarks about application in terms of stiffness and deformability are:

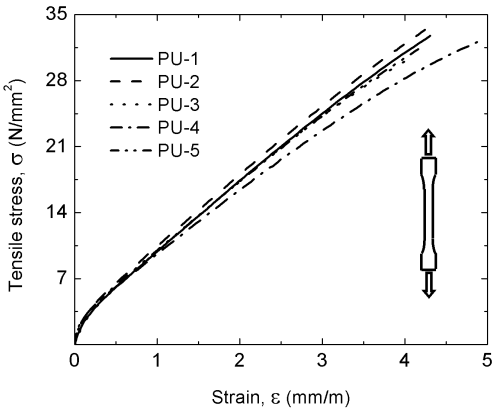
- Since the putty role in the composite is related to the substrate regularization, its high stiffness and lack of deformability illustrated in Figure 3.17a and Table 3.8 suggest the minimum quantity of material to be applied in the field;

- The second impregnated component is a highly stretchy primer, responsible for filling in the masonry remaining pores of the substrate and working as a transition layer between the others. Low strength characterized the compound, Figure 3.17b and Table 3.9;

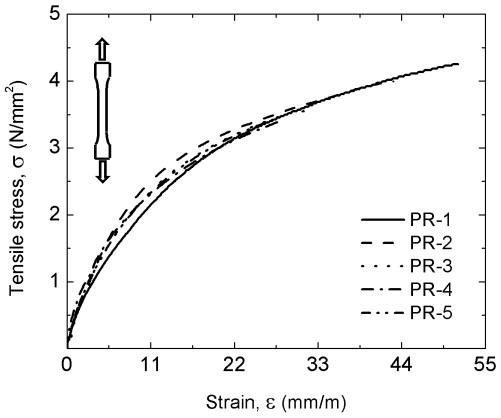
- Finally, the binding agent is responsible for the fibres impregnation. The resin component reacts with its adjacent layer, leaving proper conditions for application of the FRP sheet. The resin, which is impregnated twice over the fibres, has a stiffness in between the other component and a much higher stress, representing a key component in the composite, as shown in Figure 3.17c and Table 3.10.

Putty, primer and resin representative failure modes are presented in Figure 3.18. All putty and primer specimens break almost at the mid-gauge length representing the ideal rupture although resin specimens fail close to the grip; none of them reach the thicker specimen size, for that reason it was considered as an adequate failure.

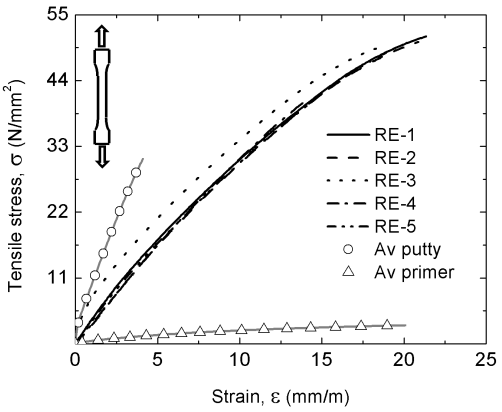
ASTM suggests a nomenclature to describe plastic failures modes, indicating: angle gauge middle for the putty (AGM), Figure 3.18a; lateral gauge middle failure pattern for the primer (LGM), Figure 3.18b, and lateral at grip tab top (LAT) for the resin, Figure 3.18c.



(a)



(b)



(c)

Figure 3.17: Stress-strain diagrams for the: (a) putty; (b) primer; (c) resin matrix components. In the last paragraph all three components are plotted.



(a) (b) (c)

Figure 3.18: Failures modes for: (a) putty; (b) primer and (c) resin.

3.6 Masonry type 1

3.6.1 General description

Following the mechanical characterization of brick and mortar specimens, stack bonded masonry prisms made from these materials were built and tested aiming at characterizing masonry mechanical behaviour. Subjected to analogue working conditions, *e.g.* compressive loading, a better understanding of its behaviour may be achieved, obtaining required properties for computer modelling. Under uniaxial compressive loading, each masonry component is submitted to a different stress state. Due to mortar and brick strain compatibility provided by bond and friction, mortar as the most deformable material, faces limitations to expand caused by the brick. Hence shear stresses and tension in combination with the vertical compression are produced in the mortar-brick interface.

Over the next sections, typical standard tests are described, where materials tested separately were arranged aiming to accomplish a comprehensive mechanical characterization. The adopted materials were Galveias clay brick type 1 and MAPEI mortar, previously described in this chapter. The specimen was type designated as masonry type 1.

3.6.2 Specimen preparation

Before the masonry prism construction, all brick units were immersed in water for 24 hours with the purpose of saturating them. Clay brick type 1 was cut into pieces having average final dimensions of $130\times90\times50$ mm^3, combined with mortar joints of approximately 10-15 mm thickness, resulting in a final height/width ratio for the prism of 2.6, Figure 3.19. A curing period of two weeks was allowed.

To assure a better contact and uniform initial stresses distribution, top and bottom masonry surfaces were previously regularized with a grinding machine aiming at obtaining smooth surfaces. Four masonry specimens were constructed to obtain its corresponding compressive strength and Young's modulus.

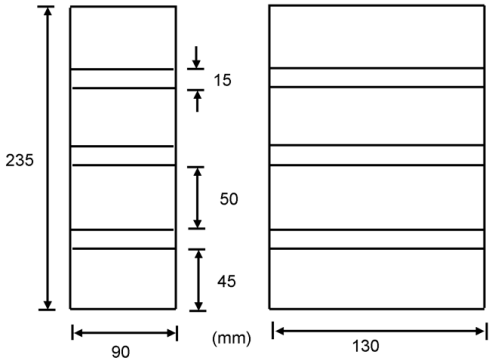
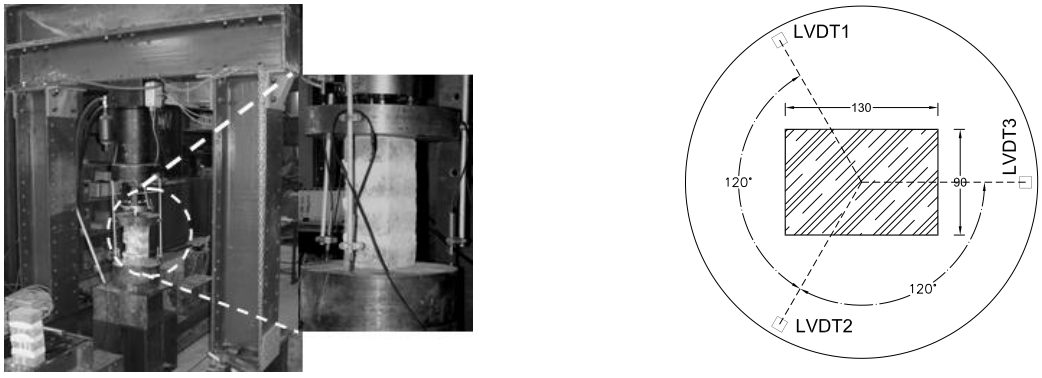


Figure 3.19: Average dimensions adopted for the masonry type 1 prism tested under compressive loading.

3.6.3 Test setup and test procedure

Compressive tests were carried out by means of a servo-controlled machine mounted on a stiff frame made of steel profiles. A load cell of 200 kN with enough capacity to bear the maximum expected load was used.

Measuring the deformation of the specimen was accomplished by adopting the same procedure used to test the bricks individually. Three lvdt's equally separated and surrounding the steel circular plate were used to measure the vertical deformability of the specimen. The final representative value was taken from the average, adopted as the reference deformation. Figure 3.20 illustrates a general view of the test setup along with a plan view of the lvdt's arrangement around the masonry specimen.



(a) (b)

Figure 3.20: (a) Test setup; (b) lvdts arrangement around the steel plate.

Masonry specimens were subjected to monotonic axial compressive loading till postpeak failure, under displacement control at a rate of 3μm/s. Masonry specimens reached their failure in about 40 minutes. The monotonic increasing displacement control assumed allowed to capture the complete post-peak behaviour.

3.6.4 Test results

Results concerning the tests carried out are showed in Table 3.11, where compressive strength and Young's modulus were computed for all prisms. The average value and the coefficient of variation of both parameters were also computed. The Young's modulus was computed considering the linear segment from the monotonic stress-strain curve in the stress range between 30% and 60% of the maximum stress, (Oliveira 2003).

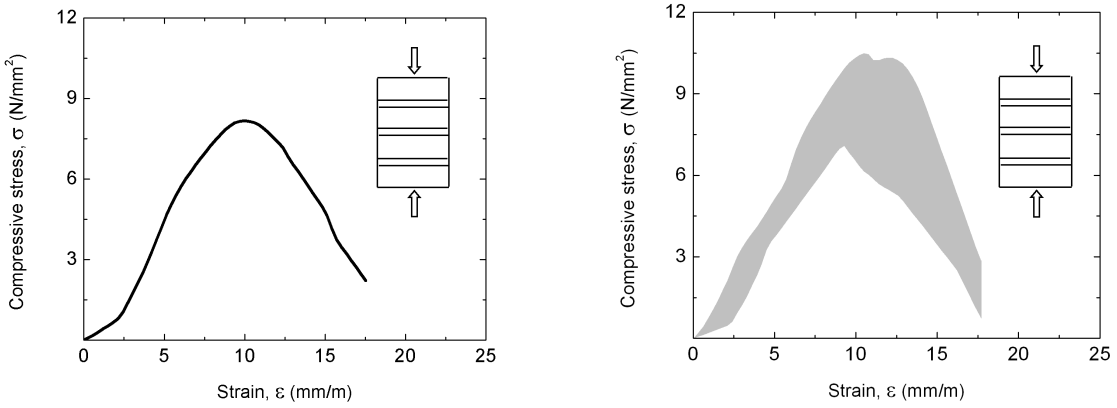
Masonry type 1 presented a slightly higher average compressive value than brick and mortar, with a similar Young's modulus, Tables 3.1 and 3.3. Others researchers working with historical constructions also reported similar results when comparing some of its specimens, Binda et al. (1996b), attributed to the large variability of the materials tested.

For masonry compressive specimens there are geometrical correction factors included in codes and guidelines (ASTM C1314-98a 1999). Such values are related to the specimen slenderness aspect ratio. Thus the average compressive strength value of Table 3.11 should be multiplied by a factor of 1.14. Such an increase came from the linear interpolation of the table included in the above ASTM guideline corresponding to the masonry height/diameter relation.

Table 3.11: Mechanical characterization of masonry prism type 1.

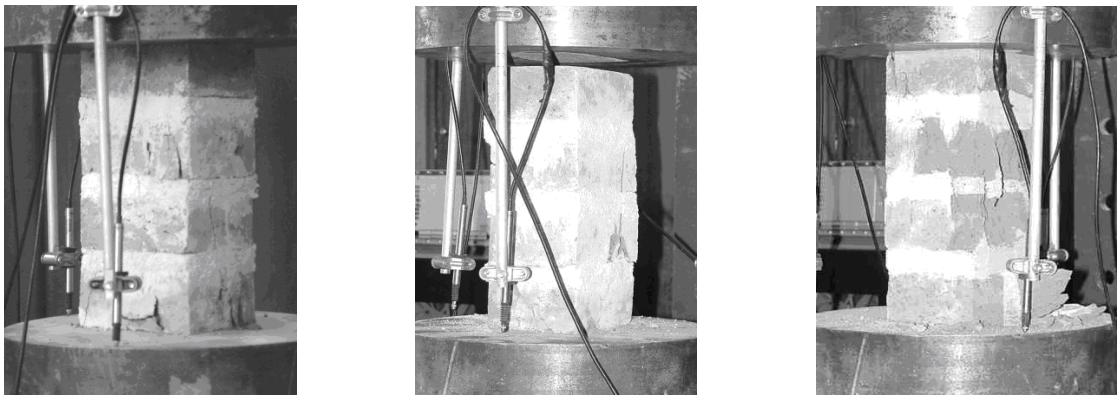
Specimen	Compressive Stress, σ (MPa)	Young's modulus, E (GPa)
YMGM-1	5.4	0.72
YMGM-2	10.5	1.48
YMGM-3	10.4	1.91
YMGM-4	8.9	1.10
Average	8.8	1.30
C.V. (%)	27.4	39.2

In Figure 3.21 a typical compressive stress-strain curve and an envelope from the test series are illustrated. Graphics show analogous deformational features for the masonry prisms considered. A similar situation which occurs with the masonry units, outlines a narrow band all over the elastic range, however the post-peak behaviour had a broad dispersion.



(a) (b)

Figure 3.21: Compressive stress strain diagrams: (a) typical single curve; (b) envelope of four curves.



(a) (b) (c)

Figure 3.22: Cracking sequence to the masonry type 1 specimens (sequence of recorded cracking).

The relative moderate loads attained made possible to record the cracking sequence, Figure 3.22 presents some of the damaged stages through the entire

masonry tests. The top of the specimen started to crush due to adjustment of the upper steel plate, then immediately vertical cracks on mortar and brick started to develop; finally, a failure pattern with extensive vertical cracking was formed. This occurs in combination with masonry spalling and localized mortar crushing.

Some of the specimens had diagonal continuous cracking crossing mortar and brick misaligned out of plane caused probably by the yielding failure condition of the specimen, observed in Figure 3.22.

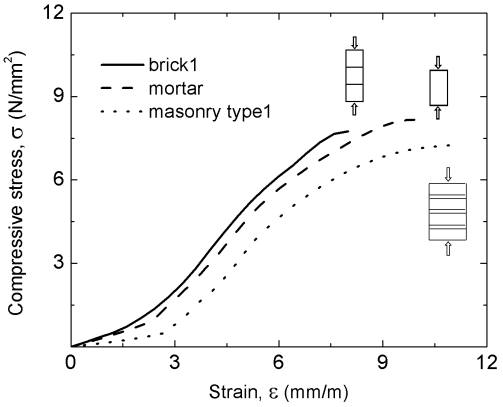


Figure 3.23: typical stress-strain diagrams obtained from masonry components and masonry prisms, plotted together.

Each masonry component was tested with similar objectives, namely to obtain their compressive strength and Young's modulus, making it possible to plot the stress-strain individual diagram together with the masonry diagram. Figure 3.23 shows the closeness on stresses and strain properties reported for brick, mortar and masonry. This is somewhat different from the modern masonry materials, in which mortar is usually much weaker than masonry unit.

3.7 FRP Pull-off test

3.7.1 Introduction and objectives

The separation of FRP as strengthening material from the masonry substrate can be generally classified into three main forms: sliding, tensile rupture and detaching. The first two forms are discussed later in the text. The detachment phenomenon, recognized as a common failure, is also a part of the extensive FRP-masonry

interface experimental characterization. By applying perpendicular tensile loading to the strengthened masonry interface it is possible to obtain a good estimation of its normal strength, by means of the standard pull-off test. The detachment of the FRP strengthening from its substrate is highly dependent on this mechanical property.

To evaluate the tensile strength normal to the masonry-FRP interface, eighteen pull-off tests were carried out, using glass and carbon fibres, as well as two different masonry prisms types.

3.7.2 Specimens preparation

With the purpose to evaluate the pull-off strength, two different types of masonry prisms were constructed as described in section 3.6 using two different bricks. On chapter 4 of this thesis, the second masonry type was also mechanically characterized obtaining a compressive strength of 9.1 MPa and Young's modulus of 2.04 GPa. The brick type 2 is slightly stronger and much stiffer than type 1. Following the same procedure shown for the masonry type 1, the values of 8.7 MPa of compressive strength and 4.89 GPa of Young's modulus were obtained.

The preparation of the pull-off specimens required cleaning up the masonry area with a portable angle grinder and a steel brush before applying the putty, to be strengthened free from dust, oils, small particles or other surface contaminates. After primer application, strips of 70 mm width were applied embedded in a couple of resin layers. Curing time and general recommendations by the manufacturer were followed.

Over the strengthened area, a 10 mm core depth was drilled with a portable drilling machine defining the surface for the circular steel pieces of 49 mm diameter and 24 mm thickness to be glued to the FRP, Figure 3.24 and 3.25.

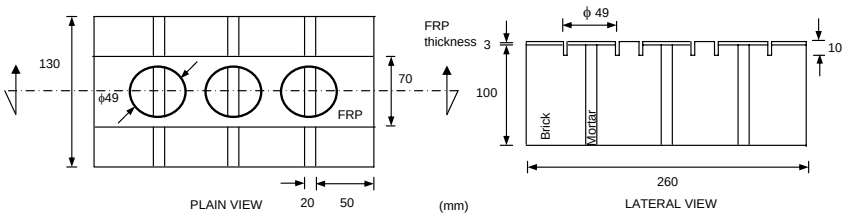
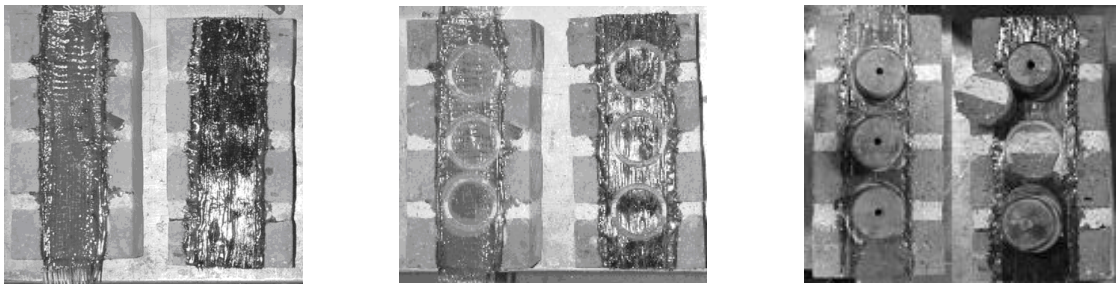


Figure 3.24: Pull-off test specimens.

The drilling was centred symmetrically with the masonry joint direction (lengthwise) capturing two bricks and one mortar joint when the specimen was tested. Subsequently, the circular steel pieces were glued to the FRP.



(a) (b) (c)

Figure 3.25: Sequential stages of the pull-off test specimen preparation: (a) strengthened masonry with FRP strips; (b) specimen after core drilling and (c) final aspect before and after testing.

Figure 3.25 presents the sequence of the specimen followed in the preparation for pull-off test using composite materials after the hardening of the composite material. Pull-off specimens, representative of both masonry types, strengthened with glass and carbon fibres followed this procedure. FRP application, surface drilling to bond the circular steel pieces and final aspect before and after testing are shown.

3.7.3 Test setup and test procedure

Tests were done using a Proceq DYNA Z15, with a 48 mm diameter disc. This equipment has a load capacity of 16 kN, an error smaller than 2% and a resolution of 0.10N/mm^2 (Proceq 1998). The small portable device allows performing these micro tests in reduced and difficult space conditions.

With the aforementioned equipment, the pull-off tests were executed assisted by a manual chronometer aiming at a stable velocity rate of 20 kPa/s so the maximum stress was attained in less than 100 s. Suggested recommendations from norm ASTM D4541-95 (1995), recommending geometry and equipment disposition were followed.

3.7.4 Test results

The pull-off strength was calculated as the applied force divided by the area of the fracture surface. Tables 3.12 to 3.13 present the pull-off test values for both composite materials selected (GFRP and CFRP) and the two different masonry prism types.

Table 3.12: Pull-off specimens using masonry prism type 1.

	Material	Specimen	Stress (MPa)	Average (MPa)	C.V. %
Masonry prism type 1	Glass	GMGPO-1	1.1	1.1	18.2
		GMGPO-2	1.3		
		GMGPO-3	0.9		
		GMGPO-4	1.4		
		GMGPO-5	1.0		
	Carbon	GMCPO-1	1.3	1.2	27.2
		GMCPO-2	0.8		
		GMCPO-3	1.4		

The average results indicate that maximum pull-off strength taken from the substrate is practically independent of the FRP material and masonry type. Despite of the relative high coefficient of variation, it is possible to observe that failure occur on the masonry substrate for all specimens independently of the material considered. Such tendency was expected.

The fact that the differences between the masonry types are low, justified the fact that the differences in strength are also low.

The average pull-off strength obtained for the masonry-FRP interface was above the minimum acceptable value (from 0.89 to 1.03 MPa) for any single tension test according to the ACI 440 (2004) and Brencich et al. (2000), where the tension adhesion tests exhibited failure of the masonry substrate indicated by a layer of masonry on the underside of the test puck following the test.

For all tests performed, the failure mode was characterized by the ripping of a thin layer of brick and mortar, as shown in Figure 3.26. The strengthened masonry specimens presented detachment of the mortar and brick at the tested area simultaneously. The tensile pull-off strength depends basically on the strength of the substrate, which is the weaker element of the FRP-resin-brick assemblage.

Table 3.13: Pull-off specimens using masonry prism type 2.

	Material	Specimen	Stress (MPa)	Average (MPa)	C.V. %
Masonry prism type 2	Glass	AMGPO-1	0.9	1.2	20.0
		AMGPO-2	1.2		
		AMGPO-3	1.5		
		AMGPO-4	1.2		
		AMGPO-5	1.1		
	Carbon	AMCPO-1	1.4	1.3	22.0
		AMCPO-2	1.0		
		AMCPO-3	1.6		
		AMCPO-4	1.4		
		AMCPO-5	1.0		

Thus, the tensile strength of the brick/mortar controls the tensile strength of the masonry-FRP interface.



(a) (b)

Figure 3.26: Typical failures modes of pull-off test for masonry strengthened using glass and carbon fibres for two different masonry specimens built: (a) type 1; (b) type 2.

3.8 FRP-Masonry bond behaviour characterization

Although bidirectional Glass Fibre Reinforced Polymer (GFRP) does not present such high mechanical properties as unidirectional Carbon Fibre Reinforced Polymer (CFRP), its application can effectively lead to a higher increase in strength. Moreover, it can be more reasonable to combine materials with "closer mechanical properties", profiting the conjunction material's performance at its best. Therefore when dealing with Fibre Reinforced Polymer (FRP) as a strengthening material on the civil engineering construction industry, GFRP can be a suitable material to apply over the masonry substrate.

Careful considerations must be taken to account when different materials are combined to work together, specifically on the external strengthening of existing structures. Double shear pulling tests (Chen et al. 2001) and bending tests (Miller and Nanni 1999; De Lorenzis 2002) have been the most common setup arrangements previously attempted to accomplish the characterization of the FRP interface with construction material. Bending tests have been commonly utilized to describe experimental bond behaviour between FRP and concrete, consisting of two separate concrete blocks joined by a spinning piece that works as a hinge at the top of the blocks. However, adjustment of this setup to masonry specimens, aiming at the characterization of masonry-FRP bond behaviour did not fully achieve the intended results, because masonry bond strength is quite low, generally making impossible the completion of experiments (Focacci et al. 2000). Therefore, the application of the bending test setup to masonry specimens requires additional devices, complicating shear stress distribution as well as adding variables to be controlled. Only a detailed bond test allows a comprehensive insight into strengthened masonry with composite materials, allowing for the understanding of the masonry-FRP interface behaviour, as well as the possibility to calibrate advanced constitutive models.

In this work, an existing test setup (Täljsten 1997a) was modified to be used for the bond behaviour characterization of unstrengthened masonry prisms. Distinct FRP materials, different anchorage lengths and different masonry shapes were used, aiming at a detailed description of the phenomenon.

3.8.1 Specimen preparation

The masonry specimens were constructed and strengthened with the same techniques employed in the preparation of the masonry prisms and the pull-off specimens previously described. For the primer and resin preparation before rolling or brushing the primer, masonry substrate was thoroughly cured, dried, and free of oils, curing solutions, moulding release agents, and dust at the time of application. The resin was applied before the primer and putty coats achieved full curing. Surfaces with a tack-free primer/putty coat were also cleaned of any dust, oils, or other surface contaminates.

The same layer sequence applied in the pull-off was also applied to bond masonry specimens, illustrated in Figure 3.27. All the masonry surfaces in contact with the testing device were carefully smoothed, aiming at an adequate fixing of specimens, thus minimizing any non-uniform stresses distribution.

With the purpose of measuring the stress distribution at the masonry-FRP interface, a couple of strain gauges were glued along the external surface of the FRP strip anchorage length, equally spaced.

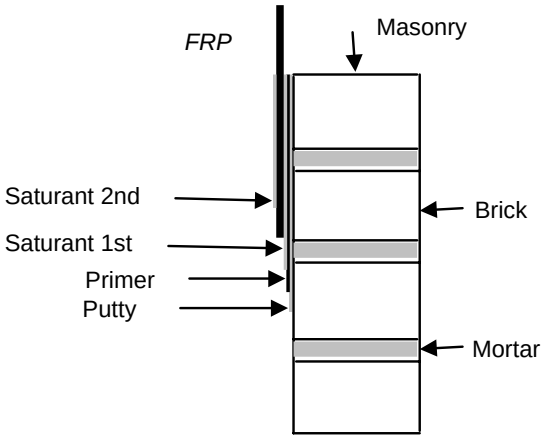


Figure 3.27: Strengthened masonry elements and applied layers including FRP.

A masonry specimen strengthened with a 25 mm width and 150 mm length GFRP strip was considered as the reference specimen (specimens G150RS-n). From this specimen, several variations were adopted. To evaluate the influence

of major parameters that dominate the bond behaviour of the masonry-FRP interface, the following variations with respect to the standard specimen were considered, Figure 3.28:

- Masonry-FRP interface length (two additional lengths of 100 and 200 mm were used), leading to specimens G100RS-n and G200RS-n ;
- FRP carbon fibres material were additionally used, leading to specimen C150RS-n ;
- Anchor scheme used (two additional anchor schemes were tested), leading to specimens G150RT-n and G150RI-n ;
- Masonry shape (convex and concave masonry geometries were also considered), leading to specimens G150XS-n and G150ES-n .

Therefore, seven different types of specimen arrangements were tested, being termed according to the following description, also shown in Figure 3.28:

- G150RS-n: Standard masonry specimen, strengthened with a 25 mm width and 150 mm length the GFRP strip along a plain masonry surface shape . The anchor of the GFRP strip was done simply by gluing it to the masonry surface. G stands for glass, 150 is the length of the masonry-FRP interface (in mm), R means that the masonry shape is regular and S indicates a simple (conventional) anchorage scheme;
- G100RS-n: The difference between this specimen and the previous is only related to the masonry-FRP interface length, being now 100 mm;
- G200RS-n: A 200 mm masonry-FRP interface length was considered in this arrangement with respect to the standard specimen;
- C150RS-n: This specimen is equal to the standard one except for the FRP material, made of carbon instead;
- G150RI-n: In this specimen a non-conventional anchorage scheme known as anchor spikes (Casareto et al. 2002) was implemented Glass fibres impregnated with resin were initially put in a cylindrical brick hole of 6 mm diameter, normal to the masonry-FRP interface, close to its end, and bent above the GFRP strip, normal to mortar joints;

- G150RT-n: Another non-conventional anchorage scheme was implemented in this specimen. A CFRP bar of 45 mm length and 6 mm diameter was simultaneously glued and inserted into the bricks and to the GFRP strip, close to the end of the masonry-FRP interface and parallel to mortar joints. For this, a groove was previously made in the brick to accommodate the bar;

- G150ES-n: In this specimen a concave surface shape was adopted instead, aiming at representing the intrados surface of masonry arches and vaults, keeping constant the remaining parameters with regard the standard specimen G150RS-n;

- G150XS-n: For this specimen a convex surface shape was considered for the application of the GFRP strip, to replicate the extrados conditions of masonry arches and vaults. All the remaining parameters were kept unchanged with respect the reference specimen.

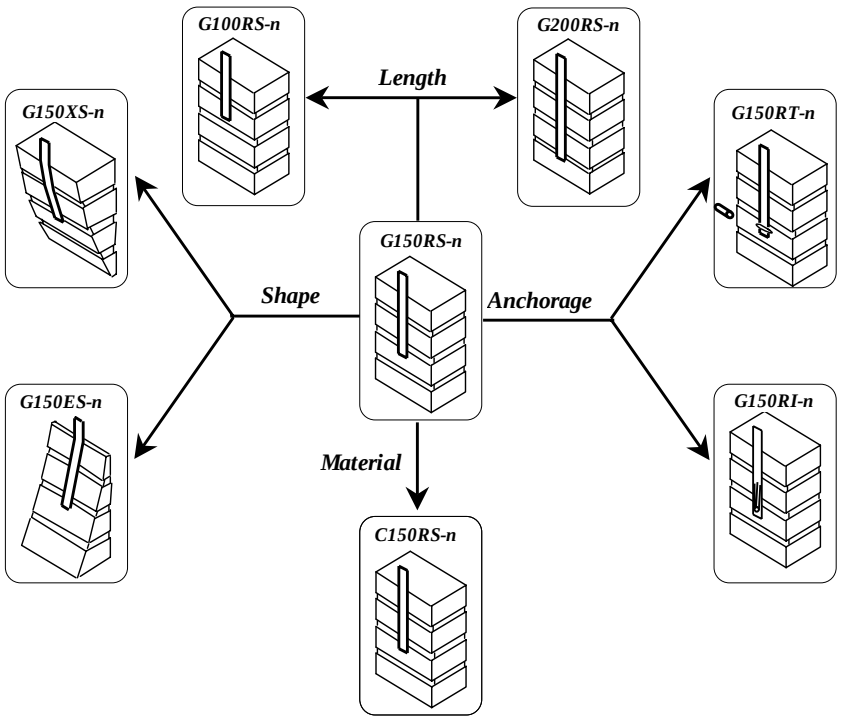
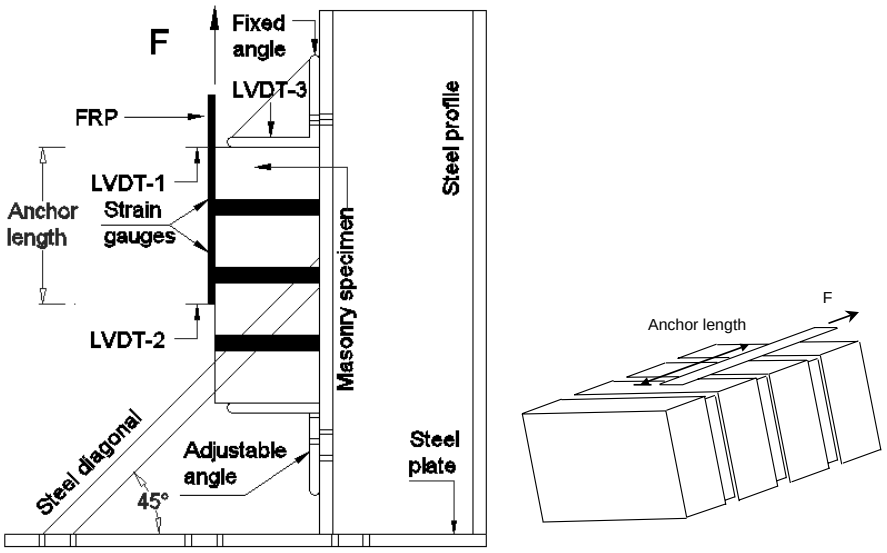


Figure 3.28: Branch tree relations derived from a reference arrangement.

Figure 3.28 illustrates the branch tree relations of the different experimental arrangements tested. In total, 5 specimens of each type series were tested under direct tension aiming at the comprehensive characterization of the composite, namely in terms of tensile strength and Young's modulus, which represent key parameters if a stress distribution along the masonry-FRP interface and failure patterns are sought.

3.8.2 Test setup and test procedure

To avoid premature shear failure and to assure an adequate test control of masonry specimens, performed under displacement control, a test setup based on direct shear loading was developed and implemented.



(a) (b)

Figure 3.29: Adapted test setup for the bond test specimens: (a) lateral view; (b) perspective

The adapted device shown in Figure 3.29 was designed to be mounted on a Universal Instron testing machine, able to work under axial displacement or load control. The test carried out consists of uniaxial direct tensile loading of the FRP strips bonded to the masonry prism. Besides the two strain gauges attached to the FRP strip, instrumentation included 3 lvdts, one placed in the upper L steel profile (lvdt-3) to measure any rigid body movement, and a couple more placed at the

anchorage boundaries to measure the relative displacement between the masonry and the FRP strip (lvdt-1 and lvdt-2), Figure 3.29.

Aiming at the post peak behaviour characterization, a displacement control rate of 0.1 mm/min was chosen in all cases. In this way, the peak load was generally reached in 45 minutes.

3.8.3 Presentation and discussion of results

Normal stress distribution

In this section, the experimental results concerning all bond tests carried out are presented and discussed. Tables 3.14 to 3.21 present the maximum tensile stresses applied to FRP strips and sustained by the masonry-FRP interface. The strain gauges attached to the FRP strip allow capturing the discrete normal stress distribution along the composite and, thus, the respective normal stress distribution. In all tables, tensile failure mechanism is indicated by (t), otherwise sliding mechanism was observed.

The results obtained demonstrate that an increment of interface length from 100 mm to 150 mm allows for a greater interface load capacity, resulting on average in an increase of 39%, Tables 3.14 and 3.15. However, when shifting from 150 mm to 200 mm, such increment in load capacity is relatively small, about 3%, Table 3.16. However in the latter a stress concentration over the anchorage length was experience since the failure mode changed partially. Half of the specimens had a tensile failure.

Table 3.14: Peak stresses for reference specimens.

Specimen	Stress (MPa)
G150RS-1	935.2
G150RS-2	1290.7
G150RS-3	1258.5
G150RS-4	$1651.4^{(t)}$
G150RS-5	1245.8
Average	1276.3
C.V.(%)	19.9

Table 3.15: Peak stresses for G100RS-n specimens.

Specimen	Stress (MPa)
G100RS-1	982.8
G100RS-2	850.4
G100RS-3	765.9
G100RS-4	988.5
G100RS-5	1018.2
Average	921.2
C.V.(%)	11.8

The application of carbon FRP strips enabled an increase of 16% in shear interface capacity (Table 3.17) modifying the shear stresses distribution as shown in the test.

Table 3.16: Peak stresses for G200RS-n specimens.

Specimen	Stress (MPa)
G200RS-1	$1172.4^{(t)}$
G200RS-2	1203.8
G200RS-3	1358.7
G200RS-4	$1524.7^{(t)}$
G200RS-5	$1331.9^{(t)}$
Average	1318.3
C.V.(%)	10.6

Based on the results extracted from the Table 3.18, it must point out that the first improved anchorage device, changes the failure pattern mode from sliding to tensile failure. Furthermore, the highest average peak load was recorded for this series with an increase of 26% with respect to the reference solution.

The modification of the standard anchoring scheme, by introducing anchor devices at the free-end of the interface, resulted on average terms, in a considerable increase in interface shear load capacity for the G150RI-n but only minor variations for the G150RT-n on average terms, Table 3.19. The use of a transversal FRP bar anchor resulted in an increase of only 3% in strength.

Table 3.17: Peak stresses for the C150RS-n specimens.

Specimen	Stress (MPa)
C150RS-1	1635.7
C150RS-2	1465.8
C150RS-3	1374.8
C150RS-4	1479.4
C150RS-5	1455.4
Average	1482.2
C.V.(%)	6.4

Table 3.18: Peak stresses for G150RI-n specimens.

Specimen	Stress (MPa)
G150RI-1	$1482.5^{(t)}$
G150RI-2	$1950.9^{(t)}$
G150RI-3	$1403.2^{(t)}$
G150RI-4	$1817.7^{(t)}$
G150RI-5	1415.6
Average	1614.0
C.V.(%)	15.7

Table 3.19: Peak stresses for G150RT-n specimens.

Specimen	Stress (MPa)
G150RT-1	1126.5
G150RT-2	1312.4
G150RT-3	1502.8
G150RT-4	1165.4
G150RT-5	1473.9
Average	1316.2
C.V.(%)	13.1

The results indicate that the masonry surface shape can influence the interface shear load capacity. For the curved geometry, with the concave and convex shape, a decrease of 13% and 4% was measured, Tables 3.20 and 3.21, respectively.

Table 3.20: Peak stresses for the G150ES-n specimens.

Specimen	Stress (MPa)
G150ES-1	945.6
G150ES-2	1296.1
G150ES-3	$1183.4^{(t)}$
G150ES-4	1217.0
G150ES-5	1464.6
Average	1221.3
C.V.(%)	15.4

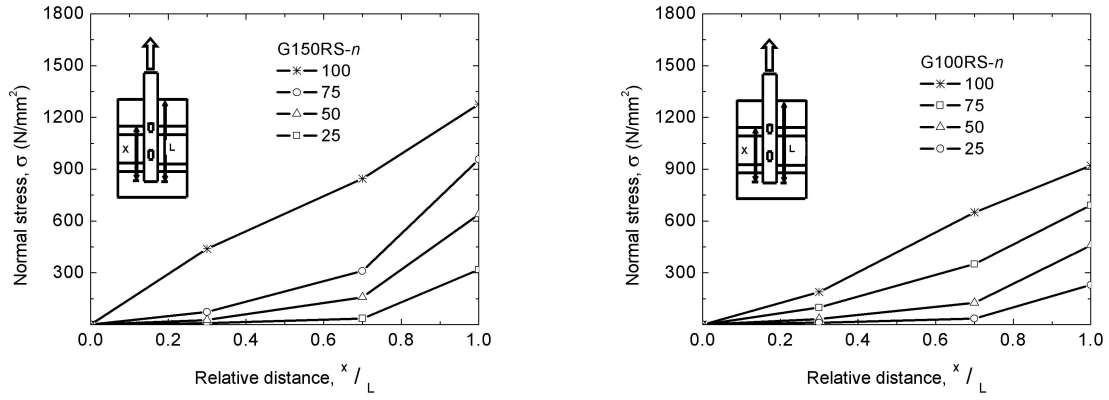
The maximum coefficient of variation computed in the framework of this set of tests was less than 20%, which reflects the quality of workmanship and testing procedures. In fact, when dealing with plain or strengthened masonry, higher coefficients of variation are usually found.

Table 3.21: Peak stresses for G150XS-n specimens.

Specimen	Stress (MPa)
G150XS-1	1220.8
G150XS-2	1007.9
G150XS-3	1026.4
G150XS-4	1218.7
G150XS-5	1089.4
Average	1112.6
C.V.(%)	9.2

Relationships between the FRP tensile stress and the location of the discrete points where the normal stress was measured, normalized by the anchorage length, are represented in Figures 3.30 to 3.33. These relationships are computed for four stress levels, *e.g.*, 25%, 50%, 75% and 100% of the peak stress. The depicted lines are mean values of five tested specimens, respectively for each stress level.

Experimental data indicates that the shear stress trend along the interface depends on the stress level as well as on the bonded length. Some scattering was found on specimens G150RS-*n* compared with smaller and bigger anchorage length specimens, respectively G100RS-*n* and G200RS-*n*, Figures 3.30a, 3.30b and 3.31a. For shorter anchor lengths, the stress distribution is more uniform, whereas for longer anchorage lengths, a peak is visible at the pulling end. As a consequence tensile failure of the GFRP occurs. For specimen C150RS-*n*, Figure 3.31b, a transition is found between the peak at the pulling end a zero at the free end, with a plateau not found in the other tests. The higher tensile strength of carbon fibres decreases the possibility of occurrence of tensile failure of the strip. The lowest scattering, in terms of peak stresses was obtained on this category.

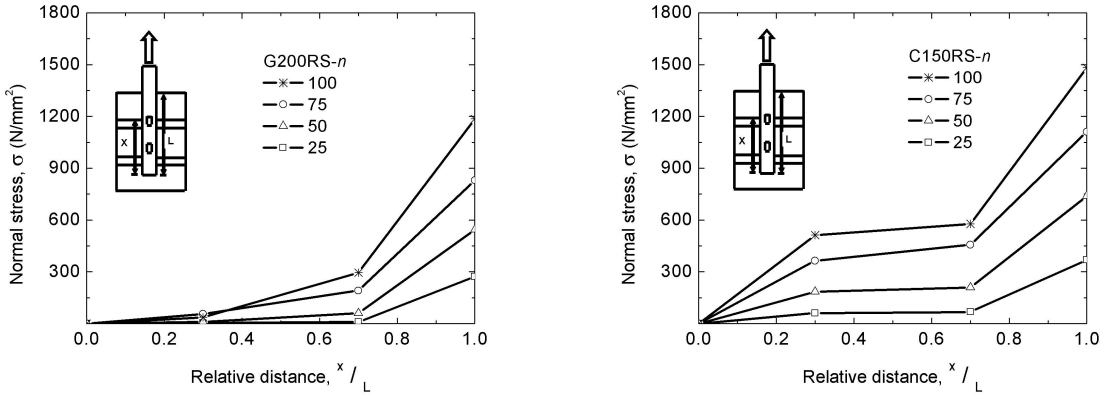


(a) (b)

Figure 3.30: Average stresses distribution along the anchorage length for: (a) reference specimens; (b) G100RS-*n*.

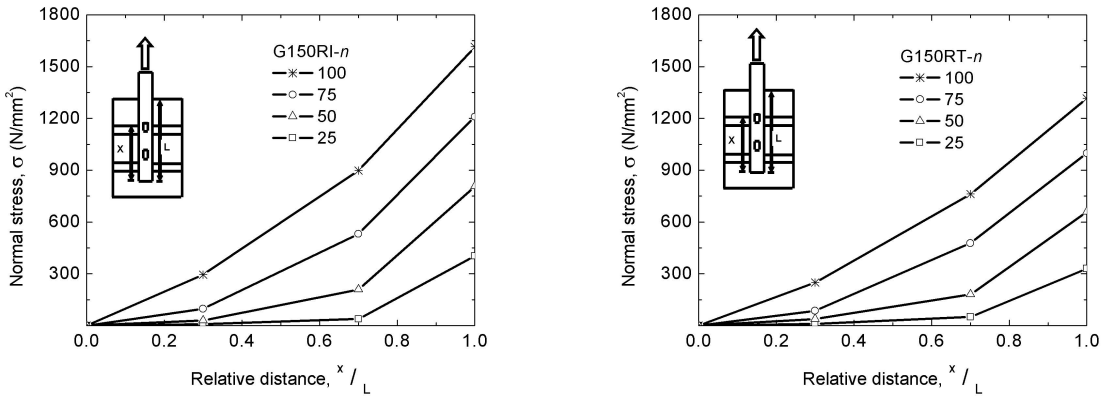
The adopted anchor devices reduced the scattering modifying the normal stress tendency along the interface length, at least for the highest stress levels, Figure 3.32. A more triangular distribution of stresses is found, indicating possible larger sliding and frictional effects. Curved masonry shapes influenced normal stress trend along the interface, at least for the highest stress levels, including a parabolic shape with concave down increasing, Figure 3.33.

The stress distribution along the anchorage length indicates that parabolic shapes at lower stress levels and almost linear distributions close to the peak load seem to describe approximately the bond behaviour of the substrate strengthened



(a) (b)

Figure 3.31: Average stresses distribution along the anchorage length for series: (a) G200RS-n; (b) C150RS-n.



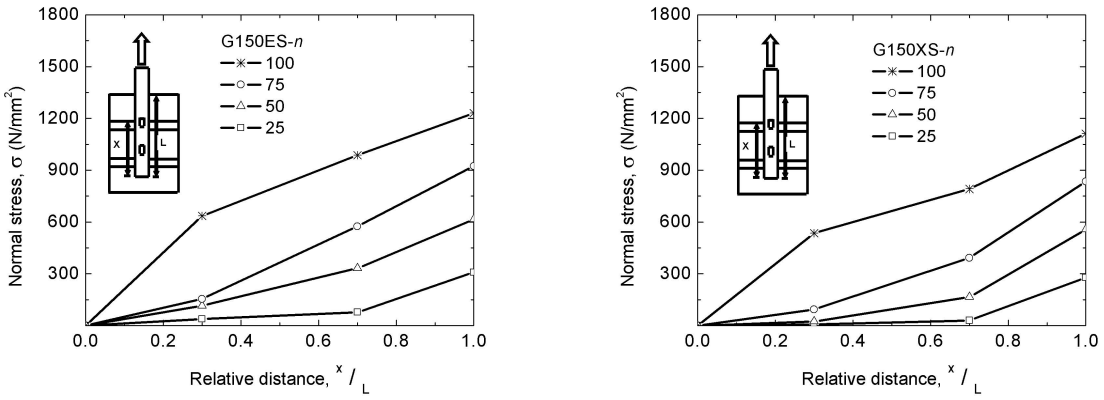
(a) (b)

Figure 3.32: Average stresses distribution along the anchorage length for: (a) G150RI-n; (b) G150RT-n.

by FRP. Analogue results with the same trend have been reported by other authors (Bizindavyi and Neale 1999; De Lorenzis et al. 2000; Valluzzi et al. 2004).

Results from the concave shapes show similarities with others authors, in terms of stress distributions along the anchorage length, see also (Aiello et al. 2004; Eshwar et al. 2005).

When comparing the stress distributions trends over the anchorage length of the concave-shape specimens (G150ES-n) with reference results, no significant differences can be found.



(a) (b)

Figure 3.33: Average stresses distribution along the anchorage length for: (a) G150ES-n; (b) G150XS-n.

A general issue for all curves of normal stress along the anchorage length, is that the stress concentration occurs close to the FRP loaded end. A brief statistical analysis of the peak stress for all tests can be observed in Figure 3.34 as a summary of results presented in Tables 3.14 to 3.21. Mean and standard deviation of tensile stresses are parameters included in the figure. Changes from the reference to different bonded length's G100RS-n and G200RS-n; convex geometry G150XS-n and carbon material C150RS-n presented moderate standard deviation from their mean values. For all remaining specimens (series reference G150RS-n, spike anchor G150RI-n, transverse bar anchor G150RT-n and concave G150ES-n) higher dispersion values were obtained. Because different failures modes are included in this broad classification, no association to the coefficient of variation can be

attributed but may be seen that the first anchor type had the biggest average peak load above all.

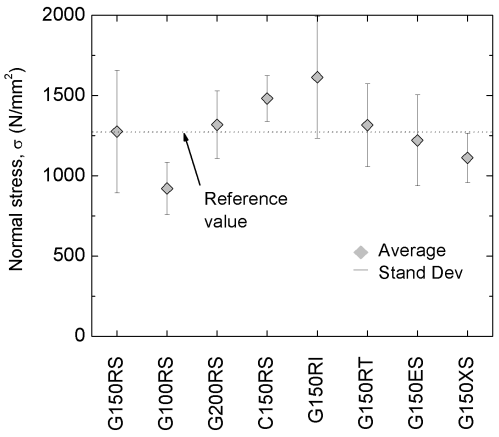


Figure 3.34: Peak stress for each series (average and standard deviation values).

The carbon fibres with higher mechanical properties than the glass, utilized to strengthen masonry did not showed significant improvement when compared with the glass fibres reference solution. Larger differences are expected for longer anchorage lengths.

Relative displacement

The fragile behaviour of the masonry-FRP interfaces under direct shear loading was also illustrated in the sense that post-peak behaviour seems to be characterized by a sharp decrease in stress, being the failure pattern dominated by sliding along the interface for small relative displacements after reaching peak load, as displayed in Figure 3.35. The complete set of curves for all tests are given in Appendix 1 where the reader is referred to for detailed illustration of the remaining cases.

All aforementioned specimens were tested under monotonic loading, as previously described. With the purpose of integrating the normal stress *versus* relative displacement (slip), ranges of variations trends from all tests in each series are illustrated in Figure 3.36 to 3.39. The FRP normal stress is related with the relative shear displacement between the masonry surface and the FRP strip, measured at its loaded end. This particular graphic type gives a quick perceptive information on scattering. The results depicted in Figures 3.36 to 3.39 ended just before the lvdt1 (Figure 3.29) base plate detached, caused by uncontrolled sliding or tensile

failure. The detachment of the lvdt from its support did not allow to obtain the entire normal stress-slip curve. However, all tests were performed until collapse, either by sliding of the FRP or tensile failure of the FRP.

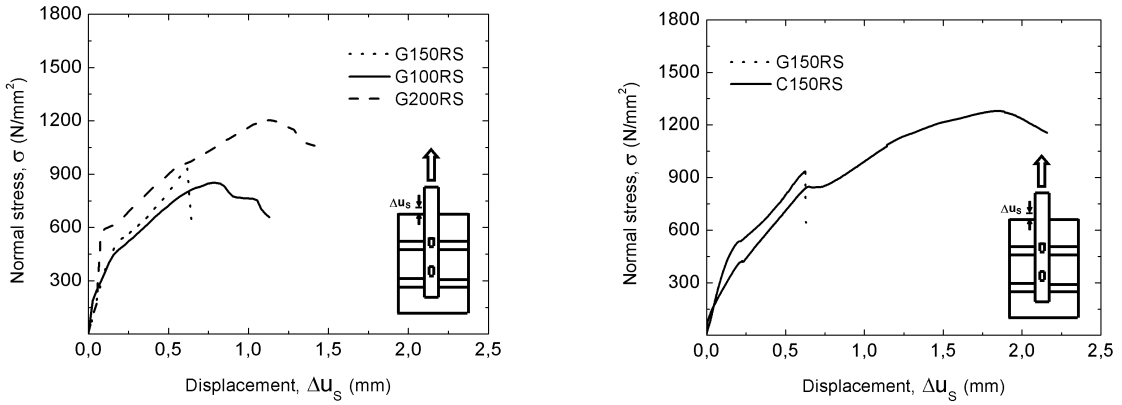


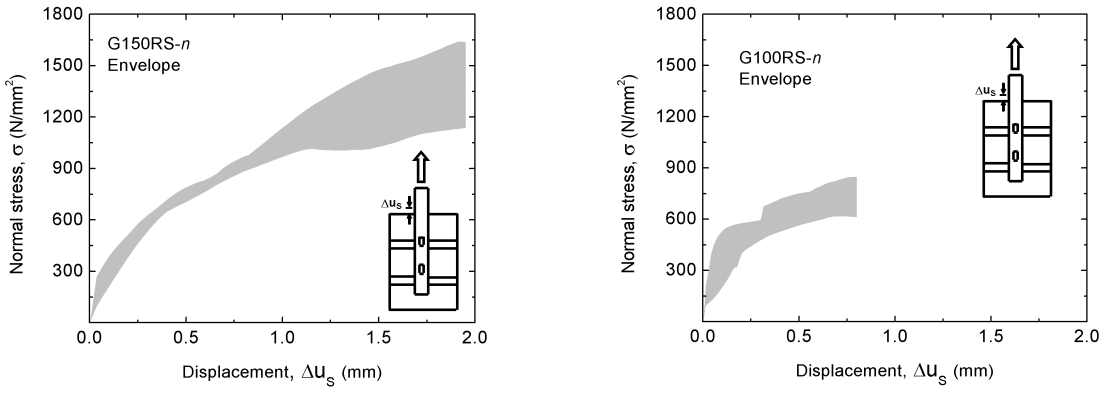
Figure 3.35: Typical curve of the normal stress along the anchorage length for different: (a) bond length; (b) material.

The experimental range of variations (tagged as envelop in the diagrams) associated to the reference series, describes a narrow band for lower stresses but a higher scattering at high stresses. The non-linear behaviour initiates at a relatively low stress level, Figure 3.36a. Decreasing of the anchorage length in the G100RS-n series causes a similar stiffness for smaller displacements, but an evident non-linear behaviour starts before the reference, Figure 3.36b.

Increasing the anchorage length up to 200 mm leads to a slight increase in stiffness, at low stresses. Afterwards, the band of the envelope increases due to the tensile strip failure mode as presented in Figure 3.37a. Even if the carbon fibres had the lowest scattering in peak load as recorded in Table 3.17, the envelope depicted in Figure 3.37b outlined the highest scatter in terms of normal stress *versus* its relative displacement.

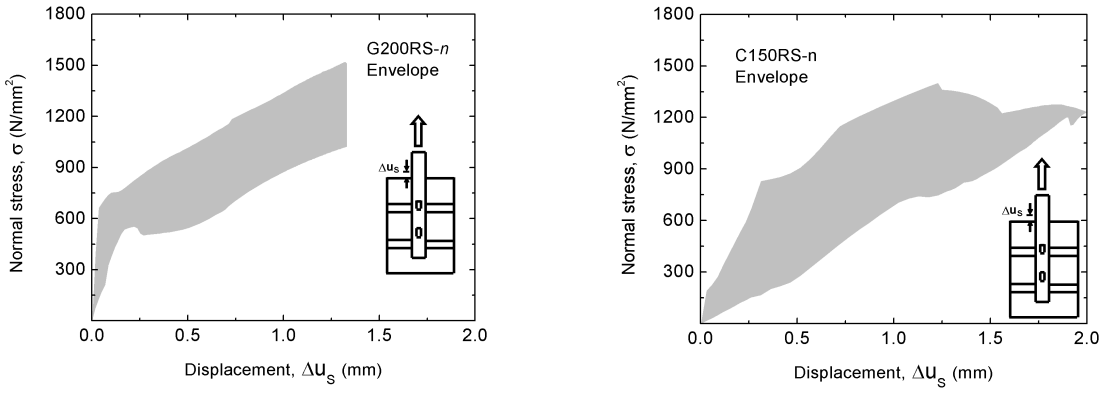
The non-conventional anchor types presented the lowest scattering when compared with the remaining categories. The decrement of ductility observed for the inserted bar anchor type, may be associated with the tensile failure reported when compared with its analogous anchor type and reference series, Figure 3.38a.

Although similar stiffness when compared with the reference, the transverse bar placed as an anchor had a smooth shape trend besides developing certain ductility



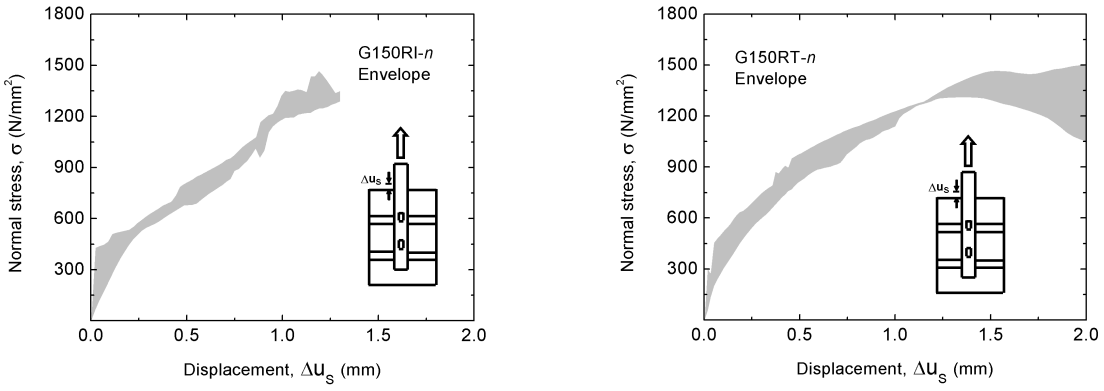
(a) (b)

Figure 3.36: Envelope of the relative displacement average *vs.* normal stress for series: (a) G150RS-*n*; (b) G100RS-*n*.



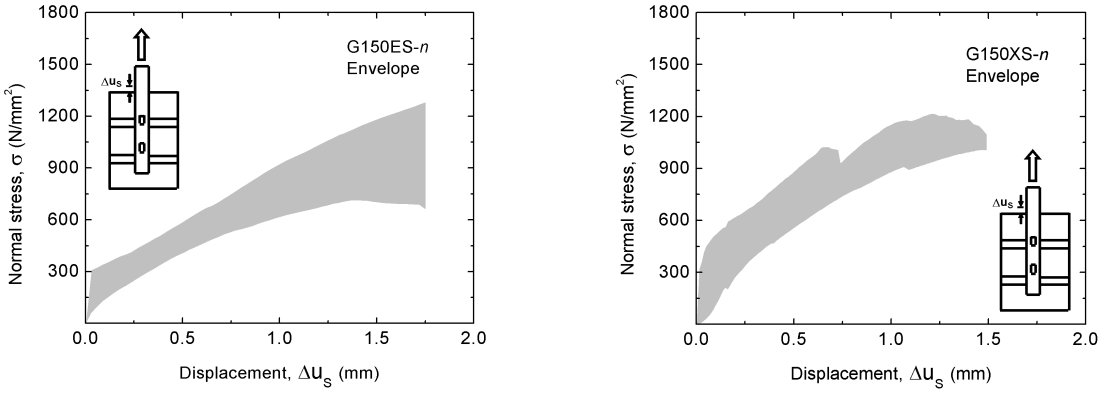
(a) (b)

Figure 3.37: Envelope of the relative displacement average *vs.* normal stress for specimens: (a) G200RS-*n*; (b) C150RS-*n*.



(a) (b)

Figure 3.38: Envelope of the relative displacement average *vs* normal stress for the specimens: (a) G150RI-*n*; (b) G150RT-*n*.



(a) (b)

Figure 3.39: Envelope of relative displacement *vs* normal stress for specimens (a) G150ES-*n*; (b) G150XS-*n*.

when Figures 3.36a and 3.38b are compared.

Changing the masonry surface from plain to curved shape did not change the scattering of the results as shown in Figure 3.39.

The application of a stiffer material presented also similar average stiffness but also the highest scattering, Figure 3.39b. The shaded envelope in this figure had the biggest band opening for all stresses levels, doubtful curve trend could be associated due to the correspondence stresses distribution outline in Figure 3.31b

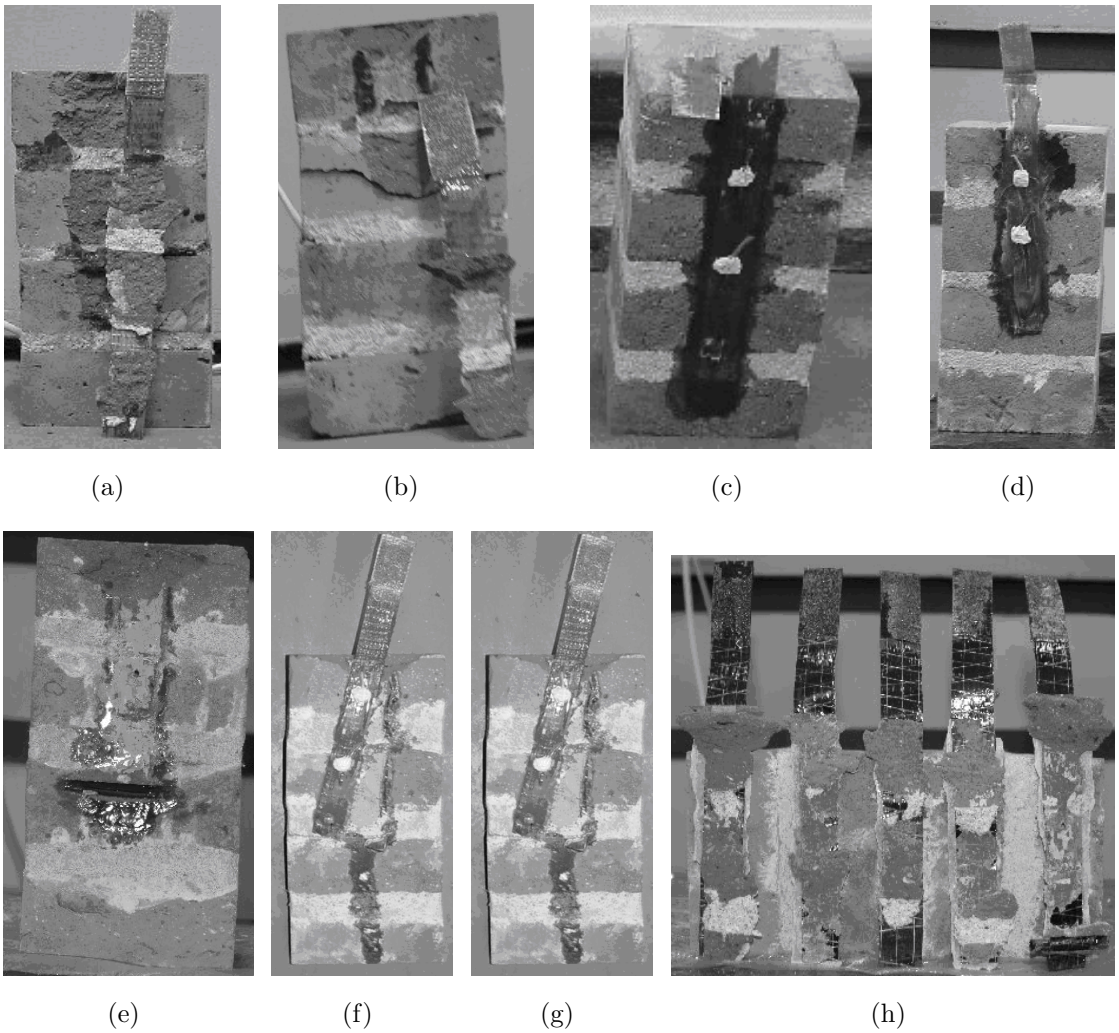


Figure 3.40: Representative failures modes for each series: (a) G150RS-n; (b) G100RS-n; (c) G200RS-n; (d) G150RI-n; (e) G150RT-n; (f) G150XS-n; (g) G150ES-n; and (h) C150RS-n.

where almost null stresses compatibility with masonry were detected.

Typical failure patterns for each series are included in Figure 3.40. The failures observed during the experimental campaign were gathered in two types of failure modes: sliding and tensile. In some cases, it was possible to confirm that maximum strength from the substrate was obtained since mortar and brick were ripped from the substrate.

3.9 Summary and conclusions

In this chapter a comprehensive mechanical characterization was performed, in different FRP strengthened masonry materials. All tests were performed at University of Minho.

Within the compressive test, linear range considered to evaluate Young's modulus had to overcome the initial deformability of the specimen known as seating effect.

In the matrix components for FRP application, small size specimens for tensile strength of the putty specimens lead to fragile shapes, causing failures outside the gauge length or even during the test accommodation. Voids must be controlled by the volume and the weight quantities to keep them to a minimum specifically for the doughy consistence. The dominating failure mode for the composite components was brittle failure, corroborated by the absence of post-peak behaviour in all cases.

By means of the setup device adopted, it became possible to characterize the frp-masonry interface behaviour, namely in terms of stress distribution along the bonded length. For FRP composite application, the quantity of the first layer (putty) must be minimized since excess impregnation can lead to low adhesion to adjacent layers. This general recommendation was based on the acquired experience during the construction of bond specimens.

Tensile strip failure must be avoided as a failure pattern by making preliminary testing on a variety of FRP anchorage lengths. Two issues should be considered in the stress distribution characterization along the frp-masonry interface are sought: optimal bond length to observe sliding and differences in FRP material, which changes the previous issue. These statements imply that experimental stress trend distributions, can change due to the fibres mechanical properties, namely stiffness, tensile failure and deformability principally. The relationship between material and optimal bond length obviously is not linear, since more parameters are included in the failure mode type localized in the fibres and matrix.

Specific results corroborate that specimens G200RS-n had more than enough bond length to attain the maximum normal stress. This means that for an anchor bonded length greater than 200 mm, the failure pattern will change from sliding to tensile failure.

In general it was observed that for a lower stress level, normal stresses were mobilized in a relatively small FRP length, close to its loaded end. However, for a higher load, normal stresses distribute along the entire interface, but keeping approximately a parabolic shape in most cases. It is believed that when a tensile failure mode occurs, FRP strip sliding already occurred and anchorage length was more than optimal. When the strip was accompanied by ripping of masonry, then optimal strength was taken from the substrate. Experimental tests carried out gave strong evidence that failure mode mechanism is strongly dependent upon the anchorage type since the G150RI-n specimens changes from sliding to tensile failure in most cases.

For the concave geometry variation, which represents the intrados application in the field, the results presented must be taken as indicative only. The presence of the perpendicular force component to the masonry inner surface, responsible for the strip detachment, may diminish assessed values. This is an important issue, because in practical situations the shape of the masonry surface can be hardly considered as plain.

Chapter 4

Experimental behaviour of masonry arches

4.1 Introduction

As a part of the widespread European cultural heritage, historical masonry constructions, namely arches and vaults due to their structural significance, deserve particular attention. In fact the preservation of cultural heritage structures is a current issue since the majority of them have considerable architectural and historical importance.

Ageing effects, movements in the abutments or other accidental factors (like earthquakes) can cause structural damage to key elements belonging to structures, thus affecting their global stability. To appraise the loading capacity, deformation patterns and collapse mechanisms of masonry arches, a good understanding of their structural behaviour is required. Because structural remedial measures may be needed after a structural evaluation, a significant concern in current research is the need for efficient strengthening techniques to upgrade the performance of these structures, preventing its brittle collapse when subjected to ultimate limit state action.

Several experimental and analytical studies have shown that FRP-based retrofits can produce remarkable increases in plane and out of plane strength of existing masonry structures (Lofti and Shing 1994). Such a restoration technique must be used prudently, since faulty design of the reinforcing system may cause the over load of the structure leading to premature failure modes. In particular, application

of high strength tensile reinforcements to a brittle substrate requires considerable caution (Ascione et al. 2005).

Among the innovative techniques to rehabilitate deteriorated structures, there has been an increasing interest in fibre composite materials, commonly known as Fibre Reinforced Polymers (FRP). These materials present several advantages such as low specific weight, corrosion immunity and high tensile strength. Their flexibility and somewhat easy application allow a wide range of intervention scenarios. Unified efforts to include FRP materials in building codes and design specifications recognise advantages and disadvantages of these materials when defining analytical procedures for design (ACI 440R-96 1996).

The specific application of FRP in construction is highly attractive and cost-effective due to durability improvement, reduced life-cycle maintenance costs and savings due to easier transportation and enhancement of on-site productivity, (Triantafillou and Fardis 1997). However, precautions in using this solution must be taken, due to its brittle nature and long term unknown behaviour. Furthermore, in addition to masonry conception complexity, the influence of FRP on the mechanical properties and stress transfer must be considered.

Following the initial researches concerning the use of FRP in masonry structures (Triantafillou 1998), numerous experimental works have been carried out showing that this technique is effectively valid as an option to strengthen or repair masonry structures, in particular arched ones, Valluzzi et al. (2001), Lissel and Gayevoy (2003) and Foraboshi (2004). Besides differences between the cost of glass FRP (GFRP) and carbon FRP (CFRP) , the latter material exhibits uneven stress distributions when small width strips are applied, changing failure mechanisms. Therefore, strengthening of masonry structures with GFRP composites seems to be a suitable and wise option (Valluzzi et al. 2001).

With the aim of characterizating and exploring the complex structural behaviour of strengthened masonry arches, an experimental research project was undertaken at the University of Minho. This chapter presents and discusses the results concerning the testing of masonry arches strengthened with FRP materials. In total, twelve arches were tested.

Considering the fact that testing of masonry arches built at 1:1 scale factor would require the use of significant human, laboratory and financial resources, it was decided to construct all the specimens at 1:2 scale. One important and

obvious consequence is the need of smaller bricks to fulfil the adopted similarity geometry. As the manufacturer that provided the handmade brick used in the previous chapter was not able to produce these smaller bricks clay bricks produced at scale 1:2 by a new manufacturer were used to built the arch specimens. It is worth mentioning that the same mortar was used along all the work.

In the previous chapter, most of the materials mechanical properties were already characterized. Therefore, results concerning the structural behaviour of 12 semicircular arches are comprehensively analysed here. The main objectives on this complementary research phase were:

- Characterization of the structural behaviour of both unstrengthened and strengthened masonry arches loaded monotonically until failure;
- Assessment of the influence of the strengthening on the mechanical behaviour and failure mechanism;
- Creation of a reliable database on the experimental behaviour of masonry arches, able to be used in the calibration of both analytical and numerical tools.

All tests described in this chapter were carried out in the Structural Laboratory of the Civil Engineering Department at the University of Minho.

4.2 Clay brick type 2

4.2.1 Brick description

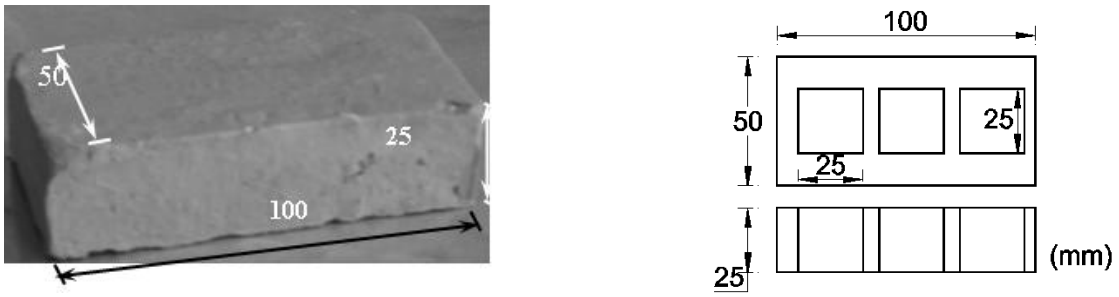
For the purpose of constructing scaled masonry arches models, reproducing old Portuguese masonry constructions new small, clay bricks were chosen from the northern area of Portugal. The orange-coloured clay bricks prepared show a low compressive strength, representative characteristic of most historical constructions. Due to the chronological tested order sequence, this second brick is hereinafter designated as clay brick type 2.

4.2.2 Specimen preparation

The specimen preparation for compressive strength and Young's modulus evaluation were conducted according to RILEM CPC8 (1975). All brick units were randomly selected from the same delivered single batch. Units presented average dimensions of 100×50×25 mm^3, Figure 4.1a, selected to fit the 1:2 scale defined for the construction of the arch specimens.

Using a machine with ball bearing grinding, the top and bottom of the specimen surfaces were smoothly regularized until a flat surface was obtained. Using a masonry saw, cubic samples of 25 mm side were cut from the original units. Because the brick manufacture process includes baking inside ovens, burning edges were commonly founded on the borders of the brick. Therefore the cubic pieces were extracted from the flatwise direction, as schematically shown in Figure 4.1b. Without any external bonding agent among single units, three cubic pieces were stacked and aligned to carry out the test. A final height/width of 3/1 was obtained. Such relation aspect ratio provides an appropriate uniaxial compressive strength characterization.

The day before testing, cubic units were immersed in water for 24 hours to saturate them.



(a) (b)

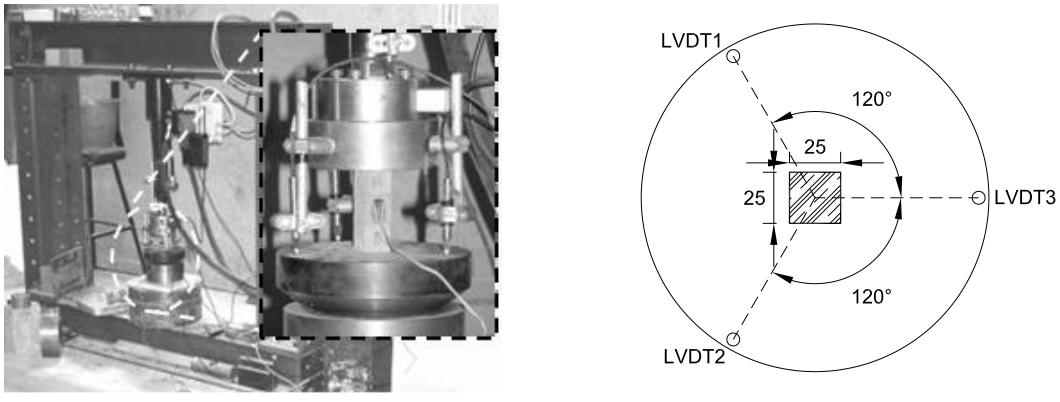
Figure 4.1: (a) Clay brick type 2 average size (mm); (b) cutting scheme dimensions adopted.

The mechanical characterization consisted on ten tests divided in two set of five specimens each. Although both sets gave an indication of the compressive strength, only the second one was used for the evaluation of Young's modulus. For the calculation of this parameter, measurements were taken from two sources of data, lvdts (linear variable differential transducers) and strain gauges. Suggested

indications from guidelines were taken into account for the specimen preparation only.

4.2.3 Test setup and test procedure

The test setup consisted of a steel frame which supports a servo-controlled testing machine with a load cell of 25 kN maximum capacity under compression loading selected, Figure 4.2a. In the second set of tests, one strain gauge for each specimen central piece was fixed parallel to the loading direction to evaluate Young's modulus. To measure the deformability of the brick, 3 linear variable displacement transducers (lvdts) were placed around the circular steel piece equally separated, as schematically presented in Figure 4.2b. Data acquisition from strain gauges and the average values from lvdts, were used to compute the deformability of the specimens. The first tests were used to asses the compressive strength only, whereas the specimens for the second set were used to compute the compressive strength and the Young's modulus. The linear segment considered to measure the Young's modulus was comprehended between the range of 30% and 60% of the maximum stress. All tests were controlled by incremental monotonic axial displacement at a rate of 5 $\mu m/s$. The adopted test procedure allows for the post-peak characterization.



(a) (b)

Figure 4.2: (a) General overview of the clay brick type 2 mechanical characterization under axial compression, test setup; (b) position of lvdt's (plan view).

General recommendations for the Young's modulus evaluation were similar to

those adopted in the clay brick type 1 assessment, described in chapter 3, and also in RILEM CPC8 (1975) and ASTM E111-82 (1988) guidelines.

4.2.4 Test results

The mechanical characterization of the clay brick type 2 is presented in Table 4.1. Although the tested bricks presented a relative high stiffness and moderate compressive strength, the clay brick type 2 can be considered as a representative of ancient bricks (Binda et al. 1996b), thus, appropriate to use in this research. From the brick average compressive strength calculated, a significant scattering was found, with a coefficient of variation higher than 30%. Based on an extensive clay brick characterization, the brick type 2 specimens are located in the lower part of the Portuguese brick compressive strength range, as reported by Fernandes and Lourenço (2005).

Table 4.1: Compressive mechnical characterization of clay brick type 2.

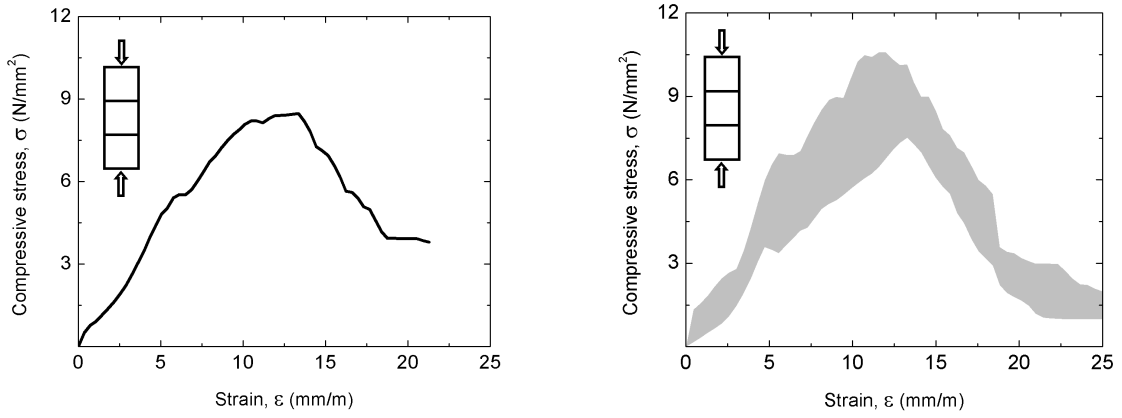
Specimen	Compressive Stress, σ (MPa)	Young's modulus, E (GPa)	
		E_{sg}	E_{lvdt}
CAB-1	7.1	-	-
CAB-2	7.3	-	-
CAB-3	7.1	-	-
CAB-4	5.8	-	-
CAB-5	5.3	-	-
YAB-1	15.5	5.30	3.19
YAB-2	10.6	3.38	1.65
YAB-3	10.2	4.10	1.10
YAB-4	9.2	6.05	1.87
YAB-5	9.1	5.63	1.34
Average	8.7	4.89	1.83
C.V. (%)	34.1	22.8	44.5

E_{sg} : Young's modulus obtained via strain gauge data
E_{lvdt} : Young's modulus obtained via the lvdt data

There were considerable differences when assessing the Young's modulus using two different data sources. As discussed in chapter 3, Young's modulus measured

by the lvdt's may be considered more accurate.

A typical compressive stress-strain curve is depicted in Figure 4.3a and subsequently Figure 4.3b shows the range of variation of all the tests carried out and shown in Table 4.1.



(a) (b)

Figure 4.3: Brick compressive test: (a) typical stress-strain curve; (b) range of variation of all specimens except the unexpected high strength specimen YAB-1.

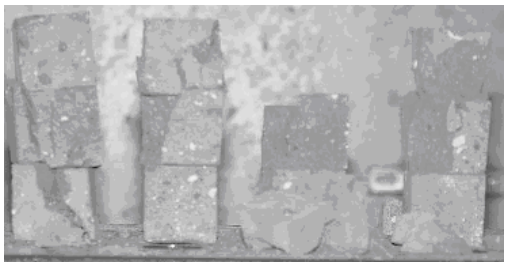


Figure 4.4: Typical failure modes of the clay brick type 2 units.

Typical failure modes are shown in Figure 4.4, with vertical cracks along the middle cube formed on most of the specimens. This kind of failure indicated that the three stacked cubes in fact behave as a whole unit.

4.3 Masonry type 2

4.3.1 Material introduction and objectives

Masonry compressive strength is an important material property. Here clay brick type 2 and the mortar described in the previous chapter were used to construct prisms of masonry utilized in the arches. For the purpose of calculating masonry strength and Young's modulus an important parameter for modelling purposes. Two sets of five tests were performed.

4.3.2 Specimen preparation

Before the construction, all brick units were immersed in water for 24 hrs with the purpose of saturating them. With the clay brick type 2, the mortar (characterized in the previous chapter) and joints of approximately 10 mm, masonry prisms with a relation height/width ratio of 3.2 were obtained, as shown in Figure 4.5. To promote a better contact and uniform initial stress distribution the top and bottom surface of the bricks were regularized with a grinding machine aiming at providing them with a flat surface. A curing period of two weeks was considered.

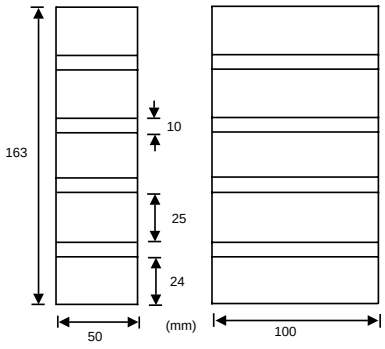


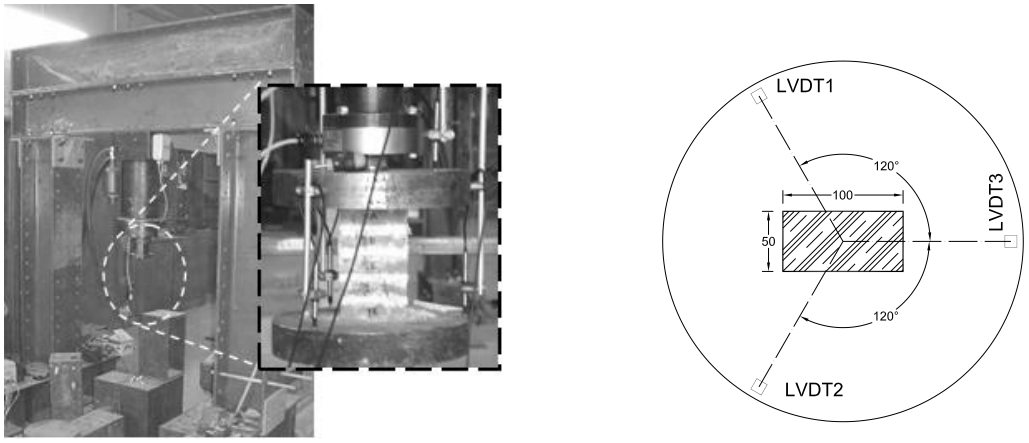
Figure 4.5: Dimensions of masonry type 2 test specimen.

All masonry prisms tested for compression and Young's modulus evaluation were constructed following ASTM C1314-98a (1999) and RILEM (1994).

4.3.3 Test setup and procedure

Using the test setup described in section 3.6.3, masonry compressive strength and Young's modulus tests were carried out by means of a servo-controlled testing

machine equipped with a 200 kN load cell capacity, covering the highest load expected, Figure 4.6a.



(a) (b)

Figure 4.6: (a) Overview of masonry setup; (b) plan of lvdt's positioning around the steel plate.

Three lvdts, positioned and fixed around the steel plate circular perimeter were used to calculate displacements. The average measurement was considered as a final deformation for the setup scheme shown in Figure 4.6b. All tests were performed under monotonic loading by imposing incremental displacements at a rate of 3 $\mu m/s$. On average, the peak load was reached in 30 minutes. The displacement controlled test type made possible to get the complete post-peak behaviour considered until ten percent of the maximum load.

Although compressive strength calculation depended on both sets, the second set defined the limits for the linear segment where linear fit adjustment represented the Young's modulus computed.

4.3.4 Test results

The information regarding compressive strength and Young's modulus including the average value and the coefficient of variation, are presented in Table 4.2. A higher coefficient of variation was obtained for the Young's modulus when compared with that of the compressive strength.

Table 4.2: Mechanical characterization of masonry type 2.

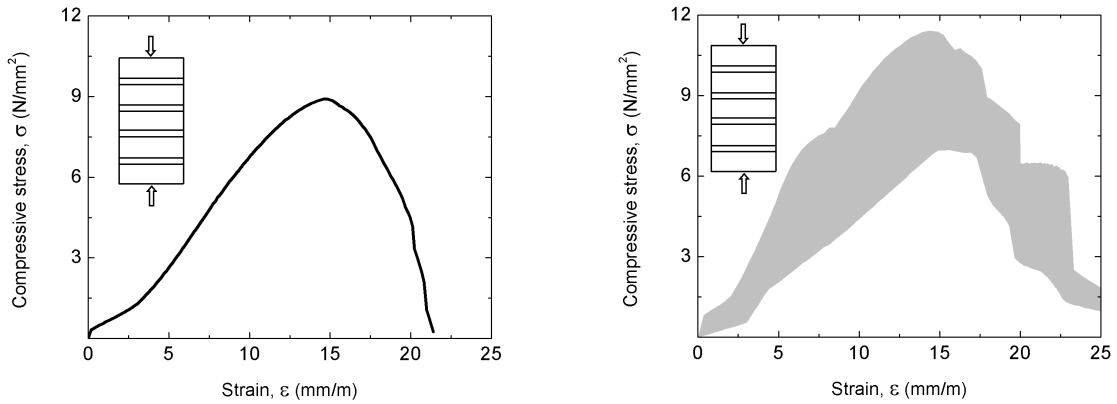
Specimen	Compressive strength, σ (MPa)	Young's modulus, E (GPa)
CMAM-1	8.39	-
CMAM-2	9.11	-
CMAM-3	8.53	-
CMAM-4	7.07	-
CMAM-5	7.98	-
YMAM-1	7.7	3.05
YMAM-2	10.9	1.32
YMAM-3	9.3	1.62
YMAM-4	11.4	1.79
YMAM-5	10.3	2.41
Average	9.1	2.04
C.V. (%)	15.7	33.9

Again a compressive strength for the masonry slightly higher than the units but a similar Young's modulus were found. Values of the same order and similar properties for ancient masonry have been reported elsewhere, Binda et al. (1996b).

A typical stress-strain curve for the specimens tested is depicted in Figure 4.7a. Figure 4.7b presents the range of variation from the ten specimens tested. The picture shows the wide variation of the Young's modulus, computed within the stress range of 30% to 60% of the peak load. All tested specimens showed low ductility.

Owing to the setup scheme adopted and the relative low load reached at failure, crack growth throughout the test could be followed up. The initiation of minor vertical cracks in the bricks indicates that the central units were subjected to mostly uniaxial compressive stresses, Figure 4.8a and 4.8b. The final stage of the masonry specimens presented brick spalling together with continuous cracking, Figure 4.8c.

For a better interpretation of the masonry behaviour, Figure 4.9 exhibits average curves corresponding to the mortar, brick and masonry together in a single stress-strain plot. After the initial seating effect of the masonry, similar stiffness and strength have been found for masonry and brick type 2.



(a) (b)

Figure 4.7: Unixial compressive behaviour of masonry type 2 (a) typical single curve; (b) range of variation from all tests.



(a) (b) (c)

Figure 4.8: Crack pattern recorded for masonry type 2.

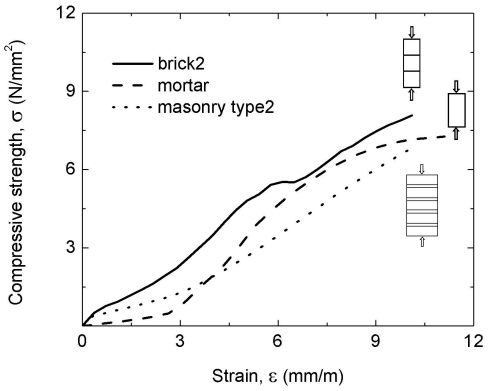


Figure 4.9: Masonry type 2 and its components on a single stress strain plot.

4.4 Initial parametric study

Before the masonry arch experimental campaign started, the influence of the FRP strip width in the load carrying capacity was examined by performing a parametric study, with different FRP widths. In the absence of experimental data at that stage, average values for material properties were adopted (Basilio et al. 2004) to have a general idea about the FRP influence on the maximum bearing load and failure mode of arches.

The arches under analysis to be studied in next section, are of semicircular-shape with a diameter of 1.50 m and a width of 0.45 m. Through numerical modelling of the arches, the selection of steel frames for the test setup, scheme of the supports tightened to the laboratory slab, and details of the equipment capable of capturing the fragile response were defined.

Also, the FRP strip widths applied to the experimental models, were based on the maximum sustained loads computed from the numerical models.

Details on this parametric study are reported in section 6.2, however the strain results wil be briefly presented here.

Figure 4.10 outlines the results from the parametric study, where an optimal FRP strip width was found for each case. All tests were computed until a wider FRP strip did not change considerably the maximum sustained load. The nomenclature for strengthened masonry follows: localized (LS), continuous at the extrados (CSE) and continuous at the intrados (CSI).

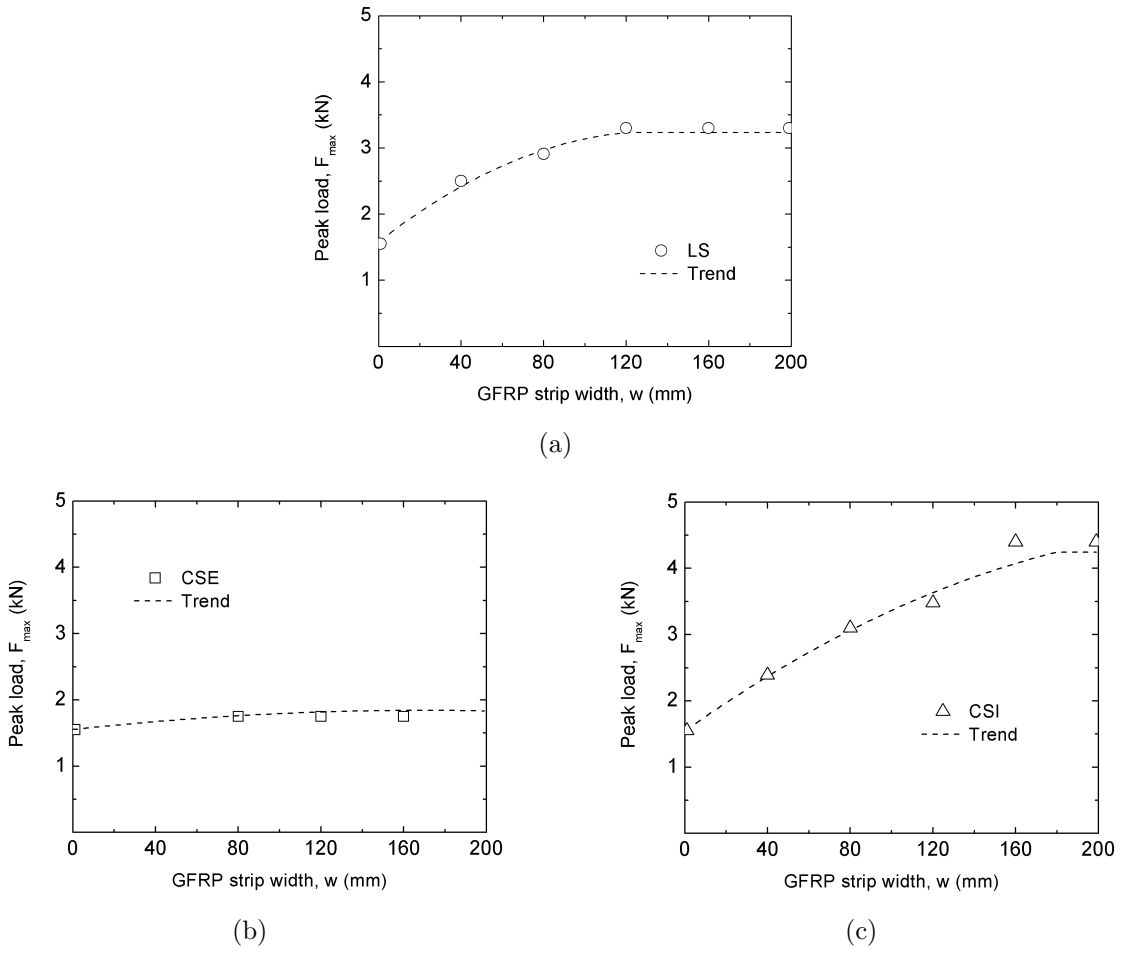


Figure 4.10: Influence of the FRP strip width on the load carrying capacity of the arches with reinforcement: (a) localized; (b) at the extrados and (c) at the intrados.

The masonry arch reinforced locally (LS) and at the extrados (CSE) presented smaller FRP optimal width when compared with the continuous strengthening at the intrados (CSI), Figure 4.10. For the first two strengthening strategies, the most remarkable changes were found for small FRP widths, since using more than 120 mm width FRP strips it provides only minor strength increase. In the case of continuous strengthening at the intrados, a steady increase on the maximum sustained load with a constant slope until 160 mm width FRP strip is found, being this value considered as the optimal width for this situation.

After the parametric analyses, two widths have been selected for the FRP strip, namely 100 and 160 mm. With these widths, three different criteria were adopted

for the experimental masonry arches strengthened with FRP materials:

- One FRP width of 160 mm localized over unstrengthened arches previously tested (LS) was applied;
- Two different FRP widths of 100 and 160 mm were tested considering the extrados strengthening technique (CSE);
- One FRP width of 100 mm was considered for the continuous strengthening at the intrados (CSI). However, anchorage devices tested in chapter three were also used in two additional CSI tests.

4.5 Semicircular scaled masonry arches

The use of stone lintels to support historical masonry above openings in walls had not allowed large spanning distances due to the low tensile strength of the stone. Therefore, the change from flat to curved structures, *e.g.*, to arches and vaults, represented a significant construction improvement, which allowed replacement of stone and timber lintels in walls, with stone or brick masonry spanning wider openings.

The main objectives sought in this section are:

- Characterize the structural behaviour of unstrengthened and strengthened masonry arches loaded monotonically until failure;
- Assess the influence of strengthening on the mechanical behaviour;
- Creation of a reliable database on the experimental behaviour of masonry arches, able to be used in the calibration of advanced numerical tools.

The series of tests carried out were designed to investigate the influence of the GFRP application on masonry arches.

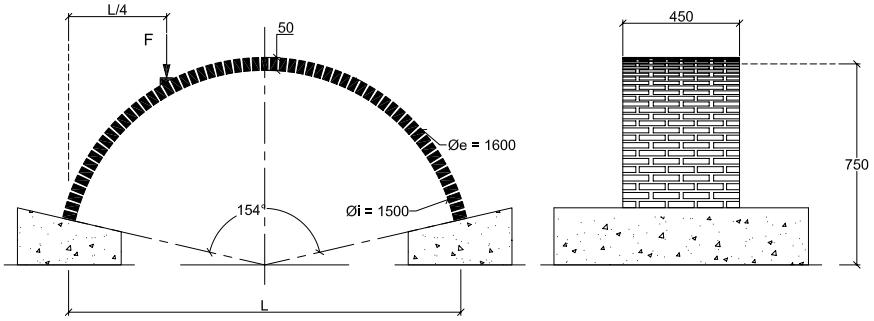


Figure 4.11: Arch geometry, dimensions in (mm).

4.5.1 Arch preparation

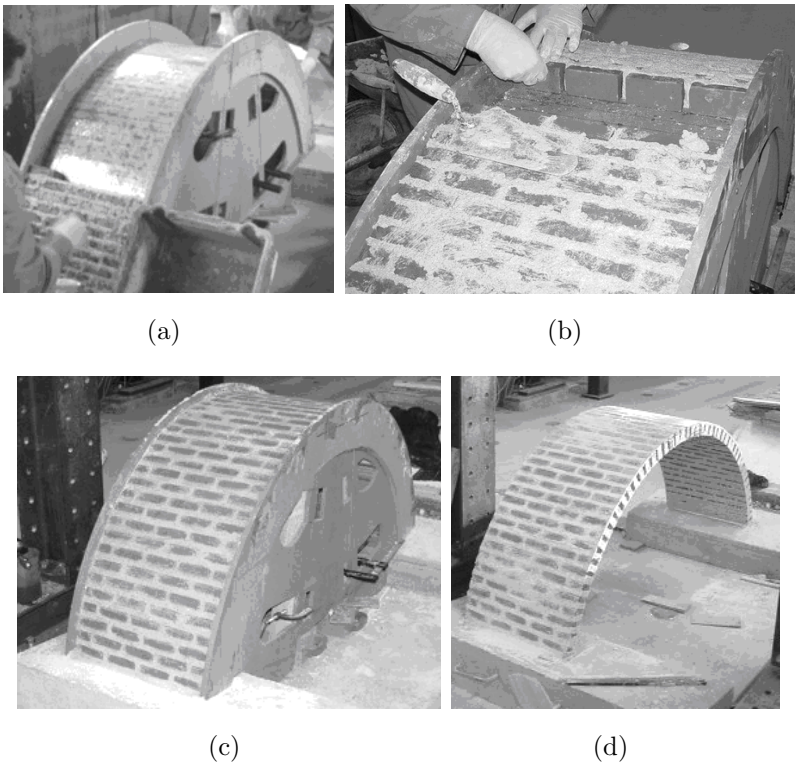
A series of twelve scaled semicircular masonry arches were built using the clay brick type 2 and the pre-mixed mortar, previously described. The mortar mentioned is defined as premixed mortar composed of sand, fibres and a hydraulic lime based binder.

All the arches were constructed with 59 brick courses and had a semicircular shape with a span of 1462 mm (with an internal diameter of $\theta_i = 1500$ mm). The single ring thickness was equal to the brick height, 50 mm, (thickness/span $\approx$ 1/30) Figure 4.11.

Estimate and design of masonry arches develop by Victorian-era engineers includes an empirical formula which estimates the arch crown thickness (y) in mm based on the arch span (S) in m, y=$\sqrt{2000S}$, (Depuit Segemental). A value of 54 mm was obtained, close enough to the adopted in the scaled masonry arches constructed which are illustrated in Figure 4.11.

The abutments were made of concrete cast over rectangular steel plates fixed to the reaction laboratory slab, Figure 4.12c. All the arches were constructed, over a wooden mould keeping a constant intrados mortar joint thickness of approximately 10 mm. The curvature shape was accomplished by increasing the thickness of the mortar joints towards the extrados. Thickness of bed joint did not exceed 16 mm according to the ACI 530.1-95/ASCE 6-95/TMS 602-95 (1995). Therefore the mortar thickness obtained falls into the range specified by the above mentioned guidelines.

The masonry arch construction was accomplished in two sequential phases, the first layer of bricks was laid over the formwork starting from both abutments



(a) (b)

(c) (d)

Figure 4.12: Different phases involved in the construction of masonry arches.

up to the quarter perimeter of the arch, as shown in Figure 4.12a. Thereafter following the same technique, remained courses were laid simultaneously from both ends such that the joint thickness could be tuned to obtain a full brick at the crown, Figure 4.12b. One week was considered as the minimum curing time to remove the mould, Figure 4.12c. All the arches were tested two weeks after construction, being the strengthened arches reinforced just after the removal of the mould, Figure 4.12d.

The specimen notation was divided into four main categories. This distribution followed the chronological testing sequence in each series, starting with plain masonry arches without strengthening until strengthening arches with additional devices to avoid FRP detachment, so the adopted general classification is as follows:

- Unstrengthened arches, US-n
- Localized strengthening on unstrengthened tested arches, LS-n
- Continuous strengthening at the extrados, CSE-n and

- Continuous strengthening at the intrados, CSI-n .

Table 4.3 Summary of tests carried out.

Masonry arches tested	Specimen
1. Unstrengthened arches, US-*n*,	US-*1*, US-*2*
2. Localized strengthening in damaged arches, simultaneously at the intrados and the extrados, LS-*n*,	
• 2 ×80 mm width GFRP strips	LS-*1*, LS-*2*
3. Continuous strengthening at the extrados, CSE-*n*,	
• 2 ×50 mm width GFRP strips • 2 ×80 mm width GFRP strips	CSE-*1*, CSE-*2* CSE-*3*, CSE-*4*
4. Continuous strengthening at the intrados, CSI-*n*	
• 2 ×50 mm width GFRP strips without anchor • 2 ×50 mm width GFRP strips with anchorages devices	CSI-*1*, CSI-*2* CSI-*3*, CSI-*4*
TOTAL	12

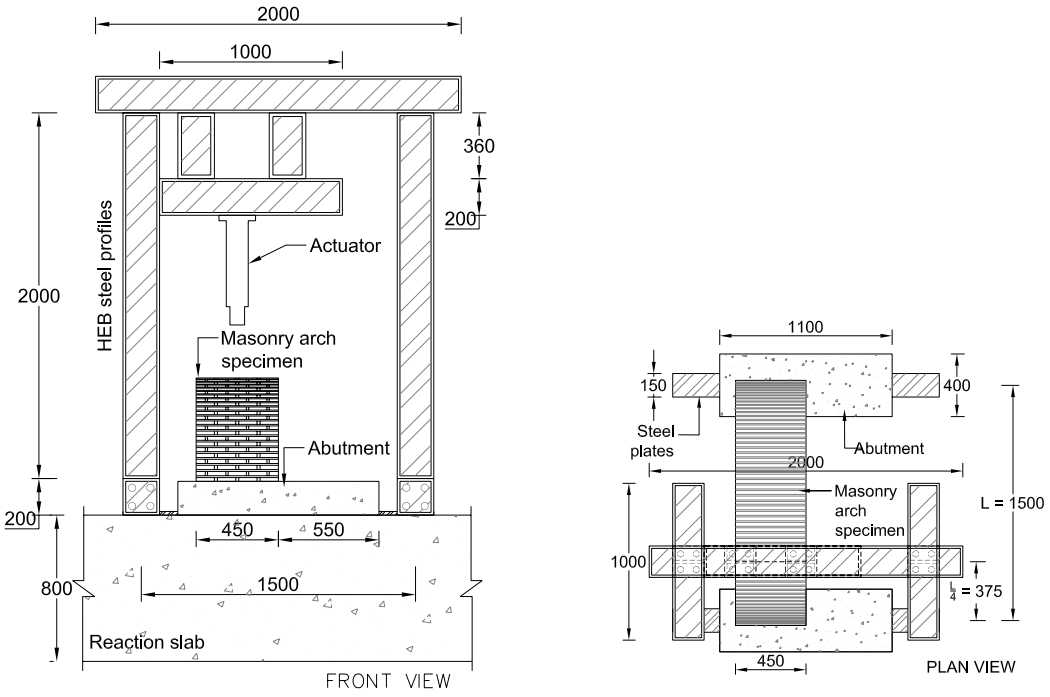
Note: the letter *n* stands for the sequential number of the specimen.

A detailed description of masonry arches tests is presented in Table 4.3, which includes the width of strips applied as well as the total number of tests.

4.5.2 Test setup and test procedure

All masonry arches specimens were tested by means of a servo-controlled actuator equipped with a 25 kN cell capacity, positioned at the middle of the arch width to reach an uniform transversal loading Figure 4.13. The load was applied at the quarter span, as shown in Figure 4.14. On the loading application point, the simulation of a hinge was obtained with a semi-circular piece of steel, free to rotate. To distribute the load along the width, a triangular bar made of wood glued to the curved masonry surface was used as a platform to lay a rectangular rigid steel

bar, centrally placed under the loading point. This member guarantees a uniform loading due to its high stiffness.



(a) (b)

Figure 4.13: Layout of the arch test setup, dimensions in mm: (a) front view; (b) plan view.

The arch deformation was captured with a data acquisition equipment composed of six linear variable displacement transducers (lvdt's) fixed at relevant locations to record the deformation. The first couple of lvdt's were placed at the quarter span of the arch, lvdt-1 controlled the vertical jack movement and lvdt-2 measured the vertical deformation at the application loading point. Lvdt-3 was also positioned vertically at the quarter span, but symmetrically to the loading point, Figure 4.14. Lvdt-4 was fixed vertically at the middle of the arch width and span. Finally, lvdt-5 and lvdt-6 were placed horizontally at the arch springing.

All tests were controlled by an imposed monotonic displacement at a rate of 3 μm/s. The total test duration varied between 30 minutes up to 4 hours for unstrengthened and strengthened arches, respectively. An acquisition frequency of 5 Hz was considered enough to capture the development of hinges together with the complete post-peak behaviour.

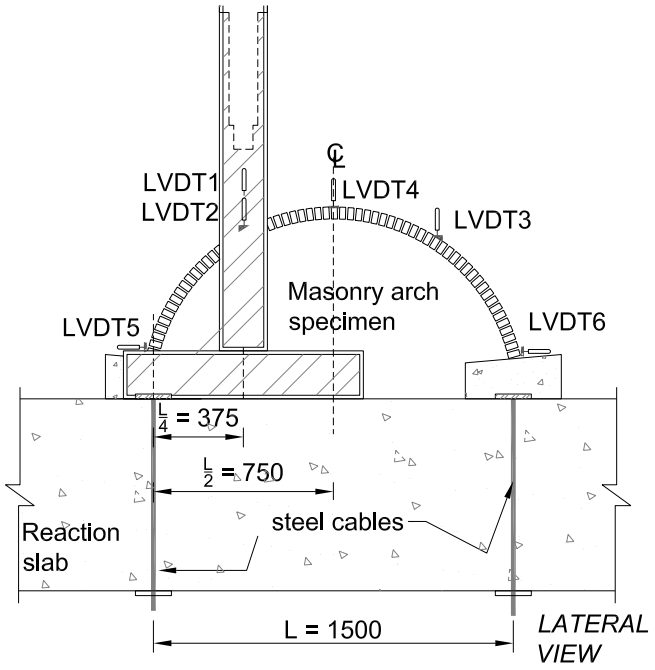


Figure 4.14: Instrumentation for the test specimen.

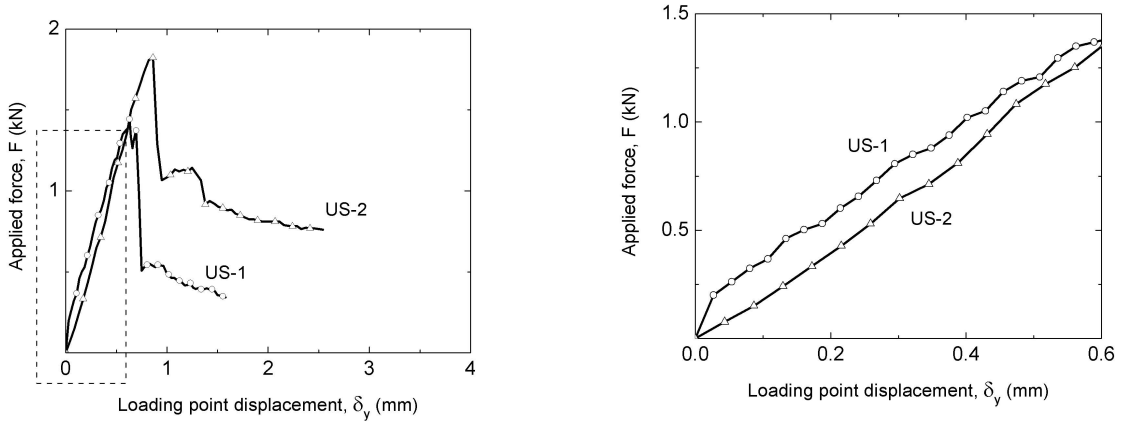
During the tests, a visual inspection of the arch was continuously performed to register the possible opening and cracking of mortar joints as well as strips detachment, hinges location and failure pattern. Negligible horizontal displacements were recorded at the springers in all tests. The subsequent sections deal with the tests results of experimental scaled masonry arches gathered from the data acquisition system. Description and comparison between unstrengthened and strengthened arches are discussed in detail. Deformed shapes and collapse mechanisms are illustrated according to the cracking and joint opening sequence, which occurred in all the arches series.

4.5.3 Unstrengthened arches

Figure 4.15 illustrates the vertical load applied *versus* displacement measured at the quarter span, for the two unstrengthened arches, measured with lvdt-2 specified in Figure 4.14.

Despite the fact that both plain arches, US-1 and US-2, kept similar stiffness until peak load, US-1 presented less deformation than US-2. A zoom of the squared

dashed line in Figure 4.15a is shown in Figure 4.15b, demonstrating similar initial stiffness trend for both arches. After the peak load was reached, a sudden load decrease followed by a rapid displacement increase, due to the low fracture energy of masonry joints was observed.



(a) (b)

Figure 4.15: Vertical load-displacement diagram measured at load point for plain arches US-1 and US-2: (a) complete recorded path; (b) zoom from the squared dashed line.

Failure mechanisms: unstrengthened deformed shape

The behaviour of semicircular shaped structures subjected to a concentrate loaded point applied at quarter span is shown in Figure 4.16, which contains the deformed shape with images from the test in-situ, localization and the sequence of hinges indicated by an associated number to the extrados or intrados according to the upper or lower appearance position. All hinges detected and reported here were based on visual inspection and some of them were difficult to detect at the very beginning.

Both unstrengthened arches US1 and US2 presented a similar structural behaviour, essentially characterized by the formation of the classical four-hinge failure mechanism.

By means of the hinge appearance and sequence location, it is possible to follow and distinguish movement from the original configuration up to failure. Figure 4.16 presents the above mentioned description, where the first hinge appears

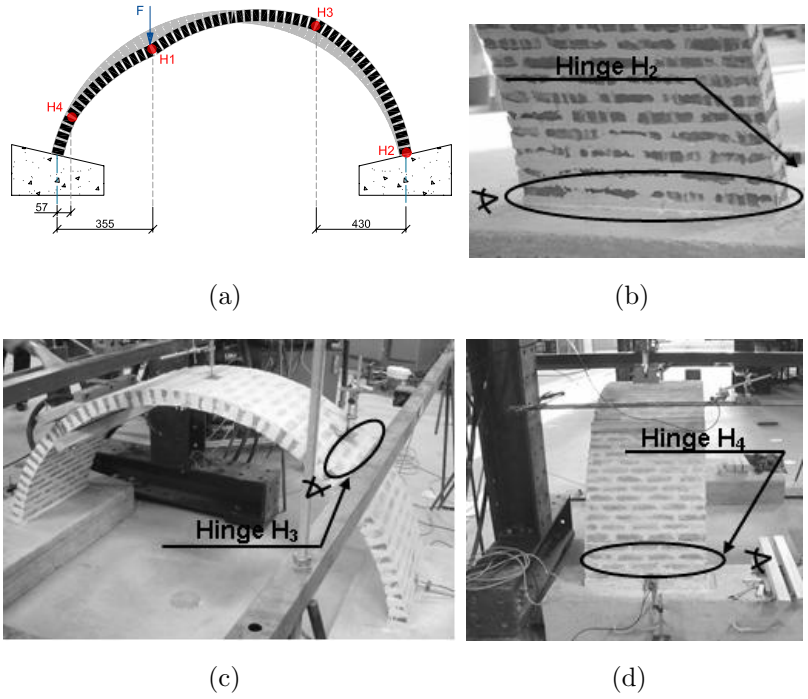


Figure 4.16: Deformed shape and localization of hinges for unstrengthened arches.

right below the application load point (H_1). Afterwards, a second hinge continues with the deformed shape at the right arch springing (H_2), Figure 4.16b. In a subsequent stage, almost at a symmetric location of the loaded point, another hinge develops at the extrados (H_3), Figure 4.16c and finally, close to the left arch springing, hinge (H_4) develops at the extrados and complements the failure mechanism, Figure 4.16d.

4.5.4 Strengthened arches

Three main strengthening strategies were tested in this work. After being tested, plain arches were strengthened locally, aiming at repairing the plastic hinges developed during testing. This strategy emphasizes a real situation when a damaged structure requires structural intervention. The other two strategies are concerned with continuous strengthening, either at the extrados or at the intrados of the arches.

The results are looked at in terms of stiffness variation, ductility, deformed shapes, maximum loads, displacement at loading point and changes of failure pat-

terns, as well as the performance of anchorage devices.

The tests performed in semicircular strengthened masonry arches, damaged and non-damaged, had different strengthening configurations applied over internal and external masonry substrate as outlined in Figure 4.17. For each configuration, two specimens were prepared and tested.

GFRP application on masonry arches

The external application process of GFRP began one week after the construction of masonry arches. The application of the strengthening was rigorously performed in agreement with the manufacturer suggestions, respecting minimum curing times for the composite components and the sequence layers. Mechanical characterization of each component may be found in chapter 3.

The composite material chosen for application was GFRP rolled sheet G-AR 90/10 MBT (1 layer of 500 mm width roll) bonded with MBrace Saturant Adhesive.

The condition of the masonry arches surfaces was generally unacceptable, with an excess of mortar at the intrados. It was noticed that the joint material was not soft enough for the wire brush to remove easily excessive material. Therefore, arches surfaces were cleaned using sandpaper adapted to an electrical driller to smooth the surface and to remove all dust from the first composite component (putty), shown in Figure 4.18a. Afterwards, a thin putty layer was applied on the cleaned surface, as shown in Figure 4.18b, waiting the minimum curing time (approximately 2 hours) to subsequently prime the arch surface using MBrace Primer (1 coating) rollered onto the surface and left to become tacky (approximately 2 hours). Figure 4.18c shows the primed area.

Subsequently MBrace Saturant Adhesive was applied to the tacky substrate with a roller (approximately 200–300 microns). The single layer of glass fibre (90/10 weave) was carefully applied into the adhesive using plastic tools and a hard plastic roller to remove as many air bubbles as possible. It was noted that several air bubbles were impossible to remove due to the profile of joints and bricks.

Finally a second layer of bonding adhesive was applied and worked into the substrate, with a roller. The finished surface with glass fibre reinforcement is shown in Figure 4.18d.

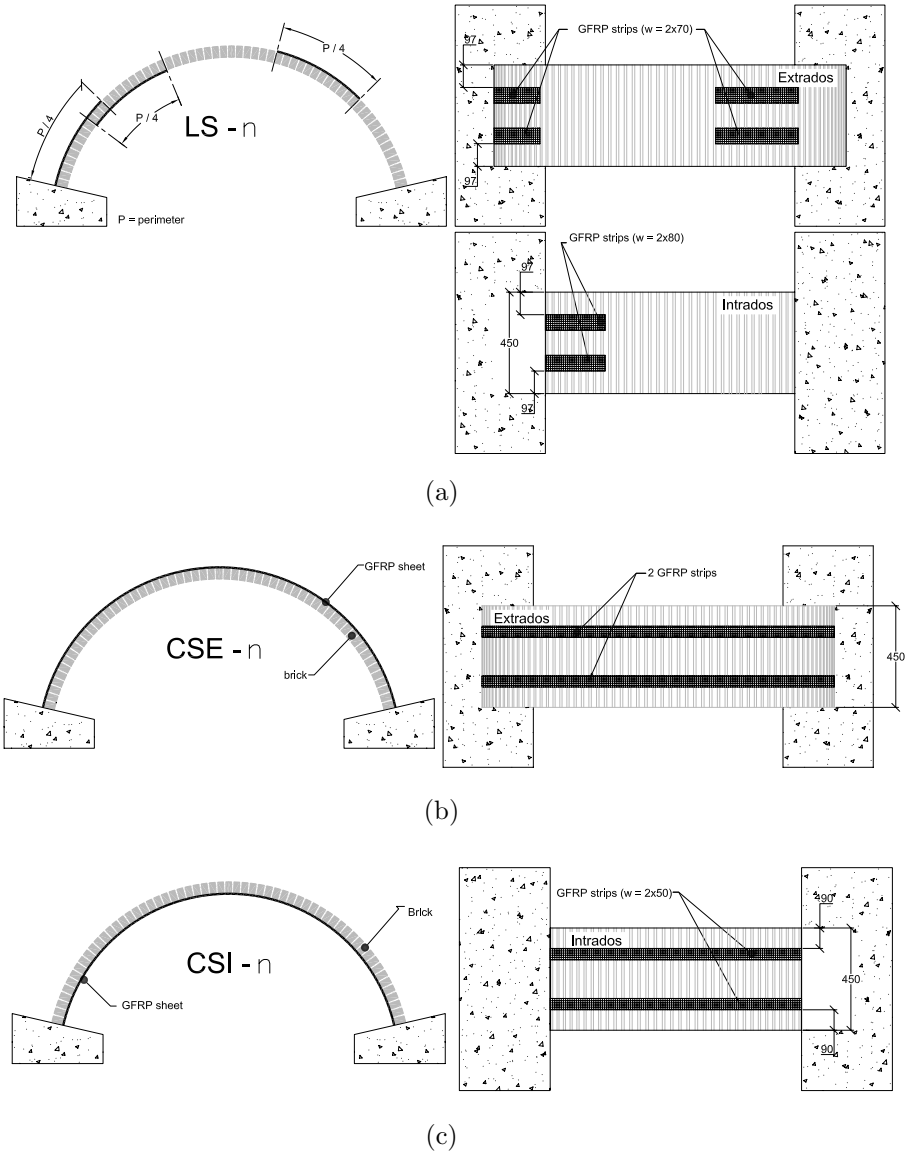
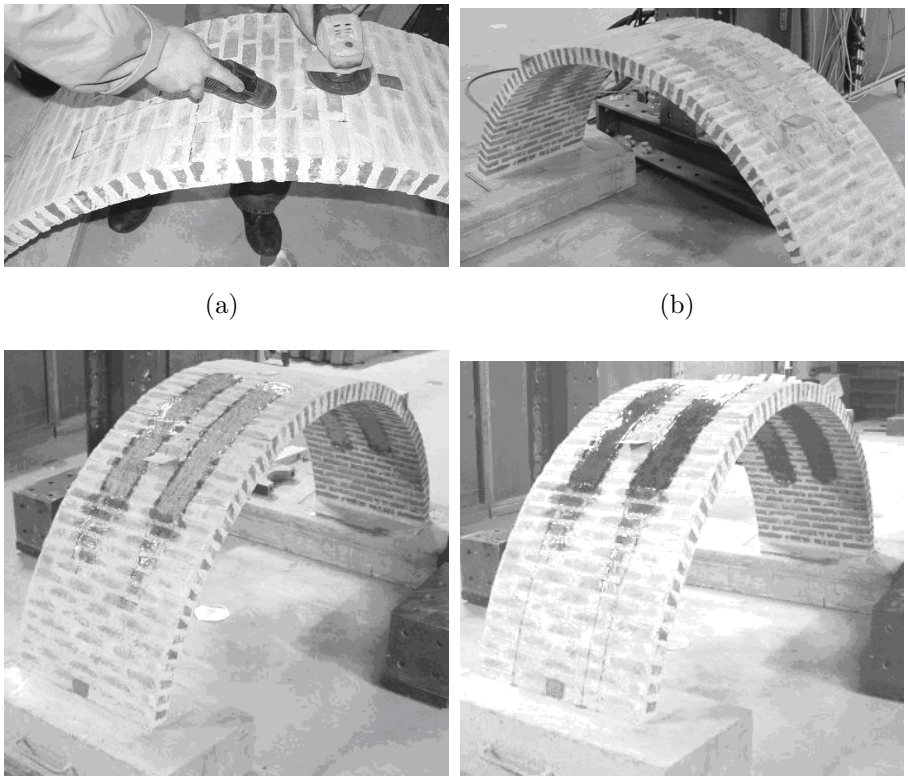


Figure 4.17: Strengthening masonry strategies: (a) Localized strengthening in damaged arches (arches US-n strengthened with two 80 mm GFRP width strips after being initially tested); (b) Continuously strengthening at the extrados with two 50 mm GFRP width strips and two 80 mm GFRP width strips and (c) Continuously strengthening at the intrados with two 50 mm GFRP width strips anchored to the substract by means of different anchorage devices.

Locally strengthened arches

The damage on the plain arches was not recovered by the local strengthening. Strengthening did not change the pre-peak stiffness or the fragile behaviour of



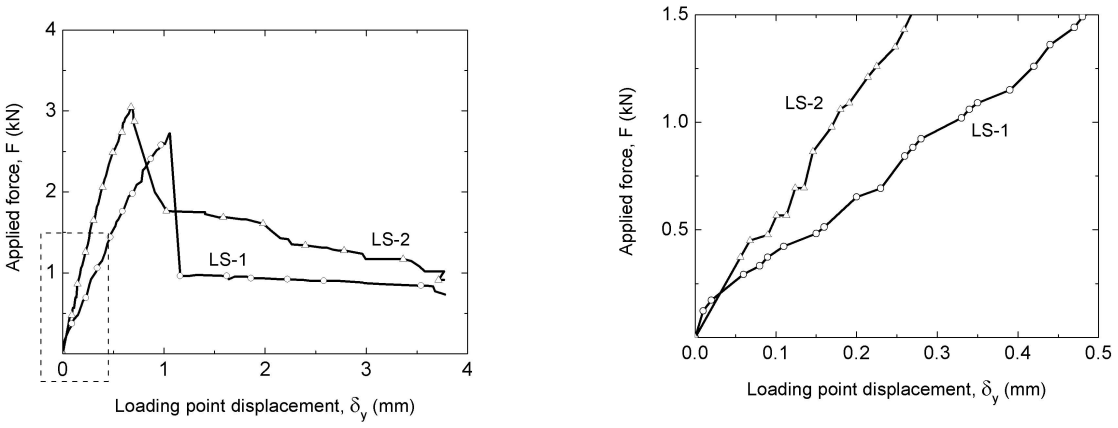
(a) (b)

(c) (d)

Figure 4.18: Strengthening procedure: (a) polishing surface; (b) putty impregnation over the prepared area; (c) primer applied and (d) final stage of strengthened masonry arch.

the unstrengthened specimens. However, besides a load capacity increase, also a slightly larger post-peak branch was possible to obtain, Figure 4.19.

Strengthened arches LS-1 and LS-2 achieved a load carrying capacity increase of 122% and 42% when compared to unstrengthened arches US-1 and US-2, respectively. The average increase is in the order of 76%.

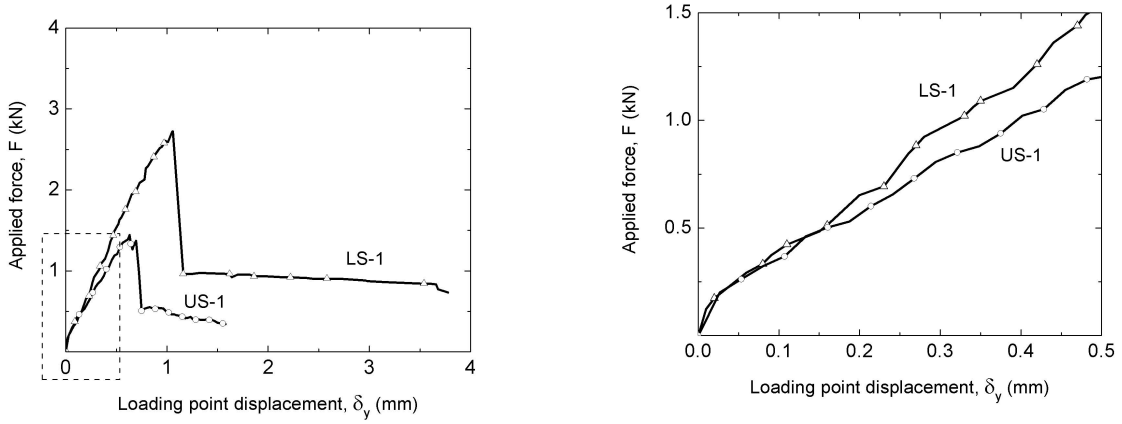


(a) (b)

Figure 4.19: Vertical load-displacement diagrams measured at load point for localized strengthening applied to arches, LS-1 and LS-2: (a) complete diagram; (b) initial behaviour.

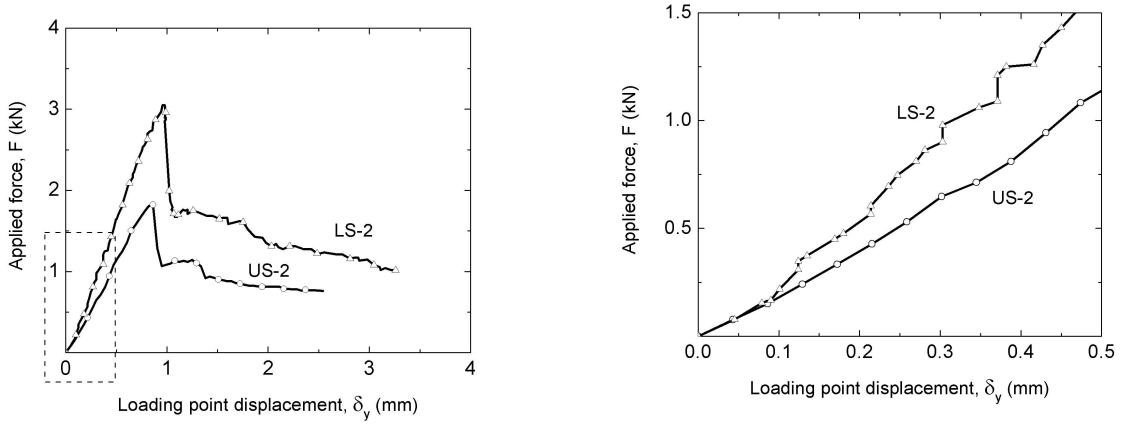
Collapse mechanism of locally reinforcement arches

Localized strengthening over the affected zones (at the intrados and extrados) modifies the original unstrengthened collapse mechanism above mentioned, moving three of the original hinges (H_1, H_3 and H_4, in Figure 4.16) and originating their re-opening at the end of the composite, Figure 4.22. The reinforced courses behaved as a rigid body. This type of strengthening may be particularly considered as undesirable because initial fragile behaviour could not be changed. Figure 4.22a depicts the typical deformed shapes for LS arches and subsequent images, Figure 4.22b and 4.22c, show the plastic hinges developed and lifting support. In fact, the GFRP strips used were able to prevent the re-opening of the existent cracks but new hinges appeared beyond the strip length instead, as shown in Figure 4.22.



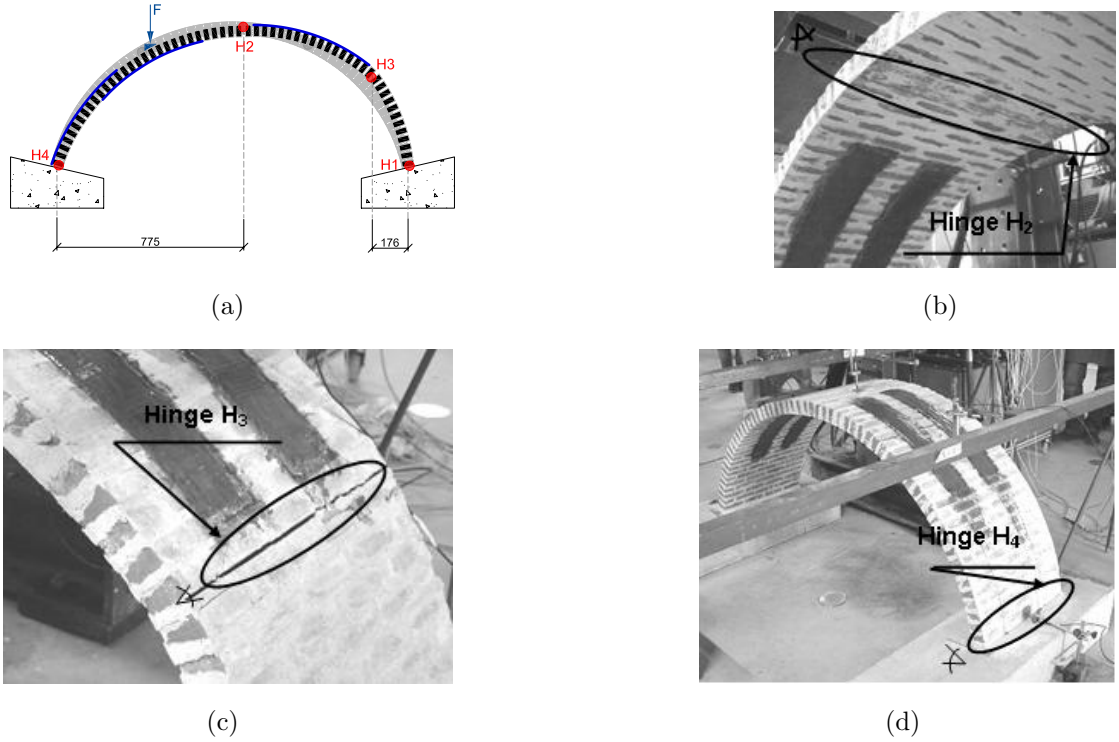
(a) (b)

Figure 4.20: Vertical load-displacement diagrams measured at load point: (a) arch US-1 before and after strengthening LS-1; (b) zoom of the initial stiffness.



(a) (b)

Figure 4.21: Vertical load-displacement diagrams measured at load point: (a) arch US-2 before and after strengthening LS-2; (b) zoom of the initial stiffness.



(a) (b)

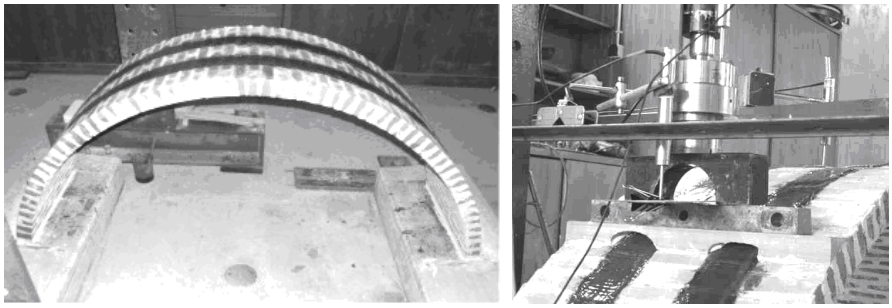
(c) (d)

Figure 4.22: Mechanism of failure of the locally strengthened arches: (a) deformed shape; (b) hinge at the intrados; (c) hinges at extrados and (d) general view.

Continuously strengthened arches at the extrados

Within this set, four arches were subjected to a similar FRP application process, but applied at the extrados and without previous damage induced to the arch, Figure 4.23a. For this external continuous reinforcement, the test setup configuration had the smallest variations at the application load zone, where the glued piece of wood was shortened to let the strip pass freely, as shown in Figure 4.23b.

For the arches strengthened with continuous strips, a different collapse mechanism was expected since the presence of the fibres would prevent the fourth plastic hinge to occur. Besides a considerable peak load increment (89% on average), no significant changes in stiffness occurred when compared with the unstrengthened arches.



(a) (b)

Figure 4.23: (a) Overview of the final stage of strengthened masonry arches at the extrados; (b) details of instrumentation at load application.

For the first pair of strengthened arches at the extrados CSE-1 and CSE-2 (2 strips of GFRP with 50 mm width), an improved ductility was obtained when compared to the unstrengthened ones. The global load-displacement curves are included in Figure 4.24.

The lower stiffness in this case is likely to be related with previous damage caused to specimen CSE-1 during its curing or mould removal, or even owing to a faulty application of the GFRP strengthening. This feature causes an important decrease in the maximum load achieved also in this case. Still the maximum load capacity was achieved for a displacement approximately twice the one corresponding to US specimens. A very important feature is the long post-peak branch recorded, which provides the structure with important ductility behaviour. In fact,

the displacement measured at ultimate stage is about 20 times greater than the corresponding one measured in specimens CSI-1 and CSI-2.

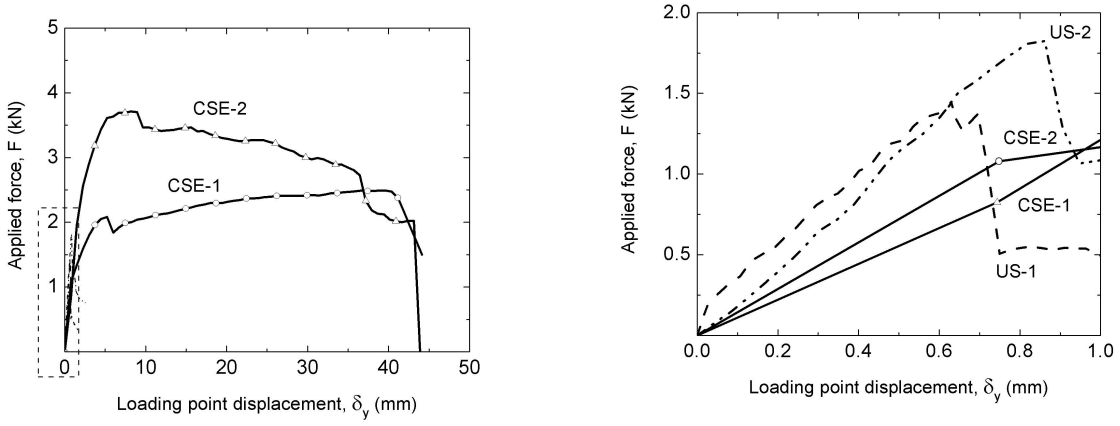


Figure 4.24: (a) Load-displacement diagrams for the continuous strengthened arches at the extrados with 100 mm width strip reinforcement. The responses of the unstrengthened specimens are represented by dashed lines; (b) a zoom of initial loading.

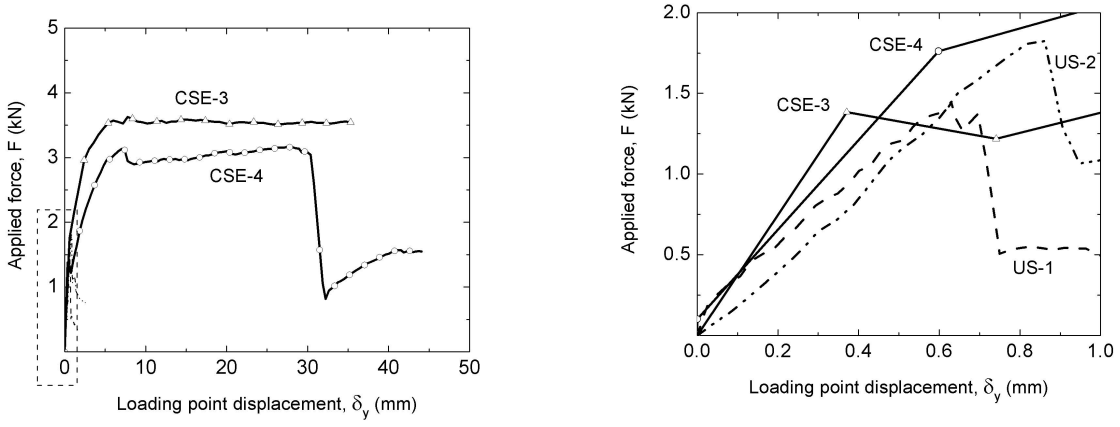


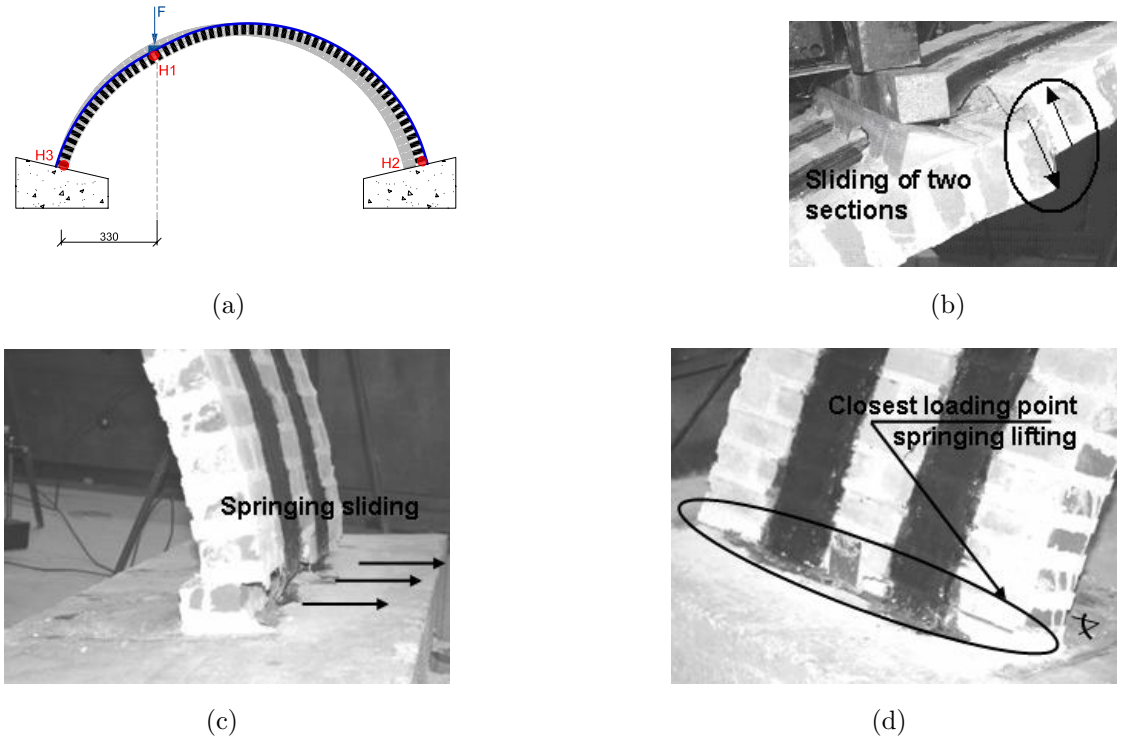
Figure 4.25: (a) Load-displacement diagrams for the continuous strengthened arches at the extrados with 160 mm width strip reinforcement. The responses of the unstrengthened specimens are represented by dashed lines; (b) zoom of initial loading.

The second pair of strengthened arches at the extrados CSE-3 and CSE-4 (2 strips of GFRP with 80 mm width) shows again a considerable increase in ductility, even if no strength increase is obtained (if specimen CSE-1 is discarded), Figure 4.25. In this case, the initial stiffness of the specimens is slightly higher than the unstrengthened specimens and, again scatter of the maximum applied load is reduced by the strengthening process.

Collapse mechanisms of arches strengthened at the extrados

According to the behaviour and failure mechanism theory, continuous strengthened arches sustaining tensile stresses (particularly strengthened with FRP), transform plain arches into a three hinge isostatic structure consisting of two curved beams strengthened at its reinforced side respectively.

Within this CSE set, the first "hinge" was formed underneath the loading point, Figure 4.26, whereas the other two "hinges" appeared at the springers. It is noted that the term "hinge" is here used generically as it includes shear mechanism or releases.



(a) (b)

(c) (d)

Figure 4.26: Failure mechanisms of continuous external strengthened arches.

For specimens CSE, failure was mostly characterized by sliding of the joint located close to the right support, Figure 4.26c, and was due to insufficient shear resistance.

This type of strengthening does not allow joint opening at the extrados, *e.g.* at the location opposite to the load application. On this zone, cracking along the mortar joints started to propagate and kept spreading to the arch support where sliding occurred. Specimens with wider reinforcement strips at the extrados diminished cracking width but did not change crack and collapse patterns.

Continuously strengthened arches at the intrados

Considering that the collapse mode expected for arches CSI should be characterized by the detachment of GFRP strips, and previous numerical results indicated that an increase of GFRP strip width seems not to be profitable, it was decided to use only two GFRP strips of 50 mm for the first pair of tests, CSI-1 and CSI-2.



(a) (b)

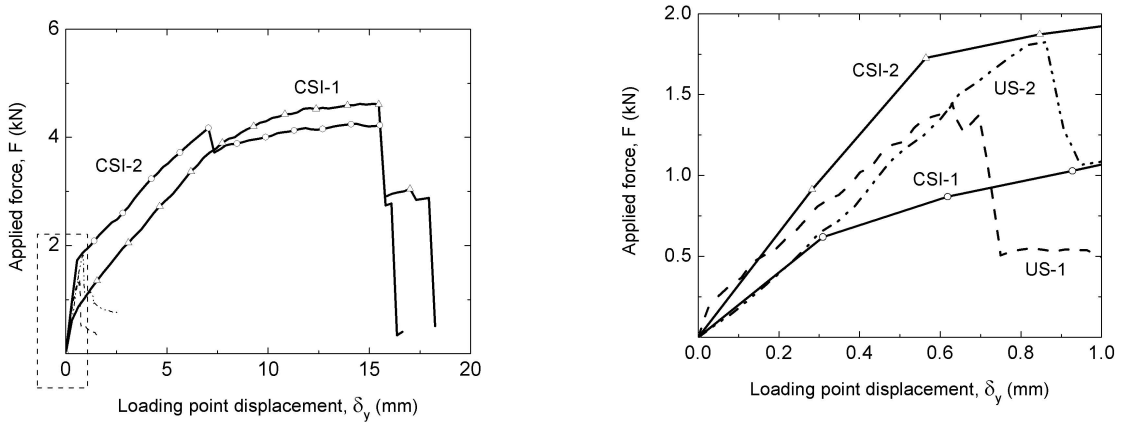
Figure 4.27: (a) Preparation of the non-conventional anchorage devices, threads inserted and bend at the intrados; (b) the same procedure was performed at the extrados.

For the second pair of tests inside the CSI series, specifically the CSI-3 and CSI-4, non-conventional anchorage devices were manually fabricated and applied to prevent FRP detachment. For those specimens, four handmade spikes threads soaked into resin and inserted into 6 mm diameter holes previously perforated in the bricks were anchored in each strip, Figure 4.27a. The fibres length of the spikes were bigger than the ring thickness. Once the spikes were placed inside the

brick the remained fibres were spreaded in radial way capturing the FRP strip reinforcement.

Spikes were applied in both FRP strips in each four course. The total inner perimeter cover by the spikes was symmetrically located under the load application point. Spikes devices had the main target to avoid strip detachment from the masonry inner surface detected in CSI-1 and CSI-2 as failure mode. General view of the finished surface is displayed in Figure 4.27b. A similar anchorage technique has been used for concrete and it can be found in the CEB-FIB (1993).

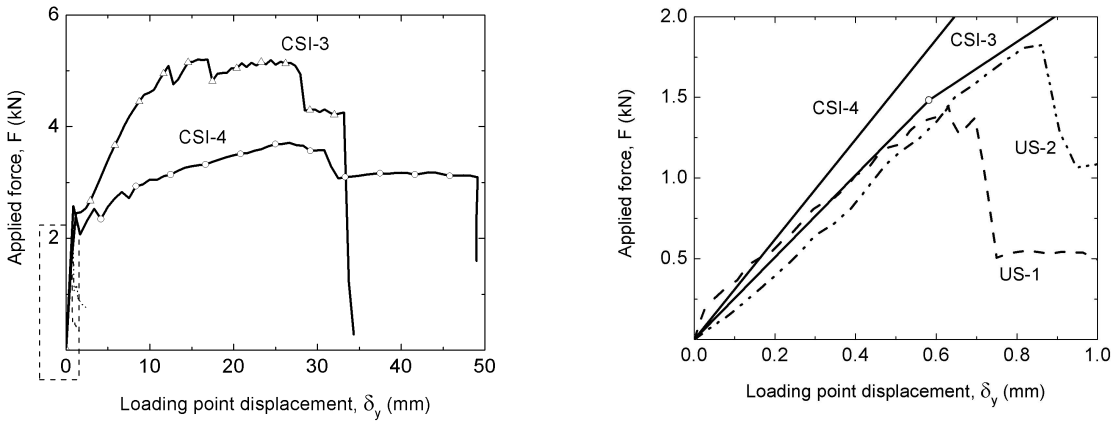
For the arches CSI-1 and CSI-2 the load capacity was increased about 165% on average, and the maximum load was achieved for a displacement about 35 times greater than the one corresponding to the unstrengthened specimens. While a significant ductility increase was found when compared with unstrengthened arches, the response is more brittle than the CSE series. Experimental results of the CSI series are shown in Figure 4.28 and 4.29. Again, for low loads a comparable stiffness compared with unstrengthened arches is displayed, with or without non-conventional anchoring devices.



(a) (b)

Figure 4.28: (a) Load-displacement diagrams for strengthened arches at the intrados with 100 mm strips width; (b) the zoom of initial loading.

Despite the occurrence of the first hinge for different load values, both CSI-1 and CSI-2 specimens presented a similar behaviour. The abrupt drops in load observed in Figure 4.28 are due to the detachment of the GFRP strips under the load application. This means that failure, which occurred for high deformations,



(a) (b)

Figure 4.29: (a) Load-displacement diagrams for strengthened arches at the intrados with 100 mm strips width along with spikes; (b) an initial zoom of the loading.

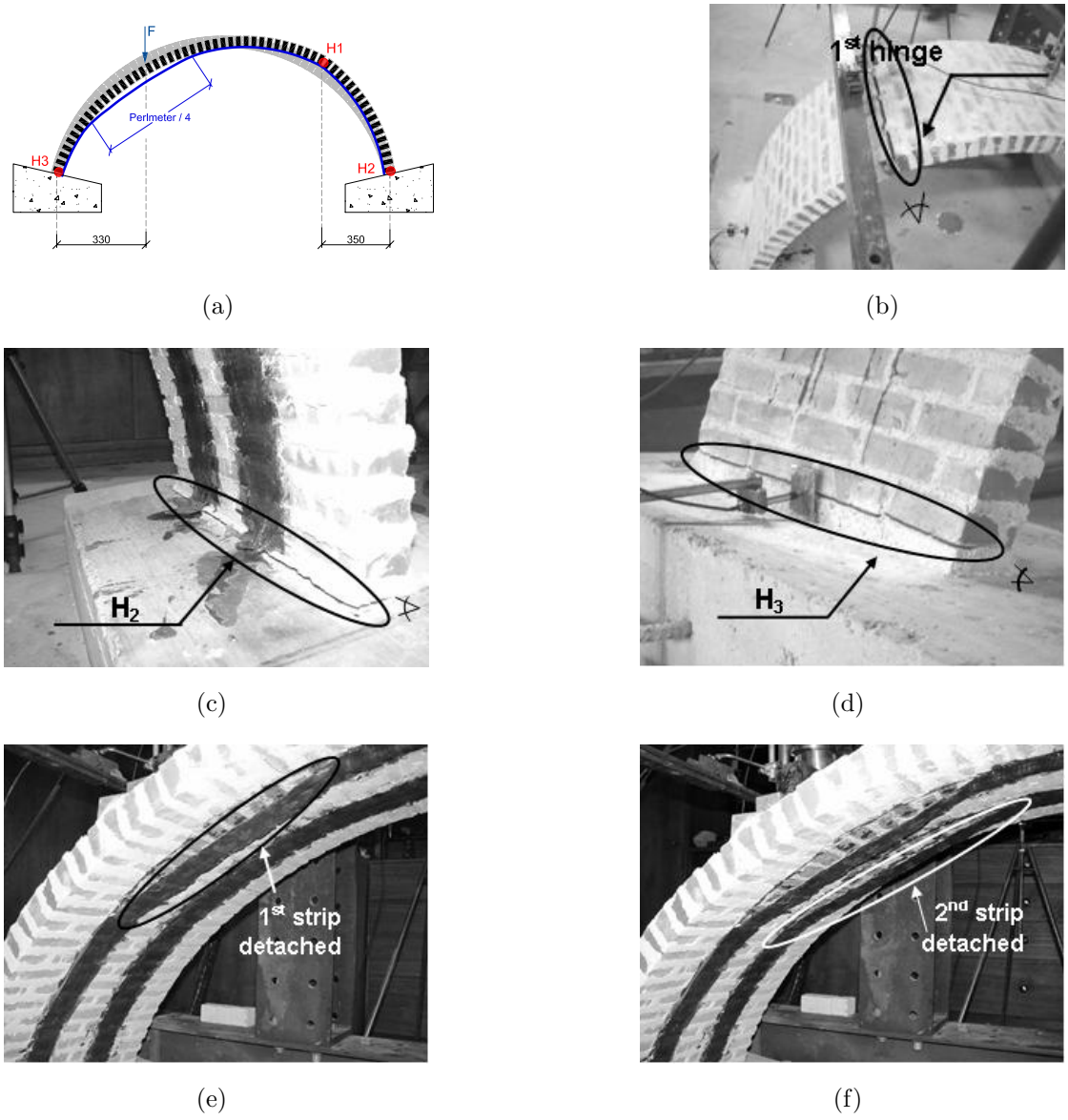
was dictated by the successive detachment of the two reinforcement strips, caused by the ripping of a thin layer of brick, Figure 4.30.

For the non-conventional anchorage scheme, specimens CSI-3 and CSI-4 demonstrated how ductile and stable the arch became using the same glass strip width, by adding a simple thread anchor device, Figure 4.29. In terms of sustained peak load and ductility, this series of arches confirmed enhanced properties of all series. Among reinforced masonry arches at the intrados, the use of spikes doubled the deformation capacity.

Collapse mechanisms of arches strengthened at the intrados

For the continuous strengthened specimens at intrados, the mechanism observed is illustrated in Figure 4.30. Two of the hinges were formed at the supports and the third one appeared symmetrically to the load application point, Figure 4.30. The fibres maintained equilibrium until their total detachment was observed, which provide a fourth "release".

All strengthened arches at the intrados had similar deformed configurations. Anchorage devices systems integrated in the second pair (CSE-3 and CSE-4) delayed the FRP strip detachment but did not change the failure mechanism. Moreover, there were two types of identified failures for the anchor devices: tensile



(a) (b)

(c) (d)

(e) (f)

Figure 4.30: Deformed shape and failure mechanism mode for the CSI series

and break failure together with the FRP strip as seen in Figure 4.30c and 4.30d. Hinges H_3 and H_2 at the springers were almost imperceptible at the intrados and extrados, as shown in Figure 4.30e and 4.30f.

4.5.5 Summary of experimental test results

A summary of semicircular scaled masonry arch results is presented in Table 4.4, including arch identification, reinforcement location, when applied, localized, at the extrados or at the intrados, final GFRP strip width applied, maximum load and average load per series and increase in resistance when compared with unstrengthened arches.

A significant increase of the load carrying capacity was evident for the strengthened series when compared with unstrengthened arches, although continuous strengthened arches reach the highest values.

Table 4.4: Summary of masonry arches results.

Specimen	GFRP strip width, w (mm)		Anchorage device	Force, F (kN)		Resistance increase
	Intra	Extra		Max	Average	(%)
US-1	-	-	-	1.43	1.68	-
US-2	-	-	-	1.92		-
LS-1	150.0		-	3.18	2.96	76
LS-2	150.0		-	2.73		
CSE-1	-	100.0	-	2.51	3.17	89
CSE-2	-	100.0	-	3.82		
CSE-3	-	160.0	-	3.62	3.44	105
CSE-4	-	160.0	-	3.26		
CSI-1	100.0	-	-	4.26	4.45	165
CSI-2	100.0	-	-	4.63		
CSI-3	100.0	-	×	5.41	4.61	174
CSI-4	100.0	-	×	3.81		

The biggest increment in strength was obtained by the intrados strengthening option with non conventional anchor systems, which also provided higher ductility when compared with the extrados and unstrengthened selection.

It is noted that workmanship seems to considerably affect the results and the results from from CSE-1 and CSE-4 are abnormally low, when compared to the other test of series.

Application of composite materials presented in a previous work (Valluzzi et al. 2001) showed larger increments of ductility for the extrados alternative when compared with the intrados application utilizing the same width FRP strip. The results obtained in this thesis confirm this remark when the CSE-1 and CSE-2 series are compared with the CSI-1 and CSI-2 series.

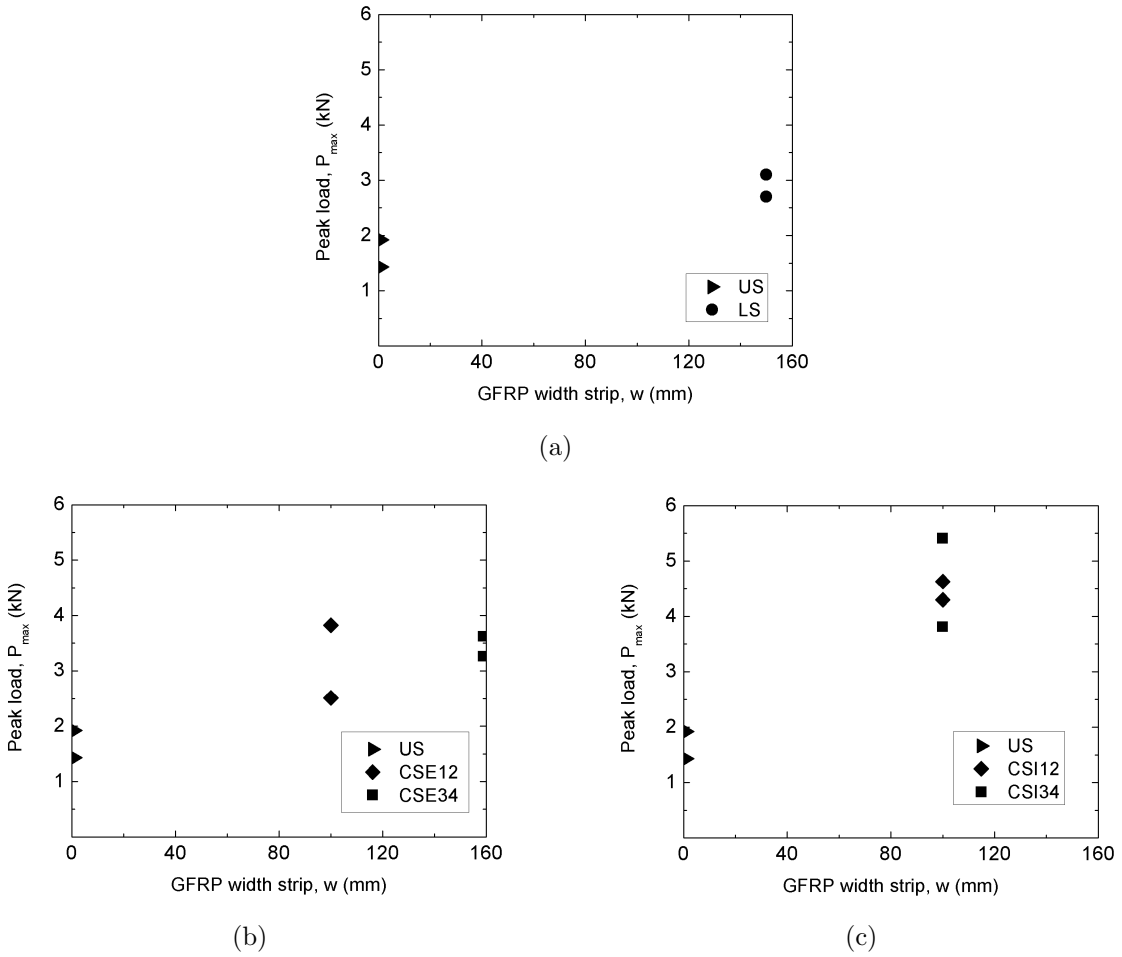


Figure 4.31: Influence of the FRP width on the load carrying capacity of the arches reinforced: (a) locally; (b) at the extrados and (c) the intrados.

A graphical representation is depicted in Figure 4.31, where the GFRP influence, as a reinforcement material on masonry arches with semicircular shape, is

exemplified. Such schemes include strip width increment *versus* maximum reached load.

Extreme care must be taken when FRP reinforcement is used. The same amount of material, but properly anchored, can lead not only to a higher peak load but also to a more significant deformability. Increasing the GFRP strip width for the CSE series kept the maximum load sustained anchoraged and provided no additional ductility Figure 4.31b. Considering the discussion on arch CSE1 given above, the results of the two sets (CSE-1,CSE-2 and CSE-3,CSE-4) can be considered similar to each other. This means that, for the FRP width and the strengthening arrangement, probably the amount of reinforcement used in the first set (arches CSE-1 and CSE-2) was enough, therefore, the use of additional strengthening material does not necessarily imply significant improvements on the structural behaviour, in terms of strength or failure modes (Basilio et al. 2005).

A desirable and optimal point location in Figure 4.31 would provide minimum width strip reinforcement and maximum reached load, without making the structure fragile. Even if the number of experimental tests is limited, intrados reinforcement with spikes seems the most appropriate solution if possible to apply in a real case study.

4.6 Conclusions

In this chapter the mechanical characterization of bricks and masonry used in the arches is detailed. Initial testing of two unstrengthened masonry arches served as the reference series where the influence of the reinforcement using fibre reinforced polymers was demonstrated. Plain arched structures were characterized by a fragile behaviour and a collapse mechanism consisting of four hinges.

Although localized strengthening for masonry arches was applied to damage arches closer to a real case study, it is also a debatable alternative since hinges originally developed on unstrengthened arches, appear once again moving to the end of the reinforcement influence area. This option must be considered carefully because a more fragile mechanism may be reached provoking an unexpected abrupt failure. Although localized strengthening arches were not tested at the same age (curing period time) than the rest, the author strongly believes that such strengthening option is hardly recommended.

Stitching the hinges with localized reinforcement did not recover the damage applied to plain arches but increased the peak load, maintaining the fragile stage characterized by the sudden drop in the load carrying capacity and insignificant residual value.

As mentioned before, all strengthening arrangements adopted in this study were able to increase the load capacity when compared with plain arches. However, while the intrados strengthening allows for the maximum load increase, the extrados strengthening provides higher ductility. Intrados strengthening can also provide very high ductility if non conventional anchoring devices are added to the same structure.

The tests with extrados strengthening indicate that the amount of reinforcement must carefully selected, as high amount of reinforcement do not necessarily increase failure load.

The debonding phenomenon only affected the arches with GFRP strips applied at intrados, whereas for specimens strengthened at extrados failure occurred due to slipping of the mortar joint at the arch support. Another important feature of the continuously strengthened specimens is the large deformation capacity exhibited prior to failure, which provides the arches with an important ductility behaviour.

Based on the results obtained, it was observed that strengthening of structures with composite materials, changes its potential damageability modifying failure mechanism and scattered response.

Experimental deformed shapes for strengthened arches were obtained similarly to the theoretical failures modes. The results can be used as guidance on structural understanding and strengthening design for more complex configurations.

Chapter 5

Numerical modelling of bond tests

The representation of physical phenomena can be accomplished in several ways *e.g.*, mathematically, graphically, experimentally, etc. The use of numerical models becomes a reliable solution when an interpretation of real situations is sought. There are several approaches that take into account material nonlinearities but a very common numerical technique applicable to problems with arbitrary geometry and boundary conditions is the finite element method (FEM).

A possible objective of the nonlinear FE analysis is to trace the response of a structural model subjected to a given loading history. This is usually done using an incremental-iterative procedure. The load is applied in several incremental steps and the structural response after each step is computed from the equilibrium equation:

$$f_{int} = f_{ext} \tag{5.1}$$

However, finite element simulations of complex engineering problems may diverge for a number of reasons, many of which are numerical and have nothing to do with the real structural failure.

Vaulted structures are usually considered as an ideal system of arches. Clearly, barrel vaults can be understood as a set of parallel arches, but also vaults of more complex shape can be generally outlined in a similar way, with a system of main arches that support secondary arches. It is noted that, in some cases, simplifications using ideal arched schemes lead to difficulties in justifying equilibrium,

especially when the loads are not uniformly distributed. Therefore, true 3D analysis and behaviour might be necessary for more complex cases (Lourenço et al. 2004).

Modelling of bond tests in this work is done resorting to a simplified 2D model. The reason for this relies on the fact that the use of fully three-dimensional models is usually a time consuming process when considering the time for the model-geometry preparation and to the time to perform the actual calculations, which can increase exponentially with mesh size and complexity.

The "bond test" term has been used for tests in which reinforcement and its interface need to be characterized. Usually the bond test is mentioned in the civil engineering literature with the notation given by Yao et al. (2005):

- Far end supported double shear test
- Near end supported double shear test
- Far end supported single shear test
- Near end supported single shear test
- Modified beam test
- Beam test

As presented in Chapter 3 the near end supported single shear test was adapted in this thesis as a masonry bond setup. In what follows, modelling of the different bond test lengths, shapes and materials is addressed.

Information concerning the structural behaviour of masonry structures strengthened with FRP materials is quite scarce, despite the fact that it is a key issue when dealing with strengthening of masonry constructions. Modelling of masonry interface behaviour has been extensively studied (Anthoine 1992; Lourenço 1994), but when dealing with reinforced masonry using FRP materials, only few studies are available in the literature (Bati et al. 2003; Ceroni et al. 2003; Aiello and Sciolti 2006).

The obtained numerical results were compared with the experimental envelope series selected at four different stresses levels, namely at 25, 50, 75 and 100% of the peak load. In addition to the numerical simulations, an analytical bond stress-slip formulation was developed at the end of the chapter, where analytical "ranges of variations" (designated as "envelopes" hereinafter) were superimposed with the numerical approach at local levels.

5.1 Structural model for the bond test

A model for the bond test specimens presented in chapter 3 was accomplished selecting continuum elements to model masonry bond specimens strengthened with FRP materials and interface elements for the FRP-masonry interface. All bond test specimen dimensions and shapes were reproduced from the experimental arrangements tested, except for the non-conventional anchorage types. Prismatic and curved shape geometries were adopted, according to the test carried out. Figures 5.1a and 5.1b illustrate the top and the side view of the models. The dotted line outlined in Figure 5.1b represents the area where the mesh was refined, to get accurate results. Hence, Figure 5.1c depicts a zoom of the area.

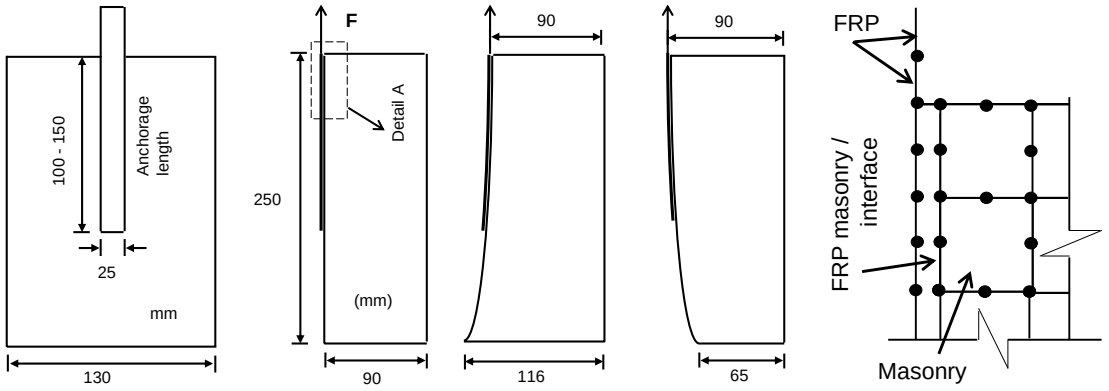


Figure 5.1: Adopted shapes for the numerical bond tests: (a) top view for all specimens; (b) side view of the rectangular, concave and convex shapes and (c) detail A of the modelling.

Numerical analyses were performed with the commercial finite element program DIANA (1999). The mesh adopted in the analyse included eight-noded plane stress elements to represent the masonry units, six-noded interface elements to simulate the FRP-masonry joints and three-node cable elements to represent the FRP, Figure 5.1c. Here, it is noted that a zero thickness interface is assumed for the joints. The whole specimen was modelled with 168 elements.

The approach followed here was based on the micro-modelling strategy, where the units behave in a linear fashion and the damage is concentrated in the relative weak joints. A composite interface model formulated within the framework of

plasticity, which includes a tension cut-off for mode I failure, the Coulomb friction envelope for mode II failure, and a cap mode for compressive failure, was considered to model the nonlinear behaviour of the joints, Lourenço and Rots (1997). Previous uses of this multisurface constitutive model to analyse strengthened masonry arches with FRP yielded satisfactory results, in terms of load-displacement curves and failure mechanisms, including peeling of FRP sheets from the masonry, see Lourenço and Martins (2001).

Simulation of the experimental procedure was reproduced enforcing a monotonic incremental displacement at the end of the FRP strip. Most of the properties used to simulate the FRP-masonry interfaces were obtained from experimental tests carried out during this investigation. For other parameters, mean values of previous works were taken from Valluzzi et al. (2001) and Lourenço and Martins (2001). The values adopted are included in Table 5.1 and 5.2, where elastic and inelastic properties can be found. Here, E is the Young's Modulus, ν is the poisson's ratio, k_n and k_s are the interface stiffness in the normal an tangential direction, respectively, f_t, is the tensile strength of the joint, G_f^I and G_f^{II} are the mode I and mode II fracture energy, c is the cohesion of the joint, ϕ and ψ are the friction and dilatancy angles respectively, f_m is the compressive strength, c_s is the parameter which controls the contribution of the shear traction to compressive failure via the elliptical cap, G_{fc} is the compressive fracture energy and κ_p is the plastic relative displacement corresponding to the peak stress.

Softening is a gradual decrease of mechanical resistance under a continuous increase of deformation forced upon a material specimen or structure. Presently, the role of the softening behaviour is accepted by all the scientific community to explain size effect. A typical stress-displacement diagram shows progressive softening until zero stress. The yield criterion used combines the advantages of modern plasticity concepts with a representation of anisotropic material behaviour, which incorporates different hardening/softening behaviour along each material axis (Lourenço 1996).

A 3-point Lobatto integration scheme for the interface elements was employed during the analysis to avoid oscillations in the solutions, in particular in terms of shear bond stress at the interface (DIANA 1999) a monotonic incremental load was applied at the end of the FRP strip. To perform the nonlinear analysis using the

Table 5.1: Elastic properties for the masonry, FRP and interface.

Element	E	ν	k_n	k_s
	N/mm^2	-	N/mm^3	N/mm^3
Masonry	850	0.2	-	-
GFRP	80000	0.2	-	-
CFRP	215000	0.2	-	-
Interface $_{GFRP}$	-	-	48	20
Interface $_{CFRP}$	-	-	60	40

arc-length method and the crack mouth opening displacement CMOD technique to surpass instabilities caused by nonlinearities.

Table 5.2: Inelastic properties for the interface, see Diana (1999) for details.

Tension			Shear			Compression		
f_t	=	0.68 N/mm^2	c	=	1.3 N/mm^2	f_m	=	8 N/mm^2
G$_f^I$	=	0.0204 N/mm	tanϕ	=	0.75	c_s	=	15
			tanψ	=	0.0	G$_{fc}$	=	45 N/mm
			G$_f^{II}$	=	2.5 N/mm	κ_p	=	75

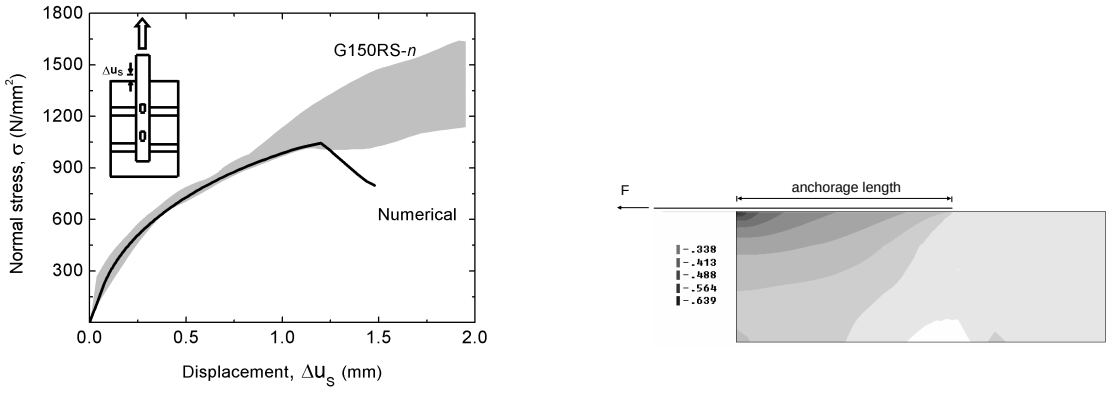
5.2 Stress distribution along the FRP

5.2.1 Normal stress at the FRP loaded-end

Consisting with the experimental campaign, the first specimen to be analysed numerically was the reference G150RS-n specimen, Figure 3.28. Figure 5.2 shows that the numerical response of the reference specimen fits inside the experimental envelope, keeping adequate stiffness but not reaching the large strains observed in the experiments. The wide experimental scattering of results, at the end of the test, was associated with a possible sliding or premature FRP tensile rupture. Analysing the complete path for both approaches, a good approximation between the numerical model and the experimental envelope was found, Figure 5.2a. Note that, inside this subsection, the area shaded in light gray is the envelop of five experimental results and the dark line corresponds to the numerical result. The

numerical response together with tensile stresses propagation in masonry is depicted in Figure 5.2b with shading adjusted according with the stress intensity.

When the anchorage length was reduced to 100 mm, the numerical output gave a reasonable approximation in terms of stiffness and relative displacement maintaining the numerical response all the way inside the envelope, Figure 5.3a.



(a) (b)

Figure 5.2: (a) Comparison of experimental envelope and numerical results for specimens G150RS-n; (b) Principal tensile stresses distribution along the model (N/mm^2).

When the anchorage length was increased to 200 mm, the initial stiffness was not so well reproduced, Figure 5.3b. Despite the global agreement between numerical and experimental results, it is noted that the ultimate experimental deformation exhibited by the envelope cannot be taken strictly till 2 mm since most of the specimens had GFRP tensile rupture. In the numerical model the FRP also had a tensile failure mode for the highest anchorage length, which is in accordance with the experiments.

The three different numerical results representing the anchorage length variation were gathered in Figure 5.3c, where the same parabolic trend was obtained for the three specimens showing an increasing deformation with anchorage size. As expected no influence of the anchorage length was found in the numerical initial stiffness. The experimental increase of initial stiffness for the largest anchorage length may be explained by a reduction of defects in the bond. The reference and the smallest anchorage length specimen presented more convergence difficulties than the largest anchorage length. This was due to the tensile failure of FRP in

specimen G200RS-*n*, which did not allow to fully explore the nonlinear behaviour of the interface. Regarding the peak load, all of three specimens show acceptable agreement with its average experimental counterpart, Table 5.3.

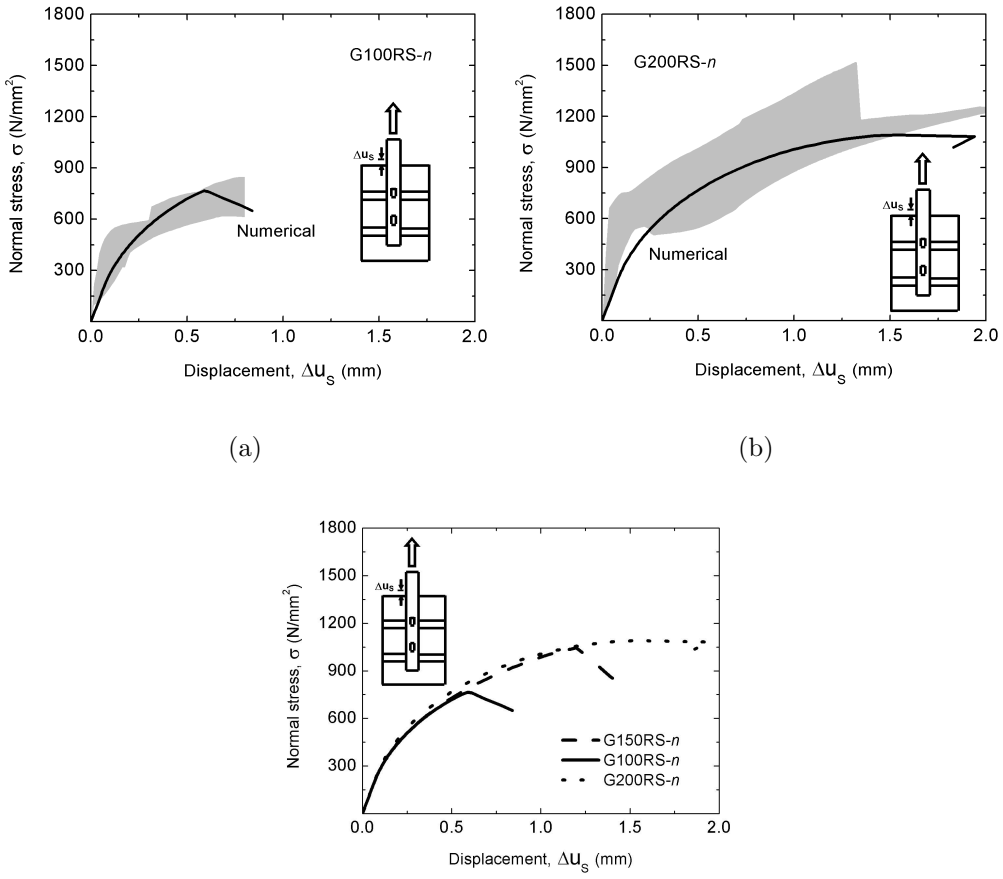
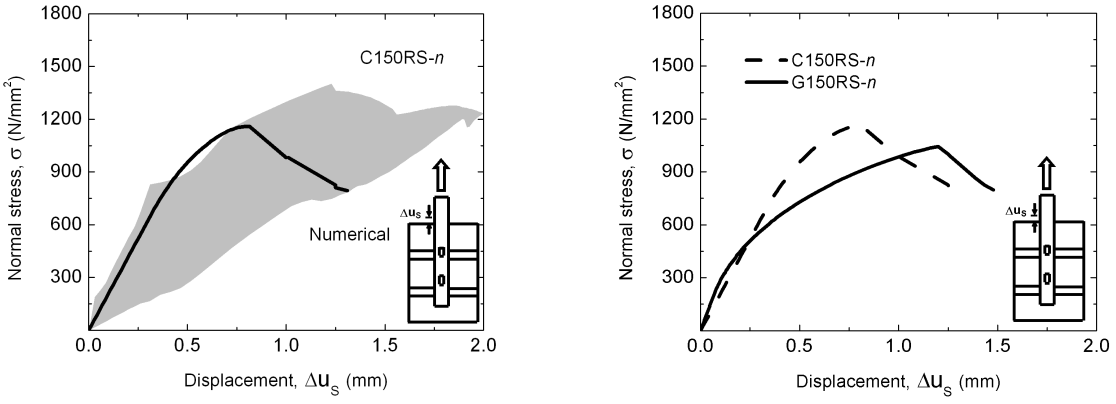


Figure 5.3: Comparison of experimental envelopes and numerical results concerning: (a) G100RS-*n*; (b) G200RS-*n* specimens; and (c) numerical results for the three anchorage lengths.

When the reinforcement material was changed to carbon, a smooth numerical response followed the experimental envelope, then postpeak is shown in Figure 5.4a. In terms of peak stress a difference of 22% was obtained when comparing the numerical with the experimental value. The highest stiffness among all models was recorded for this material, Figure 5.4b.

The numerical results obtained for curved shapes specimens are illustrated in



(a) (b)

Figure 5.4: (a) Experimental envelope and numerical response for carbon material; (b) numerical comparison with the reference G150RS-n specimen.

Figure 5.5. As stated before, curvature radii similar to those used in masonry arches where used on curved shapes specimens. The numerical results for the concave and convex shapes agree well with the experimental envelope and also with the peak stress, Figure 5.5 and Table 5.3. The superposing of the numerical curved shape responses and that of the reference specimen is illustrated in Figure 5.5c. Similar stiffness and maximum stress were observed when comparing the results from curved shape specimens and the curve from the reference specimen.

Table 5.3: Experimental and numerical comparison of bond test specimens

Variation	Specimen	Maximum stress (MPa)		Difference
		Exp Average	Numerical	(%)
Length	G150RS-n	1276.3	1045.0	18
	G100RS-n	921.2	765.7	17
	G200RS-n	1318.3	1091.6	17
Material	C150RS-n	1482.2	1160.0	22
Shape	G150ES-n	1221.3	1076.1	12
	G150XS-n	1112.6	1010.0	9

It is noted that the increase of maximum stress applied caused by the increase of anchorage length is well captured in the numerical simulations, as well as the

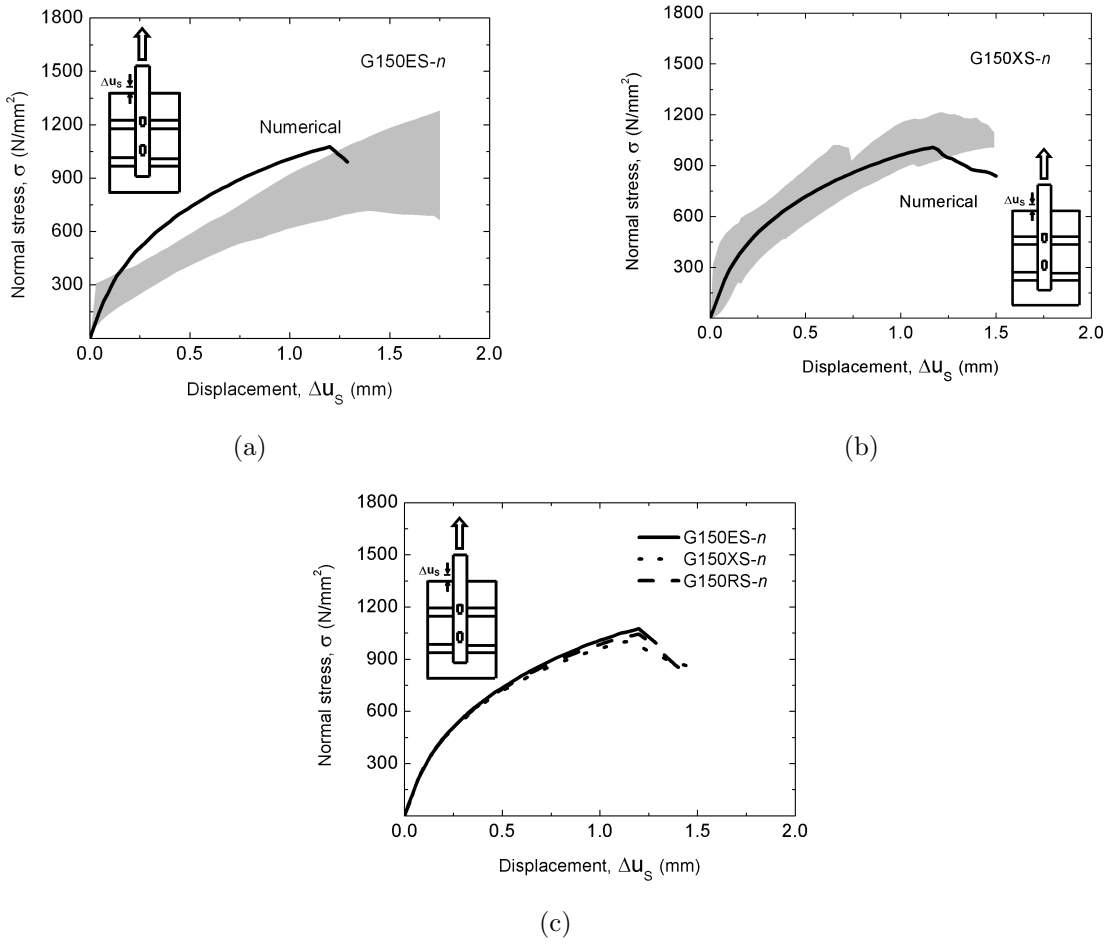


Figure 5.5: Comparison of experimental envelopes and numerical results concerning bond test specimens with curved shapes: (a) concave G150ES-n specimen; (b) convex G150XS-n specimen and (c) Numerical comparison for the two curved shapes with the reference specimen

corresponding failure modes. Similarly, the lack of significant changes due to the different specimens shape was also captured in an appropriated fashion.

5.2.2 Normal stress along the anchorage length

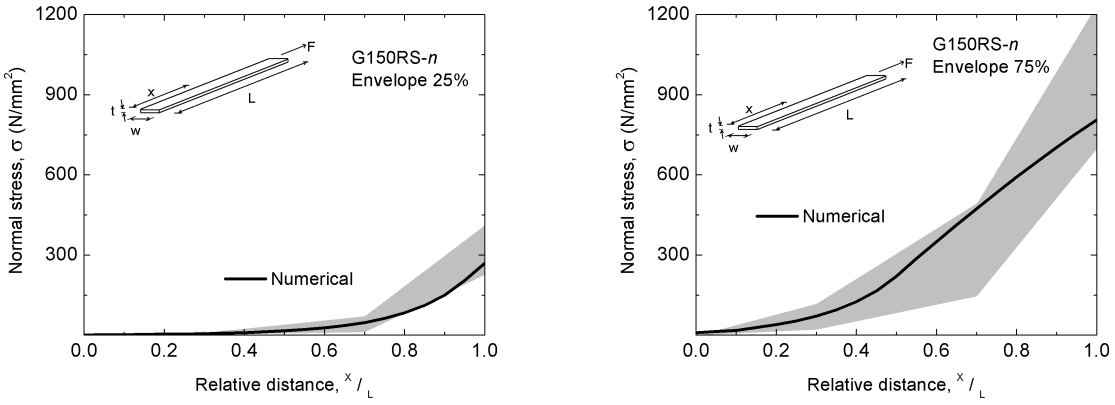
Besides the global numerical response presented in the previous section, by using of the bond test model it was possible to describe the specimens local behaviour. With this objective in mind, experimental and numerical responses were compared once again. The numerical bond test model was constructed in such a way that the integration points were located at the same position of the discrete points captured by the strain gauges. Therefore, the tendencies observed were taken from similar locations superposed at different stress levels. Aiming at a quick overview and description, only two stresses levels are included along the text while complementary graphics are given in the Appendix B.

In the next figures, each envelope and curve is related to a certain load level indicated as a percentage of the ultimate load, and the relative distance was normalized according to the anchorage length. The normalization was done to allow the comparison between different specimens at different failure loads. The convention adopted was such that zero and unit value of the x axis correspond to the free end and to the loaded end of the anchorage length respectively.

For each masonry bond test series presented in this section the figures include the normal stress in FRP for 25% and 75% of the peak stress, being each percentage presented in a separated figure.

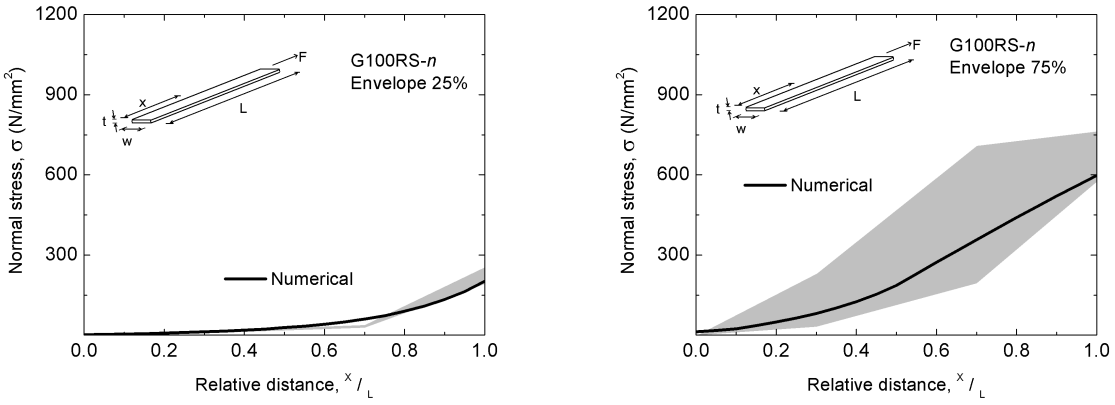
For the reference masonry bond test, comparison of the experimental envelope and the numerical response is shown in Figure 5.6, which provides a good agreement. The normal stress transmission along the anchorage length indicates a nonlinear distribution moving from the loaded end to the free end with increasing applied load.

In Figure 5.7 it is demonstrated that for a smaller anchorage length at moderate and higher load levels fine tuned estimation was found. For stresses close to the peak a linear stress distribution defined strip sliding or lack of substrate adhesion, Appendix B. Wider envelopes for the peak stress were found for the reference and the smallest anchorage length.



(a) (b)

Figure 5.6: Comparison of numerical results and experimental envelopes in terms of the FRP normal stress along the anchorage length for the G150RS-n series at two different load levels: (a) 25% and (b) 75% of the maximum load.



(a) (b)

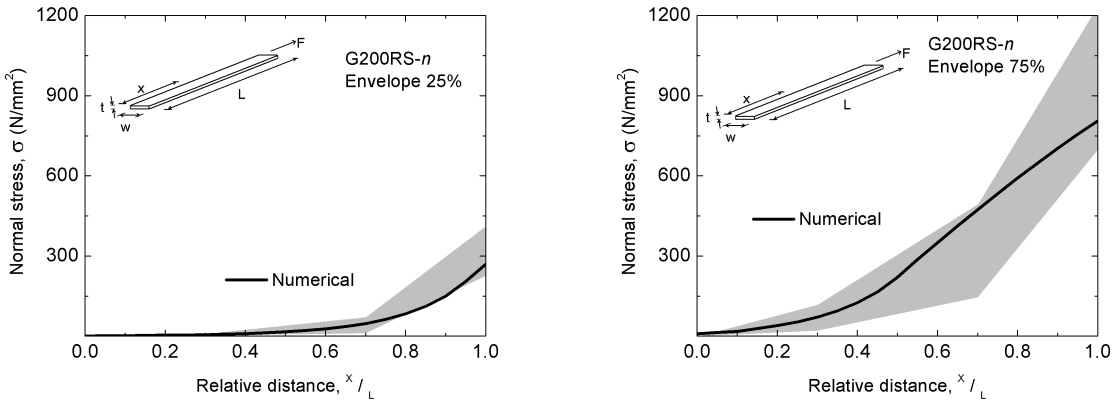
Figure 5.7: Comparison of numerical results and experimental envelopes in terms of the FRP normal stress along the anchorage length for the G100RS-n series at two different load levels: (a) 25% and (b) 75% of the maximum load.

For the biggest anchorage length specimen the model shows a slow movement along the anchorage length showing a similar behaviour to the one depicted on its experimental counterpart, Figure 5.8.

In fact, specimens G150RS-n, G100RS-n and G200RS-n seem to show a similar global behaviour in terms of stress distribution profile along the anchorage length.

Inclusion of a FRP material other than GFRP like carbon did not change the typical normal stresses profile computed. At lower stress levels, smooth distributions were found while sharper variations were depicted for higher stresses keeping a good agreement with the results of the tests. In Figure 5.9 the CFRP for two intermediate levels of the maximum normal stress, 25% and 75%, is outlined.

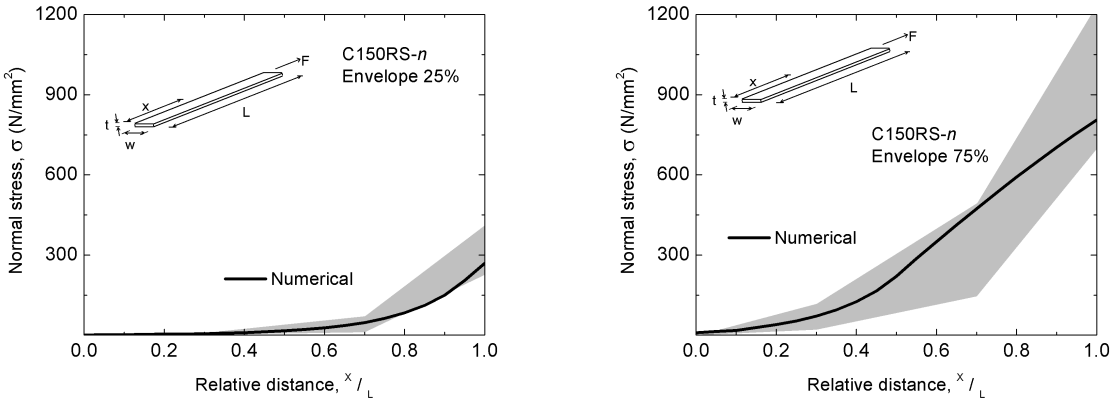
The graphical response for the concave and the convex geometries over the anchorage length at different stresses levels exhibit insignificant differences in the comparison between experimental envelopes and the results of the numerical model. The numerical response was always inside the envelope as shown in Figure 5.10 and 5.11. From the numerical results, it seems that slight modifications on curvature did not resulted in significant changes regarding its parabolic shape, as described by the numerical trends.



(a) (b)

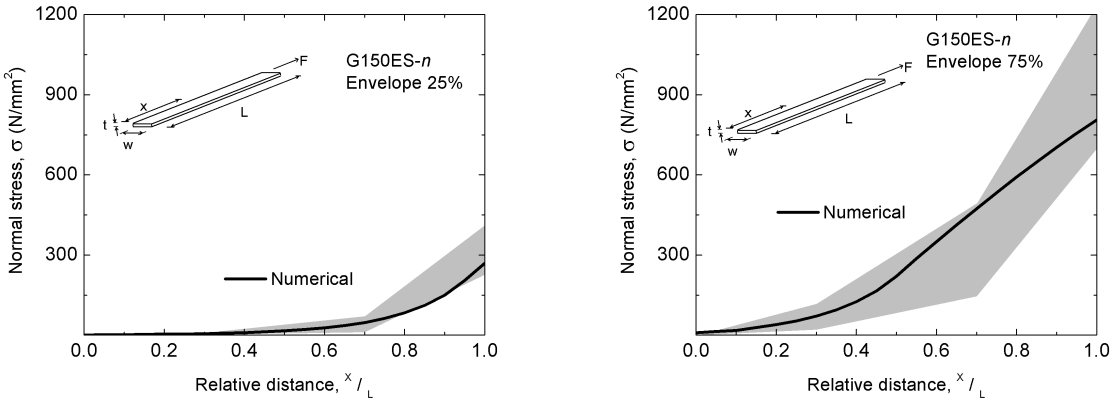
Figure 5.8: Comparison of numerical results and experimental envelopes in terms of the FRP normal stress along the anchorage length for the G200RS-n series at two different load levels: (a) 25% and (b) 75% of the maximum load.

In conclusion, a good approximation between numerical and experimental results was obtained. The irregularity of the experimental curves was in general



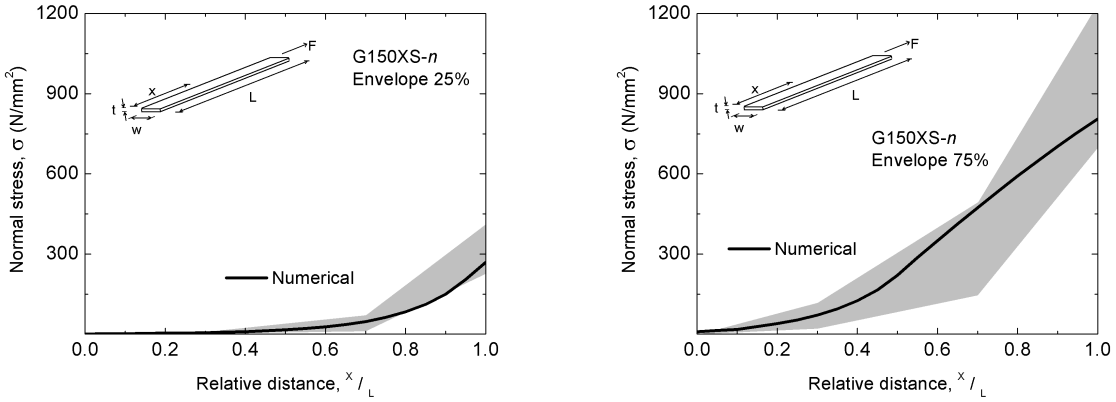
(a) (b)

Figure 5.9: Comparison of numerical results and experimental envelopes in terms of the FRP normal stress along the anchorage length for the C150RS-n series at two different load levels: (a) 25% and (b) 75% of the maximum load.



(a) (b)

Figure 5.10: Comparison of numerical results and experimental envelopes in terms of the FRP normal stress along the anchorage length for the G150ES-n series at two different load levels: (a) 25% and (b) 75% of the maximum load.



(a) (b)

Figure 5.11: Comparison of numerical results and experimental envelopes in terms of the FRP normal stress along the anchorage length for the G150XS-n series at two different load levels: (a) 25% and (b) 75% of the maximum load.

rather high, partly because the readings were taken at corresponded discrete and limited points, as described in Chapter 3.

5.3 Analytical approach

5.3.1 Bond stress-slip formulation

To get a deeper insight and better interpretation of the bond test specimens a complementary combined numerical and analytical approach is described in this section. Using the same models aforementioned and discussed, numerical output information was compared with the analytical formulation developed in this section.

For the analytical approach four discrete data sources were taken from the experimental measurements. Two points, given by the location of the strain gauges glued along the loaded FRP strip and the two extreme points (free end and loaded end), comprehend the initial available information data source. At the free end, zero movement was assumed, and later corroborated by the LVDT measurements.

The strain analytical results were obtained by integration of equation 5.5 checking the consistency of the tensile loaded FRP strip computed by equilibrium and

complemented with the experimental strain along the bonded region. With the purpose of getting an intermediate point per interval additional points between the strain gauges were considered by linear interpolation.

From the diagram presented in Figure 5.12 and considering the equilibrium of an infinitesimal length of a FRP strip dx, it can be established that:

$$d\sigma_s \, w_s \, t_s = \tau \, w_s \, dx \tag{5.2}$$

Assuming linear behavior of the composite, the next relationship is obtained

$$d\sigma_s = E_s \, d\epsilon_s \tag{5.3}$$

Substitution of equation 5.3 into equation 5.2 and eliminating common terms (ω_s), the bond stress reads:

$$\tau = E_s \, t_s \, \frac{d\epsilon_s}{dx} \tag{5.4}$$

Therefore, recalling the basic relation and isolating the FRP strain (ϵ_s) another parameter to be estimated is the sliding of the FRP strip over masonry.

Assuming that the deformability of both the epoxy adhesive and masonry are negligible when compared with the FRP and simplifying their relative displacement:

$$\frac{ds}{dx} = \epsilon_s \tag{5.5}$$

After substituting equation 5.5 into equation 5.4, the bond stress can be expressed as:

$$\tau \, (s) = \frac{d^2 s}{dx^2} \, E_s t_s \tag{5.6}$$

where:

$d\sigma_s$: infinitesimal stress of the FRP strip
ω_s : width of the FRP strip
t_s : thickness of the FRP strip
τ : bond stress
dx : infinitesimal longitude
E_s : Young's modulus of the FRP

$d\epsilon_s$: infinitesimal strain of the FRP strip
ds : infinitesimal slip

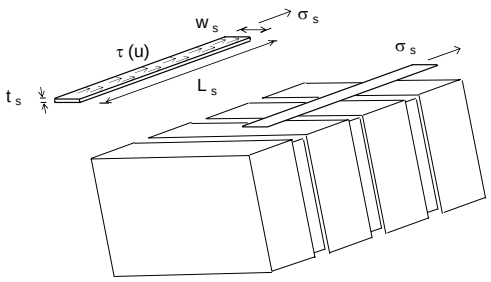


Figure 5.12: Free body diagram of the bond test specimen.

As a result, slip is evaluated with the integration of equation 5.5

$$s\,(u) = s\,(0) + \int_0^{L_s} \epsilon \, dx \tag{5.7}$$

where $\mathbf{s}\,(0)$ is the slip at the free end and L_s in the bond length. Through the strain gauges and load cell data acquired, graphs of normal stress, strain and bond stress versus location along the anchorage length were constructed taking into account that, insignificant movement was observed at the free end opposite to the applied load.

The following sections deal with the comparison of the numerical results with analytical results based on the experimental measurements and evaluated according to the aforementioned formulation. Analytical results are assessed for each specimen, allowing the construction of analytical envelops from five single results. For each bond test arrangement, the comparison is established for two different stress levels: 25% and 75% of the peak stress.

5.3.2 Strains distribution along the anchorage length

Figures 5.13 to 5.18 show the FRP strain distribution along the bonded length for the reference bond test arrangement (G150RS-n), both in terms of numerical and analytical results. It is important to clarify that a comparison in terms of numerical and experimental strains could have been done. However, in this case, the results would be identical to the ones shown in terms of normal stress distribution for

low stress levels. The strain distribution along the bond length, highly non-linear at moderate load levels, tends to approach an almost linear shape as the applied load increases, at least close to the edge of the loaded-end. This means that, as the monotonic load increases, strains become more linearly distributed along the anchorage length resulting in changes in the bond nature, such as substrate deformation or detaching.

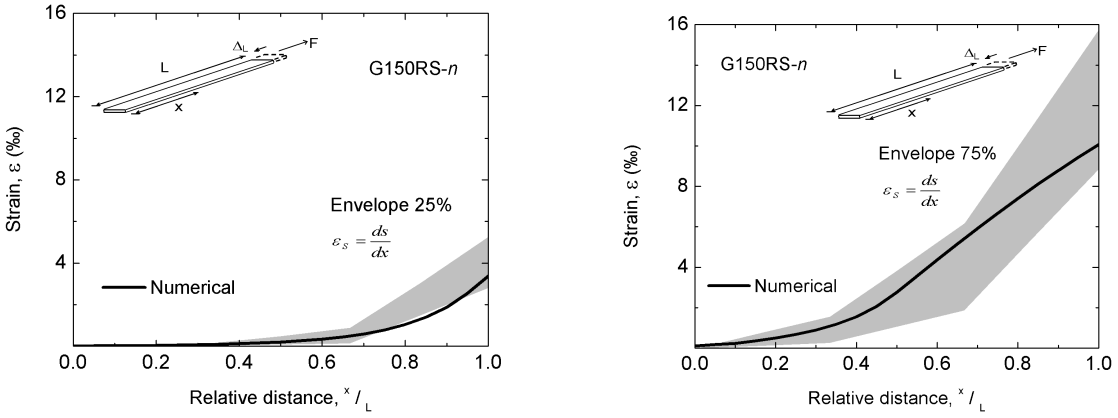


Figure 5.13: Comparison of numerical results and analytical envelopes in terms of the FRP strains along the anchorage length for the G150RS-n series at two different load levels: (a) 25% and (b) 75% of the maximum load.

Relatively narrow wide envelopes for low stresses levels characterized the reference specimen, as presented in Figure 5.13, strain and stress trends are similar, describing an uplift with the load level increase. Despite the fact that the strain at moderate load levels shows a less accurate matching, after 75% up to peak load a good agreement was observed; refer to the Appendix C for complementary figures.

For a smaller anchorage length than the reference one, Figure 5.14, the numerical and the analytical approximations matched also satisfactorily. At peak load, a smooth numerical trend was not found, instead a linear trajectory was delineated.

A less smooth strain transfer along the anchorage length was obtained with the numerical model when increasing the anchorage length to 200 mm. For the highest strains computed, larger than 50% of the peak load, slight differences were observed between analytical and numerical strains as shown in Figure 5.15. It is

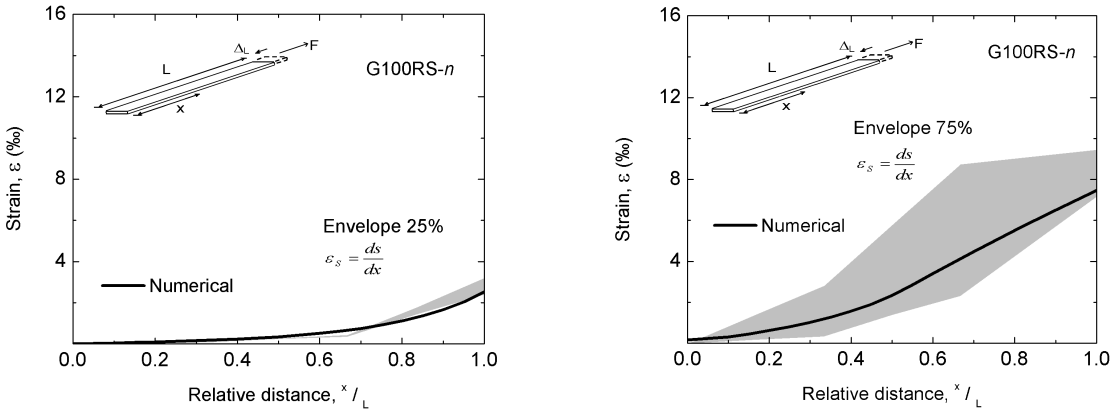


Figure 5.14: Comparison of numerical results and analytical envelopes in terms of the FRP strains along the anchorage length for the G100RS-n series at two different load levels: (a) 25% and (b) 75% of the maximum load.

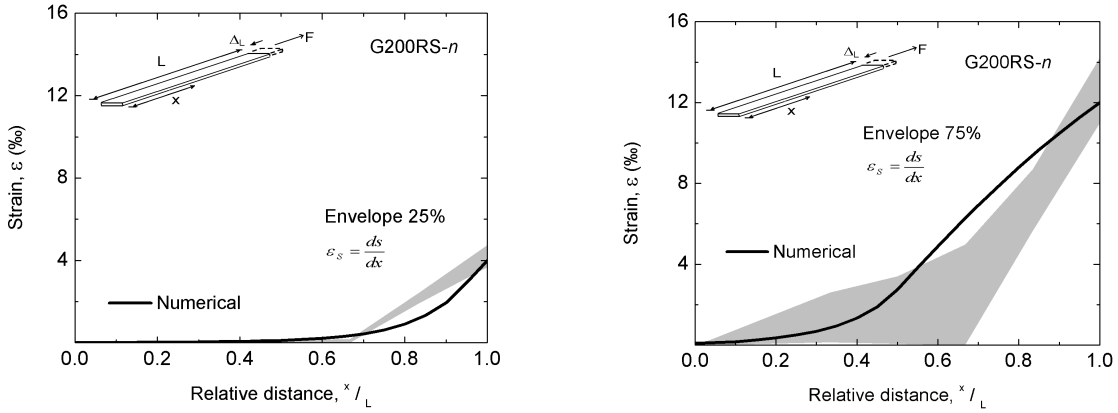
important to mention that a careful interpretation of the results must be performed since the addition of intermediate discrete points induces some uncertanties.

In general, a change from an experimental curve shape to a "S" curve shape is observed for the numerical results with increasing applied load. As widely known, the linear relation between stresses and strains is valid when the elastic regime dominates during all the imposed loading history. Sometimes, the elastic limit exceeded, since nonlinear behaviour might start at the very beginning of the loading history. This was the case for all the series tested and modelled, therefore analogies were not possible.

For a strengthening materials other than GFRP (*e.g.* Carbon, Aramid, etc.), a quick and accurate numerical model convergence characterizes its response. Up to a level of 75% of the peak strain, the straight linear trend outlined differs from the smooth curve defined by the strain values along the anchorage length when compared with the rest of the models, Figure 5.16.

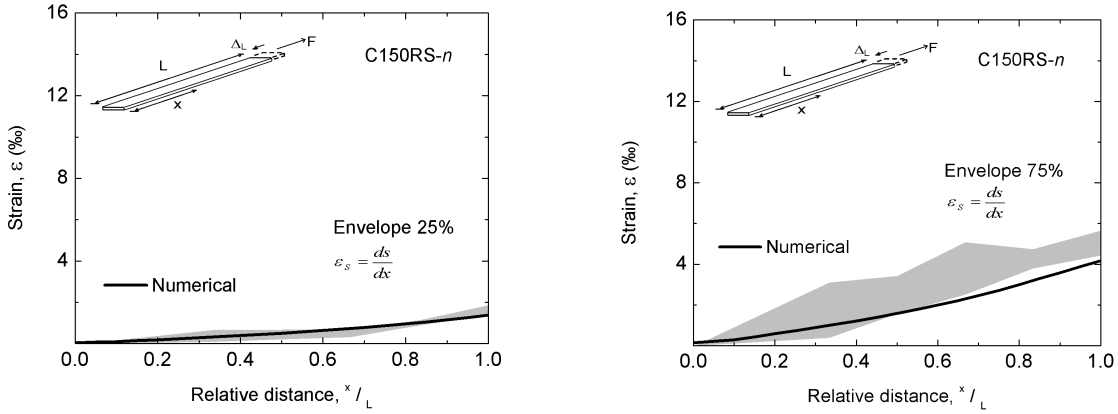
Finally, for curved bond test specimens, satisfactory accuracy was found at all load levels for both convex and concave shapes. Numerical trends are located within the envelop at each stress level, even when narrow bands were computed, Figure 5.17 and 5.18.

In conclusion, although the strain layout was discretized with additional data



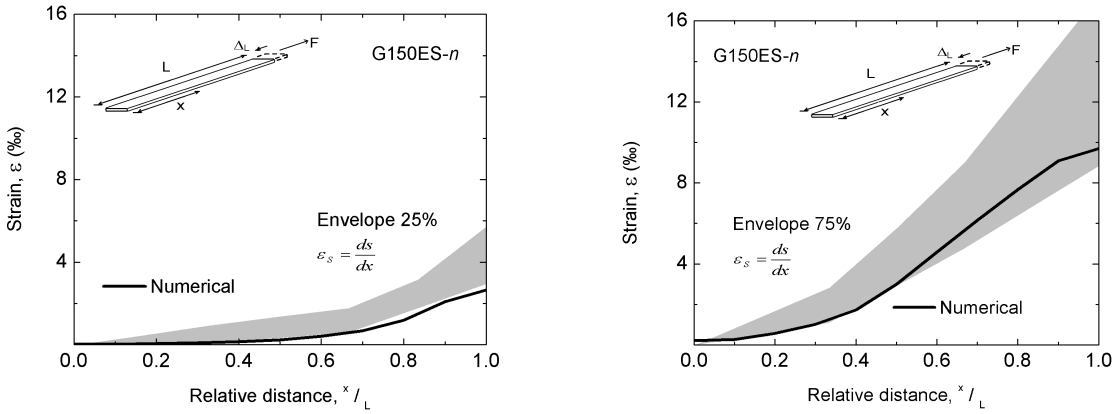
(a) (b)

Figure 5.15: Comparison of numerical results and analytical envelopes in terms of the FRP strains along the anchorage length for the G200RS-n series at two different load levels: (a) 25% and (b) 75% of the maximum load.



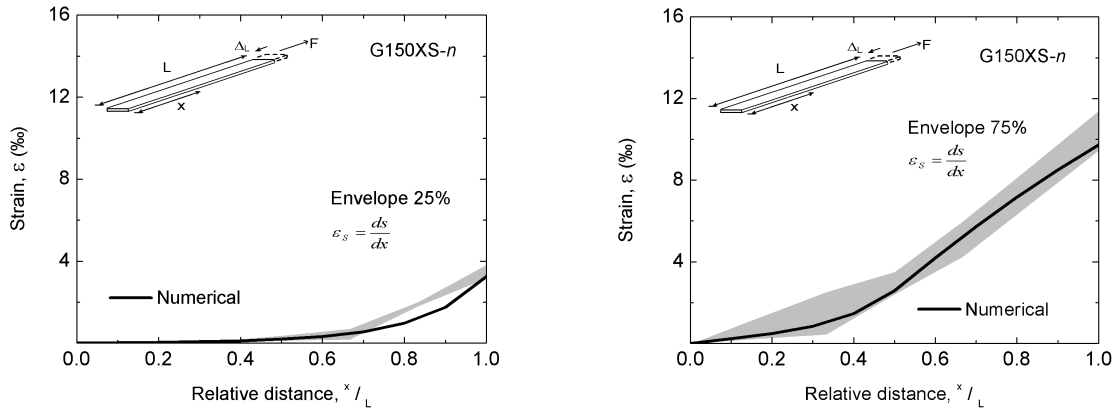
(a) (b)

Figure 5.16: Comparison of numerical results and analytical envelopes in terms of the FRP strains along the anchorage length for the C150RS-n series at two different load levels: (a) 25% and (b) 75% of the maximum load.



(a) (b)

Figure 5.17: Comparison of numerical results and analytical envelopes in terms of the FRP strains along the anchorage length for the G150ES-n series at two different load levels (a) 25 and (b) 75% of the maximum load.



(a) (b)

Figure 5.18: Comparison of numerical results and analytical envelopes in terms of the FRP strains along the anchorage length for the G150XS-n series at two different load levels (a) 25 and (b) 75% of the maximum load.

obtained from a linear interpolation between each two adjacent experimental and data points, it is worth to point out that interpretation of such results is a delicate issue, as the number of measuring devices applied was low due to the available space. It is believed that the criterion to glue strain gauges separated a certain distance along the FRP gave an adequate approximation to the strain field.

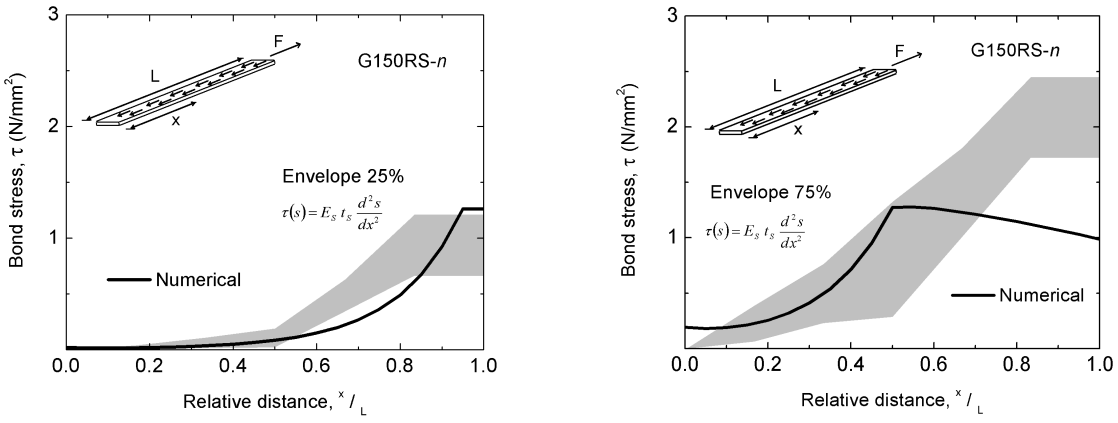
5.3.3 Bond stress along the anchorage length

Before starting to describe the bond stress distribution along the FRP strip and its influence on the bond test specimens, some issues must be taken into account regarding modelling and the analytical approach. First, in the latter approximation besides the four available discrete points, three more intermediate points were calculated by linear interpolation. Additionally, the small number of strain gauges and the influence caused on its reading by inevitable local effects due to the surface irregularity mean that the experimental bond stress *versus* slip diagrams usually contain high irregularity, as found in previous works (De Lorenzis 2002; Valluzzi et al. 2004).

The numerical accuracy was limited to the point where the model presented a failure related to premature detachment of the FRP, since only moderate load bond stresses were reasonably captured. Thus the analytical bond stress was calculated using equation 5.4. Both numerical and analytical results are presented in Figures 5.19 to 5.24.

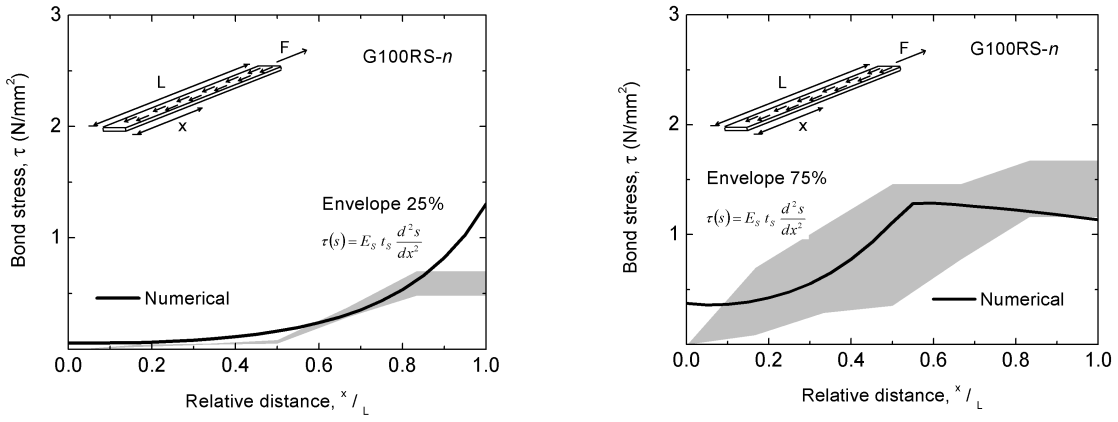
Although the bond stress distribution is influenced by many parameters, the most important parameters were the cohesion and fracture energy of the interface. When strengthened masonry structures are modelled by finite element analysis, it is quite common to assume that the bond stress depends mainly on the slip, to evaluate the remaining parameters before starting the analysis, and an appropriate bond-slip relationship must be used as an input.

The numerical results give a description of the bond stress transmission for all the specimens series. In general, a good approximation was observed until half of the peak load. Once softening reached most of the anchorage length, FRP sliding developed and collapse occurred. For the results captured at peak stress, the FRP strip concentrated bond stress at the free end, where initially zero values were found, Appendix D. The fragile surface stage, at higher bond stress levels, might



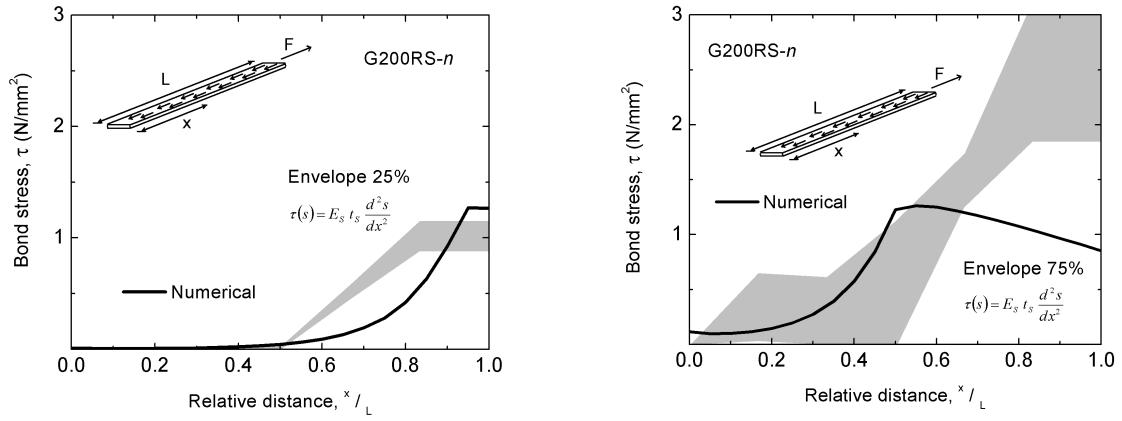
(a) (b)

Figure 5.19: Comparison of numerical results and analytical envelopes in terms of the FRP bond stress along the anchorage length for the G150RS-n series at two different load levels: (a) 25% and (b) 75% of the maximum load.



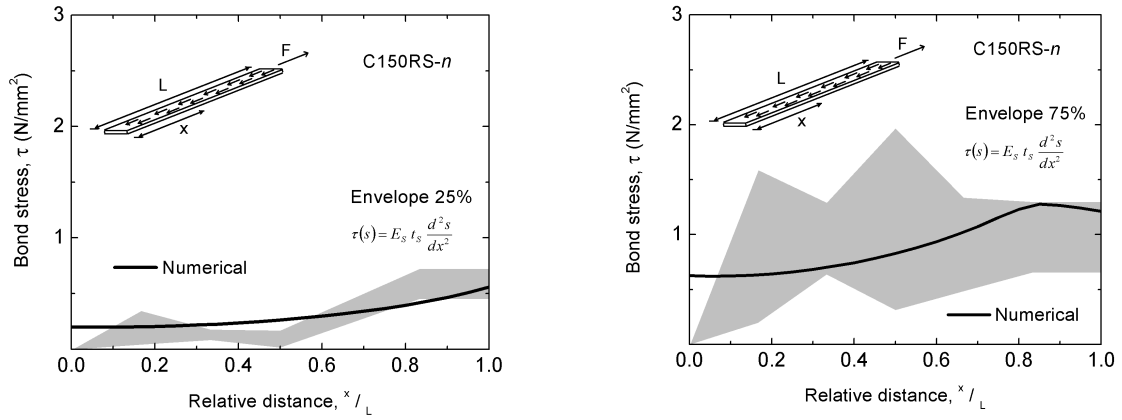
(a) (b)

Figure 5.20: Comparison of numerical results and analytical envelopes in terms of the FRP bond stress along the anchorage length for the G100RS-n series at two different load levels: (a) 25% and (b) 75% of the maximum load.



(a) (b)

Figure 5.21: Comparison of numerical results and analytical envelopes in terms of the FRP bond stress along the anchorage length for the G200RS-n series at two different load levels: (a) 25% and (b) 75% of the maximum load.



(a) (b)

Figure 5.22: Comparison of numerical results and analytical envelopes in terms of the FRP bond stress along the anchorage length for the C150RS-n series at two different load levels: (a) 25% and (b) 75% of the maximum load.

be responsible for such uneven bond stress distribution as observed in most cases and corroborated by the shape of the failure envelopes at failure.

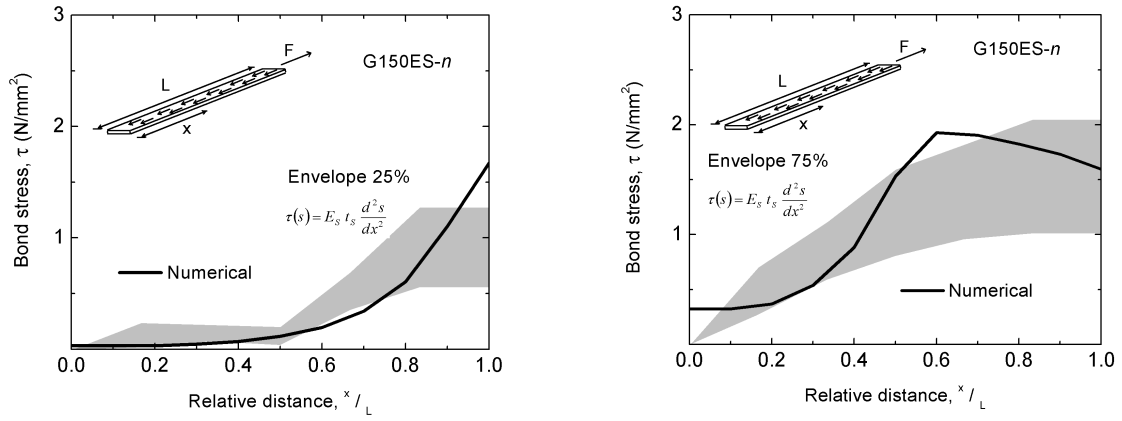
For a low value of the applied load, the bond stress shows a parabolic distribution along the anchorage length, Figure 5.19a, where the higher stresses are found close to the loaded end. Increasing the applied load makes the maximum bond stresses to reach the bond strength and causes local strengthening, Figure D.1a. This process causes the movement of the highest bond stress zone towards the free end and allows the appearance of new interface zones where softening can be observed, Figure 5.19b. For an applied load close to its maximum, almost all the anchorage length presents softening behaviour.

Besides the high scattering exhibited by some specimens, the differences between experimental and numerical results are directly related to the low number of discrete measurements (only four) and their susceptibility to local damage phenomena in the masonry substrate.

For a smaller anchorage length, Figure 5.20, the behaviour of G100RS-n specimen changed only at the smallest load levels. Beyond 25%, the same stress distribution of the reference specimen for the highest stresses was observed. This result was somehow expected because the bond stress development is basically a local issue, as discussed for specimen G150RS-n.

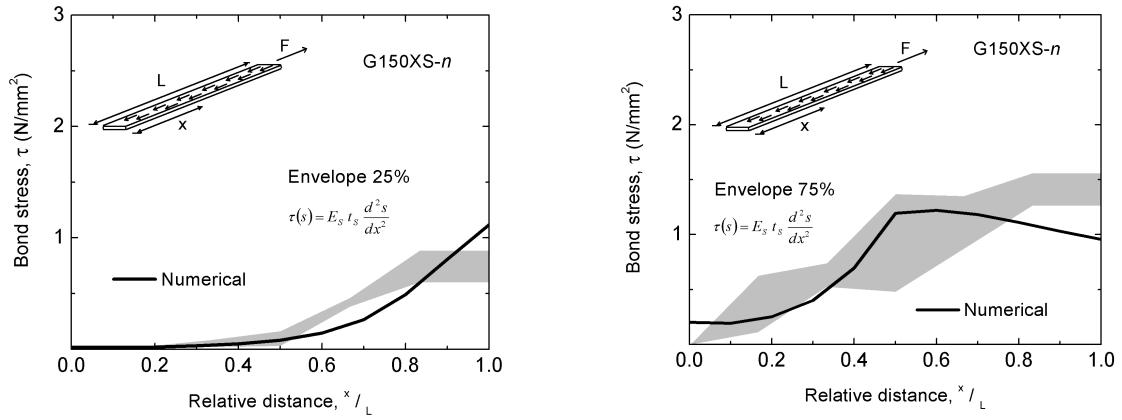
The length variations, G100RS-n, G150RS-n and G200RS-n, had a similar behaviour, in which for low stress level the tendency observed was parabolic. On the other hand, for higher stresses levels softening over the substrate changed the curvature downwards. Sliding and tensile failure mode depend on the anchorage length since the G200RS-n presented strip tensile failure. When softening reached most of the anchorage length, FRP sliding occurred together with the respective collapse. If the anchoraged length is large (200 mm), before most of the substrate presents softening, the FRP strip breaks in tension. Moreover, at peak load, the reference and the 200 mm anchorage length did not reach such high bond stresses at the opposite loaded end, refer to the Appendix D and Figure 5.21 for the G200RS-n specimen at two levels 25% and 75%.

For the alternative use of carbon FRP material, both numerical and analytical stress configurations were quite close, when superimposed as shown in Figure 5.22. Although numerical outputs reasonable adapt inside the envelopes for all load levels, steady ranges of variation characterized the analytical trends obtained. Such



(a) (b)

Figure 5.23: Comparison of numerical results and analytical envelopes in terms of the FRP bond stress along the anchorage length for the G150ES-n series at two different load levels: (a) 25% and (b) 75% of the maximum load.



(a) (b)

Figure 5.24: Comparison of numerical results and analytical envelopes in terms of the FRP bond stress along the anchorage length for the G150XS-n series at two different load levels: (a) 25% and (b) 75% of the maximum load.

discontinuities were influenced by two major aspects, namely, the discrete interpolated points as well as the general poor cohesion between the composite and the masonry substrate, which can also be responsible for it. A lack of compatibility between substrate and reinforced material indicates that a glass FRP was more appropriate, based on the analysis of the results.

In the case of curved specimens, a better accuracy between the numerical model response and the analytical envelopes was found. Just like the highest anchorage length of 200 mm, the initial numerical trend for 25% of the peak load, provides a parabolic shape for both geometries. Besides the plateau at intermediate stress level in the numerical response, it might be observed that the concave shape specimen (G150ES-n) was able to distribute stresses in a softer manner, since the analytical envelope trends for the convex shape had a wider scattering, compare Figure 5.23 with Figure 5.24. An additional observation of the bond stress transmission indicates that the peak stress in the convex geometry was attained earlier, according to numerical and analytical results.

5.3.4 Local bond stress-slip curve

An introduction of the construction of envelopes is included in Figure 5.25, where the local position of the discrete strain reading is illustrated. Each item of Fig. 5.25 clearly depicts the bond stress calculated and synchronized with the displacement recorded by the LVDT at the FRP loaded end. For the purpose of exemplifying the procedure adopted to built the subsequent envelopes, only one series was included here. For the complete reference, the reader is referred to the Appendix E.

Each of the analytical envelopes presented in Figures 5.26 to 5.28 included five specimens for each series. For the smallest anchorage length, the series do not allow the development of a full stresses distribution along the anchorage length.

After the observation of the results obtained, it is emphasized that theoretical tools may give an idea on the physical phenomena. While the concave and the convex shapes got the smoothest and widest tendencies, the smallest anchorage length (G100RS-n) and the carbon material display the smallest slip along the anchorage length. Regarding the reference specimen G150RS-n and the G200RS-n wider scattering characterized the bond stress-slip envelope.

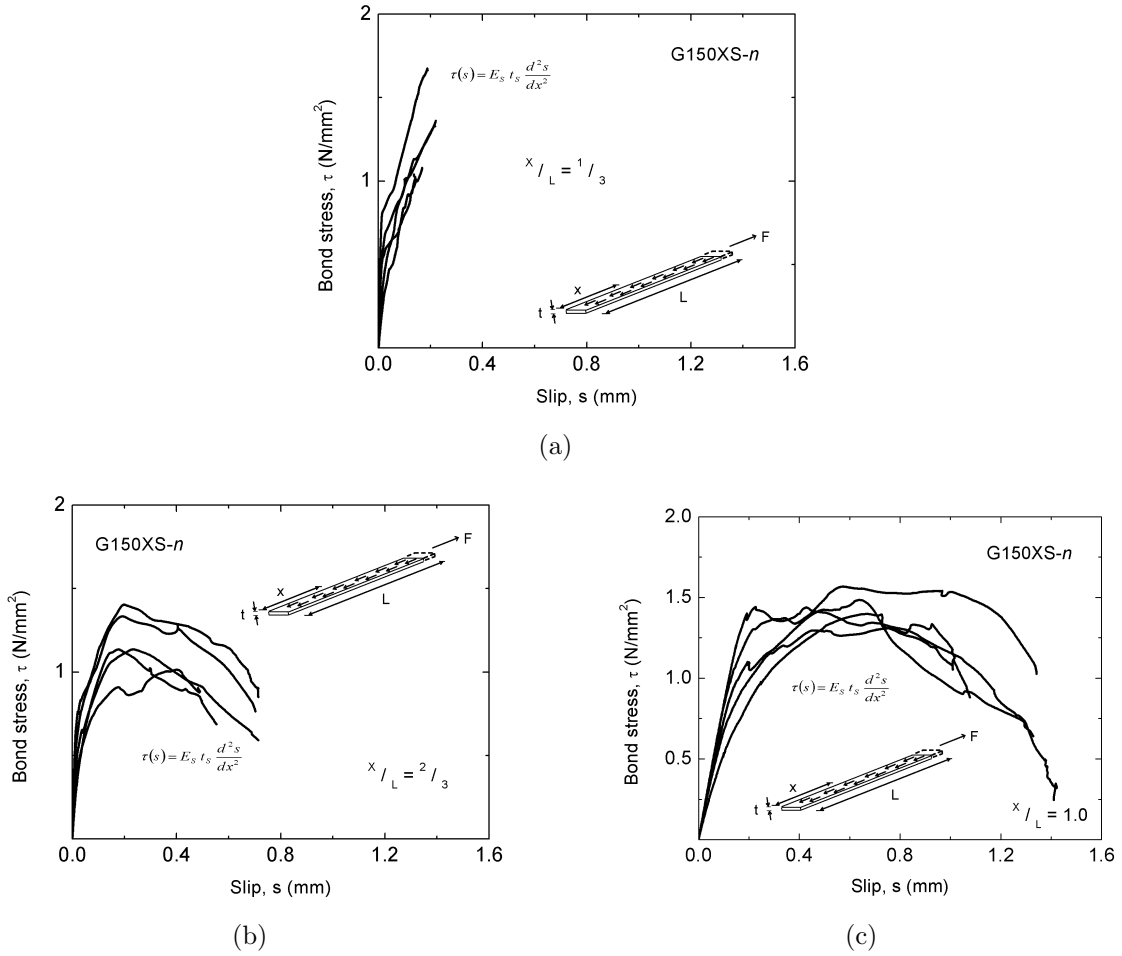
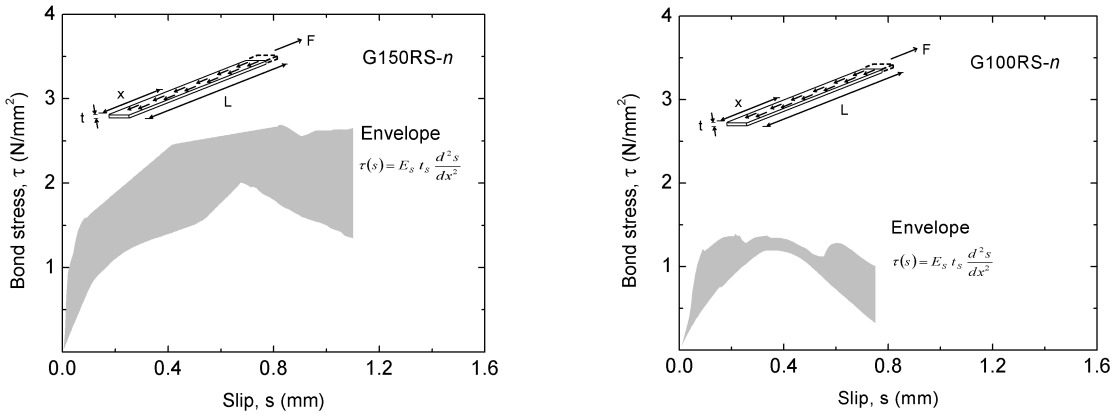
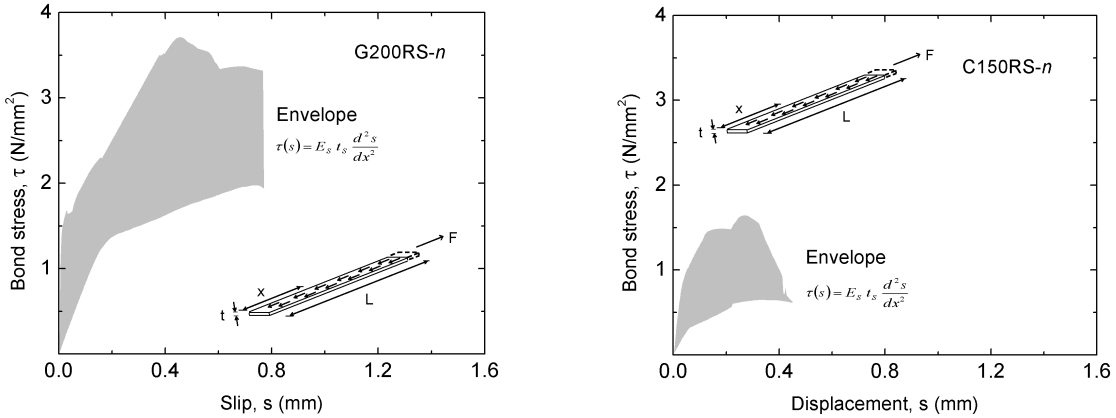


Figure 5.25: Analytical local bond stress-slip for the G150XS-n specimen at three different positions: (a) one third of L; (b) two thirds of L and (c) loaded end (full L).



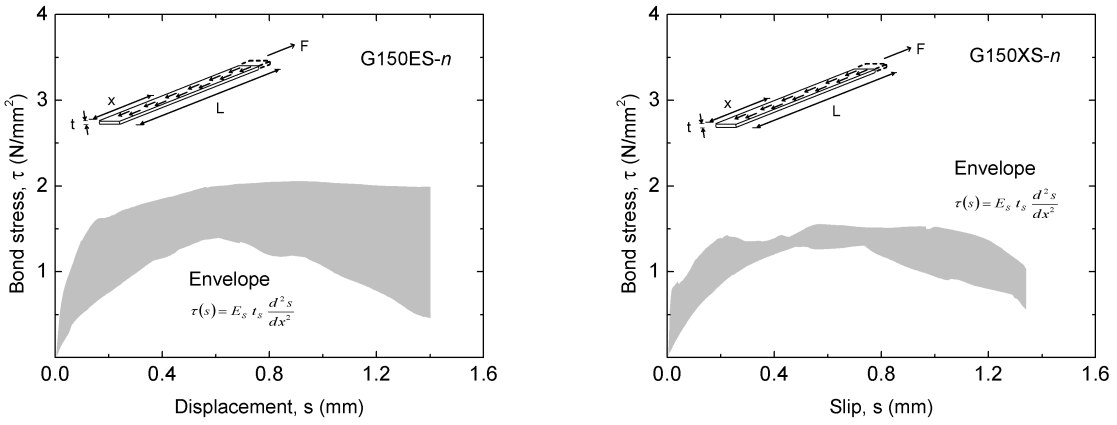
(a) (b)

Figure 5.26: Envelope of the analytical bond stress versus displacement along the anchorage length for the: (a) G150RS-n; (b) G100RS-n.



(a) (b)

Figure 5.27: Envelope of the analytical bond stress versus displacement along the anchorage length for the: (a) G200RS-n; (b) C150RS-n.



(a) (b)

Figure 5.28: Envelope of the analytical bond stress versus displacement along the anchorage length for the: (a) G150ES-n; (b) G150XS-n.

5.4 Conclusions

Throughout this present chapter, a comprehensive presentation, analysis and discussion regarding the bond test results have been described. This approach demonstrated the possibilities and potential capabilities of the bond stress numerical model. Furthermore, an analytical formulation was adopted, built from the experimental discrete points recorded by the strain gauges.

By means of the numerical responses and its comparison with the experimental envelopes, good agreement with the experimental values at the loaded end were recorded. Moreover, normal stress along the anchorage length gave, in general terms, an acceptable approximation with the experimental specimens.

It is worth mentioning that the numerical failure mode depends on the anchorage length. When softening reaches most of the anchorage length, FRP strip sliding occurs and, consequently, collapse. If the anchorage length is large (200 mm) before the anchorage slides, the FRP strip fails in tension.

Just like in the experimental procedure, extreme care was required in the analyse since nonlinear behaviour appears at a low loading level. Evaluation of reproduced results indicated that numerical brittle response was also found, as in the experimental series.

The bond stress distribution at the anchorage length obtained by the numerical model and the analytical approach demonstrates, that after demand all the possible

adhesion from the substrate, the residual friction at the bond length provoked fatigue of the surface, since the numerical stresses distribution presented higher softening for the peak stress.

The stresses distribution along the anchorage length for glass material were parabolic before reaching its maximum. On the other hand, for CFRP the shape of the stress distribution is no longer parabolic instead more uniform trends were observed.

The composite model used was capable to reproduce normal stresses together with the displacement at the loaded end for the composite glass material mainly. Changing to CFRP was not so accurate since only one series was tested and no further conclusions were possible.

Some additional observations were drawn during the calibration process carried out as a part of the analysis included. The residual stress value for the bond tests against the interface displacement was around 10% of the peak value, reasonably low in agreement with the observation that friction at the interface is quite low once the micro-cracks in the masonry are generated.

The direct strains were transformed from the gauges reading outlining a good reproduction estimation of strains transfer along the anchored length, even at the peak load where failure mode dominated the test.

Chapter 6

Numerical modelling of masonry arches

Masonry is an anisotropic material where the orientation of the joints plays a crucial role in the determination of the elastic properties and strength. In particular, the description of the tensile behaviour of masonry should include tension normal and parallel to the joints.

Masonry vaults are one of the most common structural shapes present in the architectural heritage of the world. These structures are defined as structures in which the load bearing is clearly associated with the distribution of material in space. A growing interest in the preservation of historic structures has created a need of methods for the analysis of load-bearing unreinforced masonry structures, such as arches, vaults, and buttresses.

Although the limit analysis methods, first applied to medieval structures in detail by Heyman (1982), provide a useful and intuitive approach to the understanding of the behaviour of masonry arches and vaults, their usefulness in performing actual assessments of such structures has limitations. The complexities of analysis are also due to the complexity of the system of which these elements are part of: a medieval cathedral is a convoluted assembly of piers, vaults, arches, and buttresses that all work together, and for which the load paths are not always obvious (Boothby 2001).

Membrane analyses are suitable for masonry vaults without discontinuities and whose loads are continuous, *e.g.*, no cracks and/or point loads. A membrane elastic analysis generates an acceptable force system and therefore a safe lower bound on

the collapse load. However, discontinuities in either the structure or the loading present difficulties. Most vaults are highly indeterminate and must be assessed for several loads combinations. Therefore all possible load paths should be identified (O'Dwyer 1999).

As a final objective of the present work, the construction of numerical models representing masonry arched structures strengthened with FRP materials was performed, to further discuss and validate the results.

Two parametric studies are presented and compared with the experimental results. As discussed before in Chapter 4, the optimal width, length and location of GFRP strips are addressed. Full and partial length reinforcement with GFRP strips was considered (at the intrados or at the extrados).

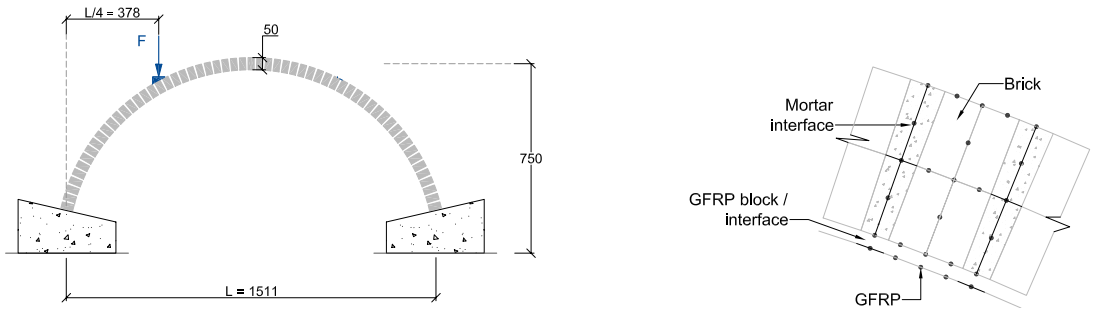
In this chapter, the numerical analysis of unstrengthened and strengthened semicircular masonry arches is presented, to evaluate the effectiveness of different GFRP strengthening strategies. The arches were loaded at the quarter span, including their self-weight, being the nonlinear behaviour of the materials considered in the analysis. Indications about width and optimal length reinforcement are established based on the results obtained.

6.1 Structural model for masonry arches

To assess the load bearing capacity and structural behaviour of masonry arches with different strengthening schemes, simulation of all arched structures experimentally tested was carried out. The constitutive models employed intended to adequately simulate the complex behaviour of masonry and FRP, and of the interface, resorting to nonlinear analysis. The micro-modelling strategy adopted in the previous chapter to model the bond-mechanism was utilized here to model masonry arches reinforced at the intrados and the extrados. However, two different interfaces are required for the modelling, namely the masonry joint interface and the masonry/FRP interface.

The semicircular masonry arches had a 750 mm radius, 450 mm width and 50 mm ring thickness. The displacements at the abutments were restrained in both orthogonal directions, Figure 6.1a. The complete setup of masonry arches is described in detail in Chapter 4. The mesh adopted in the analysis includes eight-noded plane stress elements to represent the masonry units, six-noded interface

elements to simulate the mortar and GFRP-masonry joints and three-noded beam elements to represent the GFRP, Figure 6.1b. Each masonry unit was modelled with four elements. In this case zero thickness interfaces was assumed for all the joints.



(a) (b)

Figure 6.1: Modelling of semicircular arches: (a) Elevation view (in mm); (b) Mesh detail of the masonry arch and GFRP strip.

In the analysis, subsequently to the application of the arch selfweight, a monotonic incremental load was applied at the quarter span. As described in Chapter 5, most of the properties used to simulate the mortar and GFRP-masonry interfaces were characterized in this thesis, otherwise they were obtained from mean values of previous works, Valluzzi et al. (2001) and Lourenço and Martins (2001). All the elastic and inelastic properties adopted for modelling are included in Tables 6.1 and 6.2, respectively, see Chapter 5 for full description of the symbols.

Table 6.1: Elastic properties for the bricks, FRP and interfaces.

Element	E	ν	k_n	k_s
	N/mm^2	-	N/mm^3	N/mm^3
Brick	5000	0.2	-	-
GFRP	80000	0.2	-	-
Interface $_{masonry}$	-	-	24	10
Interface $_{gfrp}$	-	-	48	20

Table 6.2: Inelastic properties adopted for the masonry and composite interfaces.

	Tension		Shear				Compression		
	f_t	G_f^I	c	$\tan \phi$	$\tan \varphi$	G_f^{II}	f_m	G_{fc}	κ_p
	N/mm^2	N/mm	N/mm^2	-	-	N/mm	N/mm^2	N/mm	-
Mason	0.18	0.03	0.3	0.75	0.0	0.1	7.8	90	10
Comp	0.44	0.15	0.65	0.75	0.0	2.5	7.8	-	-

6.2 First parametric study vs. experimental results

Before the experimental test program was initiated, a preliminary parametric numerical study was carried out using estimated mean values for the properties of the materials, due to the absence of experimental data. After the conclusion of all experimental tests, the most representative mechanical properties were obtained allowing then to perform a second parametric study based on reliable data.

Before testing each type of specimen, the first parametric focused on the FRP width influence, and gave an indication of the masonry arch peak loads (F_{max}) and failure modes.

Figure 6.2 shows the preliminary parametric study presented in Chapter 4 and the experimental results. The unfilled circles represent the numerical peak load values corresponding to a certain FRP strip width. On the other hand, the filled symbols designate the peak load values observed in the experimental specimens. An additional discontinuous line was added with the purpose of delineating the numerical trend observed.

Initially, the numerical peak loads for the plain arch and the arches locally strengthened with 160 mm FRP width remained between the corresponding two experimental values, a good agreement was also found, Figure 6.2a. With the model calibrated for this width, the numerical response for arches strengthened at extrados could not capture properly the increase in strength provided by the FRP, as shown in Figure 6.2b. Figure 6.2c shows the results for the masonry arches strengthened with composite material at the intrados. The graphics show that the model was able to reproduce the peak load evolution with FRP width increase, with a slight underestimation of the peak load. The non-conventional anchor

devices tested in the laboratory were omitted in Figure 6.2c. The modelling of the non-conventional devices can be found later on this chapter.

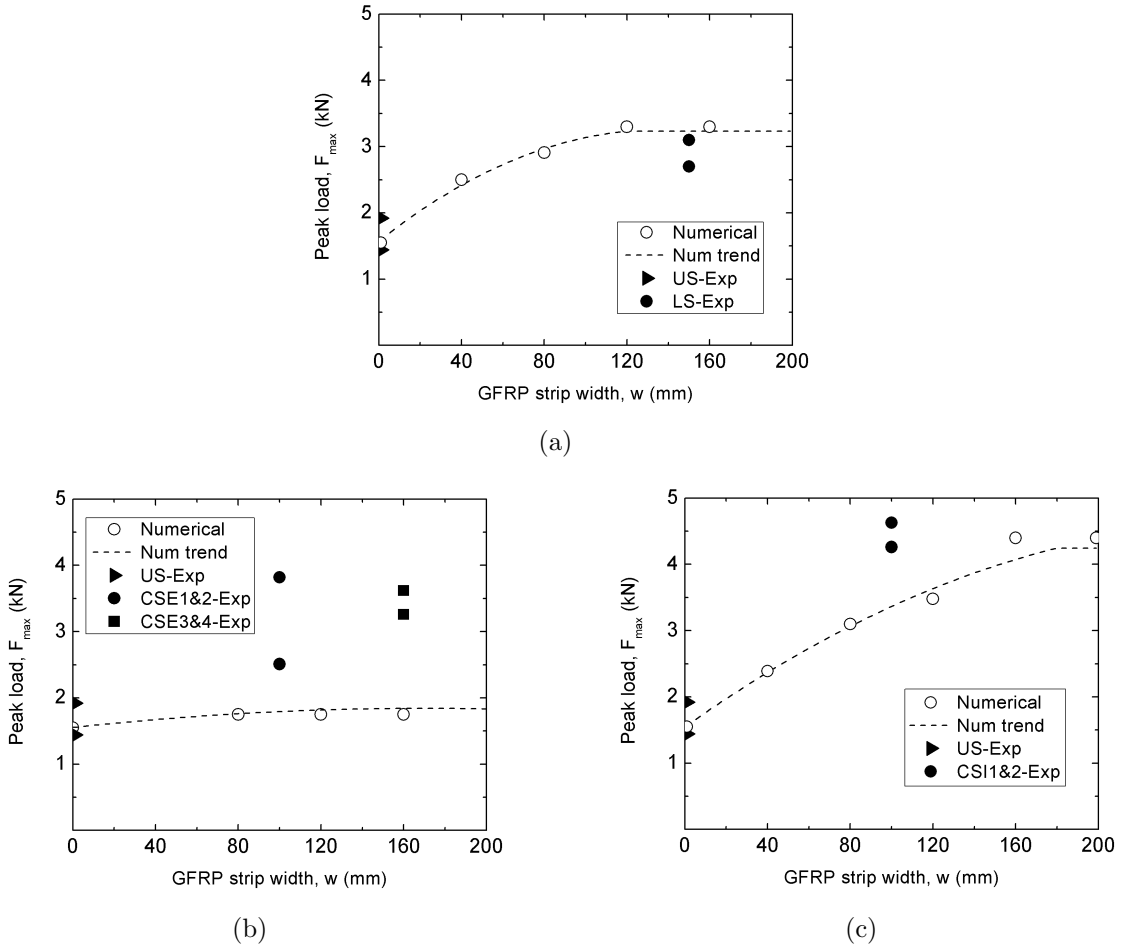


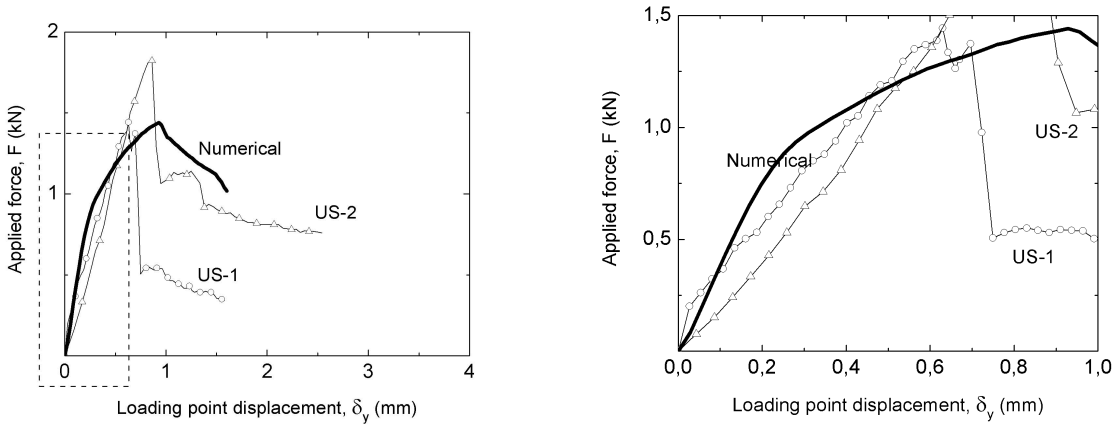
Figure 6.2: Preliminary parametric study versus experimental results showing the FRP strip width influence on masonry arches strengthened: (a) locally; (b) at the extrados and (c) at the intrados.

6.3 Unstrengthened arches

To identify the structural behaviour, the maximum load capacity and the mechanism of collapse of masonry arches, an analysis of plain arches was carried out. This analysis gave a general overview of how the structure behaved under an increasing load applied at the quarter span, without any strengthening. The deformed shape

provided an indication on its behaviour, defining where subsequent arches should be reinforced, specially when the localized option was adopted.

As illustrated in Figure 6.3 the results of the numerical model show a reasonable agreement with those of the experiments in the sense that they reproduce the initial stiffness and peak load. As observed experimentally a sudden drop in the load carrying capacity after reaching the peak load was obtained. Failure was characterized by brittle behaviour, as depicted in Figure 6.3a.



(a) (b)

Figure 6.3: Experimental US-1 and US-2 series compared with its corresponding numerical response: (a) load-displacement curve of the loaded point; (b) zoom of the initial diagram.

Good agreement was found for the experimental stiffness when compared to the numerical model reported in Table 6.3. The initial stiffness for all models ($k_{0,num}$) was calculated up to a load of 0.5 kN since the occurrence of nonlinear behaviour appears for very low loads.

In contrast with the experimental tests, the numerical model allows to perfectly identify the appearance of hinges and its sequence over the loading history. Taking advantage of this potential, Table 6.4 and Figure 6.4 show the appearance and sequence of the four hinges developed before formation of the collapse mechanism. Besides the deformed arch shape, also the principal compressive stresses are included in this figure (all values presented are in kN/m^2). Each frame of Figure 6.4 has a filled dot indicating development of the current hinge, where the unfilled circle represents a hinge developed previously. Table 6.4 presents the hinge for-

Table 6.3: Masonry arches stiffness.

Specimen	Initial stiffness, k_0 (kN/mm)			Difference
	Experimental, $k_{0,exp}$		Numerical	
	Individual	Average	$k_{0,num}$	(%)
US-1	2.85	2.45	3.15	58
US-2	2.05			
LS-1	3.31	4.42	3.7	16
LS-2	5.52			
CSE-1	1.44	1.28	3.82	9
CSE-2	1.11			
CSE-3	2.94	3.34	3.31	1
CSE-4	3.73			
CSI-1	2.00	2.62	3.26	19
CSI-2	3.23			
CSI-3	2.55	2.83	3.33	18
CSI-4	3.10			

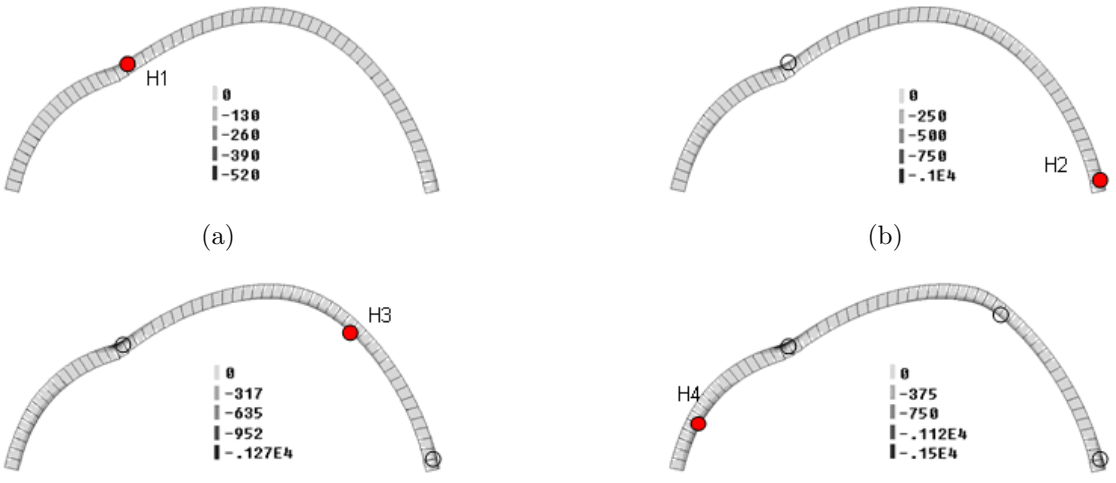
mation sequence for each arch model along with the intensity of the applied load.

For a better understanding of the structural behaviour, the location of hinges and their sequence of appearance are shown in an alternative representation on the numerical load-displacement curve outlined in Figure 6.5a. Each hinge, marked with an discontinuous circle, result in slight stiffness changes along the structural response path. All four hinges formed before the peak load and were detected at the beginning of their development. It might be worth to recall that the structure did not collapse in a stable manner after the formation of all hinges due to the displacement control adopted in the tests. In Figure 6.5b, a superposition of the deformed shape over the original configuration is presented at peak load condition.

Table 6.4: Hinges formation sequence.

Specimen	Numerical relationship between hinge formation sequence and applied load							
	1^{st}		2^{nd}		3^{rd}		4^{th}	
US-1	(0.6)	0.84	(1.0)	1.1	(1.2)	1.35	(1.4)	1.44
US-2	(0.7)		(1.1)		(1.4)		(1.8)	
LS-1	(1.1)	1.77	(1.6)	1.81	(2.1)	1.82	(2.6)	1.82
LS-2	(1.6)		(2.0)		(2.4)		(2.7)	
CSE-1	(1.0)	0.81	(1.3)	1.25	(2.0)	2.03	-	-
CSE-2	(0.8)		(1.9)		(3.6)		-	
CSE-3	(0.9)	0.86	(2.6)	1.40	(3.4)	2.71	-	-
CSE-4	(0.7)		(1.4)		(3.0)		-	
CSI-1	1.0	2.18	(2.3)	2.37	(4.2)	3.60	-	-
CSI-2	(1.7)		(2.6)		(4.5)		-	
CSI-3	(1.5)	1.29	(2.4)	1.76	(5.1)	3.5	-	-
CSI-4	(1.3)		(2.6)		(3.1)		-	

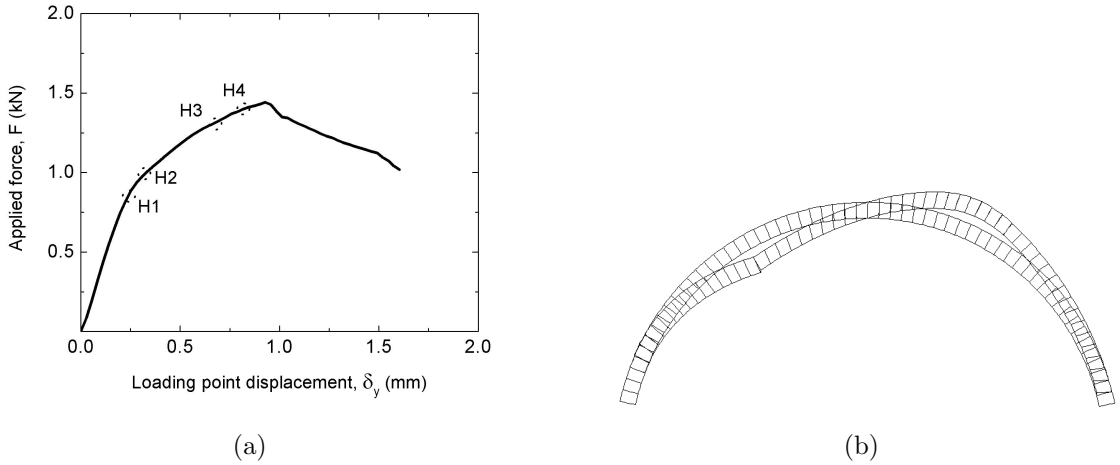
Notes: the experimental values are within brackets;
values in kN.



(a) (b)

(c) (d)

Figure 6.4: Numerical sequence of hinges formation for the unstrengthened masonry arch, including principal compressive stresses (kN/m^2) and depicted on the incremental deformed mesh.



(a) (b)

Figure 6.5: Numerical US arch: (a) indication of plastic hinges on the load-displacement diagram; (b) deformed mesh over the undeformed shape.

6.4 Locally strengthened arches

Valluzzi et al. (2001) reported that an irregular distribution of stresses in the restricted zone located under the CFRP reinforcement is produced by the combination of the small width of the strips and its high Young's modulus. Such phenomenon probably contributes to reduce the global resistance. After careful analysis of the available FRP materials on the market and also based on the bond test specimens, the glass composite was selected to reinforce all masonry arches. For a detailed explanation of the FRP sheet selection the reader is referred to the experimental bond test chapter.

Based on the collapse mechanism observed for the unstrengthened arches, originating four plastic hinges, reinforcement was applied to the damaged arches. With the exception of the foot hinge, localized reinforcement was placed in the extrados and the intrados, where hinges had formed. The aim at this phase was the global behaviour enhancement, with the purpose of utilizing the least possible material.

Three partial length strips were placed on the semicircular perimeter of the arch. The configuration adopted was arranged in such a way that 160 mm total length strip of GFRP reinforcement was placed, at the intrados and at the extrados (two strips of 80 mm each). Such pattern approximates the experimental specimen as shown in Figure 4.18a. After loading the unstrengthened arch numerical model described above, reinforcement was included before carrying out a subsequent re-

loading with the same load applied at quarter span. The structural response considering partial length reinforcement placed at the extrados and at the intrados is illustrated in Figure 6.6.

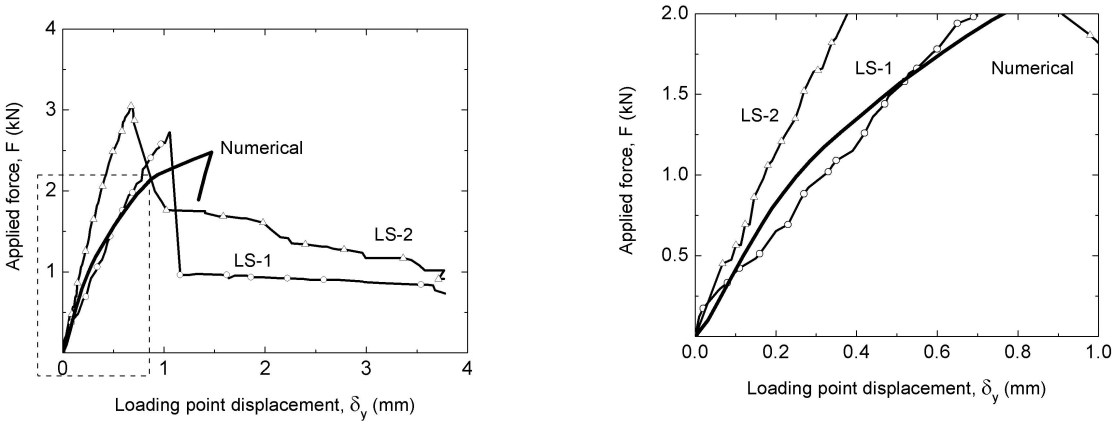


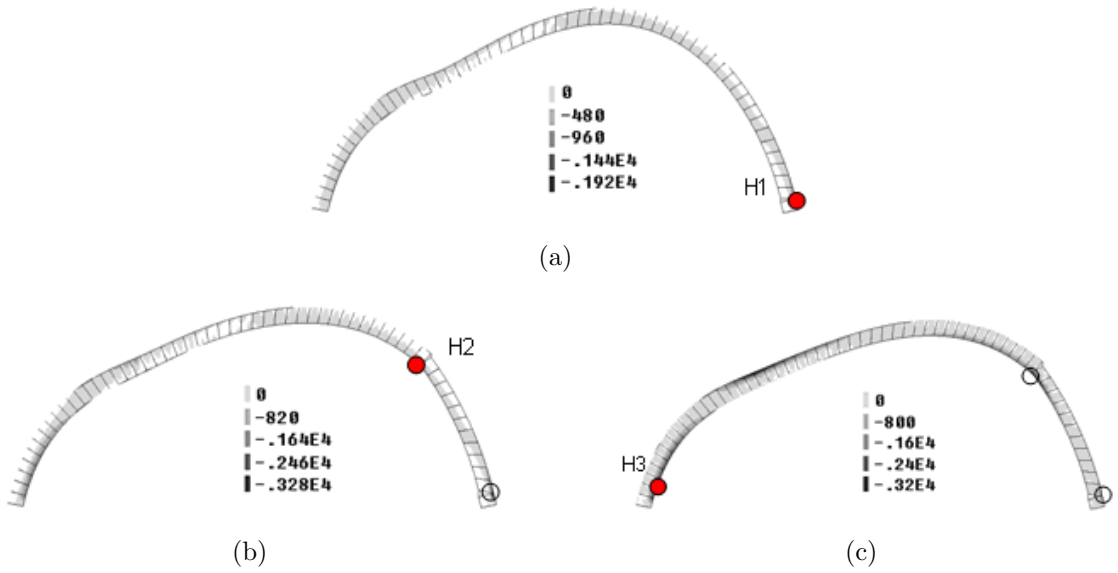
Figure 6.6: Experimental LS-1 and LS-2 series compared with its corresponding numerical response: (a) load-displacement curve of the loaded point; (b) zoom of the initial diagram.

Because the analysis was carried out using a damaged arch, the numerical response reflects differences on stiffness and peak load, when compared with the experimental series, Table 6.3 and 6.5. Only the first two hinges were timely detected by means of visual inspection in the tests, Table 6.4. The two remaining hinges were detected almost at the end of the test.

Numerical models of arches strengthened using partial length reinforcement placed at the intrados and at the extrados exhibit similar brittle structural behaviour and collapse mechanisms, when compared with the unstrengthened arches, compare Figure 6.3 with Figure 6.6. This was expected to occur since experimental specimens behave on a similar fashion.

In the mechanism of collapse, the location of the hinges moves towards the zone where reinforcement was absent. Smaller opening of hinges was developed which might be attributed to less damage in the strengthened structure. The numerical failure pattern, with sliding between brick and mortar in the first joint, close to the springer, is similar to the failure mechanisms reported by Creazza et al. (2002).

The localized reinforcement changed the mechanism of collapse of unstrengthened arch, with a new location for the plastic hinges. Hinges appearance and



(a)

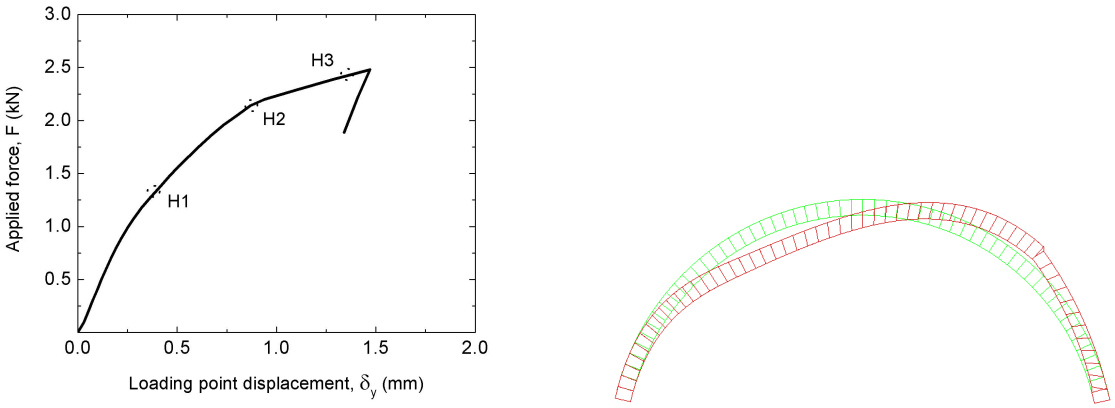
(b)

(c)

Figure 6.7: Numerical sequence of hinge formation for the locally strengthened masonry arches, including principal compressive stresses (kN/m^2) depicted on the incremental deformed mesh.

sequence are illustrated over the incremental deformed mesh in Figure 6.7. The mesh includes also the principal compressive stresses corresponding to each plastic hinge formation.

The numerical hinges detected in the load displacement diagram for the localized strengthening option had more abrupt stiffness changes than plain arches. The localized reinforcement avoided the opening of existing hinges. Both facts are highlighted in Figure 6.8a together with the deformed mesh at peak load just before collapse, Figure 6.8b.



(a) (b)

Figure 6.8: Numerical LS arch: (a) representation of plastic hinges on the load-displacement diagram; (b) deformed mesh.

Table 6.5: Maximum load sustained by arches.

Specimen	Maximum load, P_{max} (kN)			Difference (%)
	Experimental		Numerical	
	Individual	Average		
US-1	1.43	1.68	1.53	9
US-2	1.92			
LS-1	3.18	2.96	2.07	30
LS-2	2.73			
CSE-1	2.51	3.17	3.01	5
CSE-2	3.82			
CSE-3	3.62	3.44	3.50	2
CSE-4	3.26			
CSI-1	4.26	4.45	3.93	12
CSI-2	4.63			
CSI-3	5.41	4.61	4.65	1
CSI-4	3.81			

6.5 Continuously strengthened arches at the extrados

As described in Chapter 2, continuum reinforcement applied at the substrate surface modifies the arch static condition. Different mechanisms of collapse are developed for the reinforcement placed at the extrados, where failure is located in the masonry joints beneath the applied load, and masonry develops the largest hinge rotation. The mechanism of collapse produced by these openings limits the arch to continue sustaining the load. The final collapse of the arch was due to sliding at the abutments. Also, experimental research by Valluzzi, Valdemarca, and Modena (2001) has showed that, for arches strengthened at the extrados, sliding along the joints is the prevalent failure mechanism. A solution to avoid such brittle failure can be achieved by optimizing the quantity of FRP applied, increasing the amount of material near the abutments, where wider and better anchorage is needed to test how effective an anchor could improve strength.

Numerical results related to the full length reinforcement at the extrados are shown in Figures 6.9 to 6.11. For this strengthening strategy, higher peak loads were reached, when compared with plain arches and partial length reinforcement, as shown in Table 6.5.

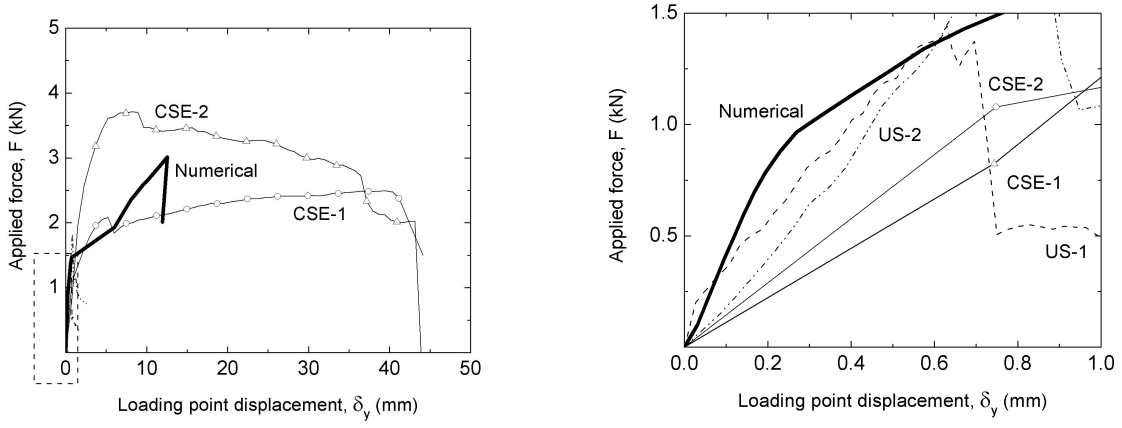


Figure 6.9: Experimental CSE-1 and CSE-2 series compared with its corresponding numerical response: (a) load-displacement curve of the loaded point; (b) zoom of the initial diagram.

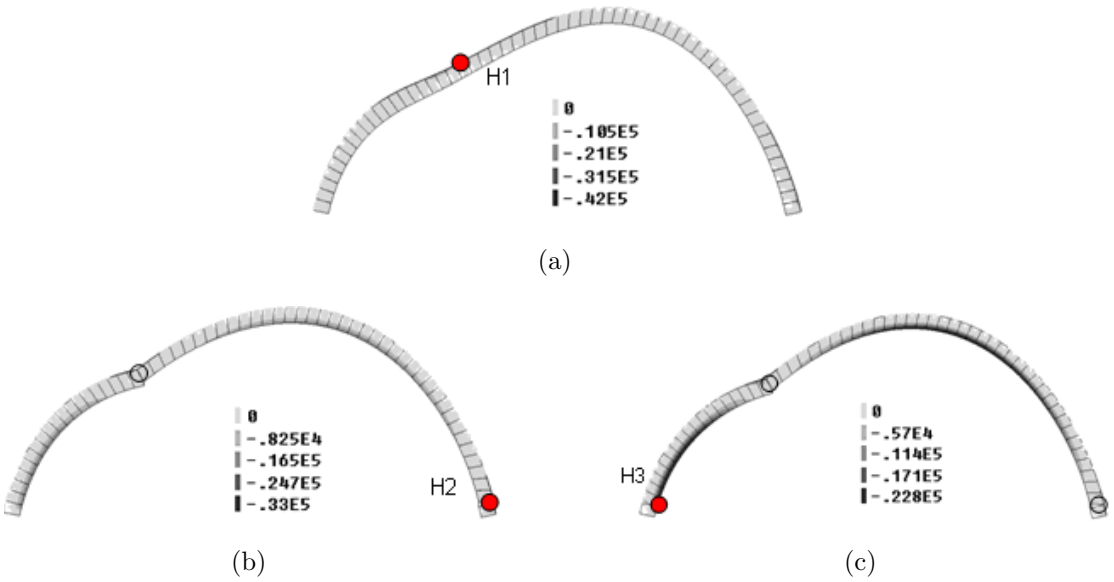


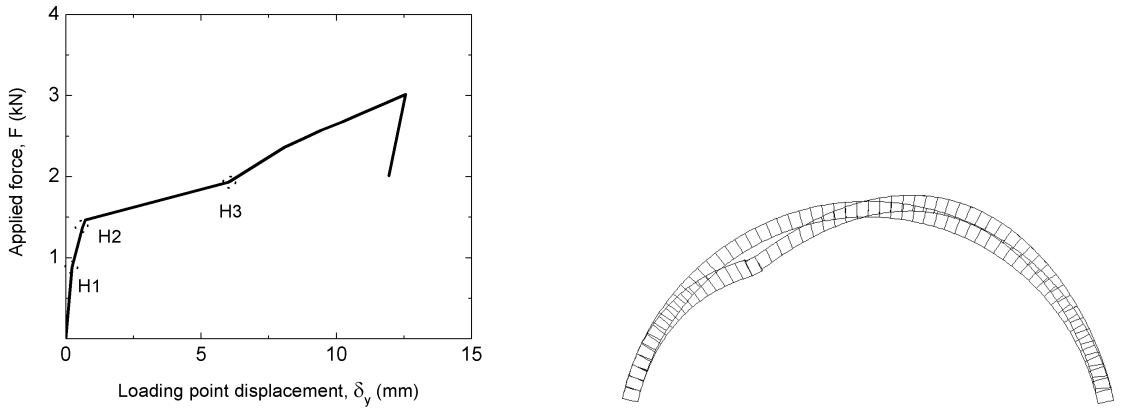
Figure 6.10: Hinge development sequence for the numerical CSE arch with 100 mm strip width, including principal compressive stresses (kN/m^2) depicted on the incremental deformed mesh.

One of the best approaches in terms of initial stiffness, captured inside the strengthened arches category was found for the 100 mm of reinforcement at the extrados, as shown in Figure 6.9b and presented in Table 6.3. The numerical results show a premature failure, not observed in experiments. Therefore, it became unfeasible to capture the ductility experimentally.

For the 100 mm FRP width reinforcement at the extrados option, three hinges were formed clearly detected at successive stages in Figure 6.10. The fourth hinge was prevented and the mechanism of collapse was due to sliding of the foot arch, opposite to the loading point.

The 100 mm reinforcement width placed at the extrados did not delay the occurrence of the first two hinges because both appeared at the intrados, where no reinforcement is available. The third hinge was detected just before the peak load was attained, Figure 6.11a and Table 6.5. A well defined deformed shape at the left half of the arch, was observed in contrast with a less deformable right half when comparing with the plain arch, as depicted in Figure 6.11b. The smaller deformability of the right half is directly related to the presence of the FRP.

Using the same numerical model but increasing the total FRP strip width up to 160 mm a different numerical response was obtained. This result presented



(a) (b)

Figure 6.11: Numerical CSE arches with 100 mm FRP width: (a) Reproduction of plastic hinges on the load-displacement diagram; (b) the deformed mesh over the undeformed shape.

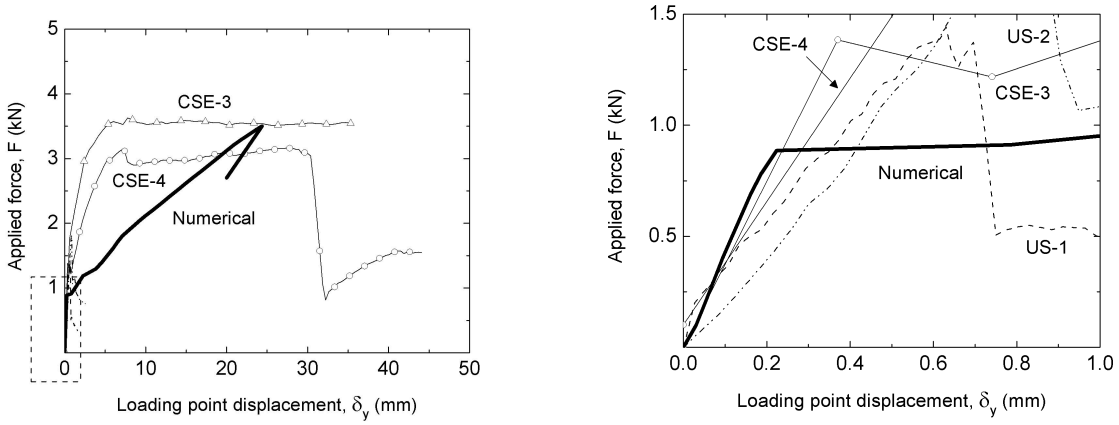
the closest peak load approach of the experimental specimen as well as the best accuracy in terms of the initial stiffness, as shown in Figure 6.12b and presented in Table 6.3.

The mechanism of collapse and the third hinge were detected sooner for the model with 100 mm compared with the 160 mm of GFRP material, Figures 6.11a and 6.14a. Based on the maximum load and deformability reached by the numerical models representing the CSE series, it seems that the second model with higher GFRP quantity results not only in a slightly stiffer but also a more deformable structure. Such remark can be made by comparing Figures 6.11b and 6.14b, together with the information of Tables 6.3 and 6.5 regarding stiffness and peak loads for the models mentioned.

6.6 Continously strengthened arches at the intrados

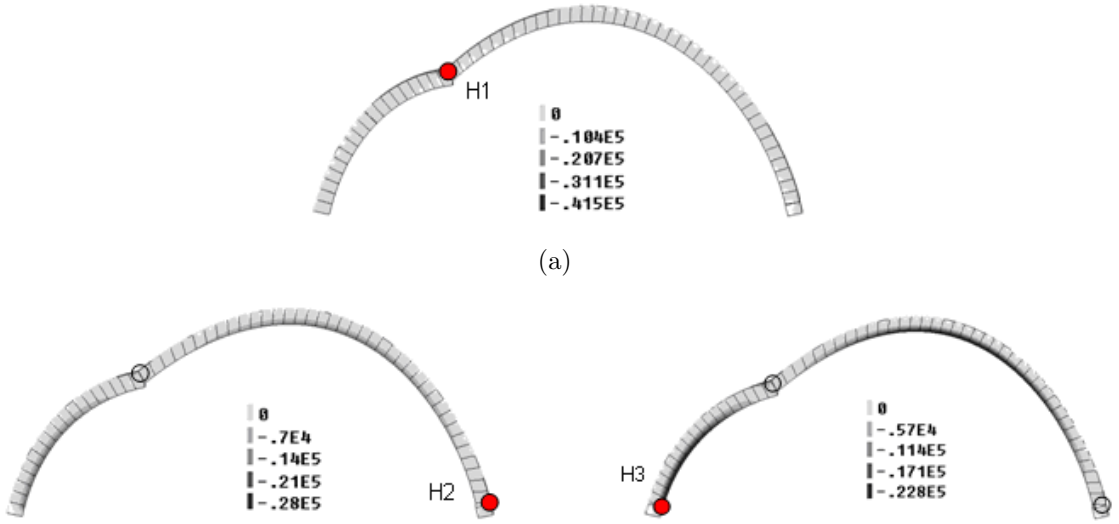
When the GFRP reinforcement is placed at the intrados, it contributes in keeping the bricks together. For the intrados reinforcement case, experimental failure was characterized by the detachment of the composite material.

Figure 6.15a compares both the numerical and experimental responses for the continuous length reinforcement option at the intrados. Numerical analyses show



(a) (b)

Figure 6.12: Experimental CSE-3 and CSE-4 series compared with its corresponding numerical response: (a) load-displacement curve of the loaded point; (b) zoom of the initial diagram.

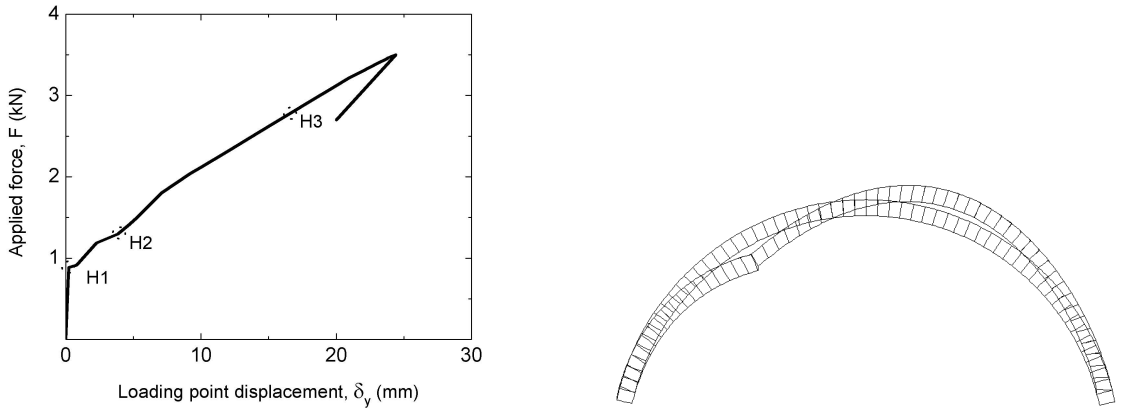


(a)

(b) (c)

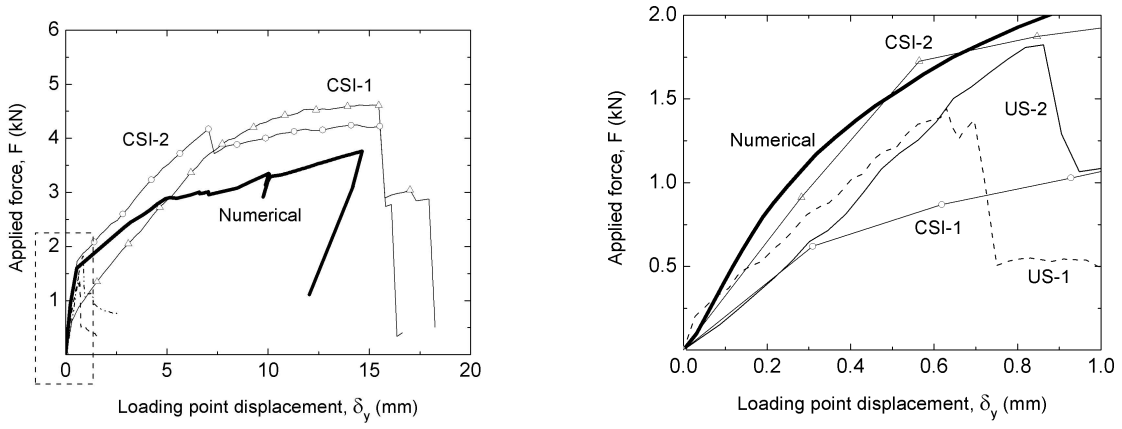
Figure 6.13: Hinge development sequence for the numerical CSE arch with 160 mm strip width, including principal compressive stresses (kN/m^2) depicted on the incremental deformed mesh.

that arches with continuous GFRP length reinforcement placed at the intrados present higher peak load average values, when compared with continuous length GFRP reinforcement placed at the extrados, Table 6.5. For the reinforcement



(a) (b)

Figure 6.14: Numerical CSE arches with 160 mm: (a) detection of hinges on the load-displacement diagram; (b) the deformed over the undeformed shape.



(a) (b)

Figure 6.15: Experimental CSI-1 and CSI-2 series compared with its corresponding numerical response: (a) load-displacement curve of the loaded point; (b) zoom of the initial diagram.

placed at the intrados, the load smoothly increases at a lower rate. The zoom of the initial diagram in Figure 6.15b is near the experimental initial stiffness. The numerical model for the continuous strengthening at the intrados utilizing 100 mm shown in Figure 6.15a can be therefore, considered one of the best approaches to experiments, in terms of maximum load and deformability.

The continuous reinforcement, applied either at the intrados or at the extrados of the arches surface allow three hinges to develop. The collapse mechanisms result in sliding of the foot arch with FRP detachment. With only 3 hinges developed for the intrados option, the deformed shape of Figure 6.16, where hinges development for the CSI standard arch is shown, is similar to the localized strengthening selection, Figure 6.7.

For both intrados and extrados continuous strengthening, the last two plastic hinges appeared approximately in the same section, whereas the first hinge location was fully conditioned by the strengthening strategy, Figure 6.16c.

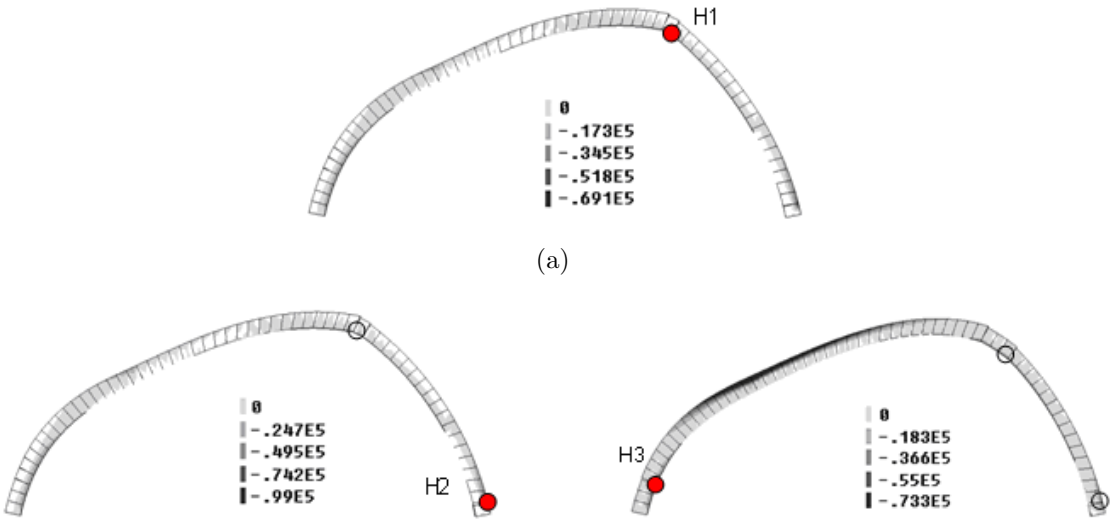
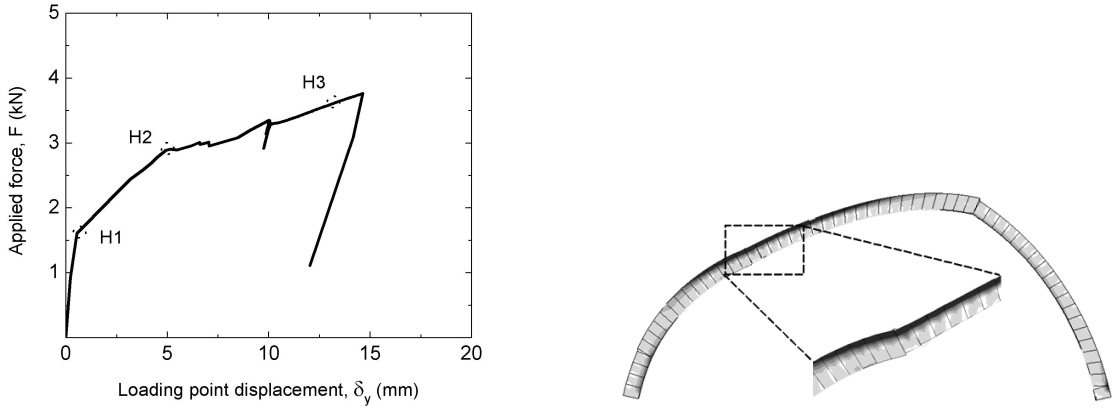


Figure 6.16: Hinge development sequence for the numerical CSI standard arch (model without anchor devices), including principal compressive stresses (kN/m^2) depicted on the incremental deformed mesh.

Figure 6.17 presents hinges detected in the numerical response along the curve of the loading point *versus* the displacement for the CSI standard arch. The hinges detected mark perceptible stiffness changes as some of the previous numerical models presented, compare Figure 6.17a with Figure 6.11a. The identification of

the plastic hinges in experiments is harder than in the numerical models since they can only be detected after presenting an extensive development, enough to be macroscopically visible.



(a) (b)

Figure 6.17: Numerical CSI arches without anchor devices: (a) Representation of plastic hinges on the load-displacement diagram; (b) FRP detachment on the deformed mesh.

On the other hand, by means of the numerical model graphical interface, hinges could be detected timely using an animated sequence of deformed meshes where stresses changes could identify stresses concentrations, Figure 6.17b.

For the continuous strengthening at the intrados surface, after three hinges were developed, the mechanism of failure was composed by the detachment of the FRP strip from the inner surface. Such fact is exemplified by a zoom at the loaded point illustrated in Figure 6.17b. Together with the experimental load-displacement curve at the loaded point, the initial stiffness and the mechanism of failure of FRP detachment was captured by the corresponding numerical model, a remarkable issue for the continuous arches strengthened at the intrados.

To avoid detachment of the FRP reinforcement, anchorage devices were used in the last pair of experimental masonry arches strengthened at the intrados. The modelling of the non conventional anchor spikes adopted was accomplished with unidirectional springs connecting the FRP to masonry. These elements were placed at masonry courses replicating its applied position in the laboratory. A stiffness calibration value of 45238 N/mm came from the pull-off tests results described in Chapter 3.

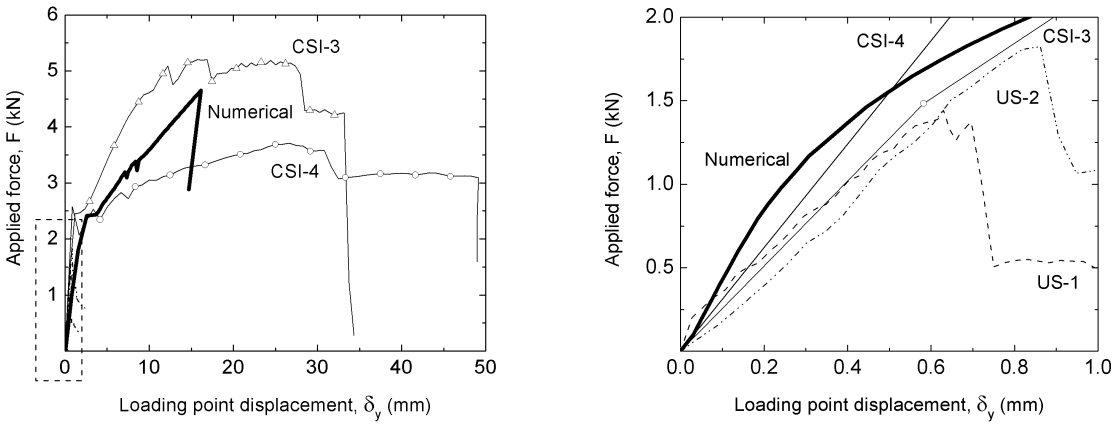


Figure 6.18: Experimental CSI-3 and CSI-4 series compared with its corresponding numerical response: (a) load-displacement curve of the loaded point; (b) zoom of the initial diagram.

The inclusion of the spikes made possible to reach a higher peak load, positioning it in the best matching result in terms of maximum sustained load (F), Figure 6.18a and Table 6.5. Because of the restrictions imposed by the simplification of the spikes, the model was capable to reproduce only half of the complete deformation for these specimens.

The use of springs in the numerical model modified the hinges appearance and sequence without changing their quantity. Despite of fact that the first couple of hinges switched their location, remaining in the inner and the outer perimeter respectively as shown in Figures 6.19a and 6.19b, the third hinge was kept at the intrados of the left foot arch. For a complete comparison, observe each frame with Figure 6.16.

The numerical model shows a slower increase of the displacement, when compared to the experimental tests results, but the value for the peak load was in good agreement with the experimental average value. Thus, the numerical model is believed to be a useful tool for the estimation of the ultimate strength for masonry arched structures, a very important task in the assessment of historical buildings.

The numerical model was capable of describing the strengthening at the intrados, maintaining the arch stiffness stability for a longer test time than at the extrados, meaning that part of the load-displacement diagram between the formation of the first hinge (region where the stiffness exhibits a sudden decrease) and

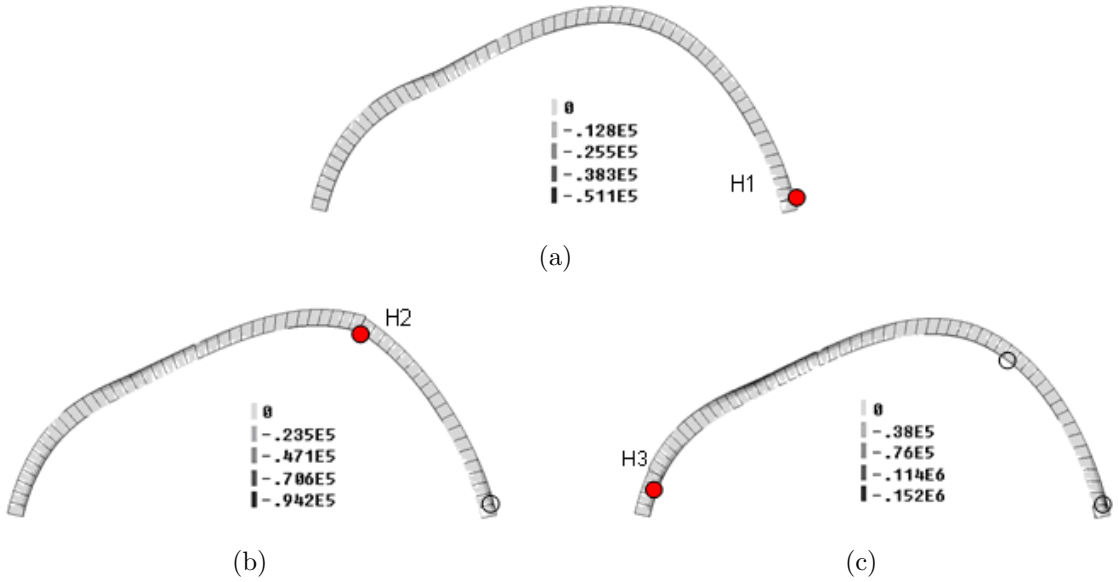


Figure 6.19: Hinges developed for the numerical CSI model with anchor devices, including principal compressive stresses (kN/m^2) depicted on the incremental deformed mesh.

the peak load notably broadens, even when a couple of hinges had been developed.

With the developed model was possible to describe failure by crushing as a result of an ultimate compressive force collected by a small fraction of the cross section if numerical compressive fracture energy and compressive strength of masonry are assessed correctly.

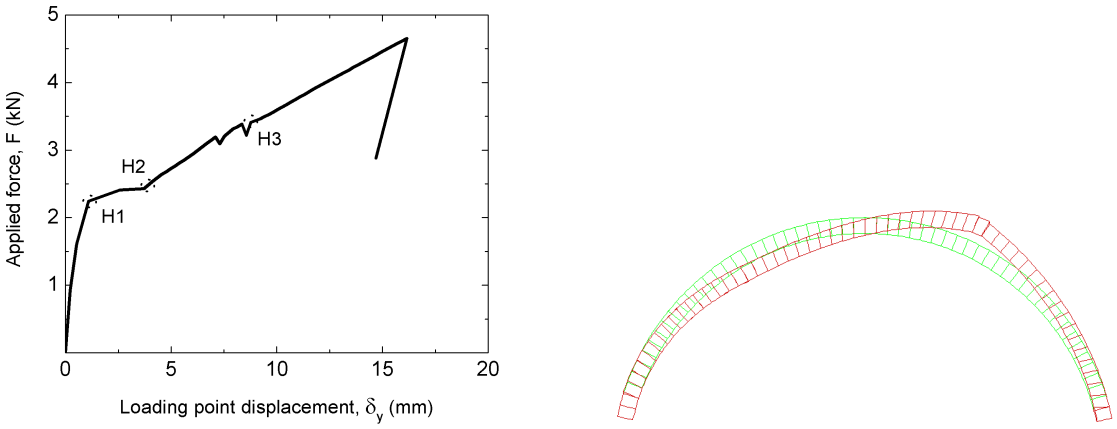
In the experiments, a rotation of the masonry joint was observed near the abutment, indicating that the values used for the cohesion and the fracture energy between FRP and masonry have to be increased to avoid the detachment of the reinforcement and thus prevent the opening of a crack at that point.

Because of probable stress concentrations, at the loading point, influenced by the springs, the spikes did not delay the hinge formation when compared to the specimen without any anchor device.

An experimental and numerical comparative information regarding peak load obtained is presented in Table 6.5.

It was observed that after crack formation, slip occurs in the bed joint and the mechanical response is influenced by dilatancy.

The composite model adopted in the numerical simulations, used in the modelling of the bond test specimens, was exhaustively tested to simulate unreinforced



(a) (b)

Figure 6.20: Numerical CSI arches with spikes anchor devices: (a) Representation of plastic hinges on the load-displacement diagram; (b) detachment on the deformed shape.

masonry . For the current research, interfaces calibrated to simulate mortar-brick joints were capable to reproduce plain masonry arches. On the other hand, when the same methodology was adopted to simulate FRP reinforcement results not always satisfactory were obtained, since the micro-modelling did not capture properly the deformation along the loading history. Nevertheless, it was noted that the peak load was very well reproduced in most cases.

From the experience gained it is believe that FRP-masonry interfaces behave in a quite different way than masonry interfaces and, therefore, a different constitutive model should be used.

6.7 Second parametric study vs experimental results

At an initial stage of this research project an assessment of the mechanical behaviour of the arches was performed, before starting the experimental test program, *e.g.*, without any experimental calibration. However, after experiments, a second and final parametric study including all the experimental properties was carried out. In Figure 6.21, adopting the mechanical values obtained in the experimental phase and utilized in the numerical models, the final parametric study

is displayed. The three frames of Figure 6.21 can be compared with those in Figure 6.1 to check the improvements achieved.

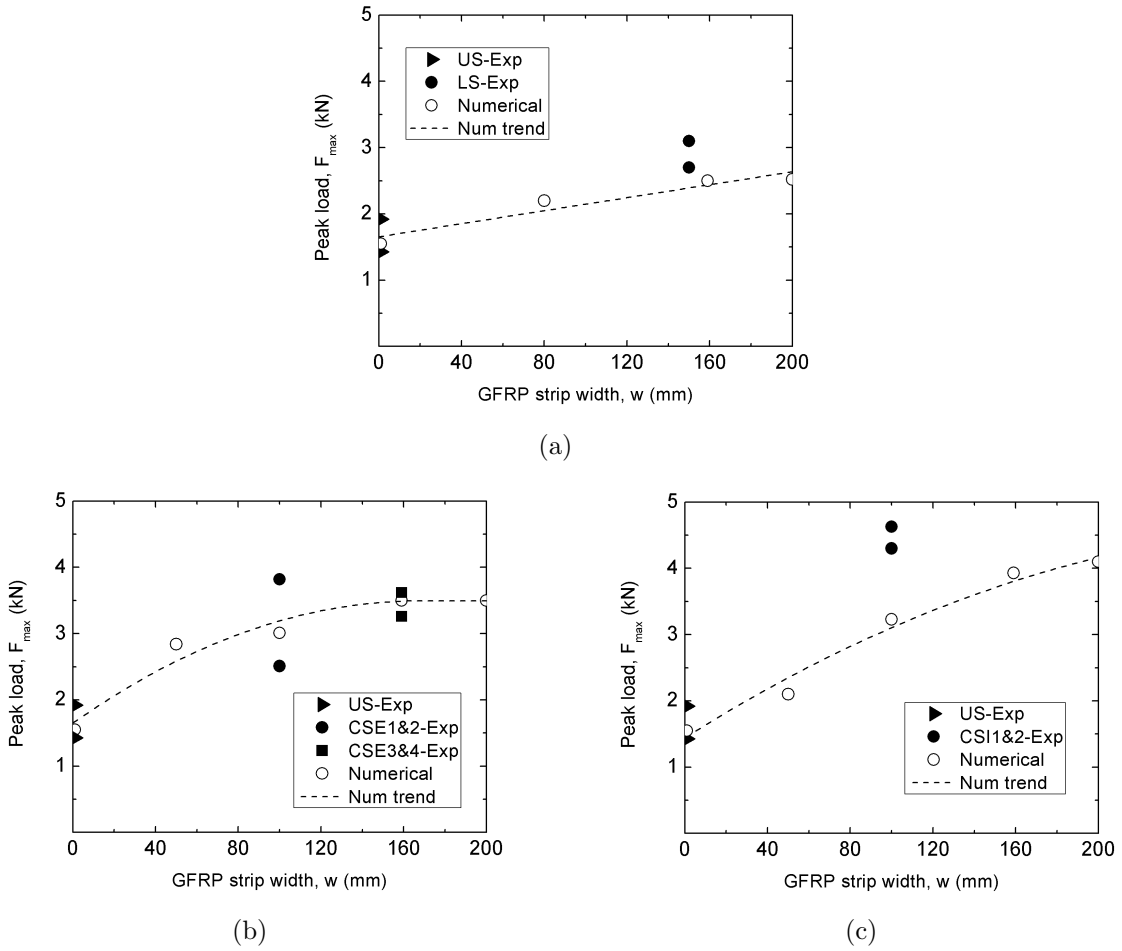


Figure 6.21: Second parametric study showing the influence of the strip width on the load carrying capacity of the arches reinforced: (a) locally; (b) at the extrados and (c) at the intrados.

Similar nomenclature was followed as previously adopted, where the empty circles represent the numerical peak values corresponding with a given FRP width in mm. The filled figures represent peak values of the load carrying capacity obtained from experimental tests. An additional discontinuous line was added with the purpose to indicate the tendency for each analysis carried out.

Since the properties of the masonry joints remained unchanged, the biggest changes were at the composite interfaces. Although such modifications did not change the masonry arch failure modes they can be easily observed by the trends

depicted.

In this second parametric study results of the model for the arches with localized reinforcement presented good agreement, compare Figure 6.1a with Fig. 6.21a. A significant improved achievement for the continuous strengthening at the extrados was marked by reaching the experimental peak loads recorded, as well as a linear tendency layout for more than 160 mm.

For the continuous strengthening at the intrados a steady increment tendency was captured and convergence of the optimal length was also founded. The optimal strip width was obtained when modelling the CSE with 160 mm of FRP strip width, just like the preliminary parametric. For smaller FRP strip width than 160 mm insignificant changes were recorded when compared with 100 mm, Figure 6.21c.

This parametric study, duly compared against experiments, represents a step forward in the definition of appropriate strengthening amounts, for different strengthening strategies.

6.8 Summarized conclusions

The current chapter presents a numerical model to reproduce experimental results concerning masonry arches reinforced with composite materials. Details of the modelling have been explained and discussed. With the plane stress numerical model constructed, it was possible to obtain similar peak loads and failure mechanisms. Regarding the experimental curve containing the sustained capacity load against displacement beneath the loaded point, the numerical model was not able to capture such deformation.

It is likely that adopting a better constitutive law for shear may possible to lead to some improvements in terms of deformation. As an alternative solution to overcome this limitation, a deeper interface characterization can solve the lack of deformation for some of the specimens. Such kind of tests requires a delicate setup and results discussion due to the fragility of the materials adopted when historical constructions is on the target, as performed in Chapter 3.

The inherent potential of the FEM used in the numerical model is demonstrated by the successful prediction of the sequence and appearance of hinges. By means of the graphical interface included in the commercial program, an animated visual

aid, allowed to display the stress distributions at different stages including its incremental and total deformed shape. Such tool, indicated stress concentration at the hinge rotation face (inner or outer).

It can be seen that the best numerical responses were the unstrengthened and continuous strengthened at the intrados arches without non-conventional anchor devices.

A successful approach using the numerical models was accomplished by capturing detachment of the FRP when simulated at the inner surface of the arched structure. It seems that the non-conventional anchor systems can be calibrated together with a different shear law as the adoption of simple springs to reproduce spikes applied in the laboratory, shows a slight increment on the peak load, without modifying the deformability obtained previously.

For semicircular masonry arches without reinforcement subjected to a concentrated load at the quarter span, four plastic hinges were expected to occur, Heyman (1982). Since the mechanisms related to failure of masonry structures strengthened by FRP sheets is barely studied, attention should be given to this matter and experimental research should focus on the structural behaviour of reinforced arches with FRP as done in this chapter.

A finite element model was developed to acquire a better understanding of the FRP-strengthening effects. The assessment of a theoretical model has been conducted using the results of tests carried out on twelve scaled specimens.

The continuous application of FRP as a reinforcement for plain arches, changed the four hinge mechanism of failure. Instead, the arches strengthened continuously develop only three hinges and one additional “release”. The mechanism of failure was due to sliding at the foot arch.

Chapter 7

Concluding remarks and future work

The present chapter reports a summary and recommendations of the work done. Conclusions and suggestions for further work within this research area are given. Since all the materials tested were chosen on purpose to reproduce the mechanical properties of historical masonry constructions, there is no specific standard process available to the knowledge of the author. The most significant contributions of this thesis are: study of the bonding between the FRP and the masonry, and the development of a new strengthening system for the masonry joints of handmade masonry using low strength material.

Since representative results are concentrated in the bonding process when structures are reinforced, main emphasis was centred on the masonry substrate. However, scarce masonry related studies are found in the literature, probably due to difficulties on the construction of a reliable setup able to capture adequate key parameters and overcome the low tensile strength of the masonry. For this reason the behaviour of the interface properties between the masonry and the composite materials was deeply studied.

With the proposed setup device described in the third chapter, it became possible to characterize the FRP-masonry interface behaviour, in terms of the stress distribution along the bonded length. For the FRP composite application, it was concluded that the quantity of the putty first layer must be minimized since excessive impregnation can lead to lack of adherence of the FRP sheets with adjacent layers.

Based on the bond test specimens results it is believed that when a tensile failure mode occurred, the total substrate strength was more than optimal. When most of the detached strips were accompanied by particles of masonry remains, then optimum strength was taken from the substrate. Experimental tests carried out gave a strong evidence that the type of failure mode is strongly dependent upon the anchorage type. Changes on the curved geometry specimens must be taken only as indicative results, since the absence of a perpendicular force (responsible for the detachment) was missing just like in practical cases.

To show the most representative objectives inside the current work, one specimen G150RS-n was taken as a reference to compare with four other categories. Although length, shape, material and anchorage were considered as the most relevant variables, there are certainly some other combinations that could be tagged as a future work including FRP durability leading to a considerable increment on the number of tests possibilities. Particular interest is reserved for the anchorage devices since it was proved, during the experimental campaign, that its effectiveness can avoid or delay the detachment of the FRP material from the substrate.

Specific results revealed that specimens G200RS had bonded length in excess to attain the maximum FRP normal stress. This means that for an anchorage length longer than 200 mm, the failure pattern will change from sliding to tensile.

In general it was observed that for a low load level, normal stresses were mobilized in a relatively small FRP length close to its loaded end. However, for a high load, stresses distributed along the entire interface keeping approximately a parabolic shape.

After testing and analysing masonry arched structures, the theoretical hypotheses were confirmed, such as four hinges form a mechanism of collapse. The experiments demonstrated how fragile plain masonry arches are. The localized strengthening of damaged arches did not changed their failure modes, instead only slightly higher peak loads were attained. Despite of this option to reinforce structures partially might be taken as a representative real case study, it may be concluded that such alternative is not recommended since the masonry fragility is kept without improving its deformation capability. The proposed work is novel as arched structures strengthened with FRP including non-conventional anchorage devices has not been addressed, previously.

For the continuous strengthening options, either at the extrados or at the intrados, the following concluding remarks are drawn: For the continuous strengthening at the extrados (CSE), the optimal width was found, corroborated not only by the results of the parametric study but also by the experimental results, which demonstrated that a FRP strip with more than 160 mm of width did not produce a relevant improvement or changes in the load carrying capacity or modified failure mode patterns. The debonding phenomenon only affected the arches where the GFRP strips were placed at intrados, whereas for specimens strengthened at extrados failure occurred due to sliding of the arch foot localized at the opposite side of the loaded point. Another important feature of the continuously strengthened specimens is the large deformation capacity exhibited prior to failure, which provides the arches with an important ductile behaviour.

Based on the results obtained, it was observed that strengthening of arches with composite materials, changes its potential damage modifying the failure mechanism and unknown response when adding non-conventional anchorage devices tested might be obtained.

Concerning the reproduction of experimental results of bond test specimens and masonry arches with the numerical models constructed, results recorded experimentally were simulated with certain accuracy considering the complex phenomena involved. Moreover, the stress distribution along the anchorage length gave, in general terms, an acceptable accuracy when compared with the experimental response.

Higher differences were encountered when the numerical response was compared with the experimental ranges of variations (designated as envelopes within the body of the thesis) calculated with the analytical bond-slip formulation. As stated in chapter five, careful considerations must be taken due to the interpolated data from the experimental data source. While interpolation between discrete points could give smoother outputs tendencies it also can introduce errors. Because the analytical formulation was based on discrete points measurement during testing, the strains computed gave better results than the bond stresses along the anchorage length.

The numerical failure mode depends on the anchorage length. When the softening behaviour reached most of the anchorage length, FRP strip sliding occurred and consequently collapse was observed. For the largest anchorage length (200

mm) the FRP strip failed in tension before all the anchorage length was under the softening effect.

The stress distributions along the anchorage length for the GFRP were parabolic before reaching its maximum. On the other hand for the CFRP the shape of the stress distribution was no longer parabolic, as more uniform tendencies were observed.

The residual stress value for the bond tests was around 10% of the peak value, reasonably low in agreement with the observation that friction at the interface is quite low once the micro-cracks in the masonry are generated. The experimental results from Chapter 3 can then be used to develop and propose an appropriate constitutive law for FRP-interfaces under tensile and shear stresses.

The numerical model constructed to simulate the masonry arches behaviour, was capable of capturing both the experimental initial stiffness and peak loads. Localization of damage indicated by hinge and analogue deformation shapes were similar to that observed in the experimental tests.

For semicircular masonry arches without reinforcement under the application of a concentrated load at the quarter span, four plastic hinges were observed in accordance with the theoretical hypothesis. Since the mechanisms related to failure of masonry structures strengthened with FRP sheets are rarely studied, attention should be given to this matter and further experimental research should be focused on the structural behaviour of more complex assembles of arches reinforced with FRP. Future work should include arrangements of the units in canon vaults built formless and crossed vaults strengthened with FRP materials. It is desirable to test experimentally structural masonry subjected to loading at mid span and compare results between scaled and real size arches.

The continuous application of FRP as reinforcement of plain arches, changed the four hinge mechanism. Instead, the arches continuously strengthened developed only three hinges and a corresponding new failure mechanism.

It is likely that by adopting another constitutive law for the interface might be possible to obtain some improvements in terms of deformation. As an alternative solution to overcome this limitation, a deeper interface characterization may solve the lack of deformation for some of the specimens. Such kind of tests requires a setup, capable to submit the specimens to direct shear stress, and careful results

discussion due to the fragility of the materials chosen when historical constructions is on the target, as done in Chapter 3.

Besides corroborating the failure modes observed at the experimental test, the numerical model for masonry arches was able to reproduce the detachment of the FRP when modelled at the inner surface. It is expected that eventually guidelines for design and theoretical simplified models for practitioners, both rational and with a guaranteed approximation could be proposed based on the results obtained here.

References

ACI 440 (2004). *Guide for the Design and Construction of Externally Bonded FRP System for Strengthening Unreinforced Masonry Structures*. ACI Committee: ACI 440.

ACI 440R-96 (1996). *State of the art Report on Fiber Reinforced Plastic (FRP) Reinforcement for Concrete Structures*. Reported by ACI Committee 440.: ACI 440R-96.

ACI 530.1-95/ASCE 6-95/TMS 602-95 (1995). *Specification for Masonry Structures*. Reported by the Masonry Standards Joint Committee: ACI 530.1-95/ASCE 6-95/TMS 602-95.

Aiello, M., L. De Lorenzis, N. Galati, and A. La Tegola (2004). Bond between fpp laminates and cruved concrete substrates with anchoring composites spikes. Technical report, Innovative materials and Technologies for Construction and Restoration, pp. 45-56, Lecce, June 6-9.

Aiello, M. A. and S. M. Sciolti (2006). Bond analysis of masonry structures strengthened with cfrp sheets. *Construction and Building Materials 20*, 90–100.

Anthoine, A. (1992). In-plane behavior of masonry: A literature review. Technical report, Report EUR 13840 European Standard, Commission of the European Communities, JRC - Institute for Safety Technology, Ispra, Italy.

ASCE 5-95TMS 402-95 (1989). *Building Code Requirements for Masonry Structures*. American Concrete Institute: ASCE 5-95TMS 402-95.

Ascione, L., V. P. Berardi, L. Feo, and G. Mancusi (2005). A numerical evaluation of the interlaminar stress state in externally frp plated rc beams. *J. Compos Part B: Eng 36*, 83–90.

Ashurst, J. (1984). Mortars, plasters and renders in conservation. Technical report, Ecclesiastical Architects and Surveyors Association, London.

ASTM C1314-98a (1999). *Standard Test Method for Construction and Testing Masonry Prisms Used to Determine Compliance with Specified Compressive Strength of Masonry*. March: ASTM C1314-98a.

ASTM C666/C666M-03 (1997). *Standard test method for resistance of concrete to rapid freezing and thawing*. Vol. 4.02: ASTM C666/C666M-03.

ASTM C67-98a (1998). *Standard Test Methods for Sampling and Testing Brick and Structural Clay Tile*. March: ASTM C67-98a.

ASTM D2247 (1995). *Standard practice for testing water resistance of coating in 100% Relative Humidity*. Annual Book of ASTM Standards, V.6.01, pp. 291-294: ASTM D2247.

ASTM D3039/ D3039-93 (1993). *Standard Test Method for Tensile Properties Matrix Composite Materials*. Vol. 08.01, April: ASTM D3039/ D3039-93.

ASTM D4541-95 (1995). *Standard Test Method for Pull-off Strength of coatings Using Portable Adhesion Testers*. February 15th: ASTM D4541-95.

ASTM D638-97 (1988). *Standard Test Method for Tensile Properties of Plastics*. Vol. 08.01, April: ASTM D638-97.

ASTM E111-82 (1988). *Standard Test Method for Young's Modulus, Tangent Modulus and Chord Modulus*. Vol. 03.01, May: ASTM E111-82.

ASTM G53 (1995). *Standard practice for operating light- and Water-Exposure Apparatus (Flourescent UV-Condensation Type) for Exposure of Nonmetallic Materials*. Annual Book of ASTM Standards V.14.02, pp. 1203-1211: ASTM G53.

Atkinson, R. H., B. P. Amadei, S. Sach, and S. Sture (1989). Response of masonry bed joint in direct shear. *J. Structural Eng, ASCE 115(9)*, 2276–2296.

Aveston, J., A. Kelly, L. McCartney, and J. M. Sillwood (1982). Long term strength of glass reinforced plastics. In *Proceedings of the ICCM-IV: Progress in Science and Engineering of Composites.*, Tokyo, ICCM, pp. 947–955.

Barros, J. and D. Ferreira (2005). Partial versus full wrapping confinement systems for concrete columns. In *ALEXANDER, Mark G. [et al.], ed. lit. - "Concrete repair, rehabilitation and retrofitting: proceedings of the International Conference on Concrete Repair, Rehabilitation and Retrofitting (ICCRRR), 1, London: Taylor & Francis*, Cape Town, South Africa, pp. 1123–1129.

Basilio, I., D. V. Oliveira, and P. B. Lourenço (2004). Optimal frp strengthening of masonry arches. In *13th International Brick/Block Masonry Conference*, Amsterdam, The Netherlands, pp. 361–370.

Basilio, I., D. V. Oliveira, and P. B. Lourenço (2005). Behaviour of strengthened masonry arches. Technical report, Report 05-DEC/E-21, Universidade do Minho, Guimarães, Portugal.

Bati, B., L. Rovero, and U. Tonietti (2003). Four point bending test on masonry elements reinforced with composite materials. In *Proceedings of the International Conference Composites in Construction September 16-19*, Consenza Italy, pp. 171–176.

Benmokrane, B., P. Wang, T. Ton-That, H. Rahman, and J. Robert (2002). Durability of glass fibre reinforced polymer reinforcing bars in concrete environment. *ASCE J. of Composite for Construction 6(2)*, 143–153.

Binda, L., C. Tiraboschi, M. Roberti, and G. Baronio (1996a). Experimental and numerical investigation on a brick masonry building prototype, measuring masonry material properties detailed results from an extensive experimental research part: I test on masonry components. Technical report, Polytechnic of Milan, April, Report 5.1 DSI.

Binda, L., C. Tiraboschi, M. Roberti, and G. Baronio (1996b). Experimental and numerical investigation on a brick masonry building prototype, measuring masonry material properties detailed results from an extensive experimental research part: I test on masonry components. Technical report, Polytechnic of Milan, April, Report 5.1 DSI.

Bizindavyi, L. and W. Neale (1999). Transfer lengths and bond strength for composites bonded to concrete. *J. Composites for Construction 3(4)*, 153–160.

Bonaldo, E., J. O. Barros, and P. B. Lourenço (2005). Bond characterization between concrete substrate and repairing sfrc using pull-off testing. *Int. J. Adhesion & Adhesives 25*, 463–474.

Boothby, T. E. (2001). Analysis of masonry arches and vaults. *Prog. Struct. Eng. Mater, Pennsylvania State University, USA 3*, 84.

Brencich, A., L. Gambarotta, and S. Lagomarsino (2000). *Catania Project: Research on the Seismic Response of Two Masonry Buildings (in Italian)*, Chapter 6. Analysis of a masonry building in Via Martoglio. University of Genova, pp. 107–151. Rome: CNR–Gruppo Nazionale per la Difesa dai Terremoti.

Bresse (1848). Etudes thoriques sur la rsistance des arcs employs dans les ponts en fonte ou en bois. *Annales des Ponts et Chausses 25*, 150–193.

Brosens, K. and D. V. Germet (1998). Plate end shear design for external cfrp laminates. In *Proceedings of FRAMCOS-3, Aedificatio Publishers*, Freiburg, Germany, pp. 1793–1804.

Cao, S. Y., J. F. Chen, and J. W. Pan (2004). Study on bond stress-slip behaviour of frp-concrete interface using electronic speckle pattern interferometry technique. In *Proceeding of the Second International Conference on FRP composites in civil engineering*, Adelaide Australia December, pp. 8–10.

Casareto, M., A. Oliveri, and A. Romelli (2002). Strengthening of masonry: Opportunities and challenges in the use of composites. Master's thesis, School of Engineering University of Genova, under the sponsorship of the Center for Infrastructure Engineering Studies (CIES), University of Missouri Rolla, CIES 03-40, April, pp. 360.

Castigliano, C. (1879). Thorie de l'equilibre des systmes lastiques et ses applications. Technical report, -, Torino.

CEB-FIB (1993). Externally bonded frp reinforcement for rc structures, technical report on the design and use of externally bonded fibre reinforced polymer reinforcement (frp ebr) for reinforced concrete structures. Technical report, prepared by the task group 9.3 FRP (Fibre Reinforced Polymers), reinforcement for concrete structures.

Ceroni, F., M. Pecce, G. Manfredi, and G. Marcari (2003). Experimental bond behaviour in masonry elements externally reinforced with frp laminates. *J. Composites for Construction 1*, 313–318.

Chen, J., Z. Yang, and G. Holt (2001). Frp or steel plate to concrete bonded joints: Effects of test methods on experimental bond strength. *Steel and Composites Structures 1(2)*, 231–244.

Chiari, G., M. L. Santarelli, and G. Toracca (1992). Characterizzazione delle malte antiche mediante l'analisi di campioni non frazionati. Technical report, 111-137., Materiali e Strutture, 3.

Chin, J. W., K. Aouadi, and T. Nguyen (1997). Effects of environmental exposure on fiber-reinforced plastic (frp) materials used in construction. *J. Compos Technol Res 19(4)*, 205–13.

CNR-DT 200/2004 (2004). *Guidelines for Design, Execution and Control of Strengthening Interventions by Means of Fibre-reinforced Composites Materials, reinforced concrete and prestressed concrete structures, masonry structures*. CNR - Advisory Committee on technical regulations for constructions, ROME CNR July 13th: CNR-DT 200/2004.

Creazza, G., R. Matteazi, S. Ana, and R. Vitaliani (2002). Analyses of masonry vaults: A macro approach based on three-dimensional damage model. *J. Structural Engineering 128(5)*, 646–654.

Crisfield, M. A. (1984). A finite element computer program for the analysis of masonry arches. Technical report, Department of Transport, Crowthorne., Technical Report Laboratory Report 1115.

Croci, G. (1998). The conservation and structural restoration of architectural heritage. Technical report, Advances in Architectures Series, Computational Mechanical Publications, Southampton UK, pp. 295.

De Lorenzis, L. (2000). Strengthening of the structures with near surface mounted frp rods. Technical report, University of Missouri-Rolla, pp. 1-153.

De Lorenzis, L. (2002). *Strengthening Of RC Structures with Near-Surface Mounted FRP Rods*. Ph. D. thesis, Univ. of Lecce, Lecce, Italy.

De Lorenzis, L. and A. Nanni (2002). Bond between near surface mounted frp rods and concrete in structural strengthening. *ACI J. Struct. Eng. March-April 99(2)*, 123–133.

De Lorenzis, L., D. Tinazzi, and A. Nanni (2000). Near-surface mounted frp rods for masonry strengthening: Bond and flexural testing. Technical report, Mechanism of Masonry Structures Strengthened with FRP Materials: Modelling, Testing, Design, Control, December 7th , pp. 7-18, Venice.

Department of Defense (1997). *Guidelines for characterization of structural materials*. Polymer Matrix Composites Handbook MIL-HDBK-17-1E, Vol. 1, Philadelphia, PA, USA.: Department of Defense.

DIANA (1999). *TNO Building and Construction Research User's Manual Release 8.1.2*. Delft, The Netherlands: DIANA.

Dillard, D. A. (1991,). *Viscoelastic behavior of laminated composite materials* (Reifsnider KL, editor. ed.). Amsterdam, Elsevier.: Fatigue of Composite Materials.

Dolan, C. (1993). Frp development in the united states. In *Fiber- Reinforced-Plastic (FRP) Reinforcement for Concrete Structures: Properties and Applications*, Developments in Civil Engineering, 42, pp. 129–163.

Drysdale, R. G., A. A. Hamid, and L. R. Baker (1993). Masonry structures, behaviour and desing. Technical report, Second Edition, pp. 888., Boulder Colorado.

Efstathiadis, E. (2000). Greek concrete of three millenniums. Technical report, Technical Report, Research Center of the Hellenic Ministry of Public Works, Athens, Greece.

Erdoğan, T. Y. (2002). Materials of constructions. Technical report, METU Press., Ankara.

Eshwar, N., T. Ibell, and A. Nanni (2005). Cfrp strengthening of concrete bridges with curved soffits. In *A. Structural Faults and Repairs, CD-ROM Version Editor-M. Forde*, Commonwealth Institute, London, UK, pp. 1–10.

EU-India ALA/95/23/2003/077-122 (2006). *Identification of strengthening strategies*. EU-India economic cross cultural programme, Improving the seismic resistance of cultural heritage buildings, October: EU-India ALA/95/23/2003/077-122.

European Norm EN 1015-11 (2004). *Methods of test mortar for masonry Part 11: Determination of flexural and compressive strength of hardened mortar*. August.: European Norm EN 1015-11.

Fernandes, F. and P. B. Lourenço (2005). On the usage of microdrilling for the assessment of the compressive strength of ancient clay bricks. *J. Material of Civil Engineering ASCE. article in press*, 15.

Focacci, F., A. Nanni, and C. Bakis (2000). Local bond-slip relationship for frp reinforcement in concrete. *J. Composites for Construction 4(1)*, 24–32.

Foraboshi, P. (2004). Strengthening of masonry arches with fiber-reinforced polymer strips. *ASCE J. Composites for Construction 8(3)*, 191–202.

Franke, L. and H. J. Meyer (1992). Predicting the tensile strength and creep rupture behavior of pultruded glass-reinforced polymer rods. *J. Mater Sci 27*, 4899–980.

Garrity, S. W. (1995). Retro-reinforcement - a proposed repair system for masonry arch bridges. In *In: Melbourne C, editor. Proceedings of the 1st international arch bridges conference*, Bolton (UK): Thomas Telford, pp. 557–66.

Giambanco, G. and L. Di Gati (1997). A cohesive interface model for the structural mechanics of block masonry. *Mech Res. Commum 24(5)*, 503–512.

Helbling, C. S. and V. M. Karbhari (2002). Environmental durability of e-glass/vinylsetr composites under the combined effect of moisture temperature and stress. In *Proceedings of the 2nd International Conference on Durability of Fibre Reinforced Polymer (FRP) Composites for Construction (CDCC'02)*, Montreal, Québec, Canada, 29-30 May, pp. 247–258.

Henriques, F. M. A. (1996). Testing methods for the evaluation of new mortars for old buildings. *Science and Technology for Cultural Heritage 5(1)*, 57–61.

Heyman, J. (1966). The stone skeleton. *Int. J. Solids Structures 2*, 249–279.

Heyman, J. (1969). The safety of masonry arches. *Int. J. Mech. Sci. 11*, 363–385.

Heyman, J. (1982). *The Masonry Arch*. Ellis Horwood Limited: Chichester, England.

Horiguchi, T. and N. Saeki (1997). Effect of test methods and quality of concrete on bond strength of cfrp sheet. Technical report, Japan Concrete Institute, Non-Metalic (FRP) Reinforcement for Concrete Structures, 1, Japan, pp. 265-270.

Huerta, S. (2001). Mechanics of masonry vaults: The equilibrium approach. In *Historical Constructions, possibilities of numerical and experimental techniques*, Meeting in Guimarães Portugal; ed. Paulo Lourenço and Pere Roca, pp. 47–70.

International Conference of Building Officials (1997). *Acceptance criteria for concrete and reinforced and unreinforced masonry strengthening using fiber-reinforced composite systems*. Whittier, AC 125, CA, USA: International Conference of Building Officials.

ISO 527-1 (1993). *Plastics Determination of tensile properties, Part 1: General Principles*. June 15$^{\text{th}}$: ISO 527-1.

ISO 527-2 (1993). *Plastics Determination of tensile properties, Part 2: Test conditions for moulding and extrusion plastics*. June 15$^{\text{th}}$: ISO 527-2.

ISO 527-5 (1997). *Plastics Determination of tensile properties, Part 5: Test conditions for unidirectional fibre-reinforced plastics composites*. April 15$^{\text{th}}$: ISO 527-5.

Karbhari, V. M., J. W. Chin, D. Hunston, B. Benmokrane, T. Juska, R. Morgan, J. J. Lesko, U. Sorathia, and D. Reynaud (2003). Durability gap analysis for fiber-reinforced polymer composite in civil infrastructure. *J Compos Constr 7(3)*, 238–47.

Karbhari, V. M. and M. Engineer (1996). Effect of environmental exposure on the external strengthening of concrete with composites short term bond durability. *J. of Reinforced Plastics and Composites 15*, 1194–1216.

Kirca, O. (2005). Ancient binding materials, mortars and concrete technology history and durability aspects. In *Structural Analysis of Historical Constructions - Modena, Lourenço & Roca (eds)*, Taylor and Francis Group, London ISBN 04 1536 379 9, pp. 87–94.

Kooharian, A. (1952). Limit analysis of voussoir (segmental) and concrete arches. *Journal of the American Concrete Institute 24*(4), 317–328.

Lissel, S. L. and A. Gayevoy (2003). The use of frp's in masonry: A state of the art review. In *Proc. International Conference on the Performance of Construction Materials*, Cairo, Egypt, pp. 1243–1252.

Litherland, K. L., D. R. Oakley, and B. A. Proctor (1981). The use of accelerated ageing procedures to predict the long term strength of grc composites. *Cement and Concrete Research 11*, 455–466.

Lofti, H. and P. Shing (1994). Interface model applied fracture of masonry structures. *ASCE J. Struct Eng. 102*, 63–80.

Lofti, H. R. and P. B. Shing (1995). An appraisal of smeared crack models for masonry shear walls analysis. *Comp. Struct 41(3)*, 413–425.

Lourenço, P. B. (1994). Analysis of masonry structures with interface elements: Theory and applications. Technical report, Delft University of Technology, Report 03-21-22-0-01, Delft, The Netherlands.

Lourenço, P. B. (1996). *Computational strategies for masonry structures*. Ph. D. thesis, Delft University of Technology, Delft, Netherlands.

Lourenço, P. B. and J. P. Martins (2001). Strengthening of the architectural heritage with composite materials. In *Proc. Composites in Constructions*, Figueiras *et al.* (eds), Swets and Zeitlinger, pp. 571–576.

Lourenço, P. B., K. Palácio, and J. O. Barros (2004). Design recommendations for reinforced masonry arches. In *Arch Bridges ARCH04 P. Roca and E. Oñate (Eds)*, CIMNE, Barcelona, 2004, pp. paper 2580.

Lourenço, P. B. and J. G. Rots (1997). A multi-surface interface model for the analysis of masonry structures. *J. Engrg. Mech. 123*(7), 660–668.

Lourenço, P. B., J. G. Rots, and J. Blaauwendraad (1998). Continuum model for masonry: Parameter estimation and validation. *J. Struct. Eng. 124*(6), 642–652.

Marfia, S. and E. Sacco (2000). Modeling of reinforced masonry elements. *Int. Journal of Solids and Structures 38*, 4177–4198.

Mays, G. C. and A. R. Hutchinson (1992). *Adhesive in Civil Engineering* (Hardback, 333 ed.). Cambridge University Press: ISNM 0521 36 677 X.

Miller, B. and A. Nanni (1999). Bond between cfrp sheets and concrete. In *Proceedings, ASCE 5th Materials Congress*, Cincinnati OH, L.C. Bank, Editor, May 10-12, pp. 240–247.

Neville, A. M. (1966). A general relation for strengths of concrete specimens on different shapes and sizes. In *Proc. Am. Concr. Inst.*, USA, 63, pp. 1095–1110.

Nkurunziza, G., A. Debaiky, P. Cousin, and B. Benmokrane (2005). Durability of gfrp bars: A critical review of the literature. *Prog. Struct. Engng Mater. 7*, 194–209.

O'Dwyer, D. (1999). Funicular analysis of masonry vaults. *Computers and Structures 73*, 187–197.

Oehlers, D. J. (2005). Development of design rules for retrofitting by adhesive bonding or bolting either frp or steel plates to rc beams or slabs in bridges and buildings. *Composites Part A: Applied Science and Manufacturing 32*, 1345–1355.

Oliveira, D. V. (2003). *Experimental and numerical analysis of blocky masonry structures under cyclic loading*. Ph. D. thesis, Univ. of Minho, Guimarães, Portugal. available from www.civil.uminho.pt/masonry.

Page, A. W. (1978). Finite element model for masonry. *J. Struc Eng., ASCE 104(8)*, 1267–1285.

Phillips, M. G. (1983). Prediction of long-term stress-rupture life for glass fiber-reinforced polyester composites in air and aqueous environments. *Composites 14(3)*, 270–275.

Poncelet, J. V. (1952). Examen critique et historique des principales thories ou solutions concernant l'quilibre des votes. *Comptes-rendus de l'Acadmie des Sciences 35(17)*, 494–502, 531–540, 577–587.

Porter, M. L., J. Mehus, K. A. Young, E. F. O'Neil, and B. Barnes (1997). Aging for fiber reinforcement in concrete. In *Proceedings of the Third International Symposium on Non-Metallic (FRP) Reinforcement for Concrete Structures: Non-Metallic (FRP) Reinforcement for Concrete Structures*, Tokyo, Japan Concrete Institute, pp. 59–66.

Proceq (1998). *Pull-off tester Dyna Z-16 datasheet*. Switzerland. S.A.: Proceq.

RILEM (1994). *Technical recommendations for the testing and use of constructions materials, LUMB1 - Compressive strength of small walls and prism*. Chapman & Hall. UK.: RILEM.

RILEM CPC8 (1975). *Modulus of elasticity of concrete in compression, - TC14-CPC. Draft: Materials and Structures*. Vol. 6, No. 30, November-December 1972. Final: 1975. French version: RILEM CPC8.

Saadatmanesh, H. (1997). Extending service life of concrete and masonry structures with fiber composites. *J. Construction and Building Materials 11(5-6)*, 327–335.

Saavedra, E. (1860). Nota sobre la determinacin del problema del equilibrio de las bvedas. *Revista de Obras Pblicas 8*, 101–104.

Schutte, C. L. (1994). Environmental durability of glass-fiber composites. *Materials Science and Engineering R13 7*, 265–322.

Sen, R., J. Rosas, S. Sukumar, and D. Snyder (1996). Durability and bond of afrp pretensioned piles. Technical report, University of South Florida, Tampa, FL, Report to the DOT, Vol. I.

Singer, C., E. J. Holmyard, A. R. Hall, and T. I. William (1965). *History of Technology* (Vol. 1 ed.). Oxford: Clarendon Press.

Slattery, K. (2000). Mechanistic model of the creep-rupture process in filamentary composites. In *Infrastructure: New Materials and Methods of Repair, Proceedings, Third Materials Engineering Conference*, San Diego, CA, pp. 215–222.

Smith, S. T. and J. G. Teng (2003). Shear-bending interaction in debonding failures of frp-plated rc beams. *Advances in Structural Engineering 6(3)*, 183–199.

Startsev, O. V., A. S. Krotov, and P. D. Golub (1999). Effect of climatic and radiation aging on properties of vps-7 glass fiber reinforced epoxy composite. *Polymer Degradation and Stability 63*, 353–359.

Sumon, S. K. (1997). Repair and strengthening of a damaged arch with built-in ring separation. In *In: Proceedings of the 7th international conference on structural faults and repair*, Edinburgh: Engineering Technics Press, pp. 69–75.

Täljsten, B. (1994). *Plate bonding: Strengthening of existing concrete structures with epoxy bonded plates of steel or fibre reinforced plastics, Doctoral thesis*. Ph. D. thesis, Luleä University of Technology, Sweden.

Täljsten, B. (1996). Strengthening of concrete prisms using the plate-bonding technique. *International Journal of Fracture 82*, 253–266.

Täljsten, B. (1997a). Defining anchor lengths of steel and cfrp plates bonded to concrete. *Int. J. Adhesion & Adhesives 17(4)*, 319–327.

Täljsten, B. (1997b). Strengthening of beams by plate bonding. *J. of Materials in Civil Engineering, November 1*, 206–212.

Täljsten, B. (2004). *FRP Strengthening of existing concrete structures - design guideline* (Third ed., pp. 228. ed.). Luleä University of Technology: ISBN 91-89580-03-6.

Tan, K. H. and M. K. H. Patoary (2004). Strengthening of masonry walls against outof-plane loads using fiber-reinforced polymer reinforcement. *J. Comput Constr-ASCE 8*, 79–87.

Tasi, M. Y., D. W. Oplinger, and J. Morton (1998). Improved theoretical solutions for adhesive lap joints. *International Journal of Solids and Structures 35(12)*, 1163–1185.

Teng, J. G., J. F. Chen, S. T. Smith, and L. Lam (2002). *FRP Strengthened RC Structures* (First ed.). UK: John Wiley and Sons.

Teng, J. G., S. T. Smith, J. Yao, and J. F. Chen (2003). Intermediate crack induced debonding in rc beams and slabs. *Construction and building materials 17*, 447–462.

Teng, J. G., H. Yuan, and J. F. Chen (2005). Frp-to-concrete interfaces between two adjacent cracks: theoretical model for debonding failure. *International Journal of Solids and Structures 42*, in press.

Teng, J. G., J. Zhang, and S. T. Smith (2002). Interfacial stresses in reinforced concrete beams bonded with a soffit plate: a finite element study. *Construction and Building Materials 16(1)*, 1–14.

Thomason, J. L. (2002). The interface region in glass fibre-reinforced epoxy resin composites: characterization of fibre surface coatings and the interphase. *J. Composites 26(7)*, 487–498.

Triantafillou, T. C. (1998). Strengthening of masonry structures using epoxy-bonded frp laminates. *Journal of Composites for Construction, ASCE 2(2)*, 96–104.

Triantafillou, T. C. and M. Fardis (1997). Strengthening of historic structures with composites materials. Technical report, Scientific Report, Materials and Structures, 30, October, 489-496.

Valluzzi, M. R., D. Tinazzi, and C. Modena (2004). Bond of cfrp strips embedded in lime mortar. Technical report, Innovative materials and Technologies for Construction and Restoration, pp. 70-80, Lecce, June 6-9.

Valluzzi, M. R., M. Valdemarca, and C. Modena (2001). Behaviour of brick masonry vaults strengthened by frp laminates. *ASCE J. Composites for Construction 5(5)*, 163–169.

Van der Plujim, R. (2000). Material properties of masonry and its components under tension and shear. In *in V.V. Neis (Ed)*, Masonry Symp. Saskatchwan, pp. Proc. 6th Can.

Van Zijl, G. (2004). Modeling masonry shear-compression: the role of dilatancy highlighted. *J Eng Mech, ASCE 130(11)*, 1289–96.

Vijay, P. V. and H. V. S. Gangarao (2001). Accelerated natural weathering of glass fibre reinforced plastic bars. In *Proceedings of 4th International Conference on Fibre-Reinforced Plastics for Reinforced Concrete Structures FRPRCS-4*, Baltimore, USA, 1-4 November, pp. 605–614.

Vitruvius (1960). The ten books on architecture. Technical report, Translation M.H.Morgan, Dover Publications, pp. 45-49, New York.

Wendel, M. S. (2001). Significance of midspan debonding failure in frp-plate concrete beams. *Journal of Structural Engineering, ASCE, July 1*, 792–798.

Winkler, E. (1879,1880). Die lage der sttzlinie im gewlbe. *Deutsche Bauzeitung 13,14(130)*, 117–119,127–128,58–60.

Wu, J. S., H. Yuan, and H. Niu (2002). Stress transfer and fracture propagation in different kinds of adhesive joints. *J. of Engineering Mechanics, ASCE 128(5)*, 562–573.

Yang, X., A. Nanni, S. Haug, and C. S. Leung (2002). Strength and modulus degradation of carbon fiber-reinforced polymer laminates from fiber misalignment. *J. Material of Civil Engineering 14(4)*, 320–326.

Yao, J., J. Teng, and J. F. Chen (2005). Experimental study on frp-to-concrete bonded joints. *J. Composites: Part B 36*, 99–113.

Yuan, H., J. G. Teng, R. Seracino, Z. S. Wu, and J. Yao (1994). Full-range behavior of frp-to-concrete bonded joints. *Eng Struct 26(5)*, 553–564.

Zienkiewicz, O. C. and R. L. Taylor (2005). *The Finite Element Method Set*. 6 edition (September 19): Butterworth-Heinemann.

Appendix A

Single curves of normal stress along the anchorage length

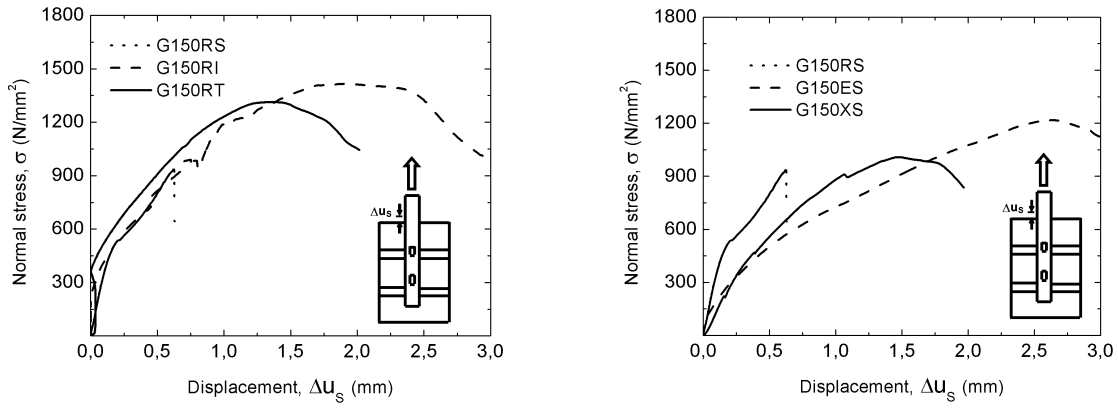
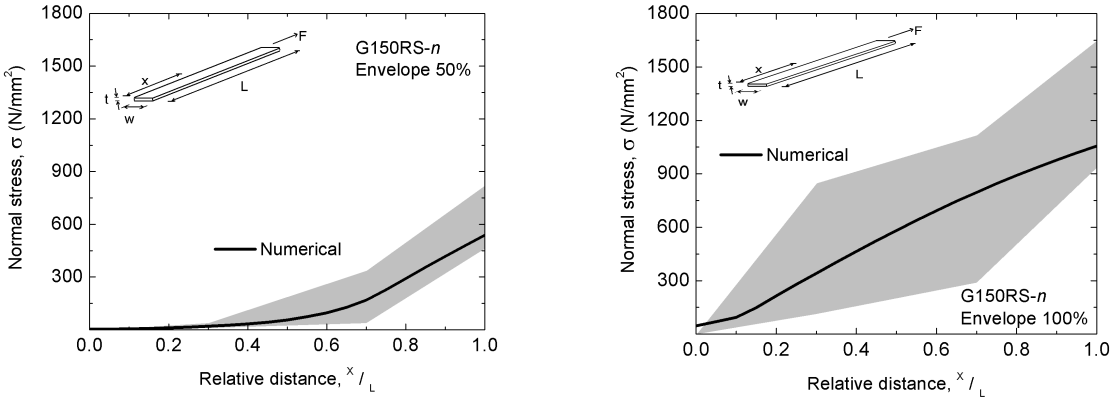


Figure A.1: Typical normal stress-relative displacement at the loaded end: (a) improved anchor specimens; (b) curved shape specimens.

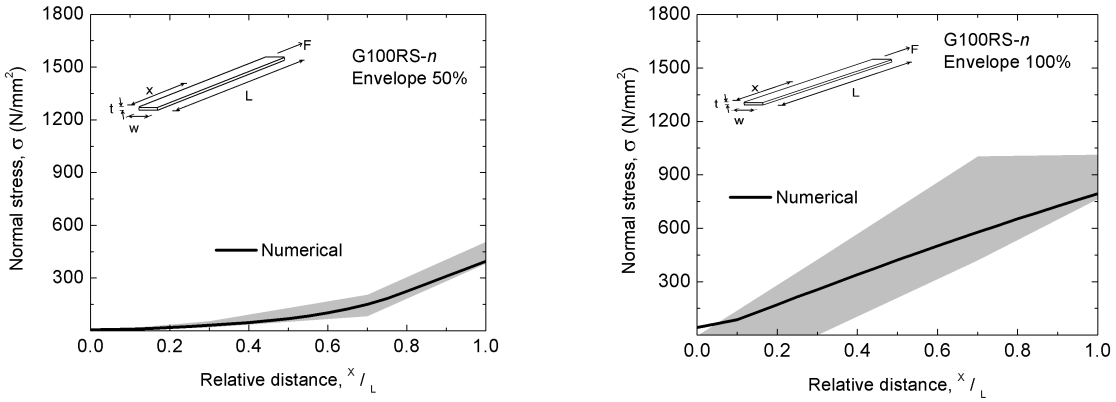
Appendix B

Numerical results and experimental envelopes of normal stress along the anchorage length



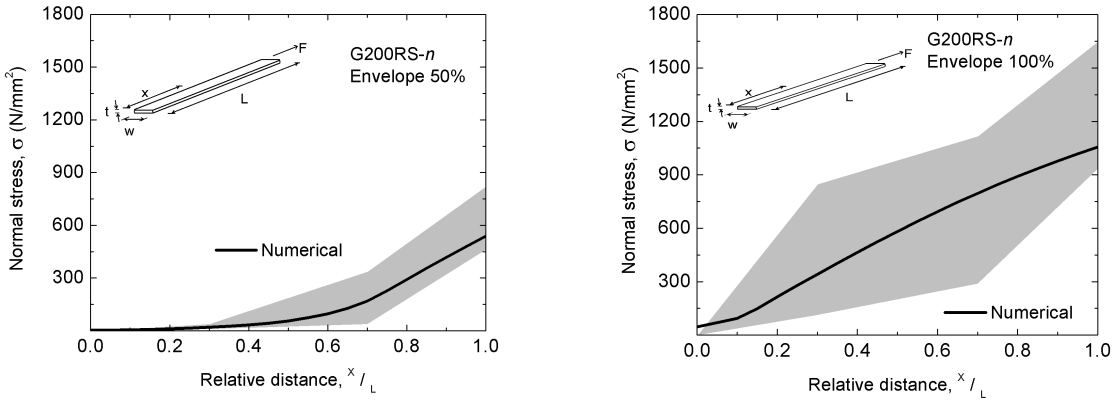
(a) (b)

Figure B.1: Comparison of numerical results and experimental envelopes in terms of the FRP normal stress along the anchorage length for the G150RS-n series at two different load levels: (a) 50% and (b) 100% of the maximum load.



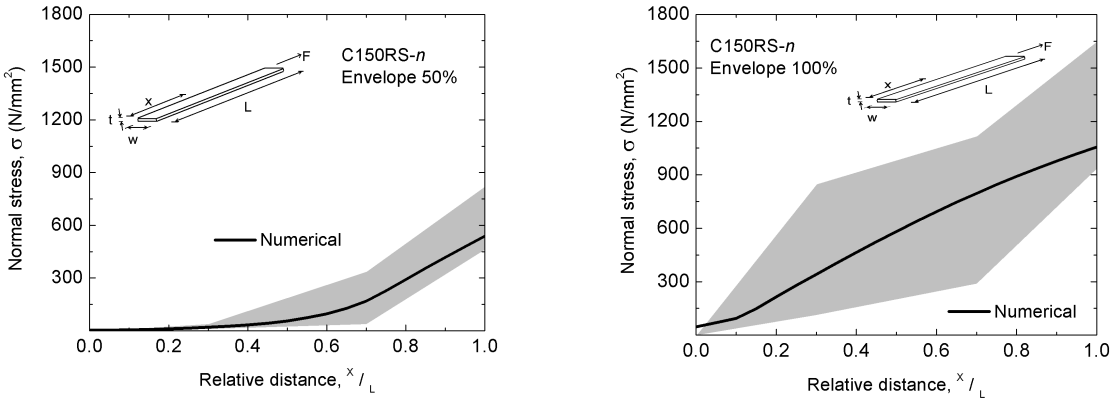
(a) (b)

Figure B.2: Comparison of numerical results and experimental envelopes in terms of the FRP normal stress along the anchorage length for the G100RS-n series at two different load levels: (a) 50% and (b) 100% of the maximum load.



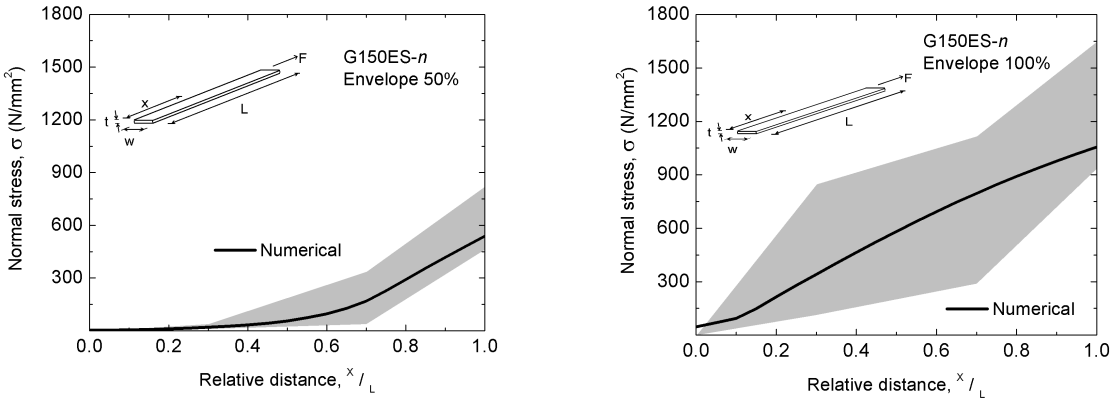
(a) (b)

Figure B.3: Comparison of numerical results and experimental envelopes in terms of the FRP normal stress along the anchorage length for the G200RS-n series at two different load levels: (a) 50% and (b) 100% of the maximum load.



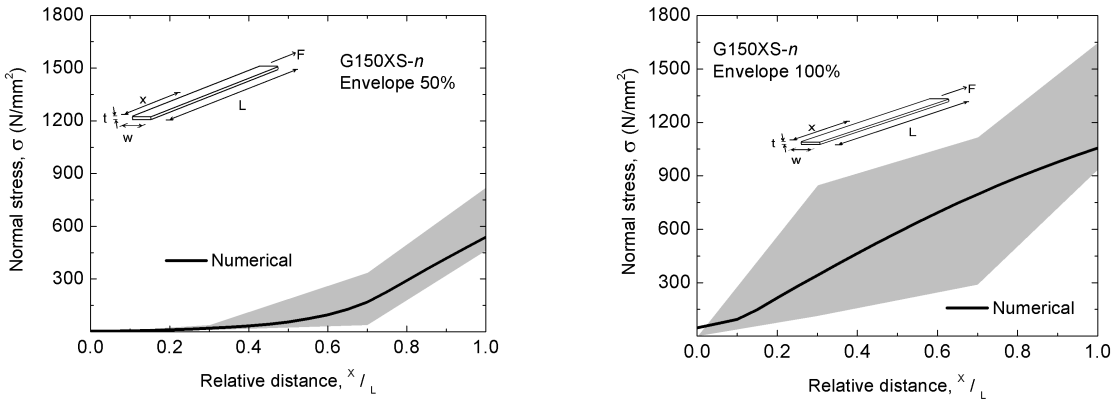
(a) (b)

Figure B.4: Comparison of numerical results and experimental envelopes in terms of the FRP normal stress along the anchorage length for the C150RS-n series at two different load levels: (a) 50% and (b) 100% of the maximum load.



(a) (b)

Figure B.5: Comparison of numerical results and experimental envelopes in terms of the FRP normal stress along the anchorage length for the G150ES-n series at two different load levels: (a) 50% and (b) 100% of the maximum load.

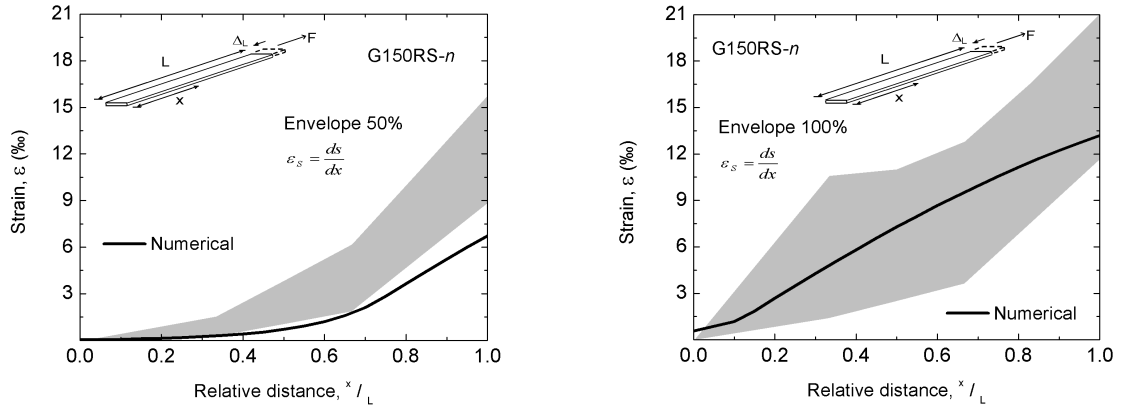


(a) (b)

Figure B.6: Comparison of numerical results and experimental envelopes in terms of the FRP normal stress along the anchorage length for the G150XS-n series at two different load levels: (a) 50% and (b) 100% of the maximum load.

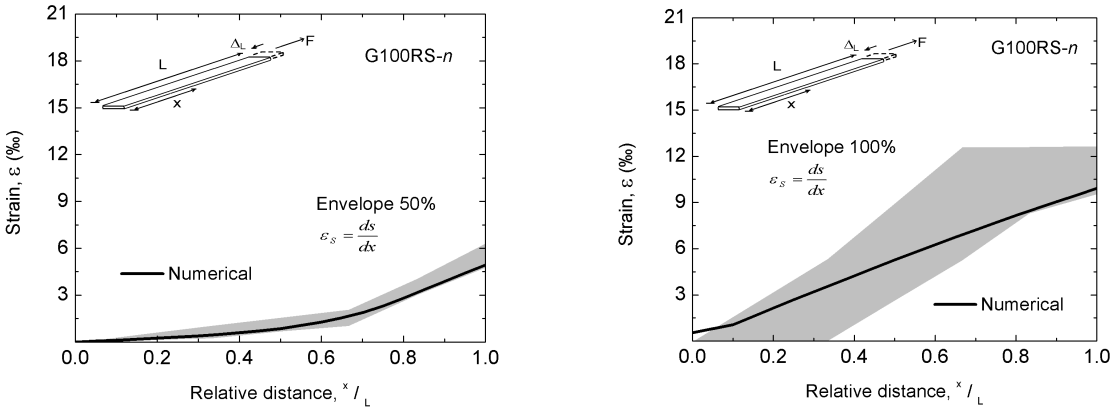
Appendix C

Strains along the anchorage length



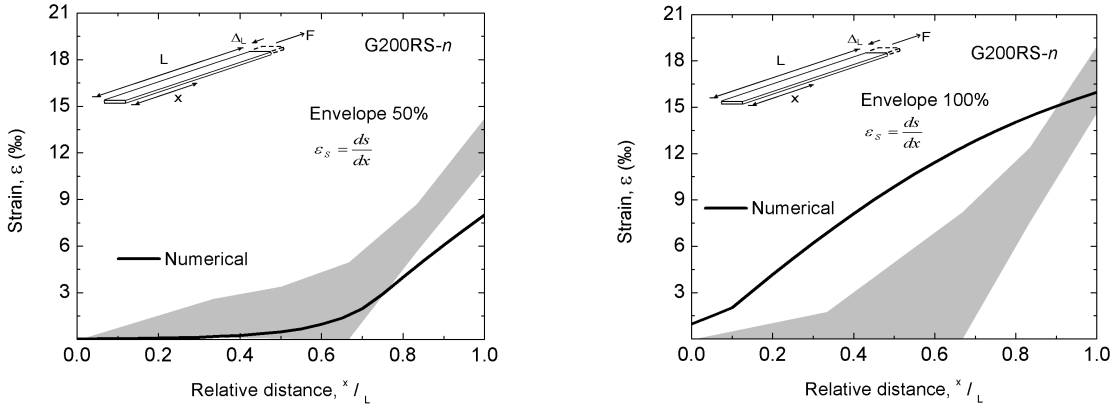
(a) (b)

Figure C.1: Comparison of numerical results and analytical envelopes in terms of the FRP strains along the anchorage length for the G150RS-n series at two different load levels: (a) 50% and (b) 100% of the maximum load.



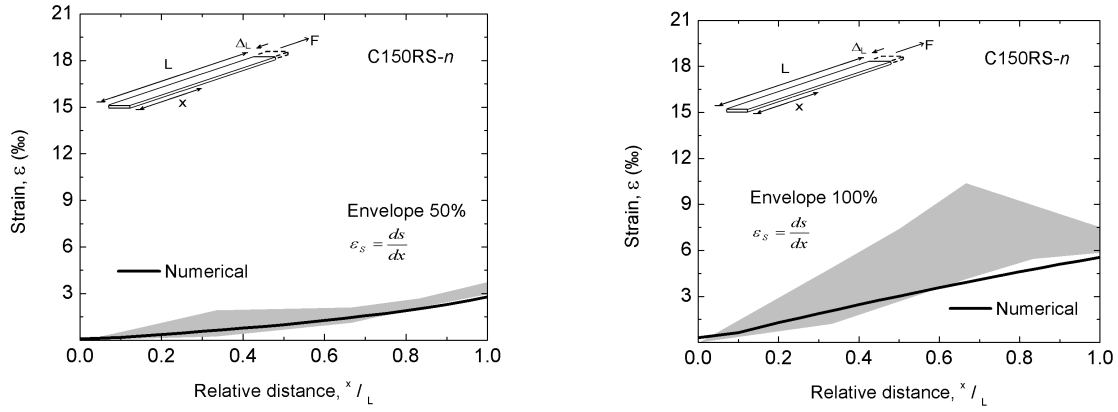
(a) (b)

Figure C.2: Comparison of numerical results and analytical envelopes in terms of the FRP strains along the anchorage length for the G100RS-n series at two different load levels: (a) 50% and (b) 100% of the maximum load.



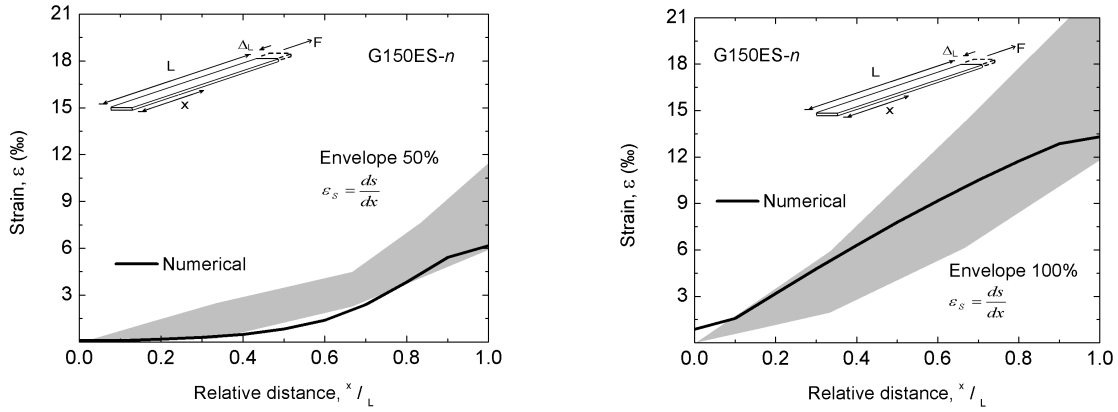
(a) (b)

Figure C.3: Comparison of numerical results and analytical envelopes in terms of the FRP strains along the anchorage length for the G200RS-n series at two different load levels: (a) 50% and (b) 100% of the maximum load.



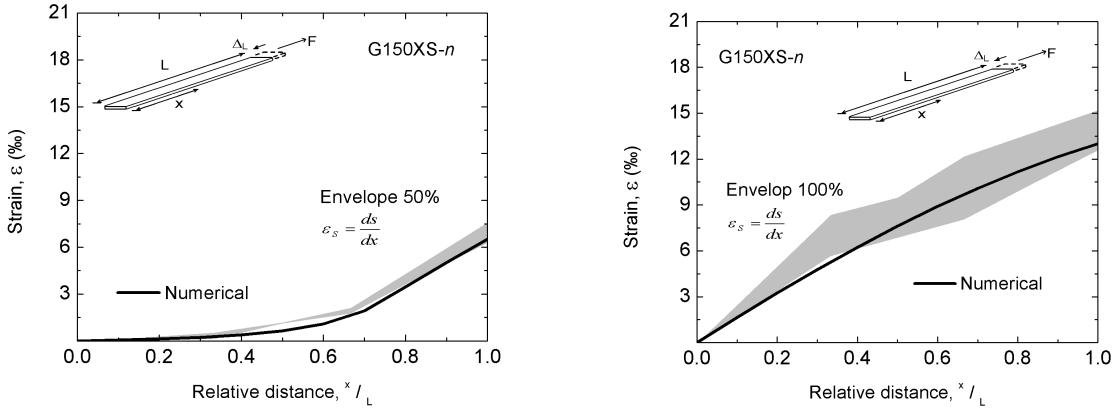
(a) (b)

Figure C.4: Comparison of numerical results and analytical envelopes in terms of the FRP strains along the anchorage length for the C150RS-n series at two different load levels: (a) 50% and (b) 100% of the maximum load.



(a) (b)

Figure C.5: Comparison of numerical results and analytical envelopes in terms of the FRP strains along the anchorage length for the G150ES-n series at two different load levels: (a) 50% and (b) 100% of the maximum load.

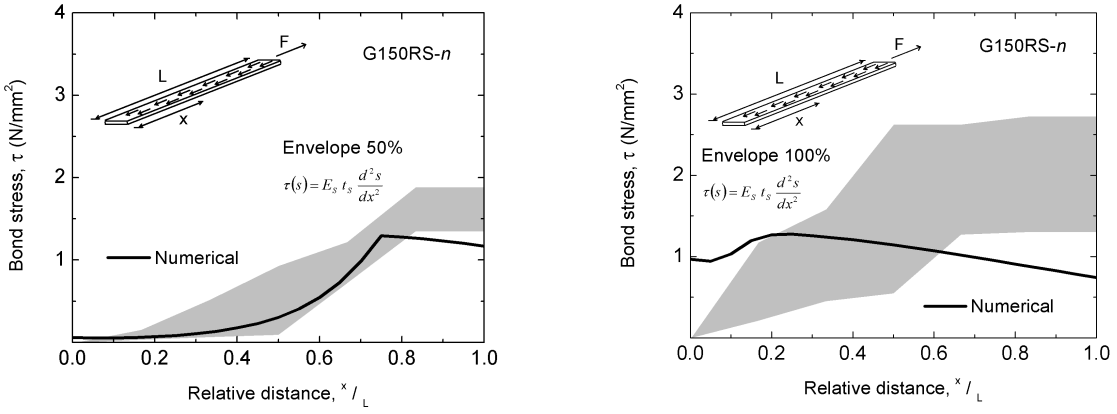


(a) (b)

Figure C.6: Comparison of numerical results and analytical envelopes in terms of the FRP strains along the anchorage length for the G150XS-n series at two different load levels: (a) 50% and (b) 100% of the maximum load.

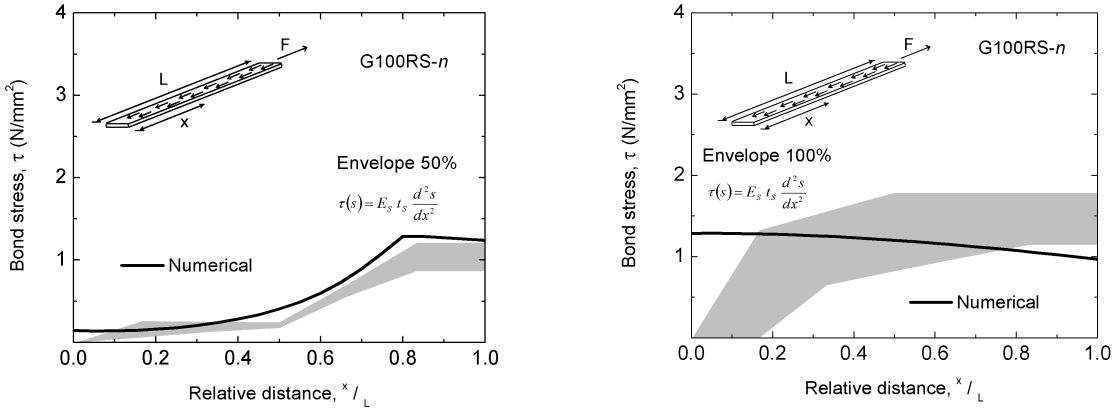
Appendix D

Bond stress along the anchorage length



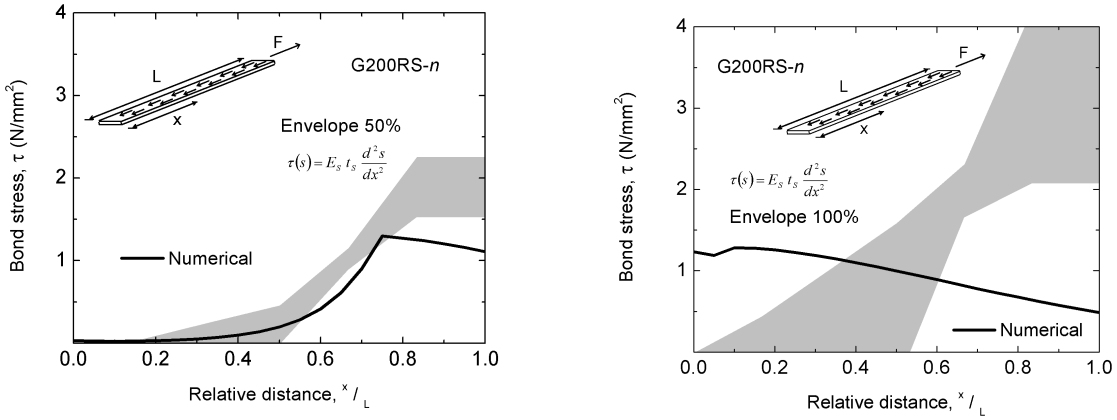
(a) (b)

Figure D.1: Comparison of numerical results and analytical envelopes in terms of the FRP bond stress along the anchorage length for the G150RS-n series at two different load levels (a) 50% and (b) 100% of the maximum load.



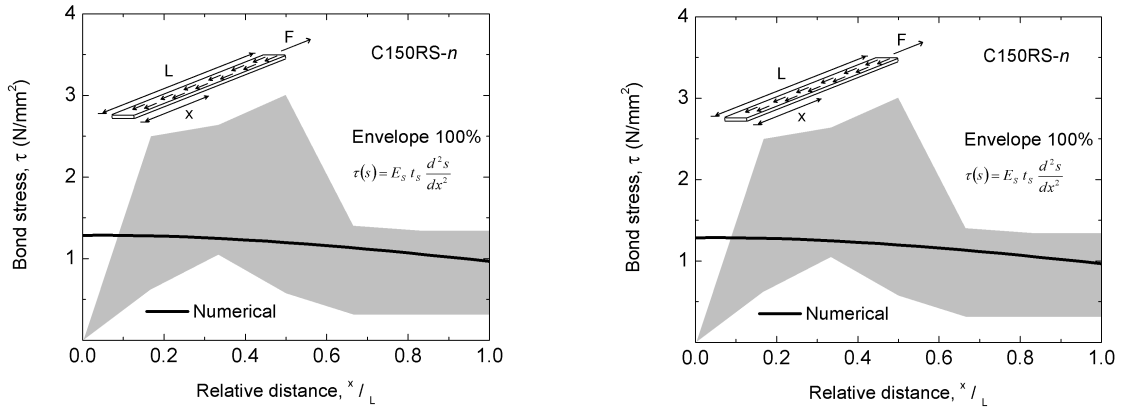
(a) (b)

Figure D.2: Comparison of numerical results and analytical envelopes in terms of the FRP bond stress along the anchorage length for the G100RS-n series at two different load levels (a) 50% and (b) 100% of the maximum load.



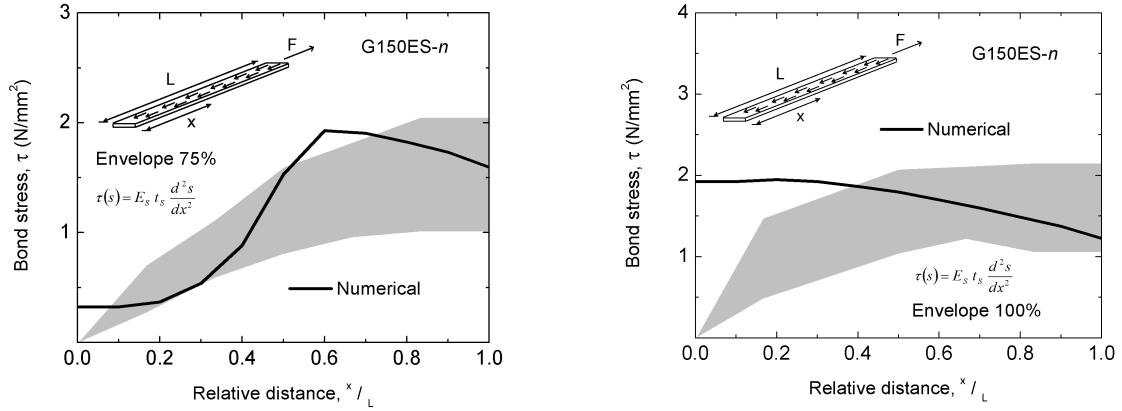
(a) (b)

Figure D.3: Comparison of numerical results and analytical envelopes in terms of the FRP bond stress along the anchorage length for the G200RS-n series at two different load levels (a) 50% and (b) 100% of the maximum load.



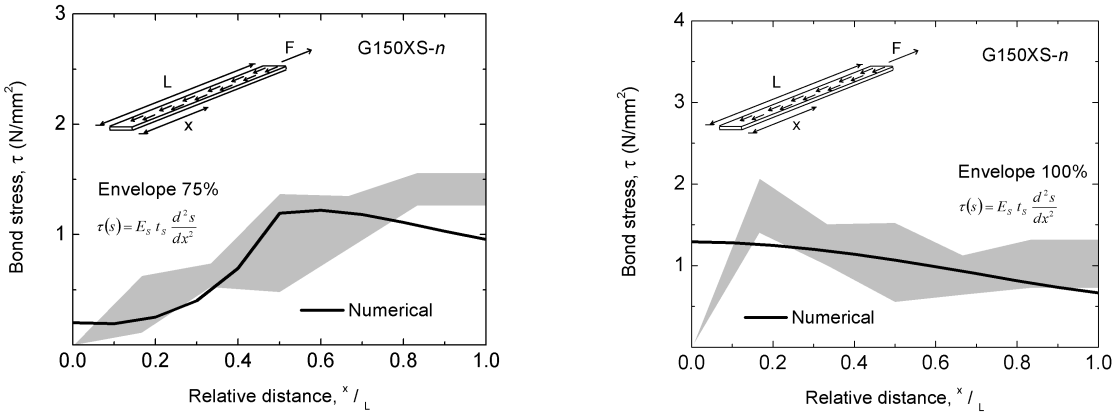
(a) (b)

Figure D.4: Comparison of numerical results and analytical envelopes in terms of the FRP bond stress along the anchorage length for the C150RS-n series at two different load levels (a) 50% and (b) 100% of the maximum load.



(a) (b)

Figure D.5: Comparison of numerical results and analytical envelopes in terms of the FRP bond stress along the anchorage length for the G150ES-n series at two different load levels (a) 50% and (b) 100% of the maximum load.



(a) (b)

Figure D.6: Comparison of numerical results and analytical envelopes in terms of the FRP bond stress along the anchorage length for the G150XS-n series at two different load levels (a) 50% and (b) 100% of the maximum load.

Appendix E

Local bond stress-slip relationships

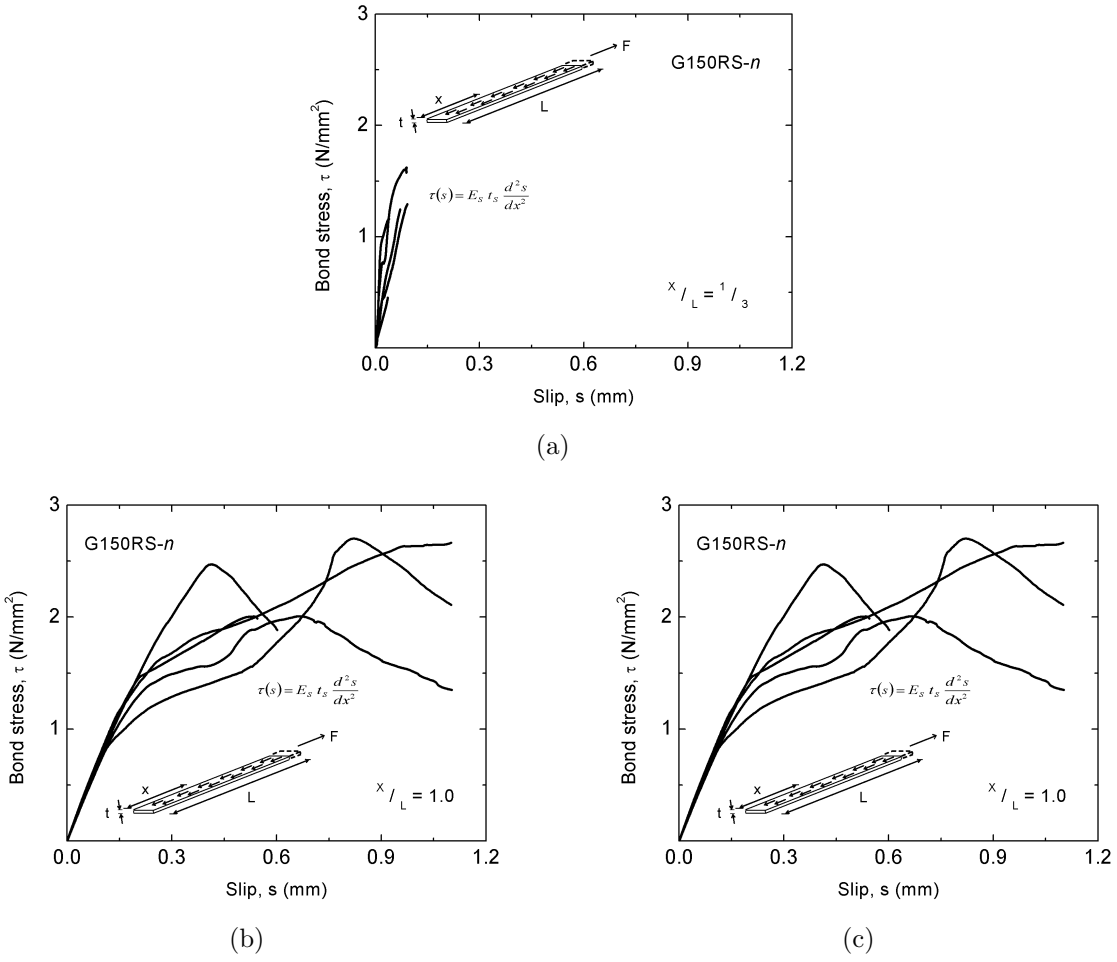
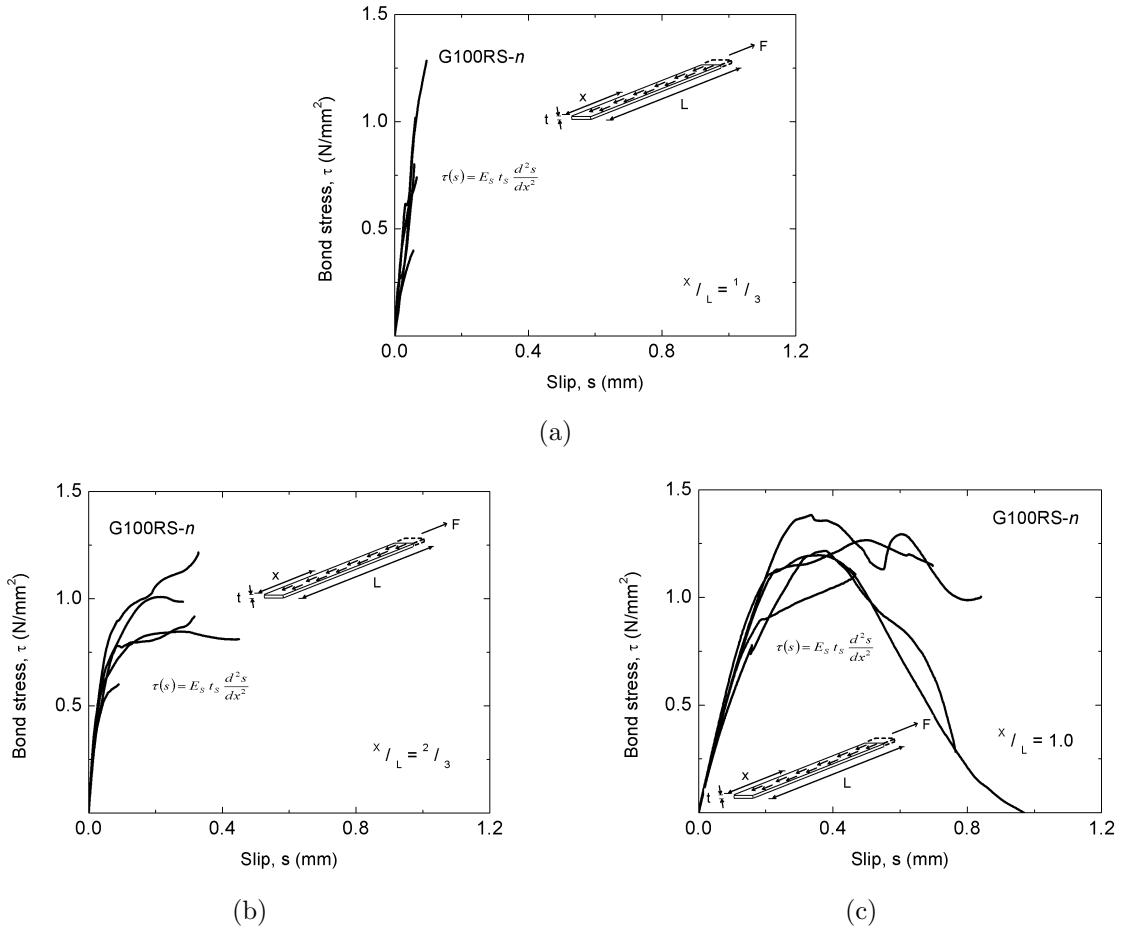


Figure E.1: Analytical local bond stress-slip for the G150RS-n specimen at three different positions: (a) one third of L; (b) two thirds of L and (c) loaded end (full L).



(a)

(b)

(c)

Figure E.2: Analytical local bond stress-slip for the G100RS-*n* specimen at three different positions: (a) one third of L; (b) two thirds of L and (c) loaded end (full L).

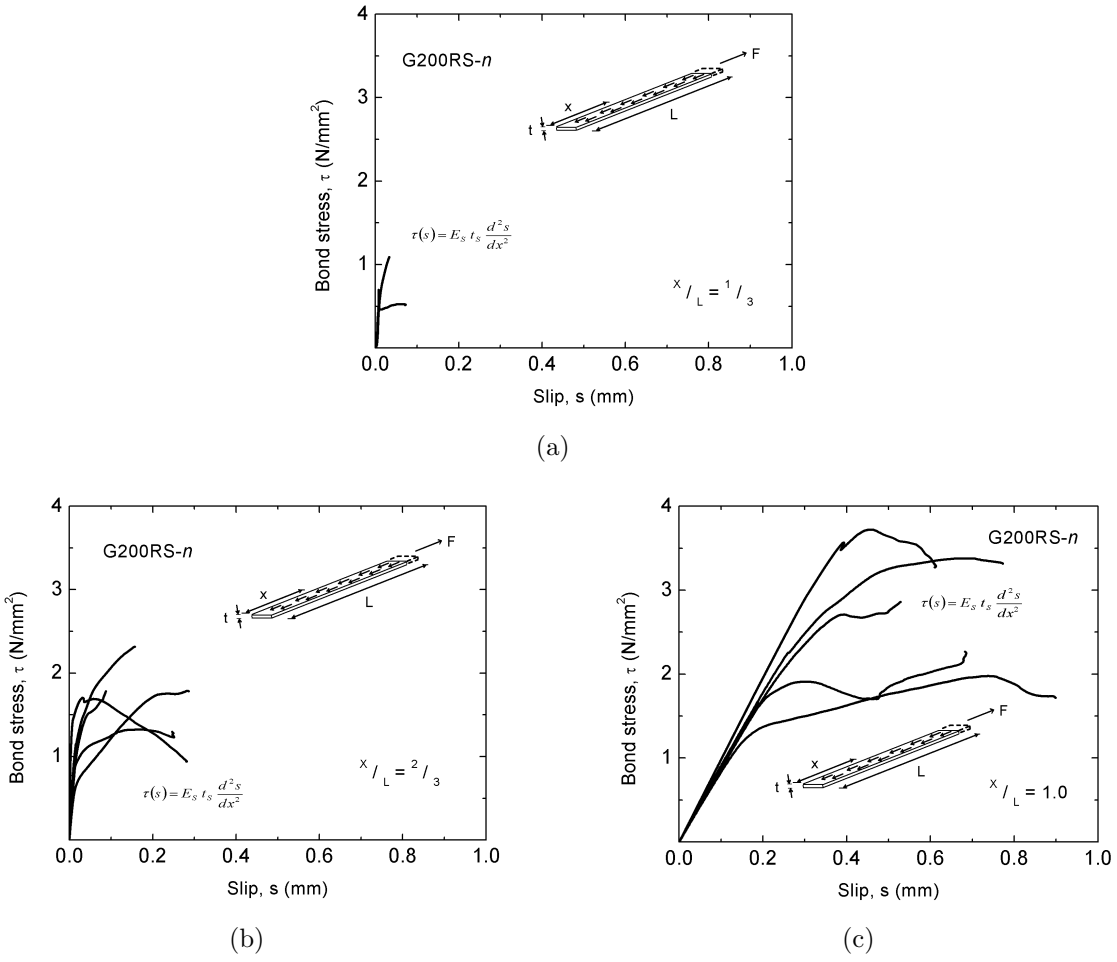


Figure E.3: Analytical local bond stress-slip for the G200RS-n specimen at three different positions: (a) one third of L; (b) two thirds of L and (c) loaded end (full L).

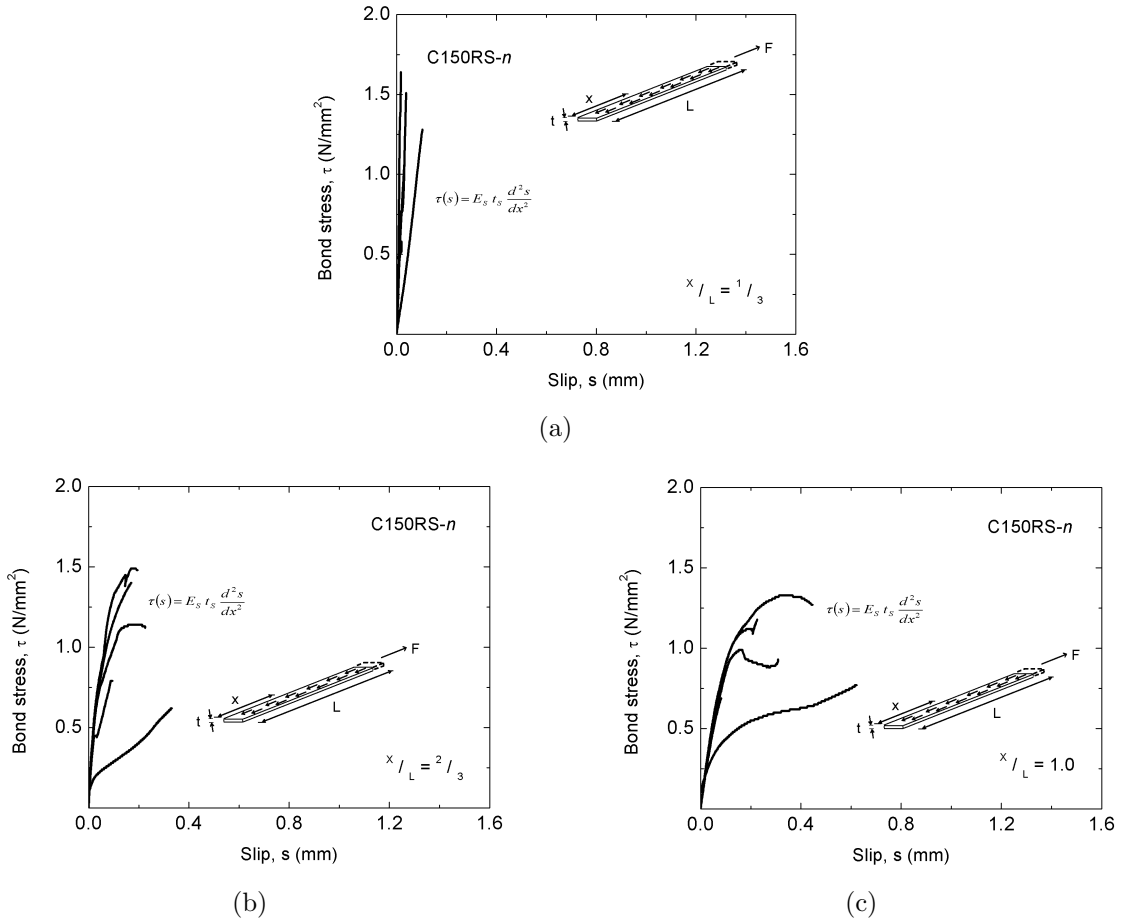


Figure E.4: Analytical local bond stress-slip for the C150RS-n specimen at three different positions: (a) one third of L; (b) two thirds of L and (c) loaded end (full L).

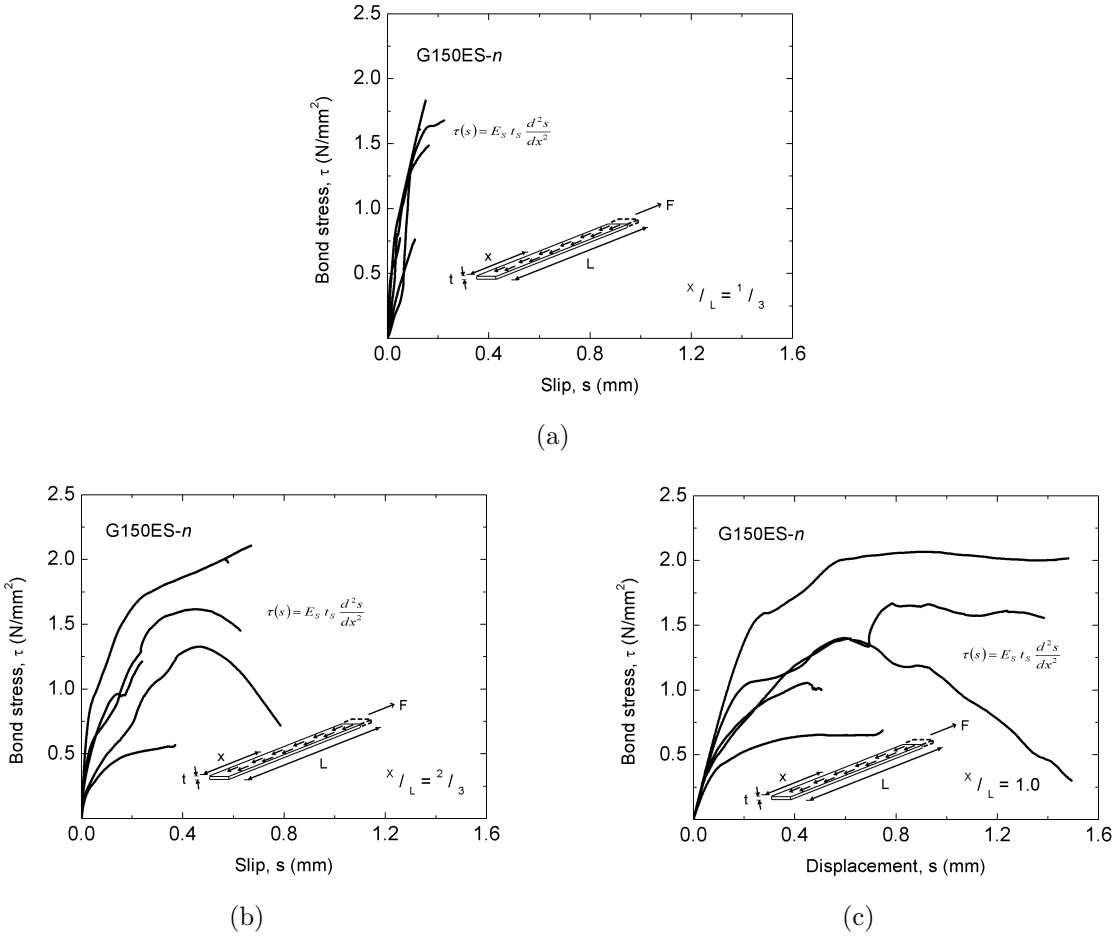


Figure E.5: Analytical local bond stress-slip for the G150ES-n specimen at three different positions: (a) one third of L; (b) two thirds of L and (c) loaded end (full L).